Numerical Simulations of Primary Break-Up in Two-Phase Flows

by

Nefeli Dimela

Supervised by: Salvador Navarro-Martinez and Stelios Rigopoulos

Department of Mechanical Engineering
Imperial College London
Prince Consort Road
London SW7 2AZ

This thesis is submitted in partial fulfilment of the requirements for the degree of Doctor of Philosophy in Mechanical Engineering of Imperial College London and the Diploma of Imperial College London

August 4, 2017

Abstract

Liquid-Gas interactions and break-up processes are found in many technological and environmental applications, from Internal Combustion and Gas Turbine engines to food processing and manufacturing. Their complete characterisation at realistic Weber and Reynolds numbers is not possible, due to the vast range of scales integrated and the requirement of a 'minimum' computational mesh size to capture these scales. To this day, a number of questions remain unanswered, with relative research still ongoing. It is crucial to understand such phenomena so that any technological applications can be optimised and the environmental impact can be reduced. Currently, there is a high need to develop appropriate numerical modelling tools that provide both mass conservation and accurate interface topological properties. Two common interface modelling approaches are the Volume of Fluid and the Level Set, typically coupled into CLSVOF methods to ensure improved surface representation and good mass properties. In this work, a novel in-house Mass Conservative Level Set (CMLS) method is developed and validated extensively. The CMLS novelty is in the Level Set coupling with the Volume of Fluid, being processed only when necessary, providing a faster and more robust approach. Doing so, some numerically imposed limitations due to the 'physics' and 'stability', are overcome.

The novel CMLS is employed for primary break-up investigations, in a single liquid droplet and jets. Single droplet break-up remains a benchmark test case, as it provides good foundations for liquid jet break-up and spray atomisation modelling. In such processes, the main effective parameters considered are the Weber and Reynolds numbers, along with the Ohneshorge (droplets) and Dynamic Pressure ratio (jets). Contrary to most studies, this work employs the surface density evolution using the $\Sigma - Y$ model. The droplet break-up cases, show a strong correlation between the break-up initiation time and the Ohneshorge number, whilst as the Weber increases so does the droplet complete break-up time. This is of particular interest as at higher Weber numbers, surface density effects become negligible and thus by definition the complete break-up time should in fact decrease. However, similar behaviours were noted in previous studies. The droplets surface density evolution shows a 'quasi-independent' relationship with the gas Weber. In the jets, a strong correlation between the surface density and ligament formation exists. However, the surface density is 'quasi-independent' of the liquid Reynolds and the gas Weber. The gas boundary layer presence in jets, shows to both reduce and delay any liquid/gas interface perturbations and the potential break-up.

To summarise, the present investigations are generally in good agreement with previous studies, with minimal contradictions in cases. The novel CMLS capabilities show promising results both in the two- and three- dimensional space. This work provides good foundations for a slightly alternative research approach in two-phase flows modelling.

Copyright Declaration

Declaration of Originality

I, Nefeli Dimela declare that the work presented in the thesis *Numerical Simulations of Primary Break-Up in Two-Phase Flows* is my own and that anyone else's work has been appropriately referenced.

Acknowledgements

First and foremost, I would like to thank my supervisor, Dr. S. Navarro-Martinez, for his excellent intellectual guidance and psychological support throughout the research process. He has been extremely supportive and genuine, even in times of pessimism and confusion from my behalf. I would also like to acknowledge the financial support from the EPSRC and DTA award through Imperial College, without which this work could not have been accomplished.

Next, I would like to thank my fellow PhDs and friends, Teddy Szemberg O$'$Connor, Nicolas Alferez, Maria Esperanza Barrera-Medrano, Ioannis Pesmazoglou, Fabian Sewerin and Petros Akridis, for always supporting me and encouraging me to continue but also providing me with useful comments and guidance throughout.

I was also very lucky to meet Alexandros Charogiannis, Ioan Hadade and Edouard Minoux, that made the experience much more enjoyable by sharing similar anxieties but also research-breakthroughs and a lot of laughs. Here, I want to thank Imperial College Gym facilities for allowing me to take out all my PhD frustration, on a daily basis.

I sincerely thank my *parents*, my amazing *grandparents*, my family friends Mireille and Helen for never leaving my side; but always being there supporting and trusting my choices. Finally I would like to thank my puppy 'Chico' and Peter, who also contributed in different ways.

Contents

List of Figures

List of Tables

Nomenclature

Symbol	Description	Units
ADV	Advection Term	-
ALE	Arbitary Lagrangian-Eulerian	-
BC	Boundary Conditions	-
CBC	Convection Boundedness Criterion	-
CDS	Central Difference Scheme	-
CFD	Computational Fluid Dynamic	-
CFL	Courant-Friedrichs-Lewy	-
CGSOL	Conjugate Gradient Solver	-
CICSAM	Compressive Interface Capturing Scheme Arbitrary Meshes	-
CLSVOF	Coupled Level-Set / Volume of Fluid	-
CON	Convective Term	-
CPU	Central Processing Unit	-
CV	Control Volume	-
CSF	Continuum Surface Force	-
DIFF	Diffusive Term	-
DNS	Direct Numerical Simulation	-
ELSA	Eulerian-Lagrangian Spray Atomization	-
ENO	Essentially Non-Oscillatory	-
FV	Finite Volume	-
GFM	Ghost Fluid Method	-
GT	Gas Turbine	-
IC	Internal Combustion	-
LES	Large Eddy Simulations	-
LS	Level-Set	-
LHS	Left Hand Side	-
NS	Navier-Stokes	-
NVD	Normalised Variable Diagram	-
PLIC	Piecewise-Linear Interface Calculation	-
RANS	Reynolds Averaged Navier-Stokes Equations	-
RHS	Right Hand Side	-
RG	Runge Kutta	-
SIMPLE	Semi-Implicit Method Pressure Linked Equation	-
SLIC	Simple Line Interface Calculation	-
TVD	Total Variation Diminishing	-
UDS	Upwind Difference Scheme	-
UQ	Ultimate-Quick	-
VOF	Volume of Fluid	-
WENO	Weighted Essentially Non-Oscillatory	-

Symbol	Description	Units
sgn	sign function	-
A	Acceptor Cell (subscript)	-
A_{liq}	Liquid Area	-
C	Color Function	-
Ca	Capillary Number	-
C_{KH}	Kelvin-Helmholtz Constant	-
D	Donor Cell (subscript)	-
E	East	-
e	east face	-
F	Smooth Function	-
f	Cell Face (subscript)	-
H	Heaviside Step Function (Marker Function)	-
h_L	Liquid Height	-
h_G	Gas Height	-
L	Left	-
L	Characteristic Linear Dimension	-
l	left face	-
La	Laplace Number	-
M	Momentum/Dynamic Pressure Ratio	-
Ma	Mach Number	-
N	North	-
n	north face	-
N_{cell}	Number of Cells	-
Oh	Ohnesorge Number	-
R	Right	-
r	right face	-
S	South	-
s	south face	-
U	Upwind Cell (subscript)	-
W	West	-
w	west face	-
∇	Del Operator (Vector Differential Operator)	-
$(\nabla_\phi)_D$	Normal Vector to Interface	-
∇F	Distance Function	-
c	Courant Number	-
C_D	Drag Coefficient	-
Ca	Capillary Number	-
c_S	Sound Velocity	-
C_T	Taylor Parameter	-
D_{32}	Sauter Spray Diameter	-
D_{max}	maximum cross-stream dimension	-
d_f	Cell Distance between ϕ_D and ϕ_A	-
D_Σ	Surface Area Diffusion Coefficient	-
dS	Interface Boundary	-
$F_{i,j}$	Liquid Volume Flux	-
f_{mass}	Liquid Volume Mass	-
F_E	Characteristic Coefficient	-
F_W	Characteristic Coefficient	-

Symbol	Description	Units
F_o	Level-Set Function Prior to Re-initialisation	
$\mathbf{f}$	Force Per Unit Volume	N/m^3
f	Scaling Frequency	-
f_σ	Surface Tension (body) Force	N
g_i	Gravitational Force	-
H	Heaviside Step Function	-
$h(\alpha)$	Interface Location	-
$\mathbf{I}_S$	Surface Identity Tensor	-
L	Characteristic Linear Dimension	-
$\dot{m}$	Mass Flow Rate	kg/s
$\mathbf{m}$	Cell Face Normals	-
$\mathbf{n}$	Unit Normal	-
Oh	Ohnesorge Number	-
$[[P]]$	Pressure Jump	-
p	Static Pressure	Pa
$\mathbf{p}$	Normal Vector on Element Edge	-
P^c	Pressure Corrector	-
P^n	Guessed Pressure Field	-
$u^{-,+}$	Cell Face Velocities	-
$\mathbf{u}$	Velocity Field Vector	-
$\tilde{u}$	Velocity Corrector	-
u^n	Guessed Velocity Field	-
U	Maximum Velocity of Gas or Liquid	m/s -
U	Characteristic Flow Velocity	-
U_L	Liquid Velocity	m/s -
U_G	Gas Velocity	m/s -
U_{air}	Air Velocity	m/s -
U_c	Interface Convection Velocity	m/s -
V_{liquid}	Liquid Volume	-
$V_{i,j}$	Liquid Volume	-
V_s	Characteristic Velocity Scale	-
S	Interface	-
S_ϕ	Source Term	-
t	Time	s
$\mathbf{t}$	Unit Tangent	-
$\mathbf{T}$	Surface Tension Tensor	N/m
T	Temperature	K
T_{IN}	Initiation Time	-
T_B	break-up Initiation Time	-
Y	Mean Liquid Volume Fraction	-
We	Weber Number	-
Re	Reynolds Number	-
$\mathbf{u}_1, \mathbf{u}_2$	Interface Velocity Vectors	-
$\mathbf{V}$	Normal Velocity	-

Greek Letters	Description	Units
α	Minimum Distance of Interface Line to Origin	-
α	Discretisation Coefficient	-
α	Small-scale Interfacial area generation	-
α_R	Characteristic Coefficient	-
α_L	Characteristic Coefficient	-
β	Discretisation Coefficient of All Other Sources	-
Γ	Diffusion Coefficient	m^2/s
$\Delta x = \Delta y = \Delta z = \Delta$	Grid Size in x-, y- and z- direction	-
Δt	Time Step	-
δ	Interface Numerical Thickness	-
δs	*Dirac* δ-function	-
θ	Angle	rad
θ_ψ	Level Set Weighting Factor	-
κ	Curvature	
κ_Γ	Interface Curvature	-
λ_{KH}	Kelvin-Helmholtz Wavelength	-
λ_{RT}	Rayleigh-Taylor Wavelength	-
μ	Viscosity	kg/ms
ξ	Blending Factor	-
$\Phi(t)$	First Order Differential Equation	-
ϕ	Volume of Fluid	-
ϕ^S	Smooth Volume of Fluid Marker	-
ψ	Level Set	-
ρ	Density	kg/m^3
$\bar{\Sigma}$	Liquid Surface Density	-
σ	Surface Tension Coefficient	N/m
Σ	Surface Density	1/m
Σ_{eq}	Equilibrium Surface Density	-
τ_{ij}	Shear Stress Tensor	N/m^2
τ	Pseudo-Time	s
ω_{RT}	Rayleigh-Taylor Growth Rate	-

Chapter 1

Introduction

1.1 Multiphase Flows

1.1.1 Scope

Liquid-Gas multiphase fluid flows are found in every aspect of life, from environmental to industrial applications, such as paint sprays, aeronautics, automotive engineering, manufacturing, metal processing and turbines [90]. Most engineering and energy processes deal with multiphase flows on some level [102], typically within the context of combustion and sprays. Over the last decades any field dealing with multiphase fluid flows have rapidly developed at the expense of environmental sterility. There is a vast range of ongoing research in understanding and predicting the instabilities involved in these liquid-gas interaction processes.

In the present environmental and energy fields, the combustion systems are now designed to reduce the level of harmful emissions and increase efficiency so fuel consumption is minimised. However, due to the complex geometries and flow types integrated in Gas Turbine fuel injectors, many difficulties arise during modelling. In the field of aeronautics, turbines and power plants, emphasis has been given on reducing the combustion noise so that any environmental noise pollution is minimised. In doing so, low emission combustors are developed that are liable to instabilities in the combustion chambers, resulting in flame blow outs [83] [90] [102]. This is due to the turbulent nature of the high speed gas flow, both at the combustor inlet and inside the fuelling system [83] [130].

In marine and steam turbine applications, both the production and performance can be improved by increasing the mixing process and reducing the drag force produced during the wind/blade interactions, respectively. To do so, the fuel injection systems are remodelled to provide higher energy efficiency. Meanwhile, the life of the pumps and valves is improved by strongly minimising any cavitation present with the aid of multiphase fluid flow simulations and modelling of such systems. Considering the extensive use of such complex flows, it is mandatory to better understand all flow integrated processes, to obtain efficient and improved models for real-life applications. In doing so, any environmental impacts can be reduced [90] [130] and all technological applications can be optimised whilst the performance levels will be maintained.

In the physics-context, fluids refer to liquids and gases that are significantly distinctive yet obey the same motion laws. Fluid flow can be driven by a range of forces, distinguished as body forces (i.e. gravity) and surface forces (i.e. pressure, shear and surface tension). Multiphase flows have more than one phase, from which are generally classified as gas-particle (i.e continuous fluid occupied by discrete solid particles) and bubbly flows (i.e. continuous fluids occupied by gaseous bubbles) [40].

In multiphase fluids context, one can distinguish between flow and model types. Two main flow types are the *disperse* flows and *segregate* flows. Disperse flows suggest that one continuous volume phase is widely distributed with drops, bubbles or particles from the other phase. Segregate flows, are occupied by more than one distinctive fluids of continuous streams, separated by interfaces [13].

Despite these two limiting flow states, further sub-separation phases are integrated within each. In the disperse flow framework, model equations are required to account for the phase interactions and particle dispersions in turbulence. Here, two model types can be distinguished, that of trajectory and two-fluid. In the trajectory models, the phase is studied by following the representative large particles present with respect to the drag, lift and momentum forces. The flow details surrounding each particle, is further based on the acting forces of drag, lift and momentum, alternating the particles trajectory.

In the two-fluid models, the phase is considered as a 'second' continuous phase that interacts with the general continuous phase. Here, the leading properties are the exchange of mass, momentum and energy [13]. In the two-fluid models, the disperse phase discrete nature is negligible and only the continuous phase effects are approximated during theoretical or computational solutions. In the sections to follow, two-phase flows are considered in the context of liquid-gas interactions, typically found in Gas Turbines and Internal Combustion engines.

1.1.2 Liquid-Gas Interactions in Jets

In many industrial applications such as a typical liquid fuel jet engine, droplets are formed at the outlet of the injector nozzle, due to high-speed injection spray. This process is known as *Atomisation* and is driven by multiphase flow dynamics. At first, it would be appropriate to accurately characterise some of the terms involved in these processes.

The term "spray" describes a gas jet-like flow conditions, where due to surrounding gas, a liquid phase is transformed into a collection of immerse solid or liquid droplets moving in a regulated manner. The term "atomiser" refers to the device via which a fluid flow is passed under controlled direction, resulting to spray formation by the liquid flow and downstream [40].

Considering the spray at the nozzle exit, two distinct regions can be considered, defined as primary and secondary, Fig. 1.1. The liquid jet break-up evolution is strictly linked to the small disturbances at the liquid surface integrated within. The disturbances are primarily caused by the liquid jet interaction with the ambient gas [90].

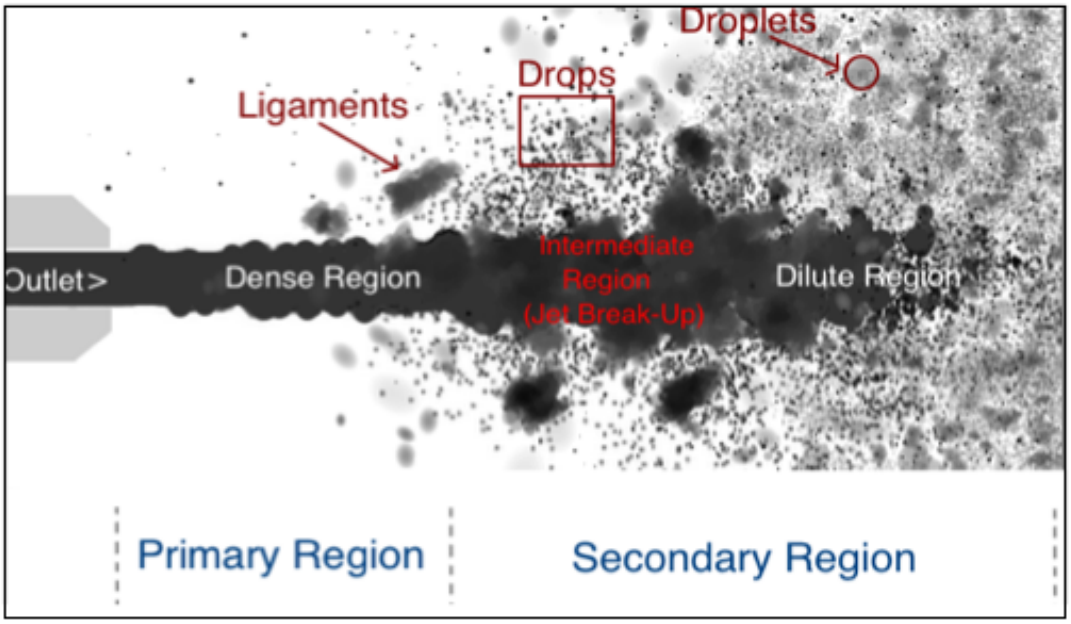

Fig. 1.1: Liquid Jet Atomization: Classification between Primary and Secondary regions; along with any various sized scales integrated within.

1.1.2.1 Primary Region

The primary region is the spray region just at the outlet of the nozzle where droplets and large blobs of fluid co-exist. The primary break-up region, highly influences the formation of the dispersed droplets and the mixing behaviour between gas and liquid. Here, the flow is characterised by the liquid and gas interactions from the Rayleigh-Taylor and Kelvin-Helmholtz instabilities, Fig. 1.1, where the latter is key for turbulence creation.

With time these instabilities grow, resulting to 'ligaments' and 'droplets' formation under the aerodynamic interaction processes, whilst further down smaller scale droplets of larger population are produced Fig. 1.1. As these instabilities are well defined both in time and space, whilst their interfacial surface area is rather small, a Eulerian method is usually employed to resolve the interface [130]. Such approach is both computationally wise and more affordable, since in such cases the main focus is at some region of the flow field and not the individual particles trail.

1.1.2.2 Secondary Region

As the liquid break-up further develops, the Secondary region forms, described as a disperse droplet region away from the nozzle outlet, with droplets being completely formed (atomised liquid) and are quasi-independent of the nozzle size [15], Fig. 1.1. Here, the interfacial surface area is very large, making Eulerian approaches very cost ineffective.

The droplets present are well defined and rather geometrically simple, making Lagrangian tracking methods more effective for numerical investigations, by enabling individual tracking of these formed droplets. Therefore, switching between Eulerian and Lagrangian methods when necessary is a popular approach, so that the primary and secondary regions can be modelled appropriately and is followed by number of researchers [7][85][108].

1.1.2.3 Liquid Jet Instabilities

During liquid-gas interactions a liquid phase comes in contact with the gas-phase and under high enough gas flow conditions, liquid parts enter the gas phase in the form of various sized ligaments or droplets. Such processes are typical of liquid jet break-up and spray atomisation, leading to numerical modelling complexities. To decrease those, research studies often investigate the isolated fundamental phenomena, from a single liquid drop break-up/deformation to typical jet-integrated phenomena like the Plateau-Rayleigh, Rayleigh-Taylor and Kelvin-Helmholtz jet instabilities.

These phenomena are mostly created from the shear force developed at the interface due to the speed difference, during the gas and fuel injections. The Plateau-Rayleigh phenomena regards cases at quite low velocity, where the exiting liquid stream from the nozzle region breaks into droplets, due to surface tensions decreasing the surface area.

Such phenomena, will occur provided the liquid stream cross-section wavelength is larger than its circumference [130]. The Plateau-Rayleigh instability is closely coupled with the Rayleigh-Taylor instability. The latter one forms due to buoyancy properties between two fluids of different densities. Here, the perpendicular destabilising gravitational forces are higher than the restoring forces of dissipation and interfacial tension, giving rise to the lighter material. Consequently, wavelength perturbations develop from linear into a non-linear growth phase, resulting to the ligament and droplet formation mentioned earlier [130][40].

Finally, the Kelvin-Helmholtz instability develops when existing small scale perturbations pull kinetic energy from the shear flow. Provided the interface of two fluids is characterised by sharp velocity gradients (i.e. large velocity difference from one fluid to another), small wave-like perturbations will rapidly grow into larger waves [40][23]. The instabilities formed due to Rayleigh-Taylor, are usually larger than the ones formed from Kelvin-Helmholtz instabilities, whilst the latter ones 'drive' any laminar to turbulence transitions.

1.1.2.4 Dimensionless Parameters in Two-Phase Flows

In multiphase flows studies, there is a range of non dimensional numbers that are highly important and dependant on the relative driving processes of the flow. The most common ones used, particularly in Atomization, are the Reynolds (Re), Weber (We), Capillary (Ca), Momentum/Dynamic Pressure Ratio (M) and Ohnesorge (Oh) numbers; summarised in Table 1.1. Here, ρ and μ is a reference density and viscosity, respectively, whilst the subscripts L and G, denote Liquid and Gas.

The Reynolds number is the ratio between inertial to viscous forces whilst the Weber number is defined as the ratio between inertial to surface tension forces. Generally speaking, higher Re suggests higher We that usually leads to droplet break-up and flow instabilities. The Capillary number accounts for the liquid viscous to surface tension forces across a liquid/gas interface. The Ohnesorge number is defined by the liquid viscous to the inertial and surface tension forces ratio, enabling a comparison between viscous and capillary forces. It is extracted through the velocity component elimination between Re and We numbers.

Non Dimensional Flow Parameters	**Expressions**
Weber	$\mathrm{We}_L = \frac{\rho_L U_L^2 \ell}{\sigma}, \quad We_G = \frac{\rho_G U_G^2 \ell}{\sigma}$
Reynolds	$Re_L = \frac{\rho_L U_L \ell}{\mu_L}, \quad Re_G = \frac{\rho_G U_G \ell}{\mu_G}$
Momentum Ratio	$M = \frac{\rho_G U_G^2}{\rho_L U_L^2}$
Capillary	$Ca = \frac{\mu U}{\sigma}$
Ohnesorge	$Oh = \frac{\mu}{\sqrt{\rho \sigma \ell}}$

Table 1.1: Common non-dimensional flow parameters in spray atomization.

One should note that in such processes, there are more non dimensional parameters, which are not used in this work. Both Re and We, are distinct for liquids and gases. However, in Ca and Oh, the velocity U, density ρ and viscosity μ are for liquid strictly, as during liquid/gas interactions the flow quality further downstream is mainly affected by the liquid structures. The ℓ variable is a characteristic dimension, which in this work is typically taken as the gas or liquid inlet thickness. Finally, U is the characteristic velocity of the gas or liquid and σ is the surface tension coefficient.

The presence of surface tension ultimately prevents infinite droplet break-up and introduces stability in the system according to Thermodynamics. At large Reynolds, the boundary layer is small which significantly affects both the potential break-up and any filaments created. The Momentum or Dynamic Pressure is the ratio of the density and velocity between the liquid and gas present. This ratio typically distinguishes the jet types. For $M << 1$, one considers a Diesel-type injector where $U_L >> U_G$ denoting jet-like conditions. For $M > 1$, denotes Air-Blast 'atomizers', with typically $U_L << U_G$ where large break-up occurs due to the surrounding gas interacting with the liquid, resulting to liquid structures of various sized scale and types. The case of $M \approx 1$ results in flows where liquid/gas interaction is minimal with small Atomization present.

Atomisation processes of liquid fuel essentially characterise the mixing product between fuel and air [130], which in turn defines the combustion performance of GT and IC engines. Thus, appropriate modelling and accurate prediction of such flows along with any phenomena integrated within is vital. In doing so, the vast range of such systems used in the industry can be optimised. However, due to the high complexity of such gas-liquid interactions, a range of unanswered questions remain to this day.

1.2 Modelling Complexities and Tools

At present, most knowledge and understanding is derived from experimental investigations. Exact analytical solutions can only be established for the basic problems, such as oscillating bubbles and steady-state droplet motion [13]. Meanwhile, more complex configurations and applications, such as turbulent flows evolving high Weber and Reynolds numbers (i.e. flow injectors in IC and GT engines), are still under extended research [102], with respect to the flow behaviour and any physical instabilities present. Here, either one or both phases are usually turbulent, establishing additional challenges both in analytical and experimental research. Some flow applications can be experimentally studied using laboratory-sized models. However, in most instances, real-life flow applications are experimentally impossible for a variety of reasons [13].

Multiphase flow modelling is defined by a lot of interactive terms based on averaging processes and thus accurate characterisation of these flows is considerably difficult. The flow morphologies present and in turn the interfacial area distinguishing the existent phases [41], results in very complex physics and mathematical characterisations of such flows. In cases where phase changes occur and chemical reactions are present, more difficulties are imposed as mass, momentum and heat transfer changes occur between the fluid phases [41]. Finally, the need to impose the solenoidal condition in the pressure Poisson equation for incompressible flows, results in increased density ratios between the liquid-gas phases, making such flows that more complex [83].

The lack of sufficient computational models is generally liable [13][102] to:

- The solution of the non-linear Navier-Stokes equations.
- The vast range of multiple scales ranging from μm (i.e. droplets) to mm (i.e. ligaments) and m (i.e. combustor chambers).
- The accurate location of the interface.
- The need of appropriate jump conditions at the interface.
- The appropriate boundary conditions.

Consequently, both experimental and accurate theoretical/computational modelling is required, whilst appropriate research is still on going.

Computational Fluid Dynamics (CFD) is a common tool towards the acquirement of the desired solutions with a number of approaches available in the literature. A typical CFD approach is the Direct Numerical Simulations (DNS), that use numerical schemes to provide accurate solutions of the governing Navier-Stokes equations. DNS models resolve all time and length scales present, making them both the most accurate but also the most computationally expensive approaches [102], even at small Reynolds. The obtained solutions are only approximations to the theoretical results and developing better accuracy in more complex cases such as turbulent multi-phase flows is still undergoing development.

In DNS simulations, only a small fraction of the flow is characterised, whilst the boundary conditions are approximated strictly to the simulations resolution. The DNS methods can in fact simulate disperse flows, evolving numerous droplets and particles, over long time periods. However cases such as liquid jet break-ups, bubble injectors or droplet break-up are yet to be well understood. Possibly in the future and provided the computational power and speed are majorly improved, any multiphase fluid flow integrated phenomena will be captured and the Navier-Stokes equations of each phase/component will be fully resolved.

Such limitations in the DNS methods, suggest the need of sub-grid models to account for the smaller scales, such as Large Eddy Simulations (LES). Some relative approaches are only well developed in a single-phase flow framework, whilst most studies employ the typical interface tracking methods that in turn lack to obtain a solution of the finest scales [8].

Current research is focusing on continuously defining the transition region between structures that are smaller than a cell size and the resolved interface. Doing so, the mean surface density (area) is obtained, denoting the interfacial area quantity within each computational cell. The latter is known as the $\Sigma - Y$ and ELSA methods [4]. However, this approach excludes any characterisation of the actual shape and geometry of the structures involved [80] [4].

Once an appropriate modelling approach is established, the final model can provide useful information on:

- The involved variables evolution.
- The different mechanisms controlling the flows.
- The quantitative aspect of the dynamics involved.
- The threshold values of the non-dimensional parameters.

Conclusively, better break-up models are required to account for all integrated phenomena and limitations, since they are found in a vast range of technological applications.

1.3 Interface Capturing Methods

In two-phase flow problems, there is a vast range of interface localisation methods available, usually distinguished into surface-tracking and volume-tracking. These methods can be typically described in a Lagrangian or Eulerian framework. Knowing the interface position and its evolution is of high importance in direct simulations of multiphase fluid flows. The variety of methods available are typically based on the type of grid size, defined as the geometric domain shape formed post discretisation. The grid size types are distinguished between *deformable* and *fixed* grids, occupied by a characteristic geometric cell arrangement. Deformable ones refer to grids using cell faces for the interface representation, whilst fixed grids employ distinct processes for the interface tracking (i.e. front tracking).

In this work the methods presented are front-tracking methods using an Eulerian approach for the NS solution [130]. The advection is done by a set of marker points, where the interface is defined explicitly and enables simple interface curvature computations. Front-tracking methods are very successful at low Re numbers but fail to work as well in cases such as the primary break-up region or droplet formation [44][50]. One can implicitly capture the interface using a Eulerian transport equation. Here, we briefly review some of the most common techniques, whilst emphasising on the Volume of Fluid (VOF) and the Level Set (LS) approaches.

1.3.1 Surface-Tracking Methods

A common surface tracking method is the Lagrangian Particle, usually employed within a Eulerian phase [70]. In this approach the particles interact with the surrounding fluid and are typically employed in sprays and bubbles investigations. One can extract information for the physical phenomena integrated in a particle motion. To do so, the Newtonian motion equations are solved in Lagrangian coordinates and the continuity/momentum equations in the continuum phase [70].

Another approach is the Smooth Particle Hydrodynamics (SPH), employed in a Lagrangian particle framework. The SPH is based on the fluid replacement by a set of particles, see Fig. 1.2. The fluid properties are computed by the particles that are used as interpolation mapping properties within a computational grid [78]. SPH can model interfaces well as it provides simple formulations of great conservation properties. However for accurate simulation in the three-dimensional space requires a large number of particles, making it computationally expensive.

The Marker-and-cell (MAC) method originally proposed in Harlow et al. [51] is a Lagrangian approach, where marker particles within the domain cells are used for the interface reconstruction. These marker particles follow the fluid motion but are not defined by the mass or other properties. MAC methods are mostly employed in two-dimensional fixed meshes of uniform size using finite difference schemes [51][72]. They are rather computationally expensive methods due to the need of large memory and CPU run times to account for the required marker particles number.

To minimise both the computational cost and the required memory, many use the Surface Marker method. Opposing to MAC, here the marker particles are defined only at the fluid surface instead, see Fig. 1.2. However doing so, the MAC volume tracking property is removed [98][51]. The Surface Marker enables uniform spacing amongst the particles and any computational difficulties between distinct surfaces are simplified. However, applications in the three-dimensional space are more complex due to the need of accurate particle ordering across the surfaces [98].

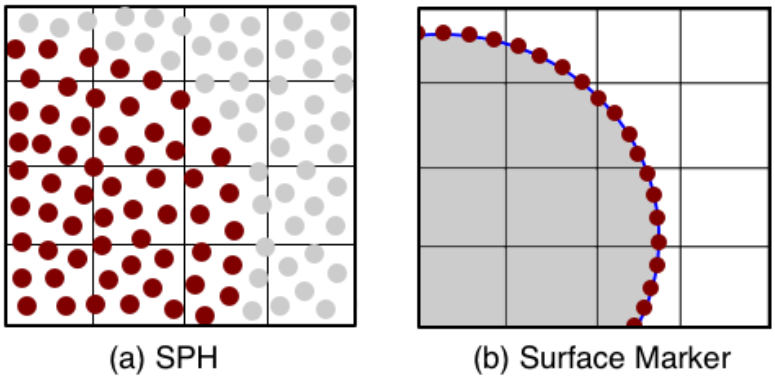

Fig. 1.2: Schematic of (a) SPH and (b) Surface Marker interface tracking methods.

1.3.2 Volume-Tracking Methods

Some studies in fluid-structure interactions, work within a Eulerian-Lagrangian framework. One approach, is the expression of all relative equations based on the initial fluid domain [72]. To do so, one can employ the particles trajectories (i.e. Lagrangian coordinates), which suggests that the transformed equations become numerically difficult due to the irregularity of these characteristic lines [72]. Alternatively, some studies use the fluid domain boundary at a time t, back in the initial boundary, to develop an interface mapping. However, such approach fails to provide conservative schemes [72].

A typical formulation is the Arbitrary Lagrangian Eulerian (ALE), which uses the initial fluid domain mesh and deforms it along with the fluid domain [72]. A major drawback in ALE is the need of the elementary matrix at each time step for the spatial derivatives computation within finite elements, due to the change in the mesh. Additionally, due to the moving mesh, a spatial point at one time step may be excluded at the new mesh, which in turns requires interpolation [72].

Alternatively, one can employ the immersed boundary method, by Peskin et al. [86]. Typical Eulerian-Lagrangian methods are applied within fixed meshes. The immersed boundary approach is based on a curvilinear mesh which freely moves in the Cartesian mesh [86], whose eulerian variable interactions with the mesh is processed using a discrete Dirac function.

In cases of very complex interfaces, particularly in a three-dimensional space framework where the re-meshing frequency is high, mesh generation becomes difficult which in turn increases the computation cost [116]. Therefore, interface-capturing techniques are employed instead, that reduce the required steps for re-meshing. Such approaches are less complex and very cost-effective, however the interface representation is not as accurate [116]. Such methods are developed in a fixed spatial domain, where the interface location is marked by an interface function. The capturing of the interface is processed within the finite element mesh resolution occupying the interface area.

A more rare approach is the Interface-Tracking/Interface-Capturing (MITICT) method [114]. Such formulation is usually employed in both fluid-solid and fluid-fluid interface flow problems of moving meshes. Here, fluid-solid interface cases are easily tracked using moving-mesh formulations, whilst fluid-fluid interface studies are more difficult to track [114]. Employing MITICT methods, one can capture the fluid-fluid interfaces based on the fluid-solid interfaces tracking mesh. This approach has mostly been applied in free surface and ship hydrodynamics [114].

Tezduyar et al. [116], showed a deforming-spatial-domain/stabilised space-time (DSD/SST) formulation with the finite element expressed in a space-time domain [116]. In this method, the mesh update occurs as the fluid occupying the spatial domain, changes with time. Here, the domain nodes motion is mainly governed by the elasticity equations. Such approach is of high convergence rate whilst any numerical oscillations and instabilities present in complex fluid flows are removed [116].

More recently, a new class of CFD methods available is the Lattice-Boltzmann (LB) approach originally proposed by Chen et al. [16]. In such methods the discrete Boltzmann transport equation is solved, describing the gas density function evolution of particle-like points [35]. Opposing to typical CFD methods, the LB method is applied in the mesoscopic scale to recover the NSE in the macroscopic framework. In principle, the state of the fluid under investigation is defined by the distribution functions that evolve in time due to the fluid molecules streaming and colliding.

Such approach enables easy microscopic modelling and droplet break-up processes [25]. The LB is typically employed in droplet collision and micro/nano-flow cases but is not limited to turbulent flows. They involve explicit procedures and are usually confined within cartesian type meshes, making their usage limited. However, time step limitations found in typical explicit methods are in fact reduced in the LB approach, making them a good alternative on the traditional CFD tools.

As mentioned, this work is developed based on the Volume of Fluid and Level Set methods. The VOF methods track the interface by solving an equation for the liquid volume fraction occupied in each cell, distinguishing the two phases. The interface reconstruction is obtained of which the curvature is computed. For $\phi = 1$, the cell is occupied by liquid and for $\phi = 0$ with gas. For $0 < \phi < 1$ then a liquid-gas interface is enclosed. This direct volume tracking and advection, makes VOF methods extremely mass conservative. However, obtaining interface topology information is rather difficult.

The Level Set method uses a smooth function to distinguish between liquid and gas regions based on its sign (i.e. positive/negative). Positive sign indicates liquid present and negative for gas. The marker (or LS function) is a signed distance function. As the LS function is smooth, both locating the interface and curvature computations are much easier and more accurate, however LS does not conserve mass during interface evolution. This method has a much easier description of the interface than VOF, defined by the 0 iso-contour that moves with the local velocity. However, the LS function needs to be modified to maintain its property as a signed-distance function [102]. Figure 1.3 provides a basic schematic demonstrating the difference in the interface capturing principle between VOF and LS.

The main objective in developing interface modelling tools, is to obtain methods that are both mass conservative (i.e. VOF) and accurate at predicting the interface location (i.e. LS). To do so, many studies couple VOF and LS into the so called CLSVOF methods, first proposed by Sussman and Puckett [110]. In this make, the reconstruction of the interface is based on the normals computation from the LS function and the VOF function is used for the interface position constraining purposes.

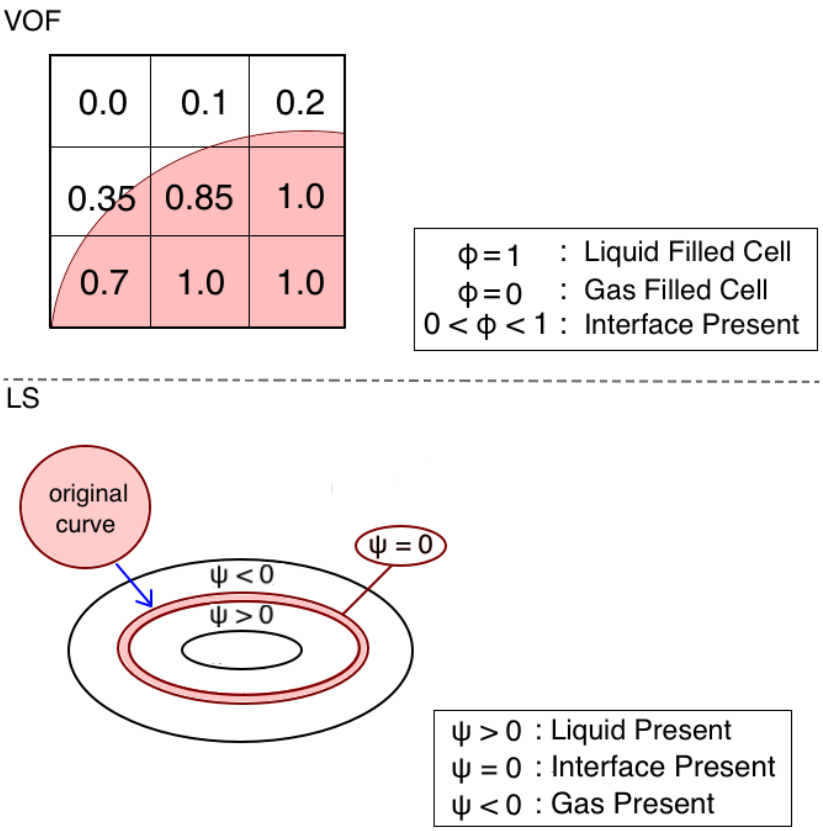

Fig. 1.3: Basic principles schematic of VOF interface tracking in a cell arrangement (top) and LS interface tracking (bottom) using the original curve points to return them as a height (signed distance function).

Mass conservation is achieved through the LS function correction as a function of VOF. The CLSOVF methods are often a good compromise in comparison with pure VOF or LS methods, however they are complex to reconstruct. Solutions obtained can be noisy, due to the need of accurate interface reconstruction and curvature computations, imposing challenges and imprecise solutions in cases.

Son et al. [109] overcame these issues by proposing a CLSVOF approach, based on necessary geometric formulations for the interface reconstruction. Their results presented solutions that are 'not worst' than other pure VOF or LS methods. Meanwhile, in Pijl et al. [100] a CLSVOF method was developed, based on VOF-PLIC and classic LS. They stated that such coupling is not as straightforward in view of the interface reconstruction due to the VOF method complexities. However good mass conservations properties were obtained comparable to VOF approaches [100].

A mass conservative and accurate CLSVOF method was presented in Barber et al. [42]. Although the desired properties from VOF and LS method were preserved, with a less diffusive approach, the CPU computations were found to be significantly more than typical VOF ones. However their CLSVOF could not achieve enough accuracy when applied in break-up cases and lacked in interface convergence, particularly in 3D [42].

Considering the current available CFD approaches and the modelling requirements for two-phase fluid flow investigations, in the present thesis a novel mass conservative Level Set (CMLS) method is developed. This novel approach uses both LS and VOF appropriately to produce a mass conservative and sharp modelling tool. The CMLS presented in this work, is extensively validated both in the two- and three-dimensional space. It is then employed in two-phase flow investigations, by focusing in the single liquid droplet and jet break-up processes.

1.4 Thesis Objectives and Outline

1.4.1 Thesis Objectives

The present work aims to investigate existent modelling tools, using DNS methods and focuses on two common interface tracking methods, Volume of Fluid and Level Set. From there, a novel in-house Conservative Mass Level Set (CMLS) method is developed. The relative numerical modelling tools are presented and the methods are both validated and compared through common test cases. The final CMLS is employed in single drop break-up and liquid jet break-up processes. All numerical methods and working procedures along with the novel CMLS method, are implemented using an in-house Boundary Fitted Flow Integrator code (BOFFIN), by the Mechanical Engineering Department of Imperial College. The present work main objectives can be summarised as follow:

- Employ, validate and compare two interface capturing methods, VOF and LS.
- Develop a novel Conservative Mass Level Set (CMLS) method that retains the advantages of VOF and LS and minimise any drawbacks.
- Employ CMLS in single Drop Break-Up processes, both in two- and three-dimensional space.
- Employ CMLS for Liquid Jet Break-Up (primary atomisation) simulations in a quasi-planar coaxial gas flow set up.

1.4.2 Thesis Outline

Chapter 2 introduces the general numerical solutions employed in a two-phase fluid flow framework and the characteristics of incompressible fluid flows are outlined. From there, the numerical discretisation methods used in this work are detailed developed. Any CFL limitations with respect to the Weber and Reynolds numbers are appropriately covered. Thereafter, interface modelling tools are presented and two methods are extensively investigated and compared, the Volume of Fluid and Level Set methods. In *Chapter 3* a novel conservative mass Level Set (CMLS) method for interface modelling is introduced. The section extensively outlines the philosophy of the method along with the numerical tools employed. The novel method is then validated and compared with the Volume of Fluid and Level Set methods, through a series of test cases. *Chapter 4* studies the break-up process of a single liquid drop in a gas flow, under the effects of the Weber numbers for a fixed Ohnesorge. The results are analysed and validated through a series of previous studies. The surface density evolution is examined in detail. *Chapter 5* presents an analysis on liquid jet break-up processes, primarily driven by the Dynamic Pressure ratio and the gas Weber numbers. The Rayleigh-Taylor and Kelvin-Helmholtz instabilities are also captured and analysed accordingly. The relative investigation of such phenomena presented interesting results, with some difference in comparison with previous studies. Finally, the surface density evolution is also examined and shows major differences than the ones in a single droplet break-up process. *Chapter 6* summarises the CMLS modelling implementation properties along with the major findings from the studies developed. Relative recommendations for future work are discussed, with respect to the CMLS method and the liquid break-up process in droplets and jets.

Chapter 2

Numerical Solutions of Two-Phase Fluid Flows

2.1 Incompressible Fluid Flows

Incompressible fluid flows refer to fluids where the fluid density (ρ) particle or the density flow variation remains constant [102], with $D\rho/Dt = 0$ (or $\nabla \cdot \mathbf{u} = 0$). The general mass and momentum conservation equations for incompressible flows, also known as Navier-Stokes equations, are:

$$\nabla \cdot \mathbf{u} = 0, \tag{2.1}$$

$$\rho \frac{D\mathbf{u}}{Dt} = -\nabla P + \mathbf{f} + \nabla \cdot \mu(\nabla \mathbf{u} + \nabla \mathbf{u}^T) \tag{2.2}$$

In Eqn. (2.2) the pressure is usually a thermodynamic function of density or temperature. However, in incompressible flows, pressure is constrained by the velocity field, thus it will take any value to ensure a divergence free flow [102].

2.2 Interfacial Fluid Mechanics

The study of two-phase flows raises two main complexities, the variable density and viscosity and the interfacial surface tension treatment. The interface motion between two phases is the first difficulty and it is vital to accurately describe the interface location prior to any modelling. In the literature, there are two methods for the interface identification; (a) to explicitly specify every interfacial point location and (b) to employ a marker function for the whole domain. In this work, the marker function method is used, which can also be denoted in many forms. The marker function is employed as a discontinuous Heaviside step function, H, defined in the entire domain, Eqn. (2.3). Note, if H is given, the interface change can be sharply defined from one value to the other.

$$H(\mathbf{x}) = \begin{cases} 0, & \mathbf{x} < 0 \\ 1, & \mathbf{x} > 0 \end{cases} \tag{2.3}$$

The jump conditions across the interface Γ in two-phase flows are derived by employing the principle of mass conservation in a control volume CV as:

$$\begin{aligned} \rho_\Gamma &= \rho_L - \rho_G \\ \mu_\Gamma &= \mu_L - \mu_G \end{aligned} \tag{2.4}$$

Assume zero thickness, then no accumulation of mass exists within. Here, two possible cases exist. If no phase change present and for arbitrary density ratios, the fluid velocity continuity in jump notation yields $\mathbf{u}_L = \mathbf{u}_G$ and $[\mathbf{u}]_\Gamma = 0$ [102]. Considering the interface normal ($\mathbf{n}$), then [$V = \mathbf{u}_L \cdot \mathbf{n} = \mathbf{u}_G \cdot \mathbf{n}$]; implying that the normal velocity V is the interface velocity. If phase change present, it is still required that the mass flux entering should be equal to the mass flux leaving a CV. This results in the mass flow rate ($\dot{m}$) expressed as:

$$\rho_L(\mathbf{u}_L \cdot \mathbf{n} - V) = \rho_G(\mathbf{u}_G \cdot \mathbf{n} - V) = \dot{m} \tag{2.5}$$

Another important aspect in a two-phase flow boundary motion, is the evaluation of the surface tension σ, which can be modelled by retaining the capillarity effect caused by the intermolecular forces (i.e. Van der Waals). This effect is due to the stress concentration at the sharp interfaces (Marangoni effect) [102]. In the microscopic equilibrium framework, surface tension generally arises as the interface is not a thermodynamically optimal region. Here, molecules 'choose' to be either at the gas or liquid density resulting in free energy reduction.

The the surface tension σ force is of $[\mathbf{f}_\Gamma \delta_\Gamma = \sigma\kappa\mathbf{n}\delta_\Gamma]$. Here δS is an infinitesimal interface, $\mathbf{f}_\Gamma$ is the surface tension force, κ is the curvature and $\mathbf{n}$ is the normal interface. Briefly, the curvature is a function of the unit tangent vector moving along a curve, with the tangent following the normal direction. The curvature sign is strictly dependent on the normal orientation choice and reads $\kappa = -\mathbf{t} \cdot (d\mathbf{n}/ds)$, where s is the arc length of the curve, Fig. 2.1. Now, employing the momentum conservation where the interfacial fluid discontinuity properties and surface tension are present, yields

$$0 = -\oint_{\partial S} \rho\mathbf{u}(\mathbf{u}\cdot\mathbf{n} - V)ds + \oint_{\partial S} \mathbf{n}\cdot\mathbf{T}\ \delta S + \int_S \mathbf{f}_\sigma \delta S, \tag{2.6}$$

Here, the first term is zero, if no phase change, as the CV motion follows the fluid velocity and $V = \mathbf{u}\cdot\mathbf{n}$. Integration of one side followed by the other, the term $\oint_{\partial S} \mathbf{n}\cdot\mathbf{T}\ \delta S$ gives the jump in the surface tension tensor $\mathbf{T}$, across the interface [102]. The $\mathbf{f}_\sigma$ term denotes the surface force per unit area expressed as $\mathbf{f}_\sigma = \sigma\kappa\mathbf{n} + \nabla_S\sigma$; the last term is the surface gradient which is zero for constant surface tension [102]. The results are true for any CV occupying the interface and must hold for any point at the interface so that:

$$-[\mathbf{T}]_S \cdot \mathbf{n} = \sigma\kappa\mathbf{n} + \nabla_S\sigma, \tag{2.7}$$

More details on the treatment of this 'jump' at the interface are presented in Section 3.3.3. The present section summarises the incompressible flow governing equations. The numerical solutions for two-phase flows are developed below appropriately.

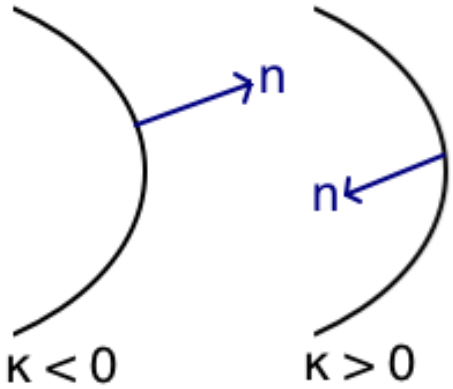

Fig. 2.1: Curvature sign based on normal orientation choice. If curvature is curving away from the interface $\kappa < 0$ else $\kappa > 0$.

2.3 Numerical Discretisation Tools

In the literature, there is a range of available methods to numerically solve two-phase flows. The most common ones are the Finite Difference (FD), the Finite Element (FE) and the Finite Volume (FV).

2.3.1 Finite Difference (FD)

The use of Finite Difference method enables the Navier-Stokes derivatives approximation in their 'strong' form [93]. It is considered to be the oldest from all and is believed that it was initially proposed by Euler. The method always begins with the differential form of the conservation equation [40]. The FD principles are simply expressed with the direct derivative definition of a Φ_x function as:

$$\left(\frac{\partial \Phi}{\partial x}\right)_{x=x_i} = \frac{\Phi(x_i + \Delta x) - \Phi(x_i)}{\Delta x} + \mathcal{O}(\Delta x) \tag{2.8}$$

The $(\partial\Phi/\partial x)_{x_i}$ derivative denotes a point with spatial index of $(i, i+1)$. Here, the partial derivatives are replaced by the functions nodal values approximation at each grid point [113]. Consequently, per grid node there is one algebraic equation, where both the variable value and a specific number of neighbouring nodes are unknowns. FD methods are only employed in structured grids, where the grid lines are essentially local coordinate lines [40][113]. The FD is a simple method that can easily achieve high-order schemes. However, global conservation is not present unless treated carefully, whilst the simple geometries restriction limits its usage in complex flows.

2.3.2 Finite Element (FE)

The FE method is employed with a set of unstructured discrete volumes or finite elements in a solution domain. More specifically, triangles or quadrilaterals grids are used in two-dimensions and tetrahedra or hexahedra in three-dimensions. In this method, a weight function is first employed and multiplied with the equations prior to any integration over the whole domain [104], which in basic form reads:

$$\left(\frac{\partial \Phi}{\partial x}\right)^n = \sum_{i=1}^{n} \Phi(x_i) a_i(x) \tag{2.9}$$

where n is the number of nodes of the domain and $a_i(x)$ is a linear shape function employed within each finite element, for the solution approximation [40]. The linear shape function is developed based on the element corner values and the weight function retains the same form. From there, the conservation law weighted integral is substituted by this approximation. Then the equations under solution need the integral derivative to be zero at each nodal value. In the end, one obtains a set of non-linear algebraic equations. FE methods work well with arbitrary geometries and refining is easily achieved with each finite element being subdivided [40][104].

However, due to its application on unstructured grids, the linearisation of the matrices equations are not arranged in the same manner with regular ones. Thus, obtaining efficient solution methods its more complex. In FE general methods, a common approach is the Control Volume based FE method (CV-FEM). Here, the variable variation over an element is described by shape functions. Around each node, CVs are constructed through the finite centroids connection. The integral conservation equations are applied similar to the FM method - described later on - and the CV boundaries fluxes and source terms are computed element wise [40][104].

2.3.3 Finite Volume (FV)

Finite Volume methods are very similar to FE, but instead use the conservation equations in integral form, which are applied in the sub-parted domain, into contiguous CVs. The variable values to be computed, are located at the node of each CV [40][107]. It is also the simplest from all whilst all approximated terms provide physical meaning. However, they are very cost ineffective when used for higher than 2^{nd} order computations and implemented in the three-dimensional space.

When numerically solving fluid flows, properties such as pressure, velocity and density must be treated carefully. This work investigates two-phase fluid flows in a structured mesh of Cartesian arrangement (see details in Appendix D). Thus one needs only $(\Delta x_i, \Delta y_j, \Delta z_k)$. Here, $\Delta(x, y, z)$ are the grid cell sizes in a three-dimensional Cartesian system and any desired properties are a function of both space and time. From there, one can solve the Navier-Stokes equations explicitly or implicitly. In this work, the NS equations are solved explicitly.

Now, considering Fig. 2.2, in the x_i vicinity, the scalar Φ_i yields:

$$\Phi_i = \frac{1}{V_i} \int_{V_i} \Phi(x) dx \tag{2.10}$$

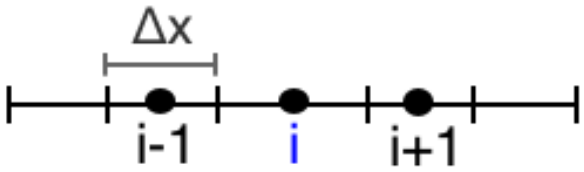

Fig. 2.2: One-dimensional domain discretization into computational cells, of Δx width. The filled circles denote the cell centres and the vertical lines denote the cell edges.

In FV methods the solution is strictly obtained at the computational nodes (i.e. the CV centres). The function values can be obtained by interpolation, using Explicit or Implicit integration formulas.

A summarising table of all three methods for comparison is shown in Tab. 2.1.

Method	**Pros**	**Cons**
FD	-Easy implementation. -High order.	-Curved Boundaries difficult treatment. -Mesh adaption difficulty.
FE	-Complex geometries easy implementation. -Boundary Conditions easy implementation.	-Order/Mesh adaption difficulty.
FV	-Conservation properties principles.	-Cost ineffective at higher orders. .

Table 2.1: Overview of the advantages and disadvantages in common Finite Methods.

The present work, employs Finite Volume methods that are explicitly solved and coupled with the conservative equations described earlier; result in a global momentum conservation upon solution [40]. However, there is ongoing research to this present, in efforts to improve all finite methods [11][59][79] and particularly the FV [37][68].

2.4 Finite Volume Discretisation

2.4.1 Convective and Diffusion Terms Discretisation

The general conservation of a scalar Φ, in differential form can be expressed as:

$$\underbrace{\frac{\partial(\rho\Phi)}{\partial t}}_{Unsteady} + \underbrace{div(\rho\mathbf{u}\Phi)}_{Convective} = \underbrace{div(\Gamma grad\Phi)}_{Diffusive} + \underbrace{|S_c|}_{Source} \tag{2.11}$$

Integrating the above equation over a CV, one obtains in conservative (integral) form:

$$\begin{aligned}\int_V \left(\int_t^{t+\Delta t} \frac{\partial}{\partial t}(\rho\Phi)dt \right) dV + \int_t^{t+\Delta t} \left(\int_A \mathbf{n}\cdot(\rho\mathbf{u}\Phi)dA \right) dt = \\ \int_t^{t+\Delta t} \left(\int_A \mathbf{n}\cdot(\Gamma\Phi)dA \right) dt + \int_t^{t+\Delta t} \int_V S_\Phi dV dt,\end{aligned} \tag{2.12}$$

denoting the CV flux balance. Discretisation of the convective (CON) term requires the Φ computation at the faces of the CV and the flux computation at the CV boundaries [40][102][123].

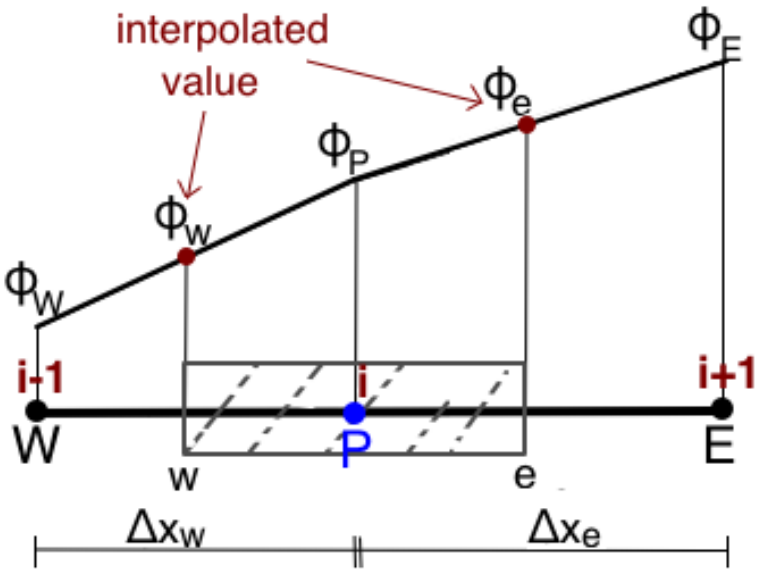

Fig. 2.3: Piecewise linear profile in x-momentum across the West and East Cell faces, denoting the interpolated values at the equivalent nodes.

Discretisation of the conservative (integral) form, Eqn. (2.12), yields:

$$\begin{aligned}\frac{(\rho\Phi_P)^{t+\Delta t}-(\rho\Phi_P)^{t+\Delta t}}{\Delta t}\Delta V+\sum_{\alpha=N,S,E,W,L,R}^{6}\rho_\alpha\Phi_\alpha V_\alpha A_\alpha=\\ =\sum_{\alpha=N,S,E,W,L,R}^{6}\Gamma_\alpha(\nabla\Phi)_\alpha A_\alpha+S_\Phi\Delta V\end{aligned} \tag{2.13}$$

where Φ is the face value, taken over the 6 near-neighbour nodes and $\alpha=(N,S,E,W,L,R)$ subscripts denote the cell faces in a staggered arrangement for a three dimensional space, (see Appendix F). Now, Eqn. (2.13) in matrix notation eventually yields:

$$\alpha_P\Phi_P=\sum_{\alpha=N,S,E,W,L,R}^{6}\alpha_\alpha\Phi_\alpha+b_P \tag{2.14}$$

With b_P standing for all other coefficients including any source terms, S_c, for instance gravity forces and surface tension. Now, recalling Eqn. (2.12), where the source terms have been dropped for clarity:

$$\frac{\partial\Phi}{\partial t}=-CON(\Phi)+DIFF(\Phi), \tag{2.15}$$

Where $CON(\Phi)$ is the convective term and $DIFF(\Phi)$ is the diffusive term. Both terms can be evaluated either Explicitly at time step n or Implicitly at *n+1*. Recalling Eqn. (2.12), the flow field should satisfy continuity in one dimension with $d(\rho u)/dx=0$ or ρu to be constant. Thus integration of (2.12), in a CV across the West to East faces, denotes:

$$(\rho uA\Phi)_e-(\rho uA\Phi)_e=\left(\Gamma A\frac{\partial\Phi}{\partial x}\right)_e-\left(\Gamma A\frac{\partial\Phi}{\partial x}\right)_w \tag{2.16}$$

with the diffusion derivatives computed using piece wise linear profile, Fig. 2.3, as:

$$\left(\Gamma A\frac{\partial\Phi}{\partial x}\right)_e=\Gamma_eA_e\left(\frac{\Phi_E-\Phi_P}{\Delta x_e}\right)\quad,\quad\left(\Gamma A\frac{\partial\Phi}{\partial x}\right)_w=\Gamma_wA_w\left(\frac{\Phi_W-\Phi_P}{\Delta x_w}\right) \tag{2.17}$$

if $A_e=A_w$ then the integral transport equation yields

$$F_e\Phi_e-F_w\Phi_w=D_e(\Phi_E-\Phi_P)-D_w(\Phi_P-\Phi_W) \tag{2.18}$$

where generally $F=\rho u$ and $D=\Gamma/\Delta x$; ρF denoting the mass flux.

2.4.1.1 Convective Term

To evaluate the face fluxes, for the Convective (CON) term one can use Piecewise Linear Profile, for instance in x-momentum, Fig. 2.3, denoting $\Phi_e = (\Phi_E + \Phi_P)/2$ and $\Phi_w = (\Phi_W + \Phi_P)/2$. Thus the transport equation gives:

$$\frac{F_e}{2}(\Phi_P + \Phi_E) - \frac{F_w}{2}(\Phi_P + \Phi_W) = D_e(\Phi_E - \Phi_P) - D_w(\Phi_P - \Phi_W), \tag{2.19}$$

Which in discretisation form reads:

$$\alpha_P \Phi_P = \alpha_W \Phi_W + \alpha_E \Phi_E, \tag{2.20}$$

Here, the coefficients are:

$$\begin{aligned} a_W &= D_W + \tfrac{F_W}{2}, \\ a_E &= D_E - \tfrac{F_E}{2}, \\ a_P &= a_W + a_E + (F_e - F_w), \end{aligned} \tag{2.21}$$

at the West and East cell faces. For the CON term, consistent discretisation is important. Thus, face density approximation should be proceeded in a conservative manner.

2.4.1.2 Diffusive Term

For the Diffusive term discretisation, we also employ piecewise linear profile. Here we apply upwind difference scheme, where the flow direction is accounted for, so that the cell face Φ will be equal to the upstream node Φ. So, if positive flow direction, (i.e. $F_w > 0, F_e > 0$), then $\Phi_w = \Phi_W$ and $\Phi_e = \Phi_P$, else (i.e. $F_w < 0, F_e < 0$), then $\Phi_w = \Phi_P$ and $\Phi_e = \Phi_E$. Thus Eqn. (2.18) now yields

$$F_e \Phi_E - F_w \Phi_P = D_e(\Phi_E - \Phi_P) - D_w(\Phi_P - \Phi_W) \tag{2.22}$$

which in final form reads:

$$\alpha_P \Phi_P = \alpha_W \Phi_W + \alpha_E \Phi_E \tag{2.23}$$

where the coefficients are $\alpha_P = \alpha_W + \alpha_E + (F_e - F_w)$, with the neighbour coefficients denoted by:

$$\begin{aligned} a_W &= D_W + \|F_w, 0\|, \\ a_E &= D_e + \|-F_e, 0\|, \\ a_P &= a_W + a_E + (F_e - F_w), \end{aligned} \tag{2.24}$$

Finally the coefficients α_R and α_L for both CON and $DIFF$ terms read $\alpha_R = -\rho_r u_r / 2\Delta x_P$ and $\alpha_L = \rho_l u_l / 2\Delta x_P$. For the y- and z- momentum, similar processes can be followed to obtain the values at N and S for the j-direction and E and W for the k-direction [123]. One should note that if the source term is constant then all other coefficients are the same and $b = S_c \Delta x$. Otherwise, if the source term is Φ dependant, then linearisation yields $S = S_c + S_P \Phi_P$ so that:

$$\alpha_P^{'} = \alpha_P - S_P \Delta x \tag{2.25}$$

2.4.2 Temporal Discretisation

Considering an ordinary first order differential equation of initial conditions, one has:

$$\frac{d\Phi(t)}{dt} = f(t, \Phi(t)) \ ; \qquad \Phi(t_0) = \Phi^0 \tag{2.26}$$

If one is looking for the solution Φ at a short time, Δt after t_0. Then the new initial condition will be the solution at $t_1 = t_0 + \Delta t$, which can be developed to $t_2 = t_1 + \Delta t$, $t_3 = t_2 + \Delta t$ and so forth. Integrating Eqn. (2.26), between the limits of t_n to t_{n+1} then:

$$\int_{t^n}^{t^{n+1}} \frac{d\Phi}{dt} dt = \Phi^{n+1} - \Phi^n = \int_{t^n}^{t^{n+1}} f(t, \Phi(t)) dt, \tag{2.27}$$

which is an exact equation and the shorthand notation $\Phi^{n+1} \equiv \Phi(t^{n+1})$ is employed. There are several discretisation methods for time integration, divided into explicit or implicit methods, such as:

- *Explicit (forward) Euler*: $\Phi^{n+1} = \Phi^n + f(t^n, \Phi^n)\Delta t + O(\Delta t)$
- *Implicit (backward) Euler*: $\Phi^{n+1} = \Phi^n + f(t^{n+1}, \Phi^{n+1})\Delta t + O(\Delta t)$
- *Midpoint Rule*: $\Phi^{n+1} = \Phi^n + f(t^{n+\frac{1}{2}}, \Phi^{n+\frac{1}{2}})\Delta t + O(\Delta t^2)$

Generally speaking, the explicit (forward) Euler result into closed-form formulas where direct computation of dependent scalars are obtained through known values. Implicit methods instead, provide a linear/non-linear equation system by coupling the unknown values at a new time level [40][64]. The midpoint rule, also known as the Crank-Nicholson (CN), uses a 2^{nd} order trapezoid rule on the partial differential equations. The CN is in fact, an implicit scheme that enables the use of much larger Δt and results in $O(\Delta t^2)$.

2.4.2.1 Explicit Euler

In the Explicit Euler method and considering (2.14), all sources and fluxes are computed at t^n with:

$$\alpha_P^n \Phi_P^{n+1} = \sum \alpha_\alpha^n \Phi_\alpha^n + b_P^n \tag{2.28}$$

In a CV or a grid point context, the new time level value is only unknown at this node, with the neighbour values being evaluated in previous time levels, thus the new unknown value at each node can be computed. Equation (2.28) denotes a solution at the new time step based on the previous steps solution. With respect to the explicit stability analysis Eqn. (2.28) is unstable at large Δt.

Now, the spatial derivation for the scalar Φ at the new value Φ^{n+1}, if one employs UDS along the x-direction of a uniform grid [40], reads:

$$\Phi_i^{n+1} = \Phi_i^n + \left[-u \frac{\Phi_i^n - \Phi_{i-1}^n}{\Delta x} + \frac{\Gamma}{\rho} \frac{\Phi_{i+1}^n + \Phi_{i-1}^n - 2\Phi_i^n}{(\Delta x)^2} \right] \Delta t \tag{2.29}$$

by defining the dimensionless parameters of $d = 2\Gamma \Delta t / \rho (\Delta x)^2$ and $c = u \Delta t / \Delta x$, Eqn. (2.29) becomes:

$$\Phi_i^{n+1} = (1 - 2d - c)\Phi_i^n + d\Phi_{i+1}^n + (d + c)\Phi_{i-1}^n \tag{2.30}$$

Where d is the time step to the characteristic diffusion time ratio, denoting the required transmission time of a disturbance due to diffusion, over a Δx distance. The c parameter is known as the Courant-Friedrichs-Lewy condition or Courant number. It accounts for the time step to characteristic convection time ratio, denoting the required convection time of a disturbance over a Δx distance [40][123]. In Eqn. (2.30) the neighbour nodal values are always positive resulting to no further unphysical instability behaviour. However, Φ_i^n can be negative and provided negligible diffusion, a maximum limit is imposed on the time step Δt size as:

$$\Delta t = \frac{c \Delta x}{u_{max}} < 1 \tag{2.31}$$

This condition states that the choice of Δt must be small enough during one time step, so that the relative material property moves by less then one grid space. This implies that in high speed flows the time step must be very small. Finally, if c is satisfied, all spatial and temporal neighbour coefficients in Eqn. (2.30) are positive [123].

2.4.2.2 Implicit Euler

Another suggested approach that ensures stability properties, is with the use of *backward* or *Implicit Euler* method. Here, all the fluxes and source terms are computed at the new time level with respect to the unknown variable values. The equation solved is of the form Eqn. (2.20) but for *n+1* instead of *n*, as:

$$a_P \Phi_P^{n+1} = \sum \alpha_\alpha \Phi_\alpha^{n+1} + b_P(\Phi^{n+1}), \tag{2.32}$$

whose solution gives a first-order time-accurate solution.

Applying CDS on Eqn. (2.24) one gets:

$$a_P \Phi_P^{n+1/2} = \sum \alpha_\alpha \Phi_\alpha^{n+1/2} + b_P(\Phi^{n+1/2}), \tag{2.33}$$

Known as Crank-Nicholson method and by employing linear time interpolation $\Phi_P^{n+1/2} = \frac{1}{2}(\Phi_P^{n+1} + \Phi_P^n)$ we have:

$$\frac{\alpha_P}{2}\Phi_P^{n+1} + \frac{\alpha_P}{2}\Phi_P^n = \sum \frac{\alpha_\alpha}{2}\Phi_\alpha^{n+1} + \sum \frac{\alpha_\alpha}{2}\Phi_\alpha^n + b_P(\Phi^{n+1/2}), \tag{2.34}$$

Rearranging the above by grouping all terms with respect to n, a new system is obtained as:

$$a_P^* \Phi_P^{n+1} = \sum \alpha_\alpha^* \Phi_\alpha^{n+1} + b_P^*, \tag{2.35}$$

Where $\alpha_P^* = \alpha_P/2$ and $b_P^* = b_P(\Phi^{n+1/2}) + \sum \alpha_\alpha^* \Phi_\alpha^n - \alpha_P^* \Phi_P^n$. Here, the solution of Eqn. (2.35) will produce a second-order time-accurate solution. Note, that regularly two steps are required, a predictor and a corrector, for an accurate estimation of $\Phi_P^{n+1/2}$ so one can obtain b_P [40].

2.4.2.3 Physics and Stability Imposed Limitations

In the context of numerical simulations for immiscible fluids, restrictions on Δt and Δx arise, when accounting for the viscous and capillary effects. The 'global' Weber number, denotes a relation between inertial and capillary effects [18], reading:

$$We = \frac{\rho U^2 \ell}{\sigma} \tag{2.36}$$

where ℓ is a characteristic reference parameter, typically a drop diameter or a liquid jet nozzle outlet and U is the bulk velocity of liquid or gas. Meanwhile, in droplet-laden flows, Weber defines the inertia and surface tension forces effects on the possible droplet break-up.

Previous experimental data [29][65] and theoretical analysis [77][112][124] (see Section 4.1), noted that a critical $We_{cr} < 10$ exists under which droplets do not further disintegrate. However, during flow destabilisation in turbulent processes $We_{cr} \leq 10$. It was therefore concluded that for the resolution of any droplets or liquid structures present, a smallest grid size requirement is imposed for the computational domain, until We_{cr} limit is reached. Now, if one assumes comparable analogy to an air stream drop break-up, the pressure balance for aerodynamic pressure, $\rho_G U_G^2$ and capillary pressure, σ/ℓ, imposes a peeled-off fragments size of $\ell \sim \sigma/(\rho_G U_G^2)$. Consequently, σ becomes an effective parameter (i.e. We number) despite the non explicit break-up mechanism, where the velocity dependence here is strong, (i.e. ΔU^{-2}), [65].

From there, Menard et al. [112] work on jet atomisation, noted that Δ is defined on the assumption that no secondary break-up develops with respect to the smallest droplet, implying all spray integrated droplets satisfy:

$$We = \frac{\rho_G U^2 \ell}{\sigma} \leq 10 \tag{2.37}$$

where $\ell \sim \Delta$, suggesting that Weber is Δx based, as $We_{\Delta x} \leq 10$ [18][112].

A flow is locally capillary driven if $We < 1$, [18]. Pai et al. [77] and Pitsch et al. [17] previous investigations in spray atomisation noted that all interface perturbations are damped strictly by the viscous forces. Provided the largest flow structures size were nozzle diameter comparable, capillary effects were negligible. However, if the ligaments cross dimension is mesh size comparable, break-up occurs due to capillary effects. Here, the droplets become mesh size comparable, as the break-up thickness goes lower than the mesh resolution [77]. Consequently, a new gas $We_{\Delta x}$ is proposed [17][28][77], reading:

$$We^G_{\Delta x} = \frac{\rho_G U_G^2 \Delta x}{\sigma} \leq 1 \tag{2.38}$$

suggesting that all computations should be over-resolved [18][17].

Thus a mesh based Weber number, ensures resolution in all types of two-phase flow investigations, from single droplets, liquid jet break-up and full atomisation processes. Building on that, restrictions on Δt and Δx arise due to the 'physics' and 'stability', accounting for the viscous and capillary effects.

Considering a local (cell) Reynolds [34], solution instabilities and possible divergence occurs in the $DIFF$ term. In addition, further limitations arise as one needs a capillary wave to travel less than a grid space, thus $Re_{\Delta x} \leq 2$ and $We_{\Delta} < 1$. These requirements impose restrictions with respect to the 'physics' (i.e. Δx), that in turn create 'stability' limitations (i.e. Δt), summarised in Tab. 2.2. Note, additional Δt constraints are imposed during solutions of high frequency perturbations, not addressed here.

Physics			
Limitations	$Re_{\Delta x} \leq 2$	$We_{\Delta x} < 1$	
$\Delta x \leq$	$\frac{\rho u_{max}}{\mu}$	$\frac{\rho u_{max}^2}{\sigma}$	
Stability			
Limitations	$DIFF$	Ca	CFL
$\Delta t <$	$\frac{u_{max}\Delta x}{\mu}$	$\sqrt{\frac{\rho \Delta x^3}{\sigma}}$	$\frac{\Delta x}{u_{max}}$

Table 2.2: Imposed restrictions on Δx and Δt accounting for viscous and capillary effects.

2.4.3 Pressure-Velocity Correction Method

The Navier-Stoke equations in incompressible fluid flows can be solved with a number of different approaches. In this work, we employ the pressure-velocity coupling scheme in a staggered grid, integrated within the Semi-Implicit Method for Pressure-Linked Equations (SIMPLE). In principle, the SIMPLE-type scheme initially employs a guessed pressure field and predicts the velocity field from the momentum equation solution. Consequently, any type of convergence and pressure or velocity fields oscillations can be avoided [99][107]. In the momentum equations, the pressure gradient already appears. However, the continuity equation does not contain the pressure gradient explicitly.

Here, we formulate a pressure that satisfies continuity, thus a pressure equation (Poisson pressure) is deduced that is then solved to obtain the necessary pressure field [102], [123]. From that, the updated pressure and corrected velocity fields are obtained to satisfy the continuity equation. The result obtained from the discretised Poisson equation, is a symmetric, positive-definite coefficient matrix solved by Conjugate Gradient Solver. Doing so in a staggered grid framework, strong coupling is enabled between the pressure and the velocities. To compute the correct pressure and velocity fields, one starts from the x- and y- momentum equations (see Appendix B) with:

$$\frac{\partial u}{\partial t} + \frac{\partial uu}{\partial x} + \frac{\partial vu}{\partial y} = -\frac{1}{\rho}\frac{\partial P}{\partial x} + \frac{1}{\rho}\frac{\partial \tau_{ij}}{\partial x} + \frac{1}{\rho}\frac{\partial \tau_{ij}}{\partial y} + f_x^{\sigma} \tag{2.39}$$

where τ accounts for the viscous effects and f^{σ} is the surface tension (body) force.

Decompressing the pressure into $P = P^n + P^C$, where P^C is the corrected pressure, a new momentum equation from Eqn. (2.39), yields:

$$\frac{\partial u}{\partial t} + \frac{1}{\rho}\frac{\partial P^C}{\partial x} + \frac{\partial uu}{\partial x} + \frac{\partial vu}{\partial y} = -\frac{1}{\rho}\frac{\partial P^n}{\partial x} + \frac{1}{\rho}\frac{\partial \tau_{ij}}{\partial x} + \frac{1}{\rho}\frac{\partial \tau_{ij}}{\partial y} + f_i^{\sigma} \tag{2.40}$$

A velocity can then be defined as:

$$\frac{\partial \hat{u}}{\partial t} = \frac{\partial u}{\partial t} + \frac{1}{\rho}\frac{\partial P^C}{\partial x} \tag{2.41}$$

Thus, the momentum equation is finalised to:

$$\frac{\partial \hat{u}}{\partial t} + \frac{\partial uu}{\partial x} + \frac{\partial vu}{\partial y} = -\frac{1}{\rho}\frac{\partial P^n}{\partial x} + \frac{1}{\rho}\frac{\partial \tau_{ii}}{\partial x} + \frac{1}{\rho}\frac{\partial \tau_{ij}}{\partial y} + f_i^{\sigma} \tag{2.42}$$

Using central difference scheme, (see Appendix C), in both time and space, one can define a numerical operator as:

$$\hat{u} = \mathcal{L}(u, \mathbf{u}, \rho) \tag{2.43}$$

Evaluating (2.41) at time $t^{n+\frac{1}{2}}$ using CDS again, one gets:

$$\left[\frac{u^{n+1}-u^n}{\Delta t}\right]^{n+1/2} = \left[\frac{\hat{u}-u^n}{\Delta t}\right]^{n+1/2} - \left[\frac{1}{\rho}\frac{\partial P^C}{\partial x}\right]^{n+1/2} + \mathcal{O}(\Delta t^2) \tag{2.44}$$

and by simplifying:

$$u^{n+1} = \hat{u} - \frac{1}{\rho^{n+1/2}}\left[\frac{\partial P^C}{\partial x}\right]^{n+1/2} \tag{2.45}$$

Now considering a Staggered grid (Appendix D), the x-velocity is stored at the faces $i-1/2$ and $i+1/2$, so that:

$$u_{i+1/2}^{n+1} = \hat{u}_{i+1/2} - \frac{1}{\rho_{i+1/2}^{n+1/2}}\left[\frac{\partial P^C}{\partial x}\right]_{i+1/2}^{n+1/2} = \hat{u}_{i+1/2} - \frac{1}{\rho_{i+1/2}^{n+1/2}}\frac{\partial P^C}{\partial x} \tag{2.46}$$

which by expansion yields:

$$u_{i+1/2}^{n+1} = \hat{u}_{i+1/2} - \frac{1}{\rho_{i+1/2}^{n+1/2}}\frac{P_{i+1}^C - P_i^C}{\Delta x} = \beta_{i+1/2}\left(P_{i+1}^C - P_i^C\right) \tag{2.47}$$

Now recalling the Continuity equation and from Eqn. (2.47), one gets:

$$\frac{\partial u}{\partial x} + \frac{\partial v}{\partial y} = 0 \tag{2.48}$$

Then, replacing Eq.(2.45) at time $n+1$,

$$\frac{\partial}{\partial x}\left[\frac{1}{\rho^{n+1/2}}\frac{\partial P^C}{\partial x}\right] + \frac{\partial}{\partial y}\left[\frac{1}{\rho^{n+1/2}}\frac{\partial P^C}{\partial y}\right] = \frac{\partial \hat{u}}{\partial x} + \frac{\partial \hat{v}}{\partial y} \tag{2.49}$$

In a staggered arrangement, the pressure is stored at the cell centre. Integrating over the $V_{i,j}$ yields:

$$\int_{V_{i,j}}\left(\frac{\partial}{\partial x}\left[\frac{1}{\rho^{n+1/2}}\frac{\partial P^C}{\partial x}\right] + \frac{\partial}{\partial y}\left[\frac{1}{\rho^{n+1/2}}\frac{\partial P^C}{\partial y}\right]\right)dV = \int_{V_{i,j}}\left(\frac{\partial \hat{u}}{\partial x} + \frac{\partial \hat{v}}{\partial y}\right)dV \tag{2.50}$$

Employing the divergence theorem strictly on the u-terms we finally obtain the corrected velocity field from the corrected pressure as:

$$\frac{1}{\Delta x}\frac{1}{\rho_{i+1/2}^{n+1/2}}\left(\frac{\partial P^C}{\partial x}\right)_{i+1/2} - \frac{1}{\Delta x}\frac{1}{\rho_{i-1/2}^{n+1/2}}\left(\frac{\partial P^C}{\partial x}\right)_{i-1/2} = \frac{\hat{u}_{i+1/2} - \hat{u}_{i-1/2}}{\Delta x} \tag{2.51}$$

2.5 Interface Modelling

As discussed, interface tracking methods are distinguished between surface and volume tracking. The latter ones, can overcome some of the surface tracking limitations, by using volume fractions for the solution regions within each computational cell. Two popular volume-tracking methods are the Volume of Fluid and Level Set. Such approaches, overcome some topology changing limitations and maintain mass conservation properties within accurate interface capturing computations. This section reviews both methods, by employing and comparing them through a series of classic validation test cases.

2.5.1 The Volume of Fluid Method

The Volume of Fluid (VOF) employs the discrete version of the marker function, also known as the 'color' function, denoted by $\phi(\mathbf{x}, t)$, which can be understood as the volume fraction of liquid in each cell [55]. It is a Eulerian approach consisting of two sequential processes:

- Interface Advection
- Interface Reconstruction.

The motion equations are closed with the density and viscosity constitutive relations of:

$$\begin{aligned} \rho &= \phi\rho_L + (1-\phi)\rho_G \\ \mu &= \phi\mu_L + (1-\phi)\mu_G \end{aligned} \tag{2.52}$$

Here, ϕ is equal to 1 for liquid and 0 for gas. This implies, that the density and viscosity are piecewise continuous as a result of ϕ being a step function [121]. By denoting a transitional area between the two fluids, (i.e. a discontinuous step), the two fluids can be modelled as a continuum; satisfying continuity $\nabla \cdot \mathbf{u} = 0$. Consequently, for $\phi = 1$ the cell is fully occupied by liquid and for $\phi = 0$ by gas, whilst for $0 < \phi < 1$ the cell contains both, Fig. 2.4[121][102].

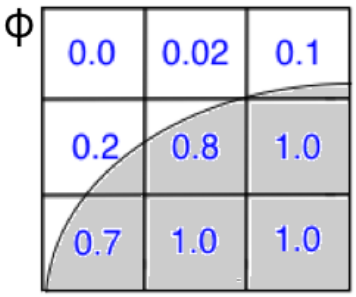

Fig. 2.4: Cell arrangement demonstrating VOF interface reconstruction with the shaded squares denoting the volume function. Note, each shaded square is representative of the equivalent size to the fractional volumes.

Finally, the scalar ϕ convection equation for the volume fractions, in conservative form, reads:

$$\frac{\partial \phi}{\partial t} + \nabla \cdot (\mathbf{u}\phi) = 0, \tag{2.53}$$

Provided the fractional volume per cell is known, an approximation of the interface can be obtained. Hence VOF accounts for the volume transfer and then imports it in the receiver cell, provided enough "space" is available.

2.5.1.1 Interface Advection

Discretisation of Eqn. (2.53) introduces numerical diffusion resulting in step profile smearing, due to the volume fraction discontinuity across the two-phase interface. To minimise such errors, one should reconstruct the interface within each cell ($0 < \phi < 1$) [102][121] and compute the interfacial cell fluxes to obtain a sharp advection of the interface [130]. To do so, high-resolution techniques are employed that also enable preservation of the monotonic variable distribution (i.e. satisfy boundedness criterion) [127]. There is a vast range of such methods available.

In Boris et al. [12], the Flux-Corrected Transport (FCT) methods were developed based on a predictor-corrector structure. FCT methods employ a first order non-oscillatory scheme for the solution advection, followed by a correction step that removes large dissipative errors. In the current VOF implementation, the Compressive Interface Capturing Scheme for Arbitrary Meshes (CICSAM) is employed, originally proposed in Ubbink et al. [121]. CICSAM is a differencing scheme based on the donor-acceptor flux approximation. It is an advection scheme that can find a solution to ϕ_{i+1} while maintaining a sharp interface [47]. The Normalised Variables Diagram (NVD) is the basis of CICSAM scheme. The NVD concept was first introduced by Leonard et al. [66] and is usually employed in convective discretisation schemes. Considering a convected scalar ϕ variation along a direction normal to the CV faces, Fig. 2.5, one gets the normalised variable as:

$$\tilde{\phi} = \frac{\phi - \phi_U}{\phi_A - \phi_U}, \tag{2.54}$$

With respect to Fig. 2.5, three different cells can be seen, the upwind (U), the donor (D) and the acceptor (A) cells. In such schemes, the face under investigation is the one located between (D) and (A), denoted with ϕ_f^+ [47], Fig. 2.5.

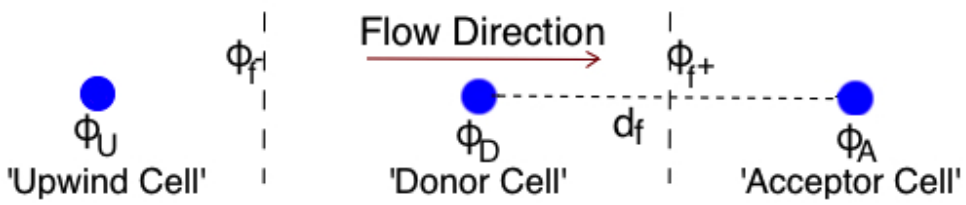

Fig. 2.5: Schematic of 1D Control Volume and its flow direction.

An important property of NVD, is known as Total Variation Diminishing (TVD), which is usually employed in cases where non-oscillatory solutions are needed. Its principle regards the flux limitation of the conserved scalar to a point where local maximum/minimum of the scalar profile are not produced [134].

The NVD is based on the normalised face value plotted as a function of the normalised donor-cell Fig. 2.6. To obtain a system where any oscillations are avoided and is not artificially diffusive, the NVD characteristics, should pass from **0** and **P** respectively, Fig. 2.6. The NVD is obtained with respect to the CBC, in which at the centres of the neighbourhood control volume, the variable distribution should remain smooth, $\phi_D \leq \phi_f \leq \phi_A$, Fig. 2.5. Recalling (2.54), the convection boundedness criteria implies $\tilde{\phi_D} \leq \tilde{\phi_f} \leq 1$, illustrated in Fig. 2.6, so the volume fraction value at the CV ϕ_f is computed as:

$$\phi_f = (1 - \tilde{\beta}_f)\phi_D + \tilde{\beta}_f \phi_A, \tag{2.55}$$

$$\tilde{\beta}_f = \frac{\tilde{\phi}_f - \tilde{\phi}_D}{1 - \tilde{\phi}_D}, \tag{2.56}$$

In CICSAM, for the CBC to be satisfied an additional assumption for the dependance region is required and is based on c. Here, the local c is used at the CV face (S_f). Combining c with the CBC, then one gets $\tilde{\phi}_D \leq \tilde{\phi}_f \leq (1, \tilde{\phi_D}/c_f)$. The coupling of donor-acceptor scheme with the NVD, is the first part of the CICSAM scheme, known as the HYPER-C scheme [121].

The HYPER-C scheme [121], is a very compressive scheme where in a scalar field, every finite gradient is turned into a step profile, due to the downwind differencing scheme used. This is not always desirable in cases of interfaces being tangential to flow direction. Therefore, it is advisable to use a less compressive scheme, such as ULTIMATE-QUICK (UQ), which is based on the QUICK scheme [121]. It uses a three-point upstream weighted quadratic interpolation for the cell face values [47] as:

$$\phi_{UQ} = \frac{6}{8}\phi_W + \frac{3}{8}\phi_P - \frac{1}{8}\phi_E \tag{2.57}$$

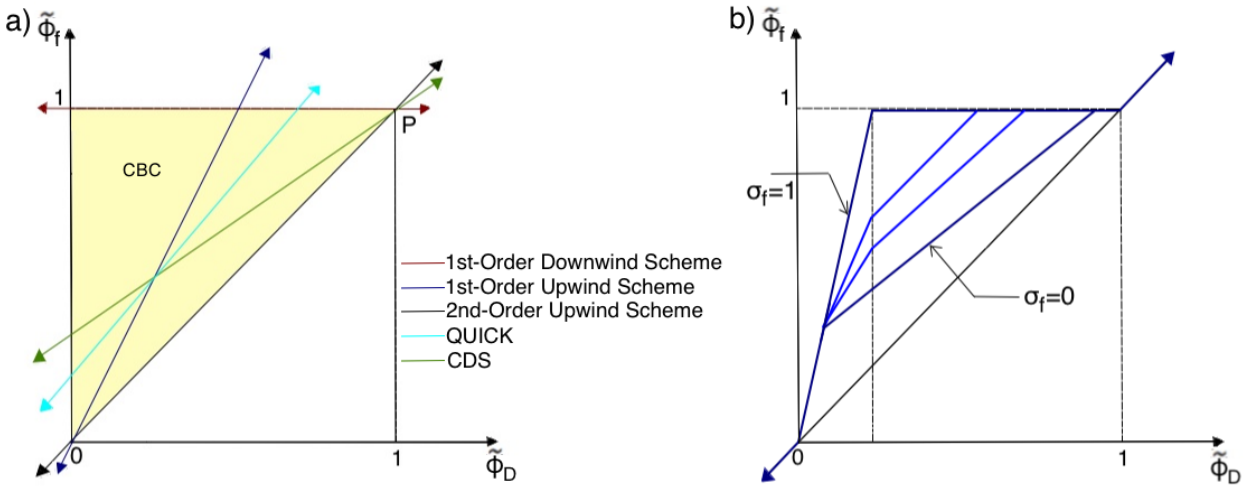

Fig. 2.6: Normalised Variable Diagram for a) different schemes and b) CICSAM scheme.

The switch between the two schemes is based on a blending factor, ξ so that $0 \leq \xi \leq 1$. The factor ξ is strictly based on the angle between the normalised face value motion direction and the interface. Here, the normal to the interface is a step described over one mesh cell, whereas in cases of tangential to the interface position, moderate gradient exists [121][127]. Thus, the normalised face value of the color function is computed by:

$$\tilde{\phi_f} = \xi\tilde{\phi}_{CBC} + (1 - \sigma_f)\tilde{\phi}_{UQ}, \tag{2.58}$$

Where σ is evaluated by the angle θ_f cosine between the vector d_f, Fig. 2.5 and the normal vector to the interface $\mathbf{n} = \nabla\phi_D/|\nabla\phi_D|$ as:

$$\theta_f = arccos|\overrightarrow{d}\,\overrightarrow{n}|, \tag{2.59}$$

$$\sigma_f = \left\{\frac{1 + \cos 2\theta_f}{2}, 1\right\}, \tag{2.60}$$

The procedure developed depends on the CFL condition. In Waclawczyk et al. [127], to overcome these limitations, they employ the High Resolution Interface Capturing (HRIC) scheme. As in the CICSAM case, the HRIC is also based on the NVD. This approach can be expressed in three steps. Primarily, the estimation of the normalised cell face values $\tilde{\phi}_f$ are computed, based on a the NVD diagram, connecting the upwind and downwind schemes continuously [127]. From there, one can use a first order UDS to satisfy CBS along with the blending factor, introduced earlier. This results in a dynamic blending scheme, accounting for the volume fraction local distribution. However, if the CFL condition is non satisfied, stability issues arise. Thus $\tilde{\phi}_f$ correction is based to the local c, enforcing a continuous switch between the scheme [127].

2.5.1.2 Interface Reconstruction

Typical geometric interface reconstruction methods, introduce geometrical interface representation. In contrast, high-resolution schemes satisfy the conditions derived above via appropriate discretisation schemes. To accurately compute the flux approximations (advection), one needs to reconstruct the interface. To do so, the normals computation is based on the gradient estimation of the discrete volume fraction. The normals are computed from the ϕ scalar, with $\phi = 0$ when normals point to gas. The $\mathbf{m} = \nabla\phi$ discretisation for the cell faces normals, Fig. 2.7, reads:

$$\mathbf{m}_x = -\frac{\phi_{i,j} - \phi_{i-1,j}}{\Delta x}, \qquad \mathbf{m}_y = -\frac{\phi_{i,j} - \phi_{i,j-1}}{\Delta y}, \qquad \mathbf{m}_z = -\frac{\phi_{j,k} - \phi_{j,k-1}}{\Delta z} \tag{2.61}$$

From there, the cell centre vectors are computed from $\mathbf{m}$, using Arbitrary Lagrangian-Eulerian (ALE) method [22]. The ALE method passes the face stored values and restores them at the cell centres; denoting a normal based reconstruction approach that employs the neighbour points, Fig. 2.7. The ALE result can be summarised as $\mathbf{n} = \sum F_k \mathbf{m}_k$, denoting the sum of the ϕ scalar values as a function of the $\mathbf{m}$ normals, at the cell centre.

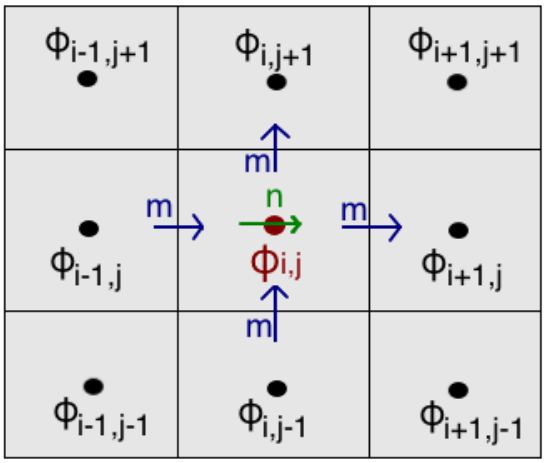

Fig. 2.7: Cell notation schematic denoting the scalars $\phi_{i,j}$ stored at the cell centres and normal vectors $\mathbf{n}$ stored at the cell faces.

2.5.1.3 Other VOF-based Methods

Other common VOF-based reconstruction methods available in the literature are the Simple Line Interface Calculation (SLIC) and the Piecewise-Linear Interface Calculation (PLIC). The SLIC method can be employed for geometric approximation of fluid interfaces. Here, the fluid surfaces are locally defined with respect to each mixed fluid zone. SLIC VOF is rather simple and accurate. Usage in three-dimensions is very easy whilst merging/breakage of the interface happens immediately. However, numerical diffusivity and accuracy limitations are the main drawbacks [81].

Meanwhile, the PLIC approach is the VOF-based method that uses a piecewise- linear interface calculation. Is an interface reconstruction method and is based on the concept of defining the interface as a line in 2D or plane in 3D. PLIC VOF is rather simple and accurate whilst interface merging/breakage happens automatically. However, implementation in 3D is rather difficult and utilisation in boundary fitted grids is complex [69]. Figure 2.8, shows the interface reconstruction differences, between a VOF-SLIC and VOF-PLIC with the Color Function VOF methods.

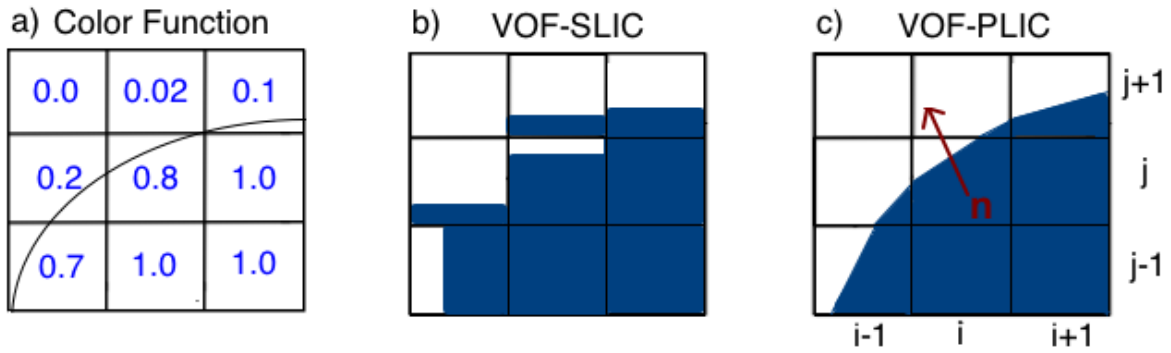

Fig. 2.8: Basic schematic of the principle VOF color function in comparison with VOF-SLIC and VOF-PLIC.

2.5.1.4 Validation

A common interface tracking validation case, is a liquid disc in a single vortex field [9]. Here, a liquid disc of radius $R = 0.15$ is placed in a unit sized domain and the disc centre is located at (0.5,0.75), Fig. (2.9), in a $[128 \times 128]$ grid points. The velocity field is described by a two dimensional stream function with:

$$\psi = \frac{1}{\pi} \sin^2(\pi x) \sin^2(\pi y) \tag{2.62}$$

Here $t \leq T$ (where $T = 3$), the time step is $\Delta t = 5 \times 10^{-4}$ with a Courant number $c = 0.1$. In the exact (ideal) solution, the liquid disc is stretched over time to develop into a much thinner ligament, due to the velocity field. At $t = T$ the disc reaches maximum deformation.

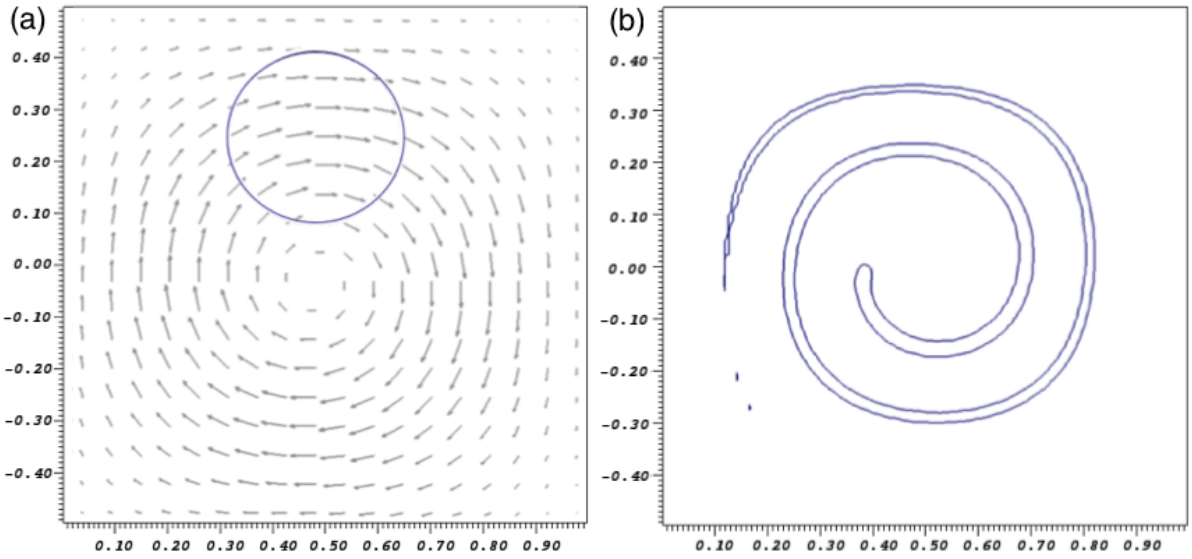

Fig. 2.9: Snapshots of (a) initial solution of a liquid drop in a 128^2 domain and (b) VOF solution for $t = T$.

2.5.2 The Level Set Method

The Level Set (LS) method, is an implicit capturing approach of the interface. A smooth marker function $\psi(x,t)$, denoting the LS function, is employed to identify the distinct fluid regions. The $\psi(\mathbf{x},t)=0$ iso-surface denotes the interface itself; with $\psi>0$ being liquid and $\psi<0$ being gas. The LS function is propagating in the normal direction, denoted as the hyper-surface fluid motion, whose velocity field is given by $\mathbf{u}|_n^I=(u^I,v^I,w^I)$ [105]. The fluid interface is a material surface, provided the interfacial mass transfer is zero, denoted with zero level set of ψ [101], as:

$$\frac{\partial\psi}{\partial t}+\mathbf{u}^I\cdot\vec{\nabla}\psi=0, \tag{2.63}$$

Typically, ψ is preferred to be defined as a *signed* distance function:

$$|\vec{\nabla}\psi|=1, \tag{2.64}$$

In principle, the ψ value in every point along the $\mathbf{n}$ direction, is equal to the minimum distance between $\mathbf{n}$ and the ψ isosurface [101][125]. The ψ advection is processed based on the condition that the material derivative must vanish.

In theory, actual zero-level set localisation is unnecessary for the advection equation solution; thus if the tracked interface is the zero-level of ψ, then the interface is implicitly represented [125]. Now, numerical errors during advection result in loss of the distance property of ψ. In the literature, there is a number of approaches available depending on the desired LS solution [105][75]. Some employ a fast marching method to find a solution for the stationary equation expressed in (2.64) [105]. In this approach, the CFL limitations are bypassed, by directly solving $|\vec{\nabla}\psi|=1$.

Others, like in Sethian et al. [105], preserve the properties of Eqn. (2.64) by using a modified velocity field to solve (2.63) [6], where the original velocity field is extended from the surface, by solving $\nabla\psi\cdot\nabla\mathbf{u}=0$. This is done, as the speed function strictly has physical meaning across the interface. Following such approach, in theory, the ψ evolution shall not result into deformation, making reinitialisation process unnecessary [105][75].

In this work, to maintain the distance property (signed function), the *reinitialisation* process is employed, solving

$$\frac{\partial\psi}{\partial\tau}+S(\psi)\left(\left|\vec{\nabla}\psi\right|-1\right)=0, \tag{2.65}$$

known as the Hamilton-Jacobi equation (see Appendix G), where τ is the pseudo-time. In (2.65), the reinitialisation process is essentially a smoothing of the ψ distribution, which in turn results in significant mass loss [125]. Equation (2.65) denotes the position of the front at time t described by the zero LS of ψ. Considering strictly the front propagation, LS is time-independent leading to a stationary LS formulation, $\tau\to\infty$, $|\vec{\nabla}\psi|=1$ so $S(\psi)$ is constant for all times [125].

However, in cases where the interface has "drifted" off the distance function during the interface reconstruction, the function $S(\psi)$ is employed as a numerically smeared *sign* function, which takes the form of:

$$S(\psi) = \frac{\psi}{\sqrt{\psi^2 + \Delta^2}} \tag{2.66}$$

where $\Delta = max(\Delta x, \Delta y)$, so that if $[\psi \to 0,\ S(\psi) = 0]$ and $[\psi \to \infty,\ S(\psi) = 1]$. Since the stability of the above must satisfy $c < 1$, $\Delta\tau$ is chosen so that the LS advection progresses at less one grid-point per pseudo-time. Here in (2.66), the distance function reconstruction is hurtled away from $\psi = 0$ and slows down near $\psi = 0$. Numerical smearing of $sign(\psi)$ function, results in a decrease in the *sign* magnitude of Eqn. (2.66). Consequently, the interfacial information propagation speed is slowed down. Discretisation of (2.65) can be very accurate, which in turn provides an accurate distance profile reconstruction. However, CFL limitations are present.

Sethian et al. [5][105] fast marching method bypassed this, by locally solving $\vec{\nabla}\psi = 1$ and using only the points near the interface. This proved to be a very efficient method but accuracy was limited and reinitialisation of the near-interface points introduced front displacement. To overcome these new limitations, Desjardins et al. [84] employed a ψ hyperbolic tangent function. The idea was based on the fact that the LS computation requires only one information, the zero iso-surface of the LS function. This implies that the LS function evolution with the advection equation over the whole domain is not required [84]. Consequently, limited treatment to the structural boundary vicinity, enables the use of the hyperbolic tangent function as:

$$\phi = \frac{1}{2}\left(tanh\frac{\psi}{2\epsilon} + 1\right) \tag{2.67}$$

where ϵ is a parameter controlling the interface profile thickness as $\epsilon = \Delta x/2$ and ψ is a Level Set function, now defined by $\psi = 0.5$, rather than $\psi = 0$. Provided a solenoidal velocity $\mathbf{u}$ field (i.e. $\nabla \cdot \mathbf{u} = 0$) and assuming $\mathbf{u}^I = \mathbf{u}$, Eqn. (2.63) can be expressed in conservative form as:

$$\frac{\partial \psi}{\partial t} + \nabla \cdot (\mathbf{u}\psi) = 0, \tag{2.68}$$

where ψ is not a distance function anymore. Thus, given a ψ definition along with Eqn. (2.68), the ψ scalar should be conservative. Solution of (2.68), does not ensure preservation of (2.67) [84]. Employing Eqn. (2.68) for the ψ transportation and restoring ψ in (2.67), both mass conservation under $\psi = 0.5$ iso-surface and numerical robustness are improved. However, a reinitialisation equation is still required (in conservative form), which reads:

$$\frac{\partial \psi}{\partial \tau} + \nabla \cdot (\phi(1-\phi)\mathbf{n}) = \nabla \cdot (\epsilon(\vec{\nabla}\phi \cdot \mathbf{n})\mathbf{n}) \tag{2.69}$$

Since Eqn (2.69) is advanced in τ, the left hand side is a compression term resulting in profile sharpening, and the right hand size is a diffusion term preserving the characteristic thickness of the profile. Consequently, solution of (2.67) and (2.69) system, implies successful $\psi = 0.5$ iso-surface transportation, maintenance of the hyperbolic tangent profile shape and ψ conservation [84]. For more details on the method one can refer to Desjardins previous works in [75][84]. In this thesis, the LS discretisation in time, is obtained using 3^{rd} Order TVD Runge-Kutta scheme [106], (see Appendix F).

The zero-level curve motion is strictly based on the normal $\mathbf{n}$, pointing from liquid to gas, as:

$$\mathbf{n} = -\frac{\vec{\nabla}\psi}{|\vec{\nabla}\psi|} \tag{2.70}$$

The interface curvature computation, κ, trails the previous work by Luo et al. [60] and is computed from the height function method. Since the normal is the gradient of the LS function ψ, the curvature is simply computed by $\kappa = -\nabla \cdot \mathbf{n}$, which in two dimensional form yields:

$$\kappa = \nabla \cdot \left(\frac{\vec{\nabla}\psi}{|\nabla\psi|} \right) = \nabla \cdot \frac{(\psi_x, \psi_y)}{\sqrt{(\psi_x^2 + \psi_y^2)}} \tag{2.71}$$

Expanding yields:

$$\kappa = \left(\frac{\partial}{\partial x} \frac{\psi_x}{\sqrt{\psi_x^2 + \psi_y^2}} \right) + \left(\frac{\partial}{\partial y} \frac{\psi_y}{\sqrt{\psi_x^2 + \psi_y^2}} \right) = \frac{\psi_{xx} + \psi_{yy}}{(\psi_x^2 + \psi_y^2)^{1/2}} \tag{2.72}$$

where the subscripts x and y denote the first ψ derivative in x- and y- directions, computed with CDS.

Finally, employing the implicit function theory (see Appendix H) and simplifying, the curvature in two-dimensions yields:

$$\kappa = \frac{\psi_x^2 \psi_{yy} - 2\psi_x \psi_y \psi_{xy} + \psi_y^2 \psi_{xx}}{(\psi_x^2 + \psi_y^2)^{3/2}} \tag{2.73}$$

which is similarly extended to three-dimensions as:

$$\kappa = \frac{\left\{ \begin{array}{c} \psi_x^2(\psi_{yy}\psi_{zz} - \psi_{yz}^2) + \psi_y^2(\psi_{xx}\psi_{zz} - \psi_{xz}^2) + \psi_z^2(\psi_{xx}\psi_{yy} - \psi_{xz}^2) \\ +2[\psi_x\psi_y(\psi_{xz}\psi_{yz} - \psi_{xy}\psi_{zz}) + \psi_y\psi_z(\psi_{xy}\psi_{xz} - \psi_{yz}\psi_{xx})] \\ +2[\psi_x\psi_z(\psi_{xy}\psi_{yz} - \psi_{xz}\psi_{yy})] \end{array} \right\}}{(\psi_x^2 + \psi_y^2 + \psi_z^2)^{3/2}} \tag{2.74}$$

2.5.2.1 Level-Set Reinisialisation Convergence Criteria

In the pure LS methods, where the normal computation and location of the interface is based on the LS function ψ, all level sets are being tracked instead of the one of interest. Consequently, the method becomes computationally expensive and introduces difficulties during interface evolution. In this work, to overcome such limitations, the LS formulation is developed within a *narrow* band (NB), originally proposed in Adalsteinsson et al. [5]. Employing a narrow band essentially provides solutions to the problems with the computational 'energy' focused within a thin band located around the front [5].

In the NB general concept, the LS function is updated within the narrow band (inner zone) and the remainder points are employed strictly for BC purposes (buffer zone), Fig. 2.10. As soon as the front motion reaches the edges (buffer zone) the calculations are stopped and a new NB is built with the zero level set. Opposingly to typical NB use, in the present work the ψ initialisation and transportation is performed everywhere, to extract the zero-ψ, whilst the narrow band is strictly employed to check the LS error. Thus an inner zone thickness is employed strictly for the LS *sign* function.

The zones in Fig. 2.10, can be summarised as:

- Narrow Band (NB): zone limited within the Buffer zone points.
- Inner Zone Thickness (ϵ): zone containing cells where LS error is checked.
- Interface Band: band containing all cells were actual interface is present.

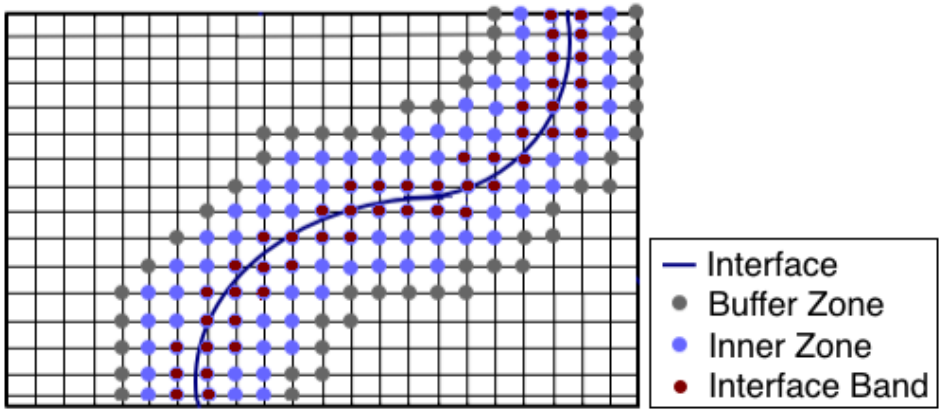

Fig. 2.10: Narrow band in a cell arrangement denoting the interface along with the inner zone, buffer zone and fixed interface band.

The inner zone thickness is a function of the mesh size, denoted by ϵ and is employed as a checking parameter reading $\epsilon < 1.5\Delta x$, implying that a change in Δ, results in a ϵ change [71][122]. Thus, it can be said that ϵ is 'data' dependent [71].

Within the inner zone, the interface band is defined based on all cells containing the interface for a restricted LS value. Doing so, ϵ ensures a narrow band size applicable to each case, whilst the interface band limits the LS computational zone to the minimum requirements for solution accuracy. Such formulation enables computational accuracy in a more cost effective manner. Recalling the previous discussion for Eqn. (2.65) and the zero LS motion limitation as a function of c, here $\Delta\tau = c\Delta x$ with $c = 0.3$. This implies that $\Delta\tau$ is dependent on the speed function nature. From there, the reinitialisation convergence criteria can be developed.

In this work, the criteria is employed as initially proposed in Sussman et al. [71] and applied in the NB as:

$$Err = \frac{1}{N} \sum_{i,j|\psi^n_{i-j}|<\epsilon} \left\|\psi^{n+1}_{i,j} - \psi^n_{i,j}\right\| < \Delta\tau\Delta x^2 \tag{2.75}$$

Here, N is the number of interfacial grid points, $\psi^{n+1}_{i,j}$ and $\psi^n_{i,j}$ are the LS function values computed at some given point for two successive iterations. The maximum tolerance limit reads:

$$Err_{max} = max[10^{-6}, \Delta\tau\Delta x^2] \qquad or \qquad Err_{grad}|_\epsilon = (\nabla\psi - 1) < 0.1 \tag{2.76}$$

where, Err_{grad} is the LS function gradient error limited within the ϵ band. It is computed with 5^{th} order Weighted Essentially Non-oscillatory (WENO) scheme, which is presented in the next section. The 5^{th} WENO implies that the stencil is at least five points, whilst to achieve solution convergence the criteria requires that $Err < Err_{max}$. Note, such method allows only one iteration per Δt, for convergence criteria to be satisfied.

Generally speaking the LS reinitialisation procedure is 'proportional' to the LS distortion itself. It is required only when steep or flat LS gradients are developed. As previously noted, an important property when numerically solving such equations, is that the relative parameter characteristics originate at the interface. This implies, that the LS equations are numerically solved for pseudo-τ steps with a pseudo-courant number. Consequently, a correct signed distance function for $c \cdot \tau$ steps away from the interface is obtained [2]. Such approach works very well coupled with the narrow band method both in terms of accuracy solution and reduced computational time.

Note, as the number of reinitialisation steps goes higher, the LS moves a lot, whilst the computational cost and time increase as well. In the literature, different suggestions are proposed for the required reinitialisation steps. In Tanguy et al. [112] is performed at every step, whilst in Shao et al. [63] every 100 steps. Theofanous et al. [82] proposed a more 'flexible' method were reinitialisation is processed every $20 - 100$ steps. In this work, reinitialisation is performed every 50 steps, satisfying the maximum number of steps required for solution to converge, thus maintain computational accuracy and ensure cost effectiveness.

2.5.2.2 Discretisation of Level Set

Hamilton-Jacobi equations, appear in numerous applications, thus a vast range of high-order numerical methods are found in the literature. Two very common ones, are the essentially non-oscillatory (ENO) and the weighted essentially non-oscillatory (WENO) methods. Both methods are effective non-linear spatial discretisation approaches. ENO scheme was first proposed by Harten et al. [3]. The scheme uses a monotone numerical Hamiltonian, a high-order ENO reconstruction and a high-order stability to preserve the Runge-Kutta time stepping process [61].

Originally, ENO was designed for hyperbolic conservation laws [3] and were later extended for the HJ solutions [105]. An improvement of ENO, the WENO [3] scheme was developed, initially proposed by Peng et al. [61]. Schemes, such as ENO can induce global instability due to the linear instability used for the linear spatial discretisation, resulting to spurious oscillations in the solutions.

In this pure LS method, the advection equation is discretised in space using 5^{th} WENO. The spatial derivatives are expressed as the weighted sum of the numerical fluxes $d_{i=1,5}$, with:

$$\left[\frac{\partial \psi}{\partial x}\right]_i = \sum_{k=0,1,2} \alpha_k d_i^k \tag{2.77}$$

Here, α_k denotes the stencil weight calculations computed as:

$$\alpha_0 = \frac{1}{10}\left(\frac{1}{IS_0+\epsilon}\right)^2, \quad \alpha_1 = \frac{6}{10}\left(\frac{1}{IS_1+\epsilon}\right)^2, \quad \alpha_2 = \frac{3}{10}\left(\frac{1}{IS_2+\epsilon}\right)^2 \tag{2.78}$$

where $\epsilon = 10^{-20}$ is chosen small enough for the denominator to be non zero.

Then, the smoothness indicators are employed reading:

$$\begin{aligned} IS_0 &= \tfrac{13}{12}(d_1 - 2d_2 + d_3)^2 + \tfrac{1}{4}(d_1 - 4d_2 + 3d_3)^2 \\ IS_1 &= \tfrac{13}{12}(d_2 - 2d_3 + d_4)^2 + \tfrac{1}{4}(d_2 - d_4)^2 \\ IS_2 &= \tfrac{13}{12}(d_3 - 2d_4 + d_5)^2 + \tfrac{1}{4}(3d_3 - d_4 + d_5)^2 \end{aligned} \tag{2.79}$$

Due to the fast/slow moving interfaces in the LS method, here it is important to maintain ($|\nabla\psi| = 1$), throughout or at least at the interface. The grid convergence criteria, amongst others, also applies when a correct numerical solution becomes independent of the grid cell size.

2.5.2.3 Validation

In this section, the liquid droplet in a shear vortex case is used for the pure LS simulations. The case is simulated in a [128 × 128] mesh for varying tolerance, as discussed in Section 2.5.2.1, for a) $Err_{max} = 1 \times 10^{-3}$ and b) $Err_{max} = 0.1$. Observing Fig. 2.11, the tail of the shear vortex in both cases is not visualised as the LS mass loss is very large, for $t = T$. In comparison with VOF, the LS is more accurate in capturing the interface.

Figure 2.11 shows that in $Err_{max} = 1 \times 10^{-3}$, a small blob indication is noted, whilst in $Err_{max} = 0.1$ the tail is sharper. However, in the latter case, the head of the vortex also seems slightly different than in $Err_{max} = 1 \times 10^{-3}$. Note, decreasing tolerance does in turn decrease CPU run time, however the results typically do not alternate much. Conclusively, the results are consistent with the LS discussions developed earlier whilst in this work we keep $Err_{max} = 1 \times 10^{-3}$ as both the test case errors and results do not change substantially.

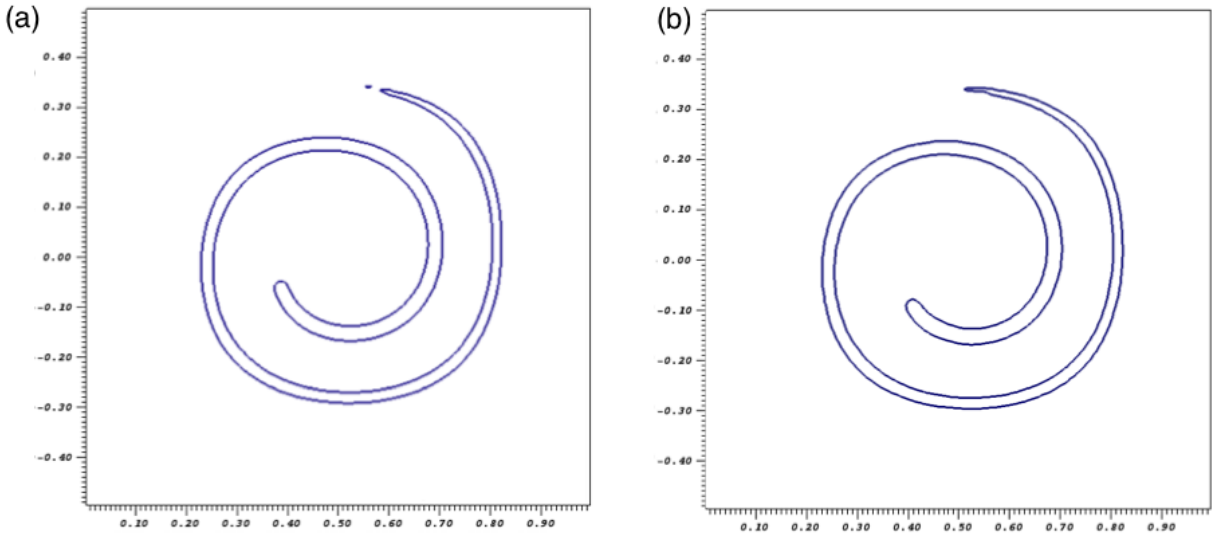

Fig. 2.11: Plot of the shear vortex of a liquid drop in a 128^2 mesh with LS for two tolerances, a) $Err_{max} = 1 \times 10^{-3}$ and b) $Err_{max} = 0.1$.

2.5.3 Comparison of VOF-CICSAM and LS

The VOF method lacks in accurate interface topology capturing, whereas LS lacks in mass conservation properties. To compare the two, a liquid disc moving in the diagonal direction (45^o) along a uniform gas flow is employed. The solutions were run for $20T$, where T denotes one period for the disc to cross the domain once and return to its original position. The simulations are first run in a $[40 \times 40]$ mesh size for $R/\Delta = 4,\ 8$.

In Fig. 2.12, snapshots for $R/\Delta = 8$ are presented. The LS disc was able to retain its shape well, but the mass loss was quite large, such that the disc had completely disappeared by $t = 20T$. On the contrary, the VOF-CICSAM disc preserved mass well but struggled to maintain the shape, resulting into a square, by $t = 20T$. Next, we tested $R/\Delta = 8$ in a $[64 \times 64]$ mesh size, Fig. 2.13. In this case, the LS was superior in capturing the interface in comparison with VOF, by preserving the disc shape quite well.

Due to the slight mesh refinement and the small increase in the number of grid points across the disc diameter, the LS mass conservation is significantly better preserved, than in $R/\Delta = 4$. In the VOF case, despite the good mass conservations properties, the shape of the disc turned into a square by $t = 20T$, denoting the method limitations in interface capturing.

Next on, the mass and curvature errors ($\epsilon\%$) with t^* are demonstrated, where $t^* = t/t_R$ and $t_R = R/U_x$. The plots are presented for $R/\Delta = 4$ and are summarised in Figures 2.14 and 2.15. Additionally, Fig. 2.16, shows the volume error for VOF and LS, at different radius/mesh size ratios, starting from $R/\Delta = 4$ up to 64. The results obtained are in agreement with the literature and the conclusions discussed within the previous sections. The VOF-CICSAM is more mass conservative than LS, but struggles in capturing the interface accurately.

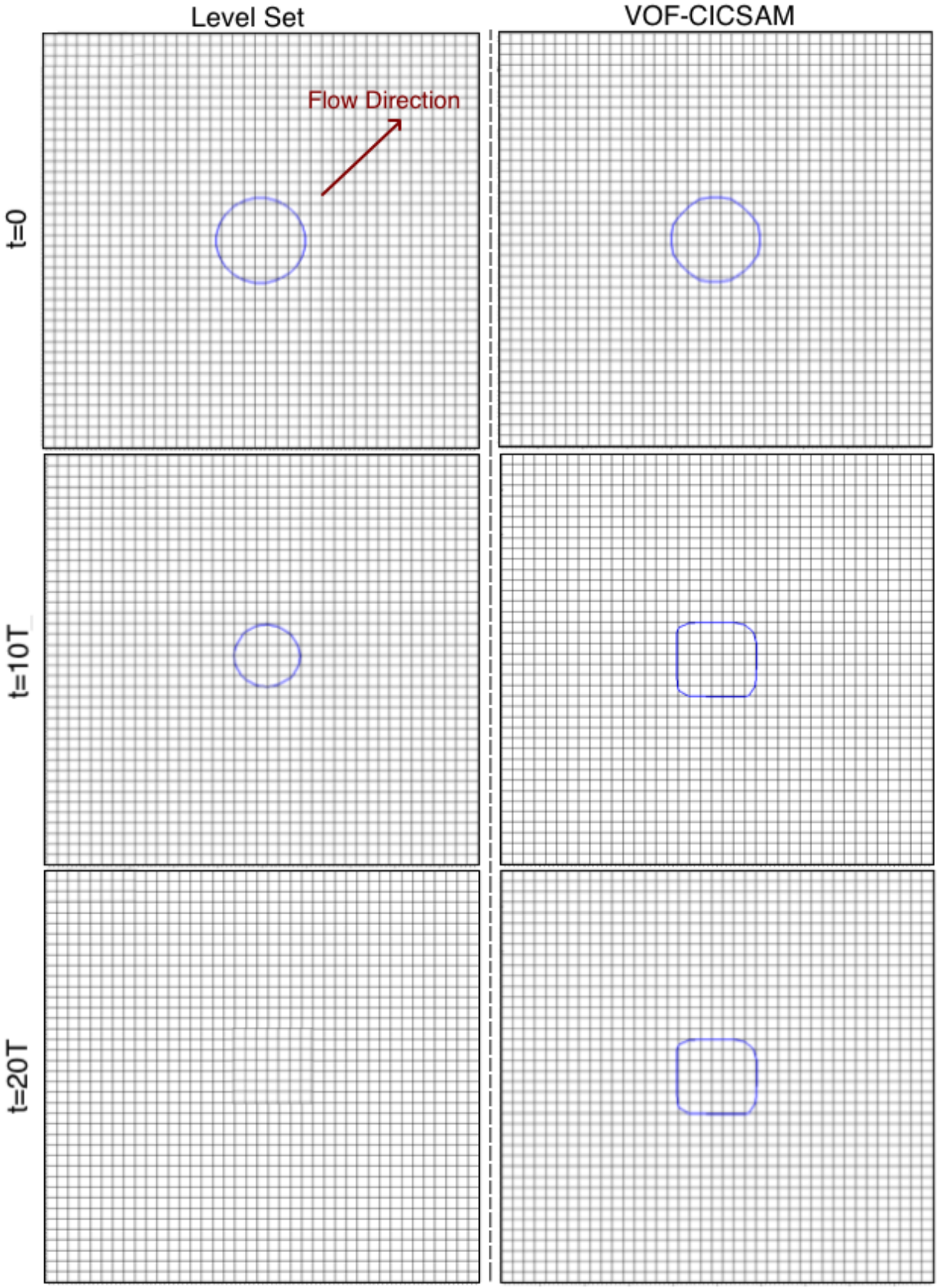

Fig. 2.12: Snapshots of disc in a uniform gas flow for Level Set and VOF-CICSAM, with $R/\Delta = 8$ in a 40^2 mesh, for $t = 0,\ 10T,\ 20T$; where LS shows $\psi = 0$ and VOF shows $\phi = 0.5$

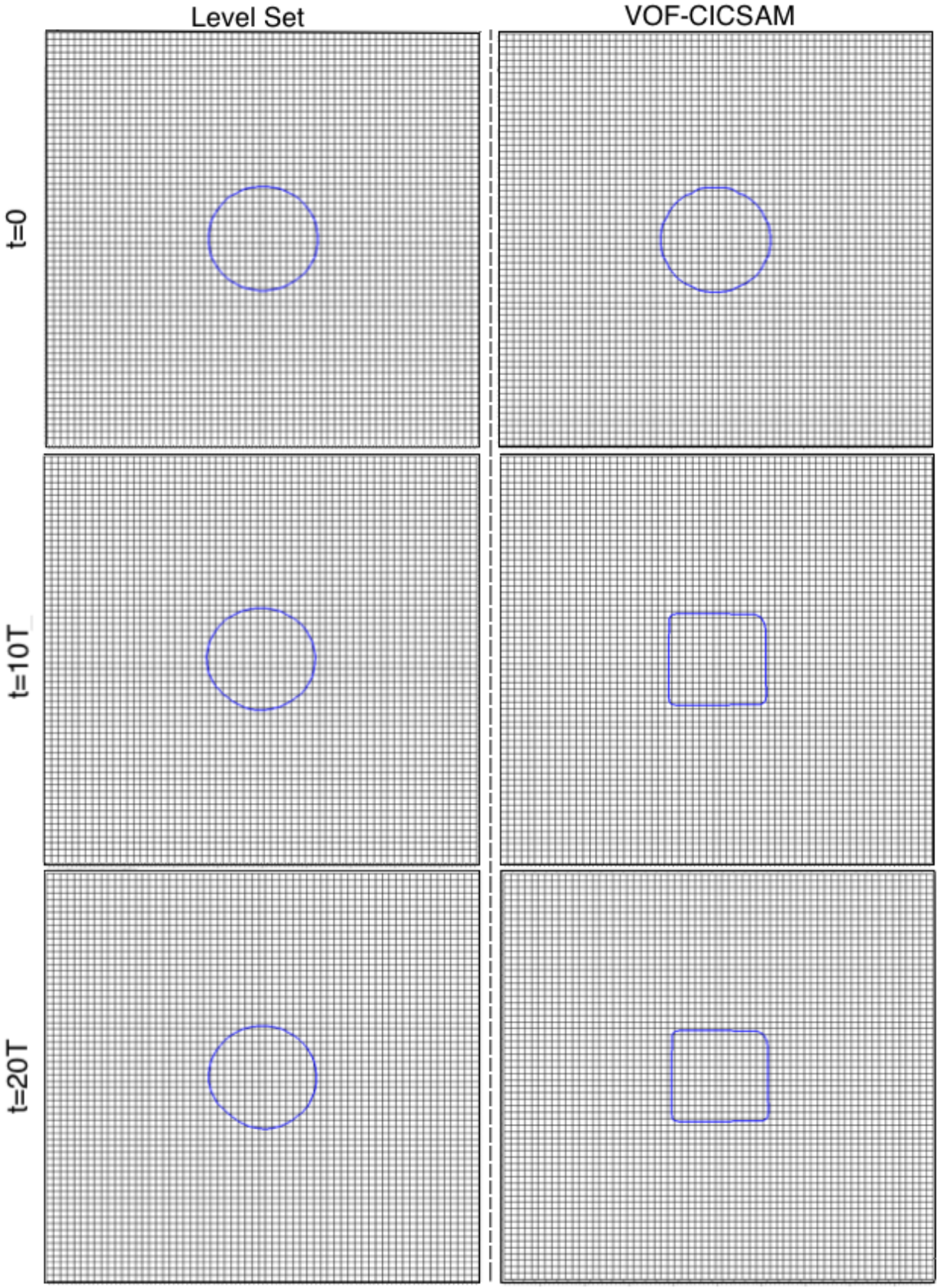

Fig. 2.13: Snapshots of disc in a uniform gas flow for Level Set and VOF-CICSAM, with $R/\Delta = 16$ in a 64^2 mesh, for $t = 0,\ 10T,\ 20T$.

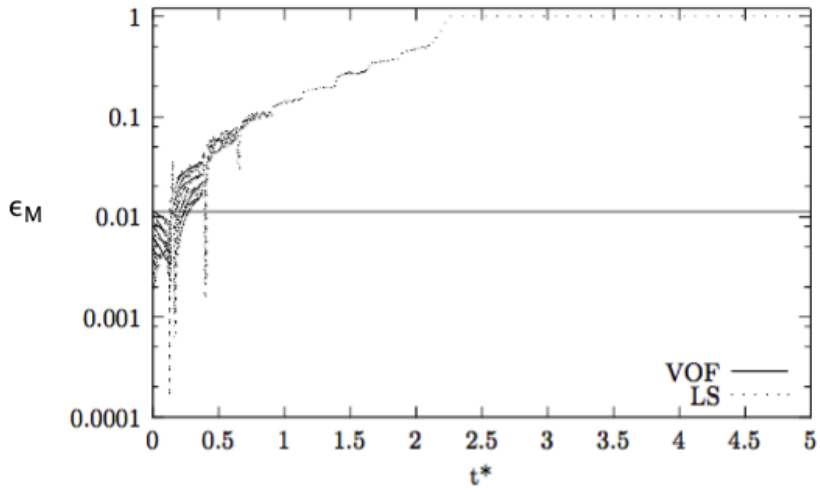

Fig. 2.14: Mass error ($\epsilon\%$) for $R/\Delta = 4$ with t^*, VOF and LS.

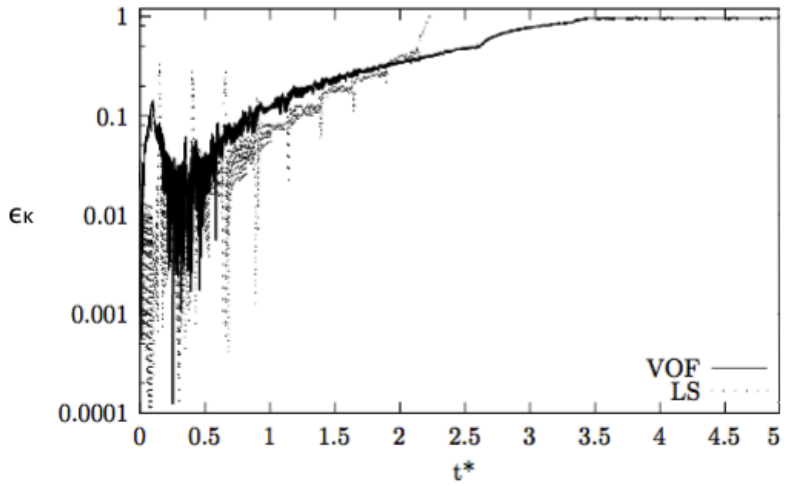

Fig. 2.15: Curvature error ($\epsilon_\kappa\%$) for $R/\Delta = 4$ with t^*, VOF and LS.

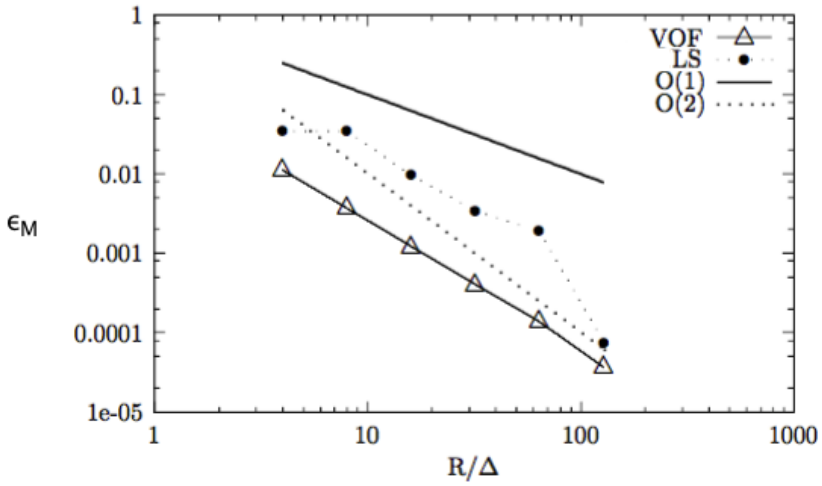

Fig. 2.16: Comparison of Mass error ($\epsilon_M\%$)with R/Δ for VOF and LS, at $t = 0$.

2.6 Summary

This section presented and validated some of the numerical solutions employed in this work. The FV method was selected for the discretisation of the NS equations which here are solved explicitly. Two interface modelling options were presented and reviewed, that of VOF-CICSAM and LS. In agreement with the literature, overall the VOF-CICSAM method is very mass conservative but really lacks accuracy in capturing the interface.

On the contrary, the LS method looses mass as expected, however interface topology properties are well captured. Both methods showed a good decreased in the mass errors with grid refinement, as is expected for any interface capturing method. The VOF method presents a more stable mass conservation as a function of the mesh size, (i.e. is always mass conservative) whilst LS showed inconsistent mass conservation behaviour.

In the Shear vortex case, the VOF method was very mass conservative independently of the mesh size. However, indications of blobs at the vortex tail, validated the inability to accurately capture the interface. Meanwhile, the LS showed improved mass conservation with mesh refinement. In the case of a diagonally moving liquid disc, both methods presented problems in cases. The VOF method showed good mass properties, but could not preserve the disc shape, regardless of the R/Δ ratio. The

LS method maintained the disc shape well even in coarse meshes. However, it struggled to preserve mass even in more refined meshes ($\epsilon_M \approx 40\%$), whilst for ratios of $R/\Delta < 8$, the mass loss eventually reached 100%, with the disc completely disappearing. Finally, as theory suggests, the LS curvature computation overruled the VOF method, regardless the mesh size. This was also validated in the liquid disc case, where the original shape was quickly altered into a square shape by early computational times.

Chapter 3

Conservative Mass Level Set (CMLS) Method

3.1 Introduction

As presented earlier, VOF and LS methods are two popular interface tracking methods. The VOF methods are very mass conservative but lack accuracy. Opposingly, LS methods provide good interface topology (i.e. normals, interface location and curvature computations) but suffer from mass loss. In this section, we present a novel mass conservative LS method (CMLS), where the normals from LS are employed for the interface reconstruction and the mass correction is enforced based on two different approaches. The actual interface reconstruction is based on a geometrical approach. The full CMLS method philosophy and all the relative numerical tools are detailed presented in the following pages. Once the basic model is presented, the code is validated through a series of test cases and compared accordingly with the pure VOF-CICSAM and LS methods. In the end, the optimum interface capturing method, CMLS is extended in 3D and evaluated appropriately.

3.2 Philosophy

In this section, we present a novel Mass Conservative Level Set (CMLS) method. Here, the LS normals are employed for the interface reconstruction. The LS mass conservation correction is based on the previous works by Luo et al. [60] using the interface curvature and Zoby et al. [134] for a uniform interfacial cell correction. From there, the mass gain/loss is computed and redistributed accordingly. The actual interface reconstruction is based on a geometrical approach initially proposed by Scardovelli et al. [103]. The general algorithm of the CMLS method employed here, can be summarised as:

- Initialisation of both Level Set ψ and Volume of Fluid ϕ functions.
- Compute interface normals with level set using $\mathbf{n} = f(\psi)$ and locate interface position from $\vec{n}_\psi$.
- Compute initial LS mass V_{ψ_o} using a smooth VOF (ϕ^S) marker, originally proposed in Sussman et al. [71].
- Compute *Theoretical* Mass loss ($V_{loss}\%$) and proceed with coupling based on $Err_{mass} > 1 \times 10^{-2}(\%)$. Once coupling processed, compute area A using LS normals with $A = f(\vec{n}_\psi)$.
- Compute the Interface Curvature (κ_Γ) using a linear interpolation of ψ as a level set weighting factor. Advect level set function ψ^n at ψ^{n+1} and recompute ϕ^{n+1} value from ψ^{n+1}.
- Correct *mass* according to $V_{loss} > \epsilon_{max}$ criteria, with ϵ_{max} denoting the *max* tolerance. Here, in principle we essentially relate the level set ψ and the general volume fraction dV, with $dV = f(\delta\psi) = V_{loss} + V_{\psi_o}$. Mass correction is processed with two different approaches, based on the 'instant' computational needs. The first approach, corrects using a uniform mass distribution at the interface cells, (dV_Γ), trailing Zoby et al. [134]. This method, assumes mass is homogeneously distributed over a planar surface. The cell mass is computed using the ψ cell value. However, cases such as local LS properties are not taken into account. Thus, if such correction is not sufficient, the mass correction is then based on the interface curvature, κ_Γ. This approach is based on the criteria $\delta\psi \propto \kappa_\Gamma V_{loss}$, trailing Luo et al. [60]. To do so, we employ the $A = f(\vec{n}_\psi)$, so that $\delta\psi = (dV/A)$, Fig. 3.1. Note the correction is limited to $0.05\Delta x$, to avoid 'over' correction and ensure accuracy. The actual mass correction from κ_Γ is processed with:

$$(dV_\kappa)_\Gamma = V_{loss}\frac{\kappa_\Gamma^p}{\sum_k \kappa^p} \tag{3.1}$$

  where p is a parameter and the sum is over the number of interface points.

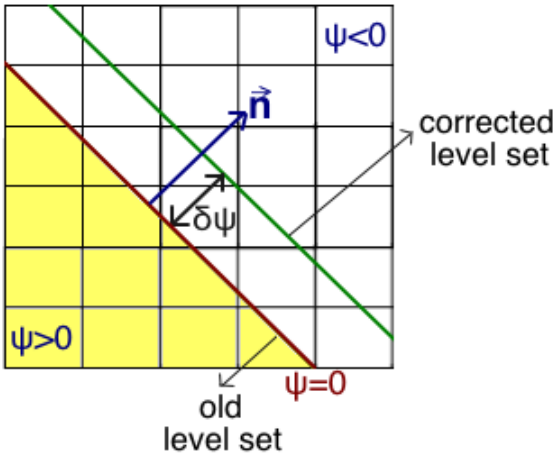

Fig. 3.1: Schematic of level set correction with $\delta\psi$.

- Reconstruct the interface using ϕ^{n+1}, based on the reconstructed points in a geometrical manner to yield a new interfacial plane, trailing Scardovelli et al. [103] work. Here, the normals and interface location necessary are level set employed, $\vec{n}_{\psi}$.
- Advect ϕ^{n+1} and the new ψ^{n+1} and reinitialise the final level set ψ^{n+1} function using 3^{rd} order Runge-Kutta scheme.

With respect to the p parameter in Eqn. (3.1), different values have been denoted in the literature. In Luo et al. [60], ($p = 1$) whilst Zoby et al. [134], uses uniform corrections, (i.e. $p = 0$). The p choice can significantly affect the computational results. In cases of large filaments present, $p = 0.05$ is enough, whilst for droplet break-up cases, $p = 0.5$ is required, to preserve any existent small droplets. To show the 'p' variation effects, a series of coarse test cases are employed, a shear vortex, a basic drop break-up and a sloshing test, Figures 3.2-3.4. Note, these are strictly for demonstration purposes on the various 'p' effects, with detailed investigations and better analysis of such test cases provided in later sections.

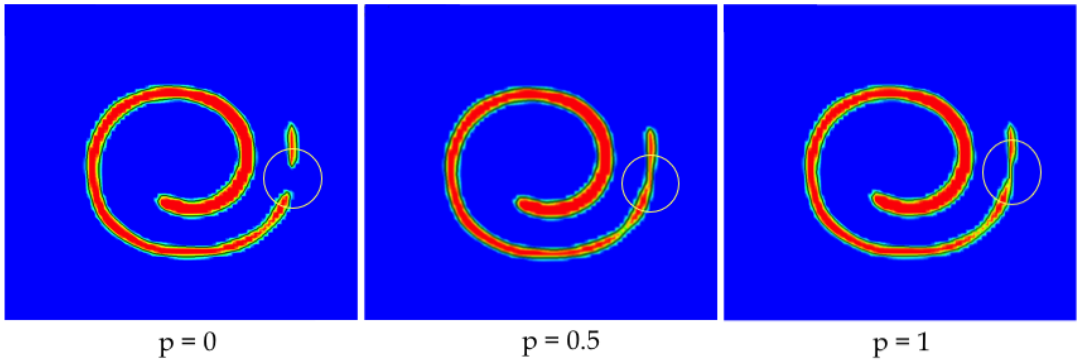

Fig. 3.2: Shear vortex for different p values in a (80×80) mesh size.

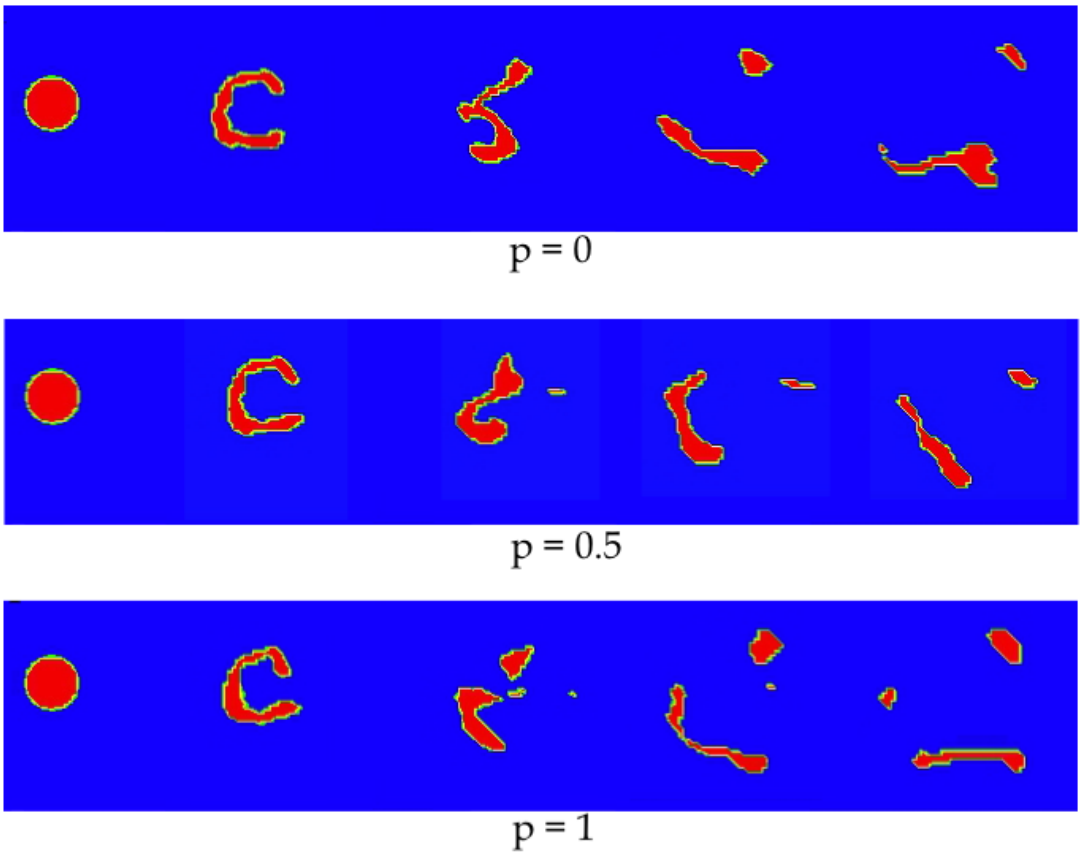

Fig. 3.3: Droplet break-up for different p values in a (80×80) mesh size.

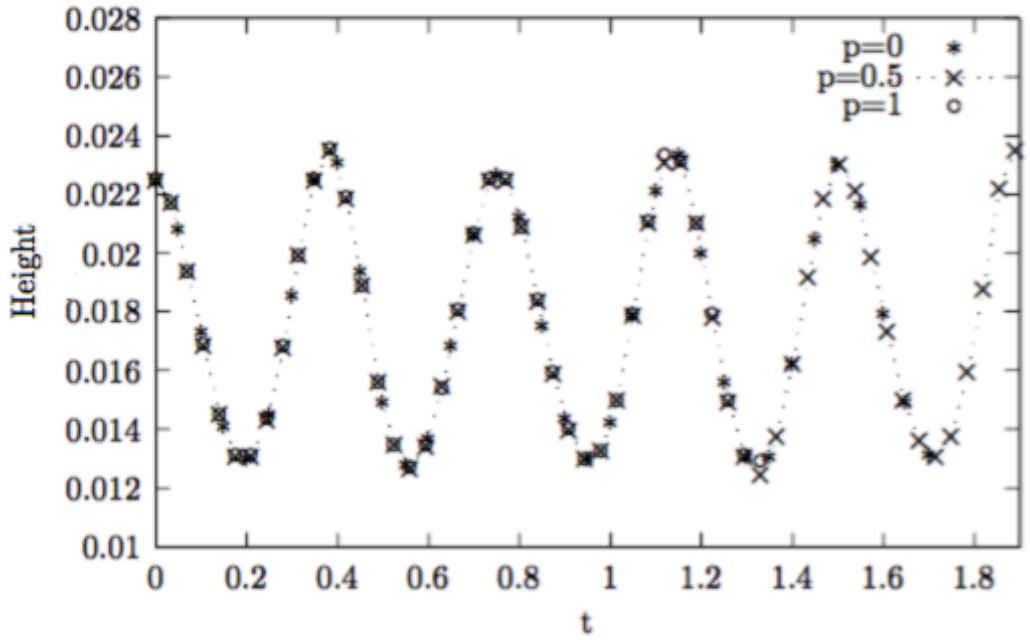

Fig. 3.4: Sloshing test for different p values in a (80×80) mesh size. Here, $p = 0,\ 1$ breaks after $t > 1$.

In the shear vortex, the 'p' choice mostly impacts the captured tail resolution. In the droplet break-up the number of fragments captured varies, for $p = 1$ three fragments are observed whilst for $p = 0,\ 0.5$ two. In the sloshing test case, $p = 0,\ 1$ fail to capture the interface position for the total simulation time and only $p = 0.5$ captures it effectively. A basic schematic demonstrating the CMLS steps is shown in Fig. 3.5. Note, the reinitialisation proceedings of the final level set ψ^{n+1} function follows Section. 2.5.2.2.

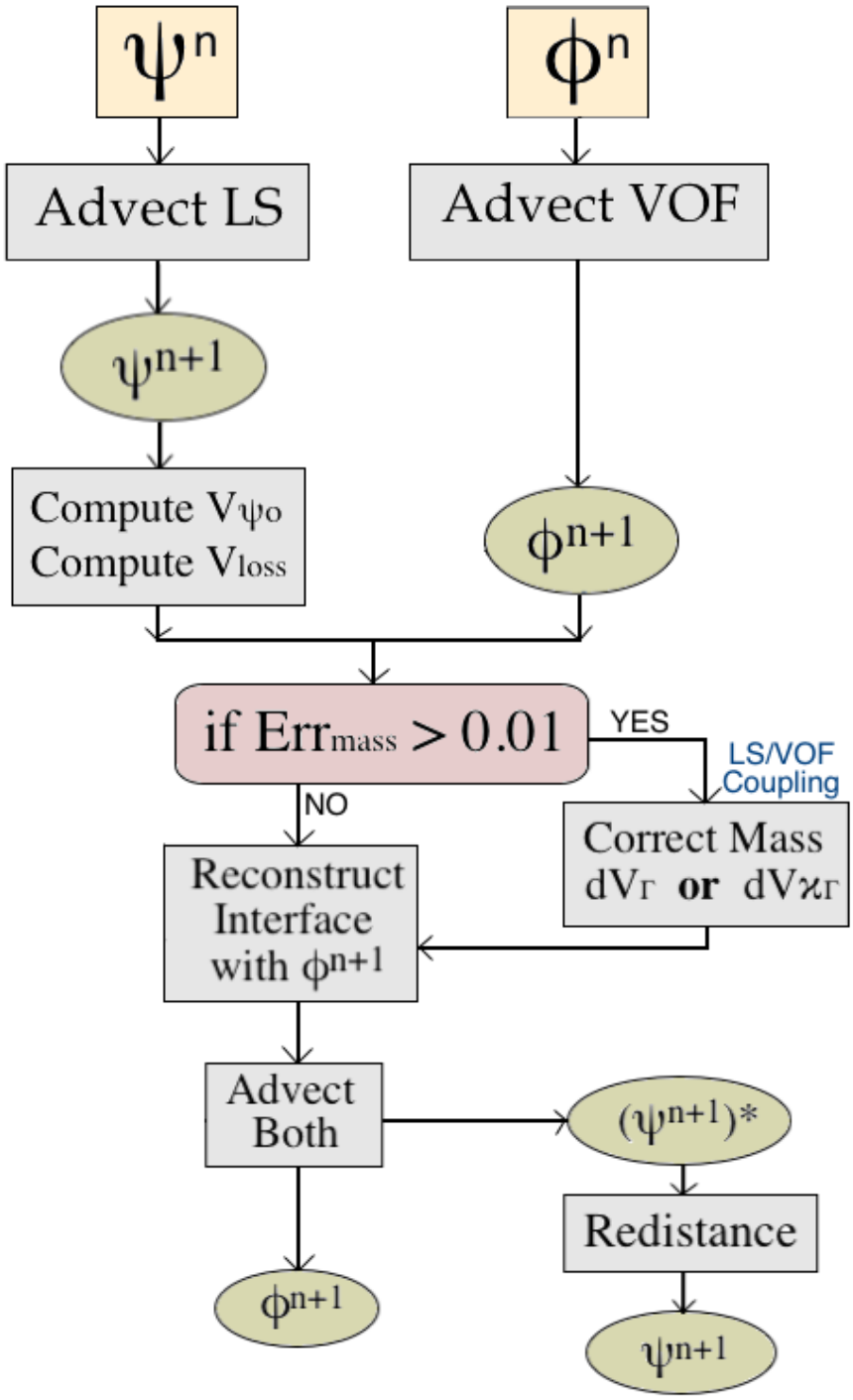

Fig. 3.5: Flowchart schematic of the CMLS method.

3.3 CMLS Numerical Tools

3.3.1 Mass and Momentum Coupling

In this section we present the mass and momentum coupling for the CMLS method in summarised steps. The process is done in two loops using LS and the pressure correction method.

First Loop

Primarily the level set is advanced with the previous time step n and is computed at an intermediate time level $n + 1/2$ as seen below, respectively.

$$\begin{aligned} \psi^{n+1} &= \mathcal{F}(u^n, \psi^n) + \mathcal{O}(\Delta t) \\ \psi^{n+1/2} &= 1/2(\psi^{n+1} + \psi^n) \end{aligned} \tag{3.2}$$

From there, the density (ρ) and viscosity (μ) are evaluated at the intermediate time level $n + 1/2$ with

$$\begin{aligned} \rho^{n+1/2} &= \rho(\psi^{n+1/2}) \\ \mu^{n+1/2} &= \mu(\psi^{n+1/2}) \end{aligned} \tag{3.3}$$

and the non-conservative velocity, using $\nabla \cdot \mathbf{u}^* \neq 0$, is computed with the momentum equation as

$$u^* = \mathcal{L}(u^n, u^{n+1/2}, \rho^{n+1/2}) + \mathcal{O}(\Delta t) \tag{3.4}$$

Employing the pressure correction method, already presented in Section 2.4.3, one gets:

$$P^C = \mathcal{G}(u^*, \rho^{n+1/2}) \tag{3.5}$$

and the corrected velocity to satisfy $\nabla \cdot \mathbf{u}^{n+1} = 0$, reads:

$$u^{n+1} = \mathcal{H}(u^*, \rho^{n+1/2}, P^C) \tag{3.6}$$

Second Loop

During the second loop, the velocity at intermediate time level $n + 1/2$ is computed as:

$$u^{n+1/2} = 1/2(u^{n+1} + u^n) \tag{3.7}$$

followed by the non-conservative velocity (using $\nabla \cdot \mathbf{v}^* \neq 0$) and with the momentum equation, yields:

$$u^* = \mathcal{L}(u^n, u^{n+1/2}, \rho^{n+1/2}) + \mathcal{O}(\Delta t^2) \tag{3.8}$$

Similarly to the first loop, the pressure correction computation is obtained with:

$$P^C = \mathcal{G}(u^*, \rho^{n+1/2}) \tag{3.9}$$

and the equivalent velocity correction to satisfy $\nabla \cdot \mathbf{v}^{n+1} = 0$, gives:

$$u^{n+1} = \mathcal{H}(u^*, \rho^{n+1/2}, P^C) \tag{3.10}$$

Finally, the Level Set is advanced with the intermediate velocity $n + 1/2$ as:

$$\psi^{n+1} = \mathcal{F}(u^{n+1/2}, \psi^n) + \mathcal{O}(\Delta t^2) \tag{3.11}$$

and the final density and viscosity at the new time level $n + 1$ yields:

$$\begin{aligned} \rho^{n+1} &= \rho(\psi^{n+1}) \\ \mu^{n+1} &= \mu(\psi^{n+1}) \end{aligned} \tag{3.12}$$

3.3.2 Compute cell density and viscosity

The density and viscosity along a particle path are both constant. However, these properties with respect to LS, change in a sharp manner at the front (i.e. 'steep' gradients exist), whilst ψ is a smooth function. Thus, ρ and μ are discontinuous across the interface. Moreover, although ψ is initially a distance function, it will not retain this property during advection, a jump is developed at the interface when two fluids are merged. So, resolving $\rho(\psi)$ or $\mu(\psi)$, numerical instabilities or numerical oscillations around the interface will be present, particularly in large density ratios.

To prevent those, the cell density and viscosity equations are expressed in terms of a smooth VOF marker ϕ^S, as:

$$\rho = \phi^S \rho_{liq} + (1 - \phi^S)\rho_{gas} \qquad \text{and} \qquad \mu = \phi^S \mu_{liq} + (1 - \phi^S)\mu_{gas} \tag{3.13}$$

The smooth VOF (ϕ^S) marker employed, as initially proposed in Sussman et al. [71], reads:

$$\phi^S = \begin{cases} 0, & \psi < -\delta \\ \frac{1}{2}\left[1 + \frac{\psi}{\delta} + \frac{1}{\pi}\sin\left(\pi\frac{\psi}{\delta}\right)\right], & |\psi| \leq \delta \\ 1, & \psi > \delta \end{cases} \tag{3.14}$$

denoting that the interface thickness is $\approx 2\delta/|\nabla\psi|$. This smooth ϕ^S marker is usually included in the smeared Heaviside function to improve numerical robustness. However, here is strictly employed to compute the VOF volume given a ψ value.

In this work, the LS front has a uniform thickness, implying the need of $|\nabla\psi| = 1$ when $\psi \leq \delta$. So, provided the LS is equal to the distance function (see Eqn. 2.64), then from Eqn. (3.14) it follows that the interface thickness is 2δ. Here, ϕ^S is limited within the transition band from 0 to 1, Fig. 3.6, over a distance $\delta = \sqrt{2}\Delta$ in two dimensions and $\delta = \sqrt{3}\Delta$ in three dimensions, accordingly. Note, δ is essentially the cell diagonal, which is the maximum cell distance possible. Increasing δ makes the function smoother. The smooth marker (ϕ^S) is a first-order approximation to the liquid area in 2D and volume in 3D, in the domain, Eqn. (3.15) below.

$$A_{liq} = \sum^{Ncell} \phi^S_{i,j}\Delta^2 + \mathcal{O}(\Delta) \qquad \text{and} \qquad V_{liq} = \sum^{Ncell} \phi^S_{i,j,k}\Delta^3 + \mathcal{O}(\Delta) \tag{3.15}$$

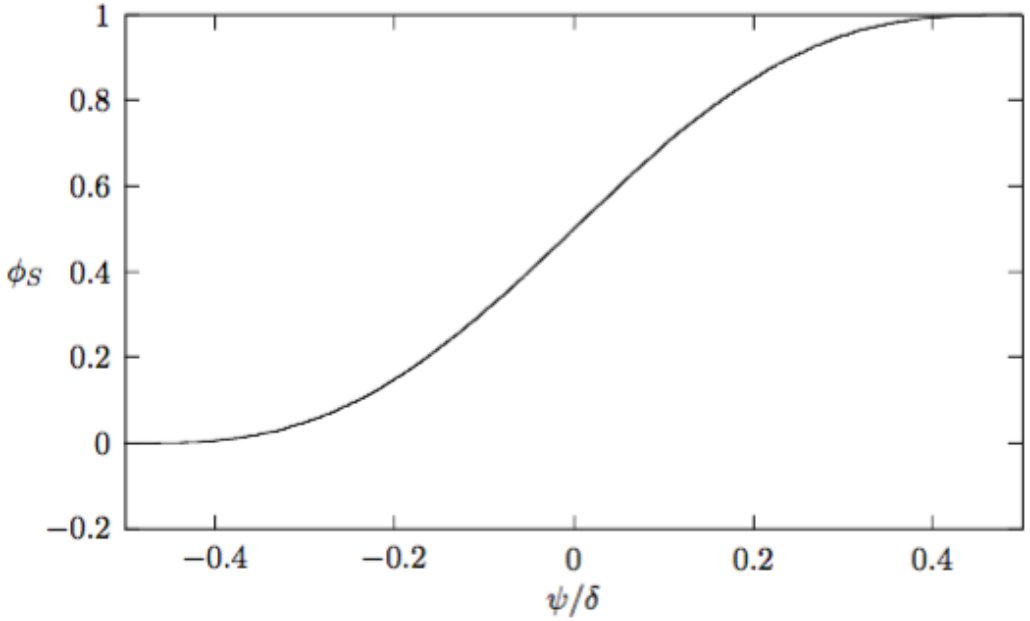

Fig. 3.6: Marker function transition zone with ψ/δ.

3.3.3 Surface Tension Treatment

Two-phase flows modelling using interface tracking methods typically involves an immersed boundary (phase interface). This is the surface tension forces locus and any fluid property discontinuity, is usually expressed with the jump conditions. There are two main methods in the literature to treat such singularities, the Continuum Surface Force and the Ghost Fluid Method. CSF method was initially proposed in a VOF formulation by Brackbill et al. [62]. The model does not treat surface tension as a boundary condition, instead it appears as a continuous function, where the surface tension is modified as a localised volume force near the interface. In cases of dominant surface tension, a spurious velocity field is developed which in turn introduces numerical errors. These errors are due to the imbalance between surface tension and pressure gradient forces along with any curvature estimation errors [62].

To tackle this issue, the method requires that an exact balance is introduced of the normal component for both surface tension forces and pressure gradient. The CSF method is of first order accuracy due to the numerical smoothing inherited [62]. To treat the numerical smoothing evolved in the CSF method, Fedkiw et al. [91] proposed the Ghost Fluid method (GFM). The GFM is employed in multiphase flows, where both the CON and DIFF terms are discontinuous at the interface, this results in a viscosity and density jump at the liquid/gas interface. In Fedkiw et al. [91], the discontinuity imposed by the multiphase interface is captured within the inviscid compressible Eulerian equations [91], [130]. The GFM treats the oscillations inherited and the interface jump conditions are not used explicitly. The appropriate interface conditions are implicitly applied by creating a 'ghost' fluid. Consequently, GFM is well coupled with Level Set which in turn implicitly represents the interface.

The surface tension in the pressure gradient discretisation is directly imposed, this also satisfies the force balance concept [130]. The density, viscosity and curvature are computed by linear interpolation, which in turn imposes the need of a signed distance from the interface. Note, in VOF formulations this signed distance is reconstructed from the VOF function temporarily, whilst in LS it already exists by definition. The surface tension force is a singular term that can lead to the presence of numerical stabilities, known as parasitic currents. The effects of these instabilities are reduced by the discretisation of the pressure field resulting in a discontinues solution [30][130]. At the interface, both the CON and DIFF terms are discontinues in time due to the viscosity and density jump during a phase change from liquid (gas) and gas (liquid).

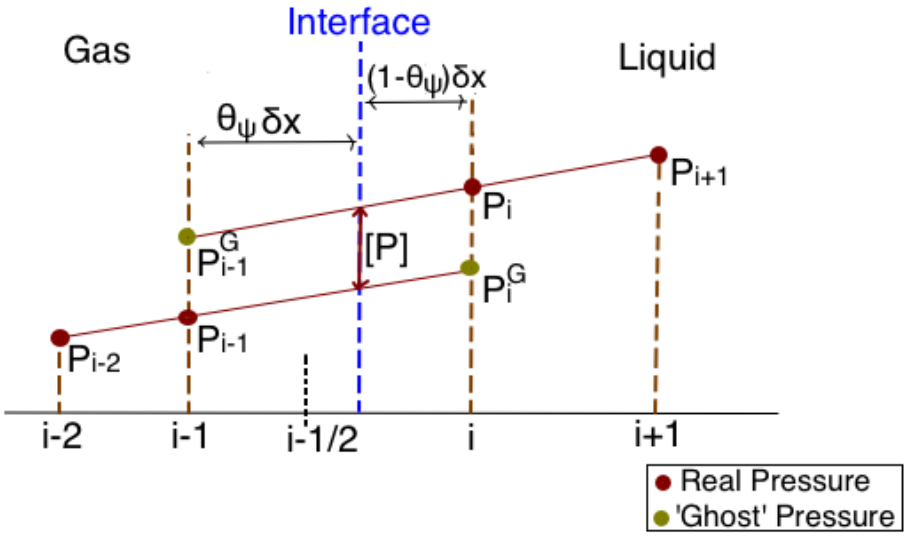

Fig. 3.7: Ghost Fluid Method schematic demonstrating the ghost and real pressure values.

In the Ghost Fluid method, the pressure gradient discretisation with location $i-1/2$, reads:

$$\left(\frac{\partial P^*}{\partial x}\right)_{i-1/2} = \frac{P_i^G - P_{i-1}}{\Delta x} = \frac{P_i - P_{i-1} - [\![P]\!]}{\Delta x} \tag{3.16}$$

where $[\![P]\!]$ is the Pressure jump at the cell face, which in terms of the surface tension σ yields:

$$[\![P]\!] = \begin{cases} \sigma\kappa_\Gamma & \text{if} \quad \phi_{i-1} \leq 0 \quad \text{and} \quad \phi_i > 0 \\ -\sigma\kappa_\Gamma & \text{if} \quad \phi_{i-1} > 0 \quad \text{and} \quad \phi_i \leq 0 \\ 0 & \text{otherwise} \end{cases} \tag{3.17}$$

where x is the direction towards the interface and ϕ_i is the scalar value at the interface.

The interface curvature, (κ_Γ) is simply computed from linear interpolation using the Level Set function ψ, as a level set weighting factor of:

$$\theta_\psi = \frac{|\psi_{i-1}|}{|\psi_{i-1}| + |\psi_i|} \tag{3.18}$$

For Eqn. (3.18), away from the interface $\theta_\psi \approx 1$. Close to the interface $\theta_\psi \approx 0$ provided the left cell $\theta_{i-1/2} \to 0$ (near the interface) and ψ_{i-1}. From there, the interface curvature is computed with:

$$\kappa_\Gamma = \kappa_{i-1}(1 - \theta_\psi) + \kappa_i \theta_\psi \tag{3.19}$$

3.3.3.1 Interface Curvature Validation

To show the validity of the method for κ_Γ, primarily a static liquid disc was placed in a uniform domain. The disc was tested for $R/\Delta = [4,\ 8,\ 16,\ 32,\ 64]$ and the relative $|\epsilon_{\kappa_\Gamma}|(\%)$ was computed and plotted in 2D, Fig. 3.8. The interface curvature appears to be of $\mathcal{O}(\Delta)$. The curvature denotes a sufficient convergence overall, however the last two points, $R/\Delta = [32,\ 64]$, are slightly off. As the cell curvature computation is LS based, which is discretised using 5^{th} WENO, the stencil will be at least 5 points. At $R/\Delta \approx 2$, denotes that the stencil is the whole liquid disc and the expected errors will be large. So, as we compute the curvature in a point, correct solutions will only be obtained across the interface, with inaccuracies present every where else.

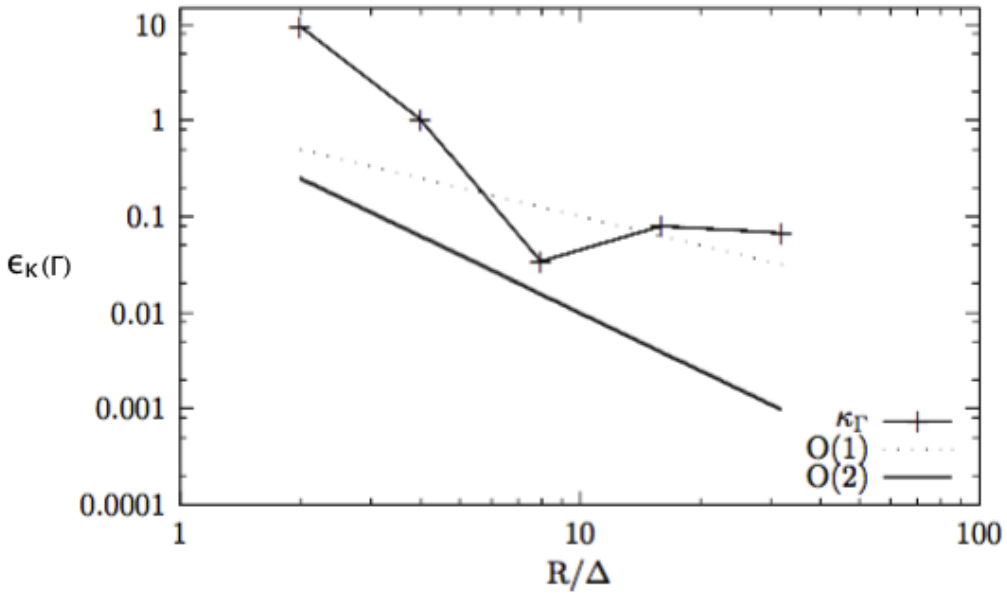

Fig. 3.8: Interface curvature error $|\epsilon_{\kappa_\Gamma}|\%$ with R/Δ.

Next, a diagonally moving droplet with $R/\Delta = 8$, was placed in a uniform coarse mesh of $[64 \times 64]$. The circle crosses the boundary fifteen times. The case was tested with VOF-CICSAM and CMLS for a brief comparison. The relative error ϵ_κ with t^* is plotted in Fig. 3.9, where $t^* = t/t_R$ and $t_R = R/U_x$. It is clear, that the CMLS curvature computation is very stable even for a coarse mesh and demonstrates superior accuracy than a VOF-CICSAM approach.

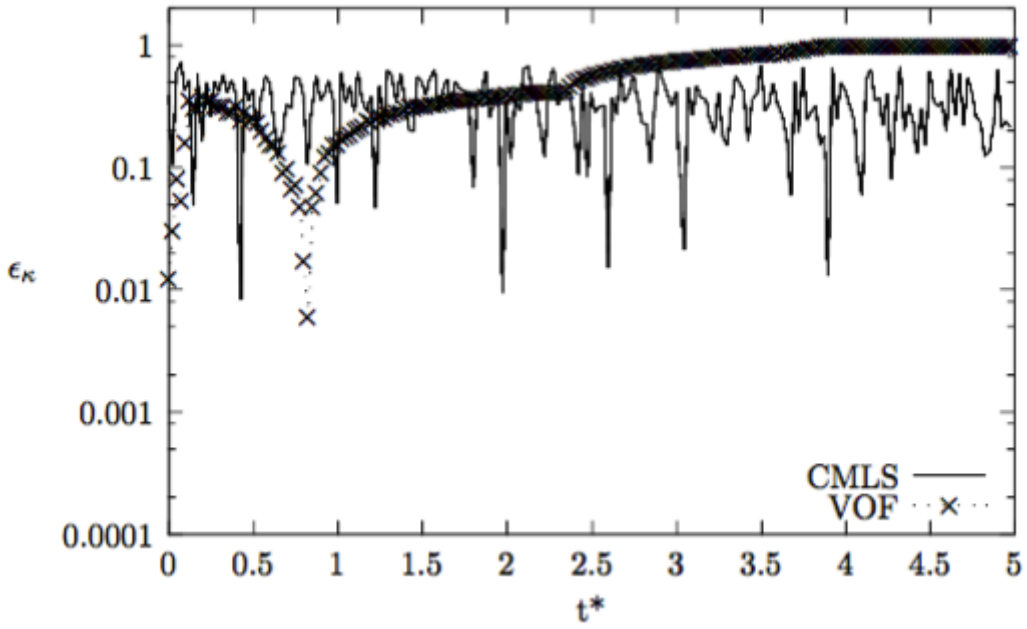

Fig. 3.9: Curvature error $\epsilon_\kappa\%$ with t^* in $R/\Delta = 8$ domain, for VOF and CMLS.

In Brackbill et al. [62] CSF method, the force density in the transition region is proportional to the surface curvature. In their work, they showed that the interface can be expressed by a continuous model, implying a non grid-aligned transition region exists at the interface of two fluids. They found that the interface curvature is quasi-continuous along the interface, provided $\kappa\Delta \leq 1$, where Δ is the mesh size. In this work, GFM method is used instead. By definition the curvature reads as $\kappa = 1/R$. Thus the present calculations in terms of the mesh size and the disc radius, denoted $\Delta/R = 0.693 < 1$, suggesting κ_Γ varies quasi-continuously across the interface.

3.3.3.2 Parasitic Currents in a Liquid Static Drop

Parasitic currents develop in the adjacent interface fluid regions due to the local GFM body force variation. To primarily understand their origin, the forces acting on a liquid static drop, suspended in a continuous phase of zero gravity are considered. In theory, all the velocities in this case would be zero once equilibrium is established [111]. Now considering the momentum conservation equations, all the velocity-related terms are zero and in cases of static drops, the equations reduce down to:

$$0 = -\nabla P + \sigma\kappa\nabla\psi \tag{3.20}$$

known as the Young-Laplace equation, relating the pressure different at the interface, where the inner drop pressure is larger than the outer one. During numerical computations of the curvatures, small errors are produced by the pressure equation resolution from the interface jump conditions. Taking the curl of Eqn. (3.20), then κ should satisfy $\nabla\kappa \times \nabla\psi = 0$ [111]. Provided the latter condition is unsatisfied, artificial velocity values are generated across the interface, known as parasitic currents.

To compliment this discussion, the development of parasitic current due to surface tension acting on a fixed liquid drop are investigated. Considering a [128 × 128] mesh, a static drop of $R/\Delta = 24$ is centred in a unit sized domain. A constant time step $\Delta t = 2 \times 10^{-5}$ is used, with a density ratio of $\rho_L/\rho_G = 1000$ and the viscosities are $\mu_L = 10^{-4}$ and $\mu_G = 1.6 \times 10^{-5}$. The surface tension effects are tested for $\sigma = [0.01,\ 0.05,\ 0.07,\ 1.0,\ 2.0]$ and a sample result for $\sigma = 1.0$, is presented in Fig. 3.10.

Additionally, a three-dimensional snapshot is shown in Fig. 3.11, with the pressure field enclosed within. The Capillary number based on the parasitic currents is plotted with time t^* in Fig. 3.12 and are summarised in Table 3.1. For the dimensionless time we employ $t^* = t/t_\sigma$ with $t_\sigma = \sqrt{\rho D^3/\sigma}$ and D being the drop diameter [111].

σ	Capillary
0.01	10^{-5}
0.05	10^{-6}
0.07	10^{-7}
1.0	10^{-8}
2.0	10^{-12}

Table 3.1: Summarised values of Capillary number for the different surface tension.

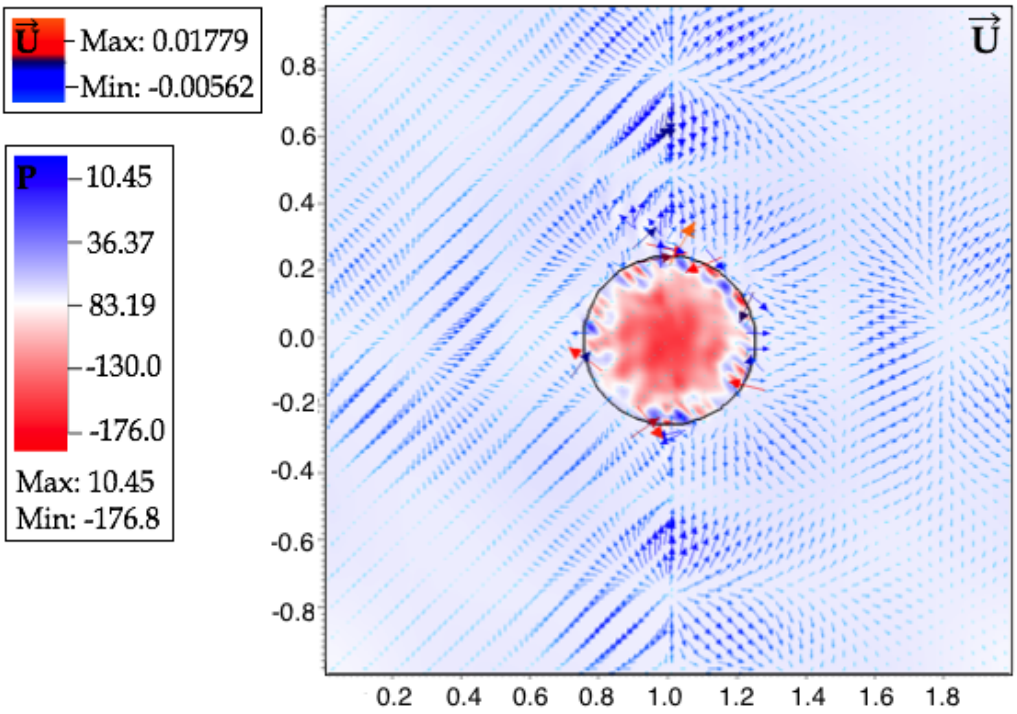

Fig. 3.10: Two-dimensional sample snapshot of parasitic currents in a fixed liquid drop, for $\sigma = 1.0$. Here the velocity field is shown outside and across the periphery of the drop along with pressure field enclosed within the drop.

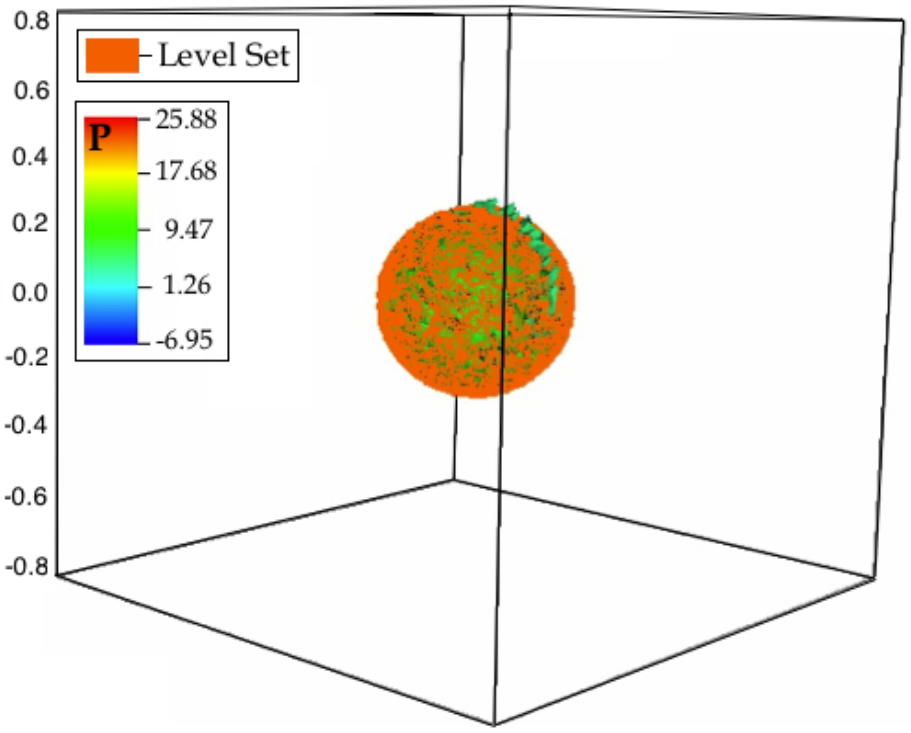

Fig. 3.11: Three-dimensional sample snapshot of parasitic currents in a fixed liquid drop, for $\sigma = 1.0$, with the orange contour denoting the level set solution and the pressure field enclosed within the drop (i.e. green colour).

Note, in two-phase flow studies such as liquid droplets and liquid jet break-up processes, the Capillary number is a key parameter, determining the break-up dynamics. The two processes are directly linked, as in high velocity jets, droplet break-up occurs due to the effects of the capillary forces acting on it. These forces account for a range of recorded instability modes, such as the Rayleigh-Taylor that induces any drop deformation/break-up by capillary pinching [28][118]. In the upcoming sections, such processes are investigated, within the $0.01 \leq \sigma \leq 0.07$ range, presented in Tab. 3.1.

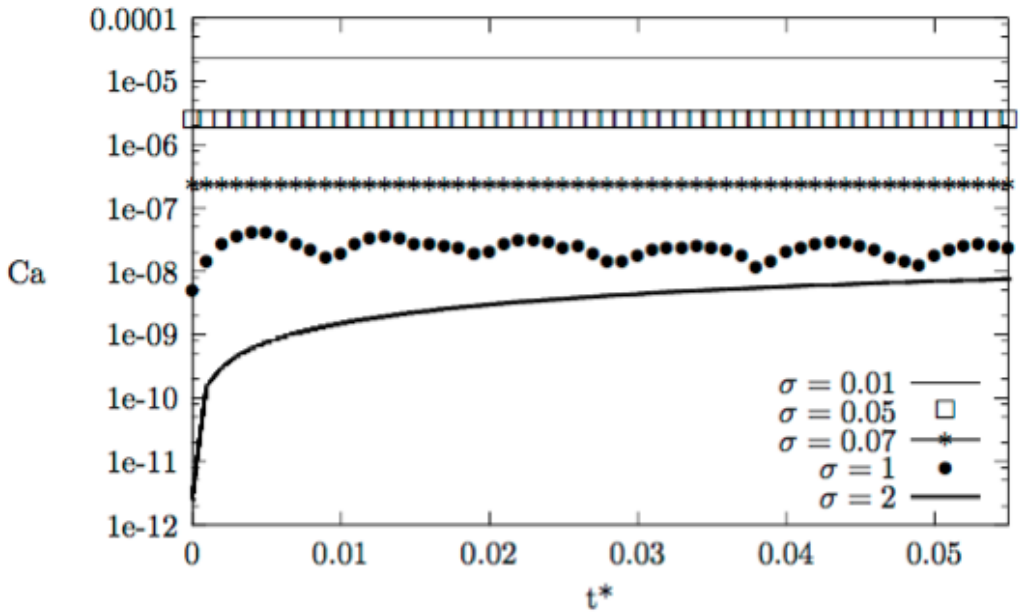

Fig. 3.12: Plot of Ca number with time t^* for various σ.

In Harvie et al. [32], a study of the parasitic currents effect in a CSF environment was presented. Their work suggested that the effects can be limited both by the NS inertial and viscous terms. When the densities and viscosities are equal and under low enough We parameters so that inertial effects are negligible, the parasitic currents effect is limited by the viscous terms [32]. They also concluded that a mesh refinement leads to an increase in the parasitic currents, and their magnitude scales with $1/Ca$.

However, they noted that the magnitude of these currents does not depend on the computational time step. The latter statement, has also been validated in this work. By definition, an increase in σ should result in a decrease of Ca. In Figure 3.12 this behaviour is observed, however it is interesting to note that for a small σ increase, the Ca number decreases by at least one order of magnitude.

Another important parameter in such test cases, is the spurious currents intensity, denoted by the La number. Here, we study the spurious currents evolution in terms of the Ca number as a function of the Ohnesorge number, that can be expressed as a function of Laplace, as $Oh = 1/\sqrt{La}$. By definition, an increased in σ denotes a decrease in Ca, which follows an increase in La and equivalently a decrease in Oh, in a inversely proportional manner [111].

Figure 3.13 shows the Ca behaviour as a function of Oh. Legendre et al. [111], noted that the interfacial uniform κ_Γ tangential should remain the same over time. They also stated the exact velocity field should be zero throughout the domain and pressure should follow the La pressure jump at the interface [111]. The present results are in agreement with their work.

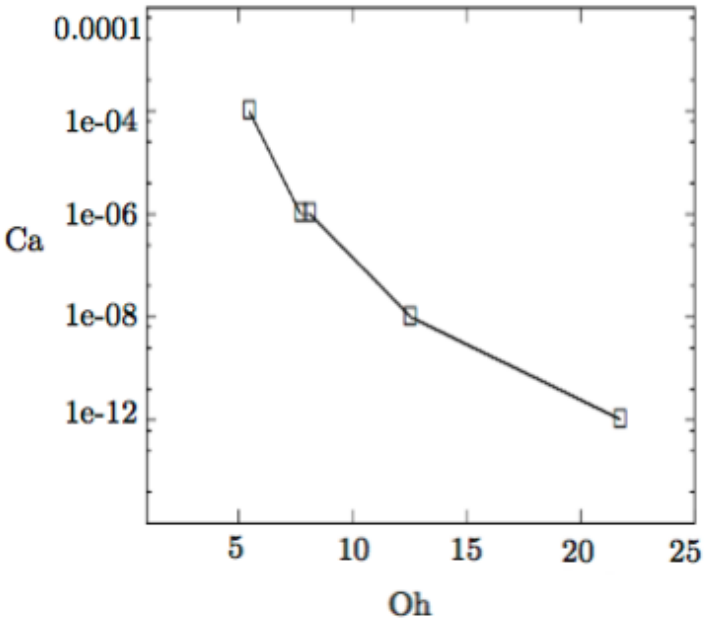

Fig. 3.13: Maximum spurious currents (Ca) as a function of Oh, for various σ.

3.3.4 Interface Reconstruction

There is a range of VOF sub methods for interface reconstruction as discussed before, such as the PLIC [69], SLIC [81] or ELVIRA [88] methods. In this work the interface reconstruction is based on the previous work by Scardovelli et al. [103]. Since in our CMLS method the LS is strictly linked to the area computation (Section 3.2), an accurate interface reconstruction method is needed. Here, the interface is reconstructed in a geometrical manner were the reconstructed points are chosen to yield a new interfacial plane, within each cut cell.

Interface reconstruction in such manner, requires both the forward and inverse problem. Here Δ is the cell side and is denoted by $c_1 = c_2 = c_3$ in x-, y- and z- directions, Fig. 3.14. Note, the working procedures will be presented only in two dimensional space and the equivalent three-dimensional expressions are just summarised.

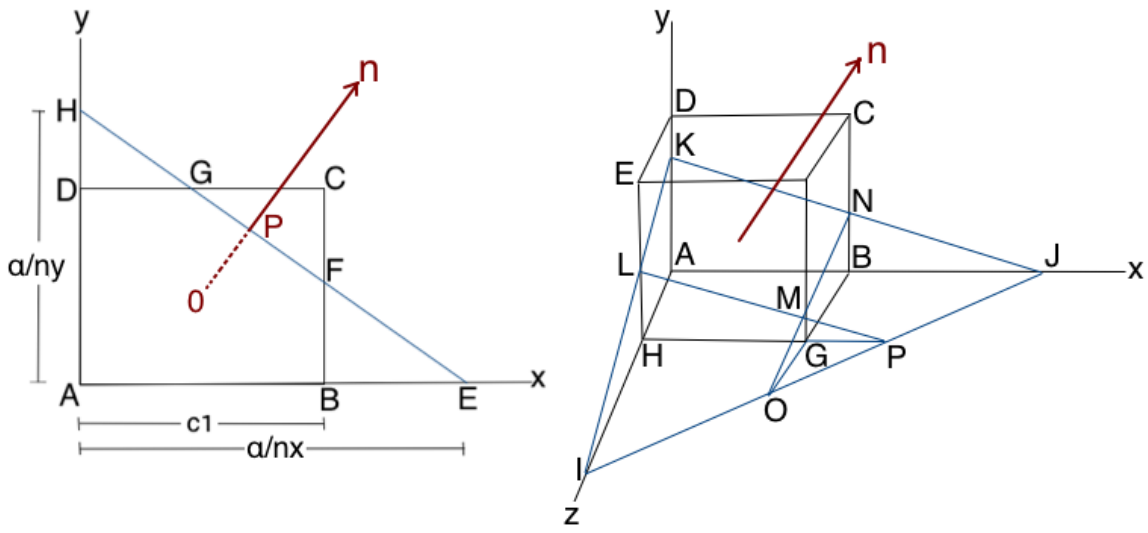

Fig. 3.14: Interface reconstruction in a computational cell demonstrating the cut area 2D (left) and cut volume 3D (right).

Primarily the forward problem is treated where one can consider a computational cell, Fig. 3.14. The cell can be divided into two parts by a linear interface, where each fluid area is found accordingly. To do so, one can define an explicit expression relating the cut cell area to a parameter, here its α, so that the linear interface (straight line) can be defined [24] as:

$$n_x x + n_y y = \alpha \tag{3.21}$$

with (n_x, n_y) being the unit normal vector and α denoting the minimum distance of the interface line to the origin. Since $\mathbf{n}$ is a unit normal then α is the distance. From Fig. 3.14, a square cell of sides $c_1 \times c_2$ in the (x, y) plane is cut by the straight line EH, with a normal vector $\mathbf{n}$.

Here, one needs to find the area below EH line that is included within the square cell, given by $ABFGD$ area. Assuming the normals n_x and n_y are positive, if one of the two vanishes then the area computation is straight forward. Note, the normals sign can be manipulated accordingly from basic coordinate transformation [24][103]. The linear interface denoted by EH cuts the (x,y) plane at $(\alpha/n_x, \alpha/n_y)$, respectively [24][103]. Thus, the desired area $A_{liq} = \phi\Delta x\Delta y$ to be computed, is the one enclosed in the $ABCD$ and under the EH line, which in two dimensional form reads:

$$\phi\Delta x\Delta y = \frac{\alpha^2}{2n_x n_y}\left[1 - H(\alpha - n_x c_1)\left(\frac{\alpha - n_x c_1}{\alpha}\right)^2 - H(\alpha - n_y c_2)\left(\frac{\alpha - n_y c_2}{\alpha}\right)^2\right] \quad (3.22)$$

Here, the AEH area is denoted by $\alpha^2/2n_x n_y$ and H is the common Heaviside step function, Eqn. (2.3). This method can be generalised in three dimensional space, Fig. 3.14, right, but it will not be further analysed.

To summarise, the normal $\mathbf{n}$ to the surface is similarly obtained as $n_x x + n_y y + n_z z = \alpha$ and the cut-volume, $\mathbf{V} = V_{liq}$, now reads:

$$\begin{aligned}\phi\Delta x\Delta y\Delta z = \tfrac{1}{6n_x n_y n_z}\Big[\alpha^3 - \textstyle\sum_{j=1}^{3} H(\alpha - n_j c_j)(\alpha - n_j c_j)^3 + \\ \textstyle\sum_{j=1}^{3} H(\alpha - \alpha_{max} + n_j c_j)(\alpha - \alpha_{max} + n_j c_j)^3\Big]\end{aligned} \quad (3.23)$$

where $\alpha_{max} = n_x c_1 + n_y c_2 + n_z c_3$.

Note Eqn. (3.23) is a continuous, one-to-one, monotonically increasing function, relating the volume contained within the $ABCDEFGH$ parallelepiped below the interfacial plane, with α, enabling full plane characterisation [24][103]. To validate the method, a liquid drop of various $R/\Delta = (4,\ 8,\ 16,\ 32,\ 64)$ was employed in a 2D fixed mesh of $[128 \times 128]$. Figures 3.15 and 3.16, show the errors for area (perimeter in two-dimensions) $\epsilon_A\%$ and mass $\epsilon_M\%$ with R/Δ.

Considering the area error with R/Δ, interesting behaviours are observed. In Fig. 3.15, for $R/\Delta = 16$ an 'off' point occurs in comparison with the remainder R/Δ values. Computing area values demands accurate approach of the interface location. Here, this 'off-point' could be possibly liable to the interface locating method for measuring area errors. In contrast, for the mass error, a converging behaviour is observed with R/Δ, Fig. 3.16.

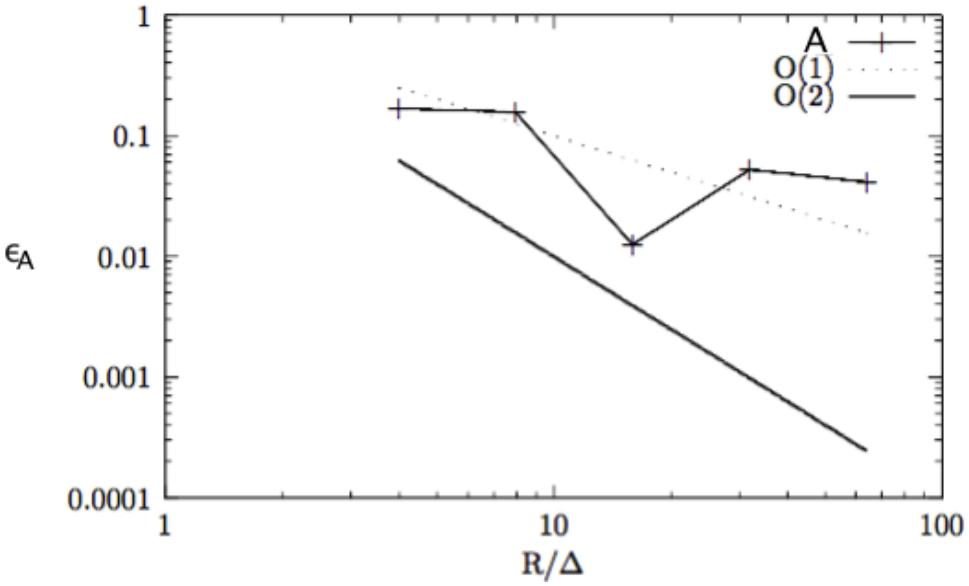

Fig. 3.15: Area (perimeter) error $\epsilon_A\%$ with R/Δ for a fixed liquid drop in a uniform mesh of 128^2 in 2D.

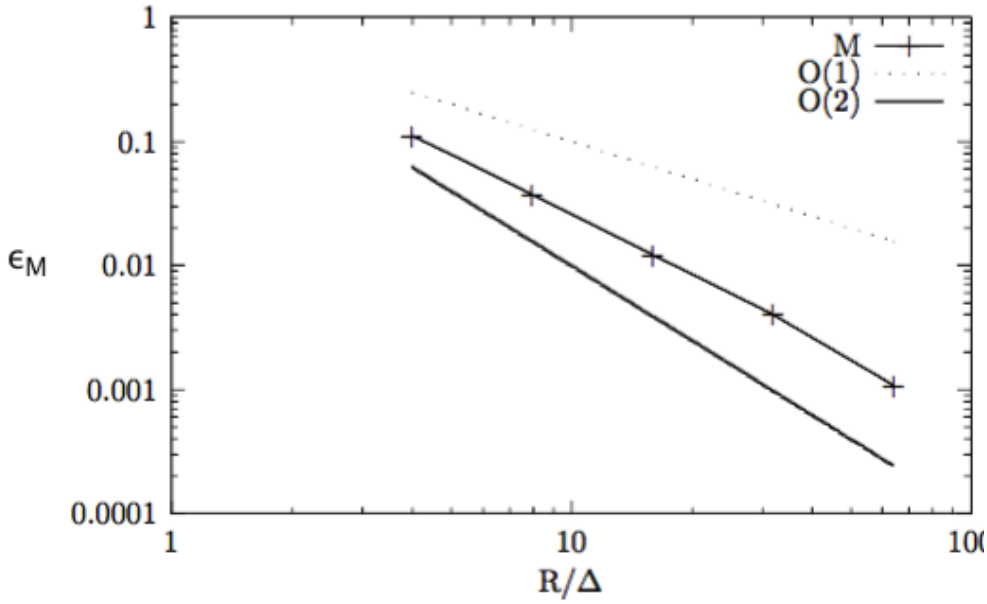

Fig. 3.16: Mass error $\epsilon_M\%$ with R/Δ for a fixed liquid drop in a uniform mesh of 128^2 in 2D.

As discussed, interface reconstruction in that manner requires both the 'forward' problem, $\phi = \phi(\alpha)$ and the 'inverse' problem, $\alpha = \alpha(\phi)$. Thus, one can obtain the correct value in terms of the cut area/volume and normal vector to the computational cell. The 'forward' problem is rather straightforward as presented above and $\vec{n}$ is explicit. Note, this ϕ is not a smooth function on the mesh size (unlike ϕ^S) and should be a second order approximation to the volume $\mathcal{O}(\Delta^2)$.

However, if one is solving for the 'inverse' problem, $\alpha = \alpha(\phi)$, here a specified volume fraction with a set normal is denoted by α. This is more complex due to the need of fast convergence and easy calculations of the function derivatives. The solution to the 'inverse' problem will only be presented briefly.

At first, one can obtain the two lines intersection between $\vec{n}$ and HE, Fig. 3.14. The Liquid/Gas interface is assumed to be a line within the cell and passing through HE, that reads as Eqn. (3.21) and can be rearranged to solve for y. Similarly, by basic geometry, the equation of a line given a parallel vector $\vec{n}$ and a point (x_o, y_o), which is the position of vector P, is taken as $(x, y) = (x_o, y_o) + (n_x, n_y)$. The latter is the parametric equation passing through P and can also be rearranged to solve for y. One can then solve for the intersection by equating the two. Next, the Level Set distance between (x_I, y_I) and (x_o, y_o) reads as:

$$(y_I - y_o)^2 + (x_I - x_o)^2 = \psi^2 \tag{3.24}$$

Which here, one solution of α is liquid and the other is gas. After some relative manipulations we obtain an expression for $\alpha = f^{-1}(\psi)$. Since level set (ψ) by definition is the distance from the cell centre towards the interface, by computing this distance the constant α can be determined. The solutions of α will correspond to a cell filed with liquid or gas.

3.3.5 Validation

As in pure LS, the CMLS method developed here, employs 5^{th} WENO and RG methods for the LS evolution. Recalling the classic shear vortex, the CMLS solution is presented in Fig. 3.17. The solution appears smooth with good capturing of the interface. The lack of numerical blobs at the liquid tail, demonstrates good mass conservation properties. Note, the method of the LS normal calculations, can significantly affect the numerical break-up zone and thus the solution.

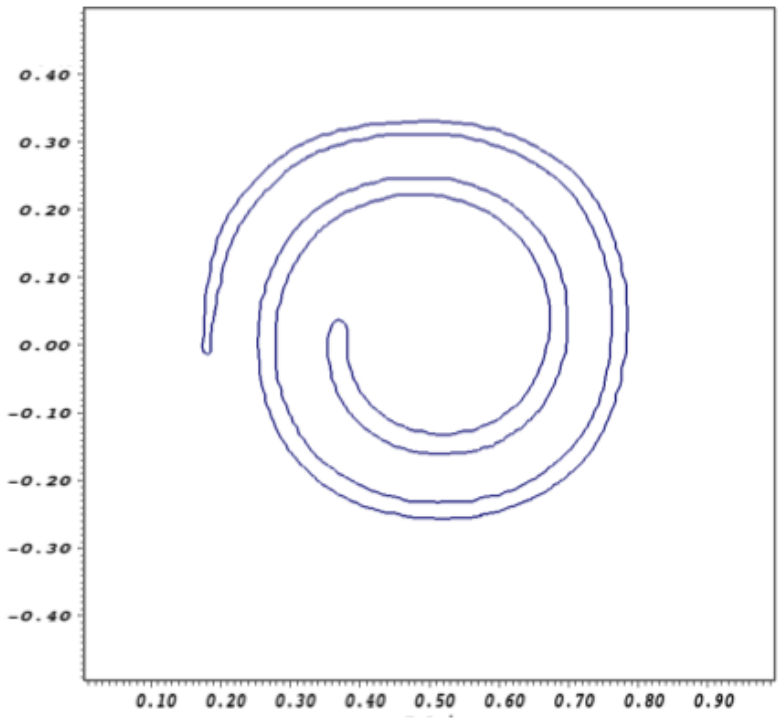

Fig. 3.17: Plot of the shear vortex of a liquid drop at t=T in a 128^2 mesh with CMLS.

3.3.6 CPU run time as a function of Mesh Size

In the context of multiphase fluid flows, CPU run times are highly important, by defining the computational cost. High order of CPU hours is required for even a few seconds of flow computations. Adding on that, the choice of explicitly or implicitly solving the NS equations also affects the CPU run times. Here, the NS equations are explicitly solved. In the literature [20][128], it was noted that implicit solutions provide smaller CPU run times, apart from increasing processor numbers. Thus, CPU run times are mainly affected by the NS solution choice, the number of processors and Δx choice, which in turn is a function of Δt, whilst higher meshes denote higher CPU run times. Note, if the mesh size is increased the time step should be decreased, to preserve the CFL criteria and thus system stability.

Figure 3.18 shows the CPU run time as a function of number of cells (N), for two- and three- dimensional cases, using 16 processors. Here, the CPU times increase with the mesh size.

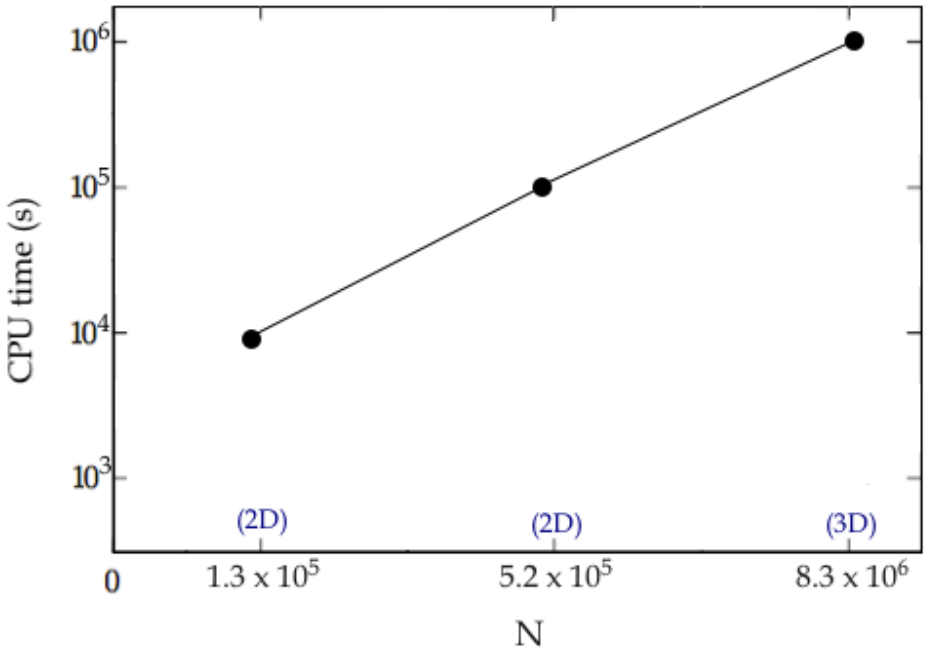

Fig. 3.18: CPU run time at each mesh size with 16 processors.

The previous work by Reynolds et al. [33], presented the effects on the CPU times, by implicitly and explicitly solving the NS equations. It was shown, that implicit methods do in fact decrease CPU run time by almost one oder, whilst for the explicit cases, CPU results were similar to the ones presented here. Meanwhile, in Zaleski et al. [132] spray formation studies, a range of Δx was employed with a minimum of 32 processors. Their computer set up and processor type were very different than the ones employed in this work. However, the present CPU run times are comparable to the ones in Zaleski et al. [132], that could potentially reflect on the interface modelling method capabilities, (i.e. CMLS).

3.4 Comparison of VOF, LS and CMLS in 2D

3.4.1 Liquid Disc in a Single Shear Vortex

After exploring the VOF, LS and CMLS methods individually, the three are compared based on the same liquid disc deformation case. The methods were tested in three mesh sizes of [64 × 64], [128 × 128] and [256 × 256]. For a more quantitive analysis, the mass error of each method has been computed and summarised in Table 3.2, at $t = T$. Looking at Table 3.2 and Fig. 3.19, the mass error difference between VOF and CMLS in comparison with LS is significant. Both VOF and CMLS methods are considerably more mass conservative from LS. With mesh refinement, mass conservation properties improve, even in the case of LS. The CMLS method, in all mesh sizes appears to conserve mass well and maintains errors in the order of $\sim 10^{-2}$.

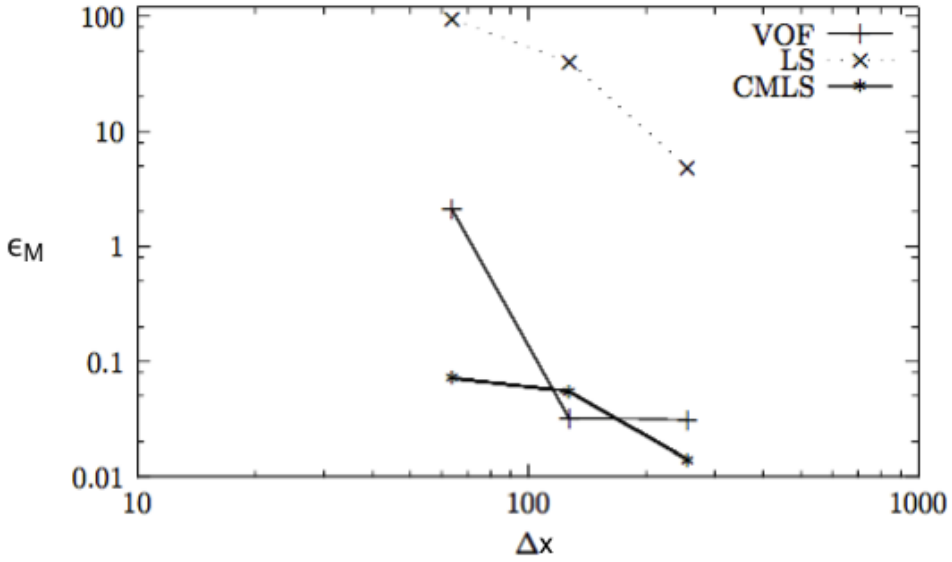

Fig. 3.19: Mass error $\epsilon_M\%$ with Δ for VOF, LS and CMLS.

	Method $\epsilon_M\%$		
Mesh	**VOF**	**LS**	**CMLS**
$\mathbf{64^2}$	2.1	94.1	7.1×10^{-2}
$\mathbf{128^2}$	3.2×10^{-2}	39.5	5.4×10^{-2}
$\mathbf{256^2}$	3.1×10^{-2}	4.8	1.4×10^{-2}

Table 3.2: Mass error $\epsilon_M(\%)$ for a single liquid vortex at $t = T$ for different mesh size.

Additionally, a relative qualitative analysis is presented in Fig. 3.20 of the same liquid disc deformation test case. Comparing the three methods, the CMLS is the most accurate in capturing the interface, however in the refined mesh cases all three methods present good results, Fig. 3.20. In the VOF case the tail of the vortex is captured more accurately, in comparison with LS and CMLS. Note, in the VOF [128×128] solution, Fig. 3.20, numerical blobs are observed at the liquid mass tail. This can be denoted to the inaccuracy of the CDS approximation for the normals. In the CMLS case, although some mass is lost in the tail, the mass is till conserved and redistributed everywhere else.

To further validate the performance of this novel CMLS method, we compare our results with the works by Desjardins et al.[84], Herrmann et al. [54], Xiao et al. [130] and Sabelnikov et al. [122], both qualitative and quantitative. A relative table summarising the mass error $\epsilon_M(\%)$ of each work, for [128×128] is demonstrated in Tab. 3.3. The mass errors presented here are based on the mass loss computed for a full run at $t = T$.

In comparison with Desjardins et al.[84], the present study demonstrates better interface topology and good mass conservation properties. In Herrmann et al. [54], a high resolution equidistant Cartesian grid was employed and a refined LS method was developed. They demonstrated good mass conservation properties in more refined meshes. However, considering the results for [128×128] and [256×256], the present work demonstrates better mass conservation and interface topology properties, in both pure LS and particularly with the CMLS method.

In Xiao et al. [130] work, similar test cases were employed with VOF, LS and their CLSVOF version, for [128×128] mesh size. In the case of VOF and LS, Xiao's result are highly more mass conservative, however the actual capturing of the interface in this work is more accurate in the VOF case, but not in the LS. In the case of CMLS, the mass conservation is similar to the CLSVOF work in Xiao [130], with the latter one being in the order of 10^{-4}.

However, the CMLS interface topology results are better, in comparison with Xiao [130], where their shear vortex tail demonstrates some break-up at $t = T$. Finally, Sabelnikov et al. [122] presented good mass conservation properties in the order of 10^{-3}, thus slightly more conservative than the CMLS method. However, the interface topology properties were not as accurate as the present CMLS.

$\mathbf{128^2}$	**Xiao**[130]	**Desjardin**[84]	**Herrmann**[54]	**Sabelnikov**[122]	**CMLS**
$\epsilon_{\mathbf{M}}\%$	5×10^{-4}	< 4	< 30.86	5.7×10^{-3}	1.4×10^{-2}

Table 3.3: Comparison of liquid disc shear vortex mass error $\epsilon_M(\%)$ with other studies, for [128×128].

To summarise, the in-house CMLS developed here, overall denotes very good interface topology properties, with quite accurate interface capturing and curvature computations, whilst maintaining good mass conservation properties even in very coarse meshes.

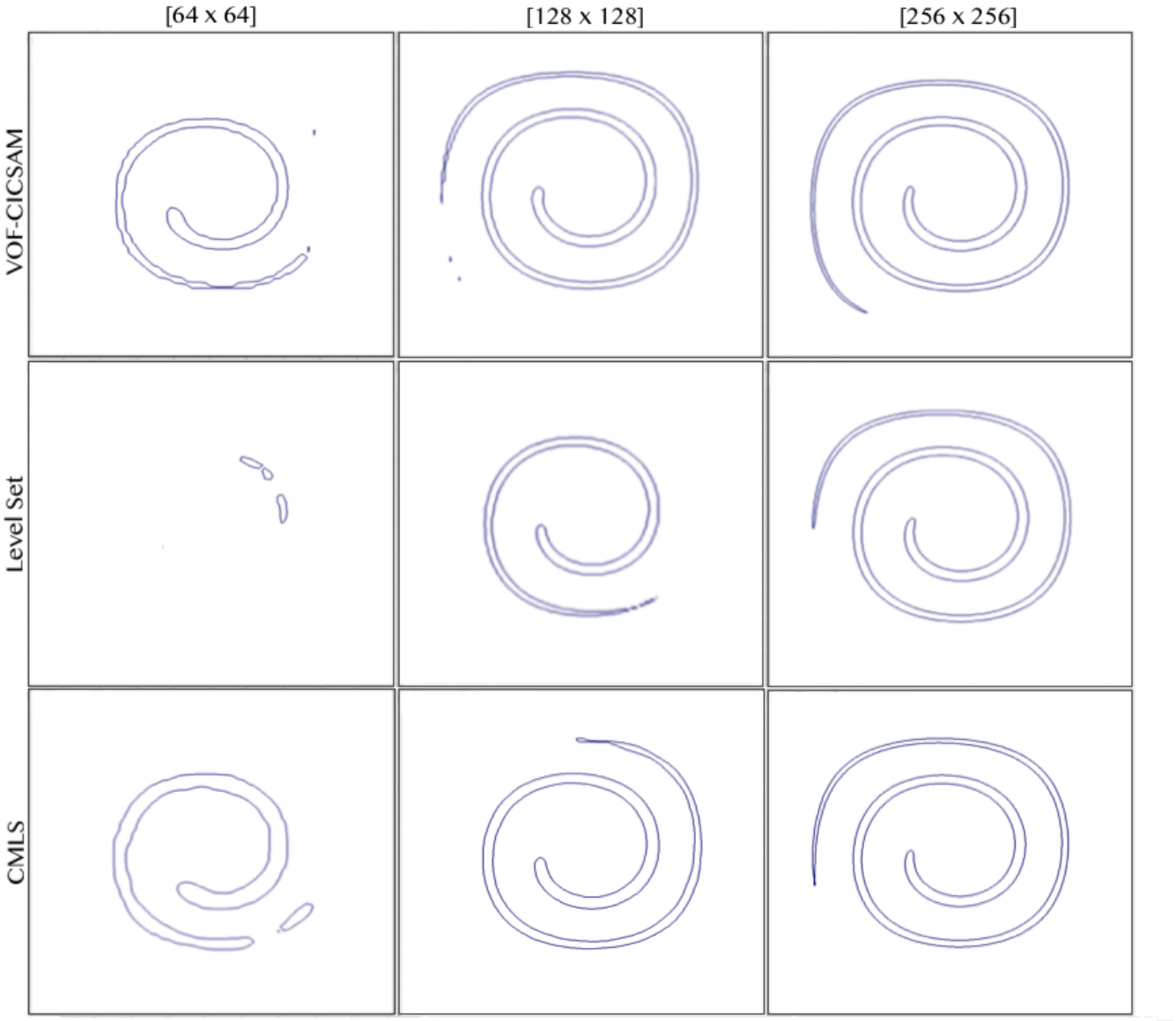

Fig. 3.20: Liquid drop in a shear vortex in a 128^2 (left) and 256^2 (right) meshes, with VOF, LS and CMLS at $t = T$.

3.4.2 Sloshing Test

The sloshing of a liquid wave, of low amplitude under gravity effects is typically employed to evaluate the interface capturing properties of interface modelling methods [47]. Here, a typical sloshing case is tested in a two-dimensional tank. Gravity was applied on the liquid wave and the surface was assigned to one halved cosine wave of amplitude 0.005, described by:

$$y = 0.017 + 0.005 \cos\left(\frac{\pi x}{L}\right) \tag{3.25}$$

The initial set up configuration is demonstrated in Fig. 3.21. The top of the tank is treated with zero gradient pressure and the remaining borders with wall conditions. The mesh size follows [160 × 104] with time step $\Delta t = 2 \times 10^{-4}$ and $c = 0.2$. Note, the liquids are inviscid ($\mu_{L,G} = 0$), whilst the densities were chosen at $\rho_L = 100 kg/m^3$ and $\rho_G = 1 kg/m^3$. The interface position was recorded for six periods of oscillation. In Fig. 3.21, the computational interface position is demonstrated with respect to the theoretical one, for VOF, LS and CMLS.

In all cases, the interface position is located quite well to match the theoretical one, for all periods of oscillation. Observing Fig. 3.21, it is notable, that for every second oscillation period, the computed interface position is slightly off, in comparison with the theoretical one. In the case of VOF, this is expected due to method limitations of accurately capturing the interface. Meanwhile, for LS and CMLS this can be liable to the lack of viscosity, creating some 'wiggling' when interface is present, that can not be avoided.

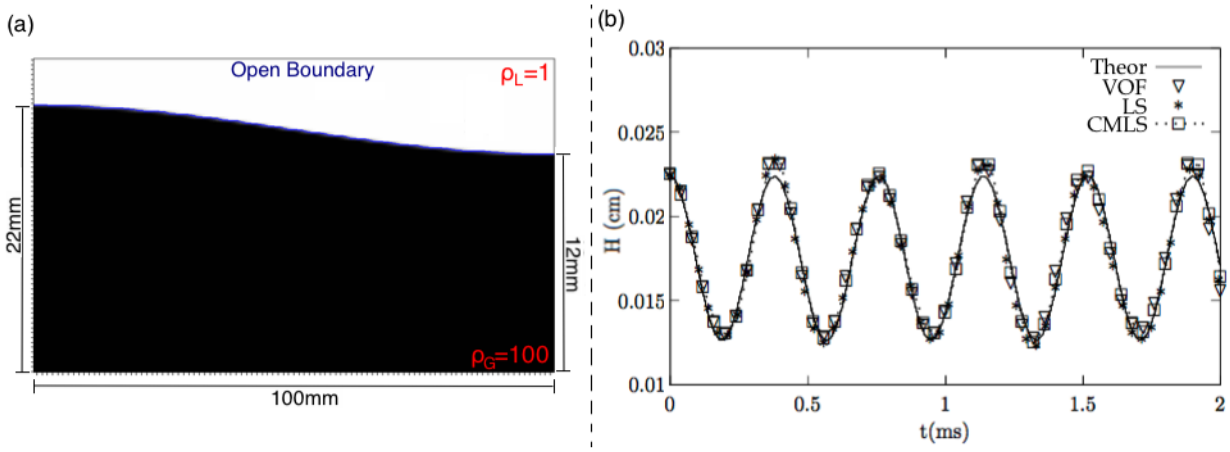

Fig. 3.21: Sloshing case of (a) initial set up arrangement and (b) computational and theoretical interface position as a function of time for six periods of oscillation with VOF, LS and CMLS.

3.4.3 Rayleigh-Taylor Instability

A common test case for both method validation purposes and 'smaller' jet-integrated phenomena, is the Rayleigh-Taylor instability, first presented in Rudman et al. [97]. Here, a high density liquid is placed at the top half of the domain and is deposited over a low density liquid. The domain is a rectangular shape of $1m \times 4m$ and mesh size 64×256. The set up parameters are employed from Gopala et al. [47]. The viscosity for both fluids is $\mu = 3.13 \times 10^3 kg/m/s$ and the densities of liquid and gas are $\rho_L = 1.225 kg/m^3$ and $\rho_G = 0.169 kg/m^3$, respectively. A constant time step $\Delta t = 2 \times 10^{-4}$ was chosen denoting $c = 0.06$. A perturbation is applied at the interface given by $y = 0.05 cos(2\pi x)$.

For the boundary conditions at the domain wall, no-slip boundary conditions where applied. The simulations for all three methods are presented in Figures 3.22 - 3.24. With respect to all three methods, good mass conservations properties are observed with the RT tip captured sufficiently in all. The CMLS method does show better accuracy properties from all three, however some asymmetry is noted, possibly liable to to the level set normals.

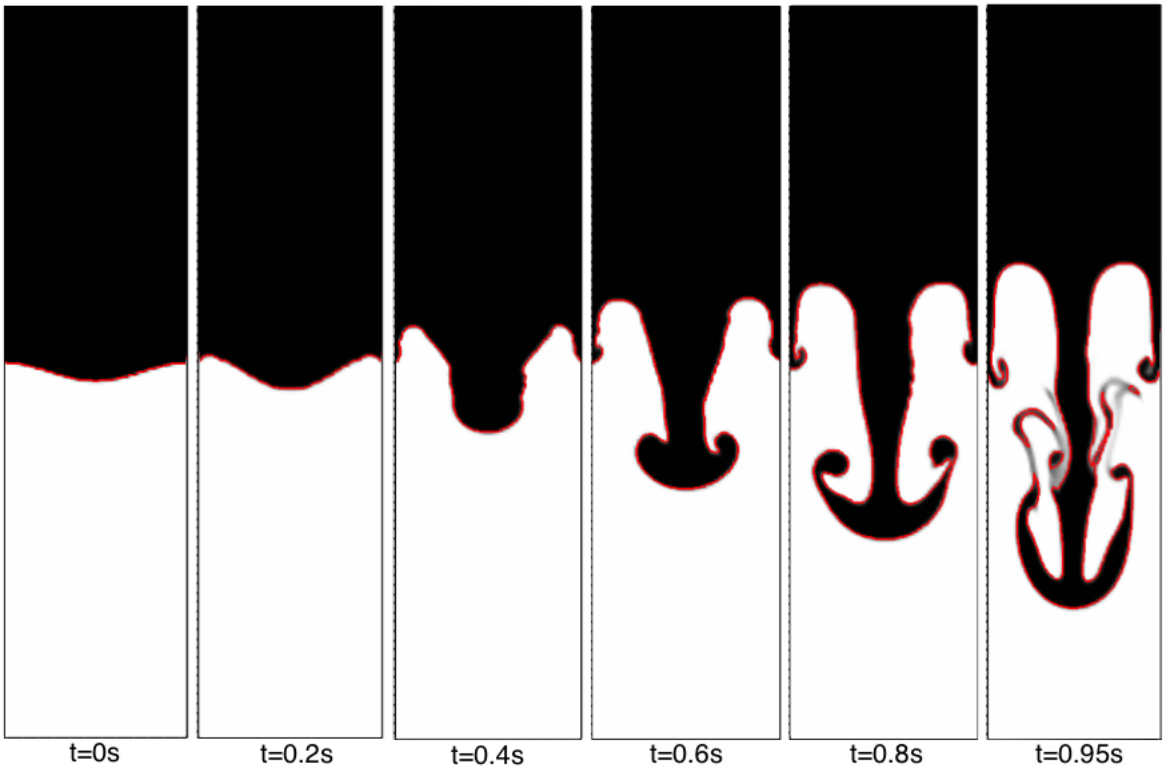

Fig. 3.22: Rayleigh-Taylor Instability with VOF-CICSAM at $t = [0, T]$, with red denoting the $\phi = 0.5$ -contour.

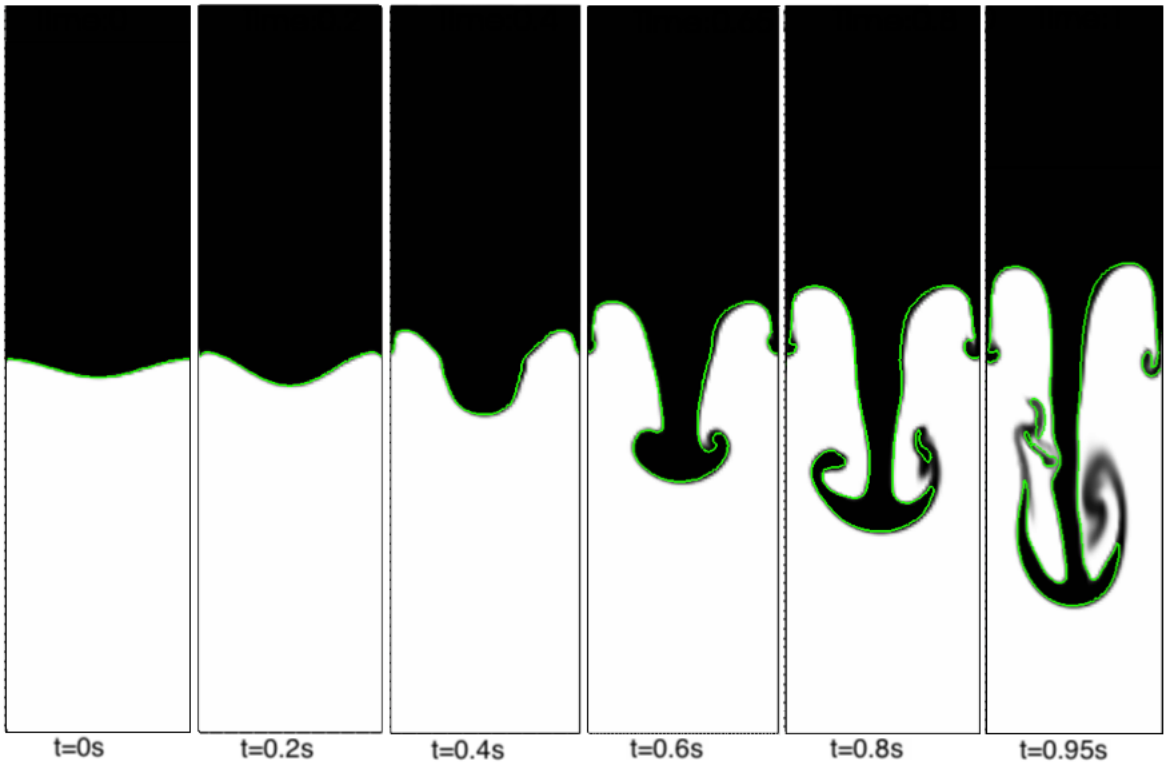

Fig. 3.23: Rayleigh-Taylor Instability with LS at $t = [0, T]$, with green denoting the $\psi = 0$ -contour.

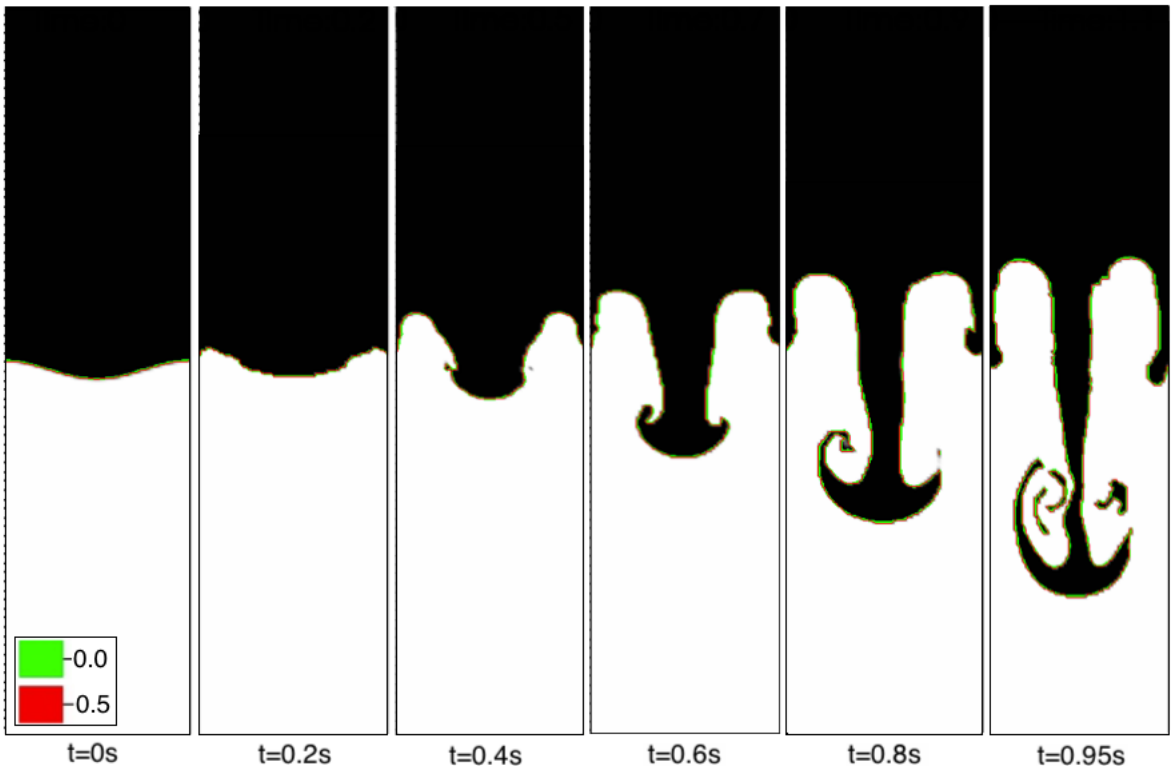

Fig. 3.24: Rayleigh-Taylor Instability with CMLS, with green and red contours denoting the ψ^{n+1} and ϕ^{n+1} at $t = [0, T]$.

3.5 Evaluation of CMLS in 3D

In the previous sections, the 2D CMLS presented the optimum results in comparison with VOF-CICSAM and pure LS methods. To further investigate the capabilities of this in-house CMLS, the latter was extended in 3D, using the numerical methods described earlier. To validate the 3D CMLS performance two test cases were employed; (i) a liquid sphere diagonal translation in a uniform gas flow and (ii) the liquid disc in a single shear vortex.

3.5.1 Liquid Sphere Diagonal Translation in Uniform Gas Flow

A liquid sphere moving in the diagonal direction of a uniform gas flow, is placed in a $[128 \times 128 \times 128]$ for $R/\Delta = 8,\ 16,\ 24$. The 3D velocity field is uniform with $[u = v = w = 10]$. The liquid sphere presented here, crosses the boundaries ten times and returns to its original position.

Figure 3.25, shows the initial and final positions of the liquid sphere, for all R/Δ. At $R/\Delta = 8,\ 16$ the sphere is slightly distorted whereas for $R/\Delta = 24$ the sphere preserves its shape. Note, the normal computation during the diagonal translation of the sphere is more complex, possibly leading to this distortion present. Increasing R in a fixed domain, means the cell number across the sphere diameter is increased, thus spherical shape is retained.

Table 3.4 shows the area and volume errors $\epsilon(\%)$ for the two R/Δ. The 3D CMLS captures the interface quite accurately as it crosses the BC over and over in time, despite the small distortion in $R\Delta = 8,\ 16$. To compliment the discussion, all errors for A, M and κ were plotted with time $t*$, Figures 3.26 - 3.28. In all cases, the results are satisfactory and all properties of the sphere are well preserved, with $R/\Delta = 8$ demonstrating the least mass conservation. However, the results are still satisfactory considering the coarse properties for this specific point. In the area and curvature computations, all cases present similar results. Meanwhile, regarding the volume behaviour, as we increase the grid points in the radius diameter, the mass is better conserved.

$\mathbf{R/\Delta}$	$\epsilon_{\mathbf{A}}\%$	$\epsilon_{\mathbf{M}}\%$
8	6.43	0.16
16	5.02	4.49×10^{-2}
24	4.21	3.27×10^{-2}

Table 3.4: Area and Volume errors for a liquid sphere in a diagonal translation with 3D CMLS for $[128 \times 128 \times 128]$ mesh size at $t = 0$ (left) and $t = 10T$ (right).

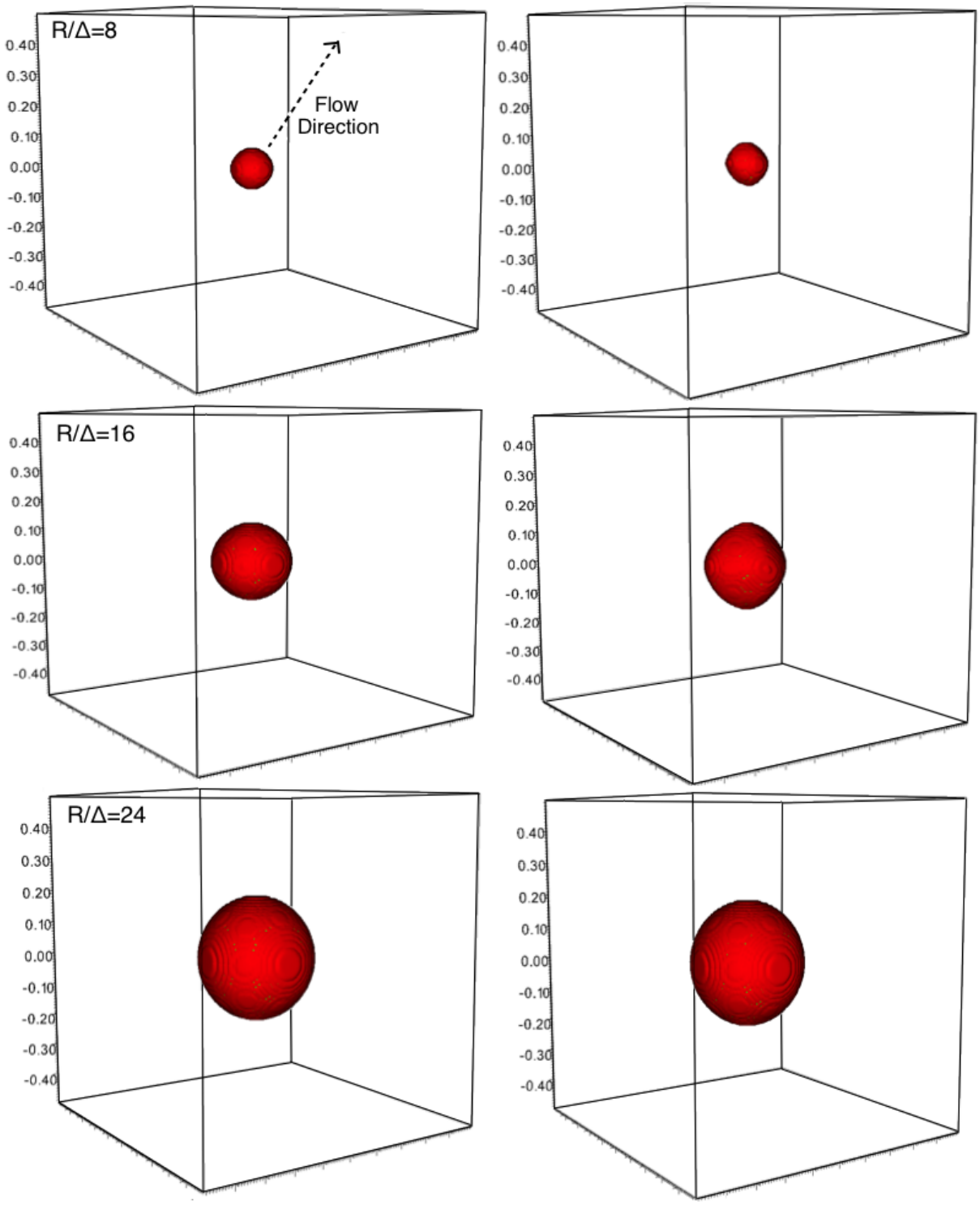

Fig. 3.25: Liquid sphere in the diagonal direction for $R/\Delta = 8,\ 16,\ 24$ in a 128^3 mesh, at $t = [0, 10T]$.

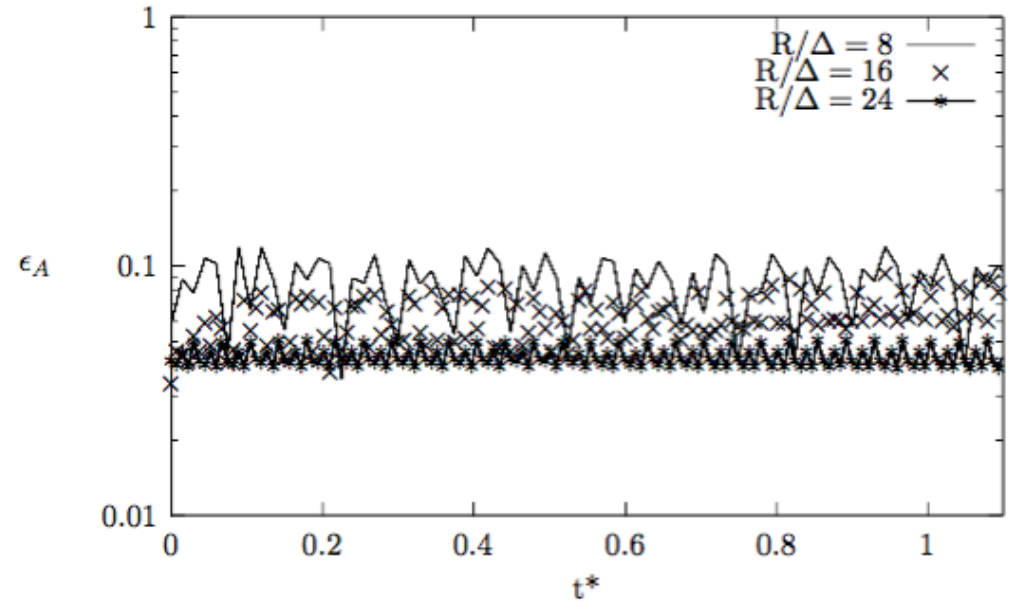

Fig. 3.26: Area error $\epsilon_A\%$ with t^* for $R/\Delta = 8,\ 16,\ 24$.

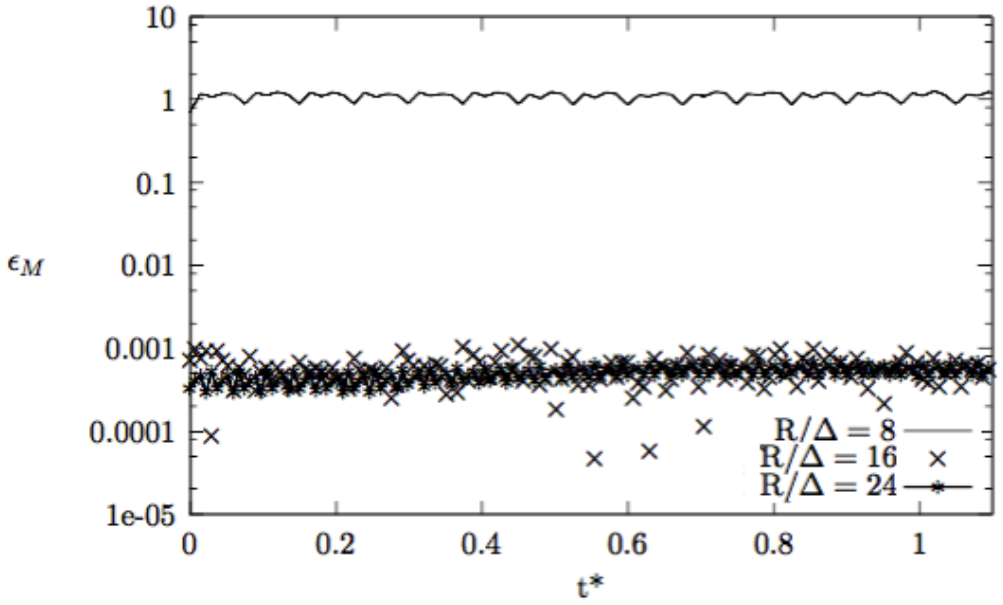

Fig. 3.27: Mass error $\epsilon_M\%$ with t^* for $R/\Delta = 8,\ 16,\ 24$.

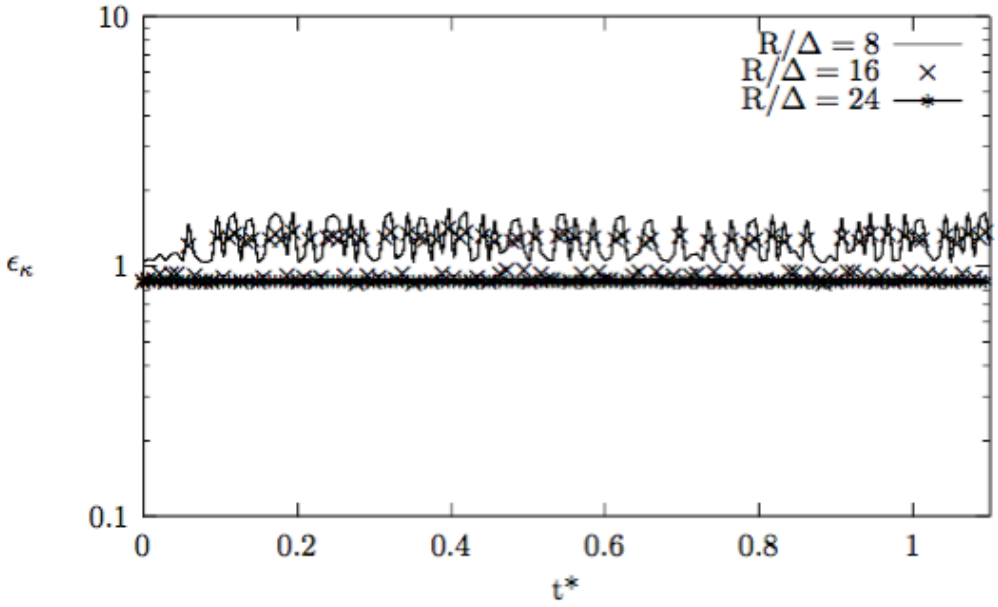

Fig. 3.28: Curvature error $\epsilon_\kappa\%$ with t^* for $R/\Delta = 8,\ 16,\ 24$.

3.5.2 Liquid Sphere in a Single Shear Vortex

To further validate the CMLS performance in 3D, we employ the shear vortex case. Here, the liquid sphere stretches within a single vortex velocity field, into a thin film. The stretched sphere reaches maximum deformation by $t = T/2$ before it reverts to the original sphere shape. The sphere radius is $R = 0.15$, placed in a uniform sized domain with initial position at $(0.35, 0.35, 0.35)$. The sphere is tested in two meshes of $[80 \times 80 \times 80]$ and $[164 \times 164 \times 164]$, with a velocity field of:

$$
\begin{aligned}
u(x,y,z,t) &= 2sin^2(\pi x)sin(2\pi y)sin(2\pi z)cos(\pi t/T) \\
v(x,y,z,t) &= -sin(\pi x)sin^2(\pi y)sin(2\pi z)cos(\pi t/T) \\
w(x,y,z,t) &= -sin(\pi x)sin(2\pi y)sin^2(\pi z)cos(\pi t/T)
\end{aligned}
\tag{3.26}
$$

where the period is taken as $T = 3s$.

Relative snapshots at different times are presented in Fig 3.29. The CMLS method captures the deformation process well, with some distortion present at $t = T$, when the sphere has reverted back to its original position. Conclusively, the CMLS method demonstrates good properties, suggesting its implementation in the sections to follow.

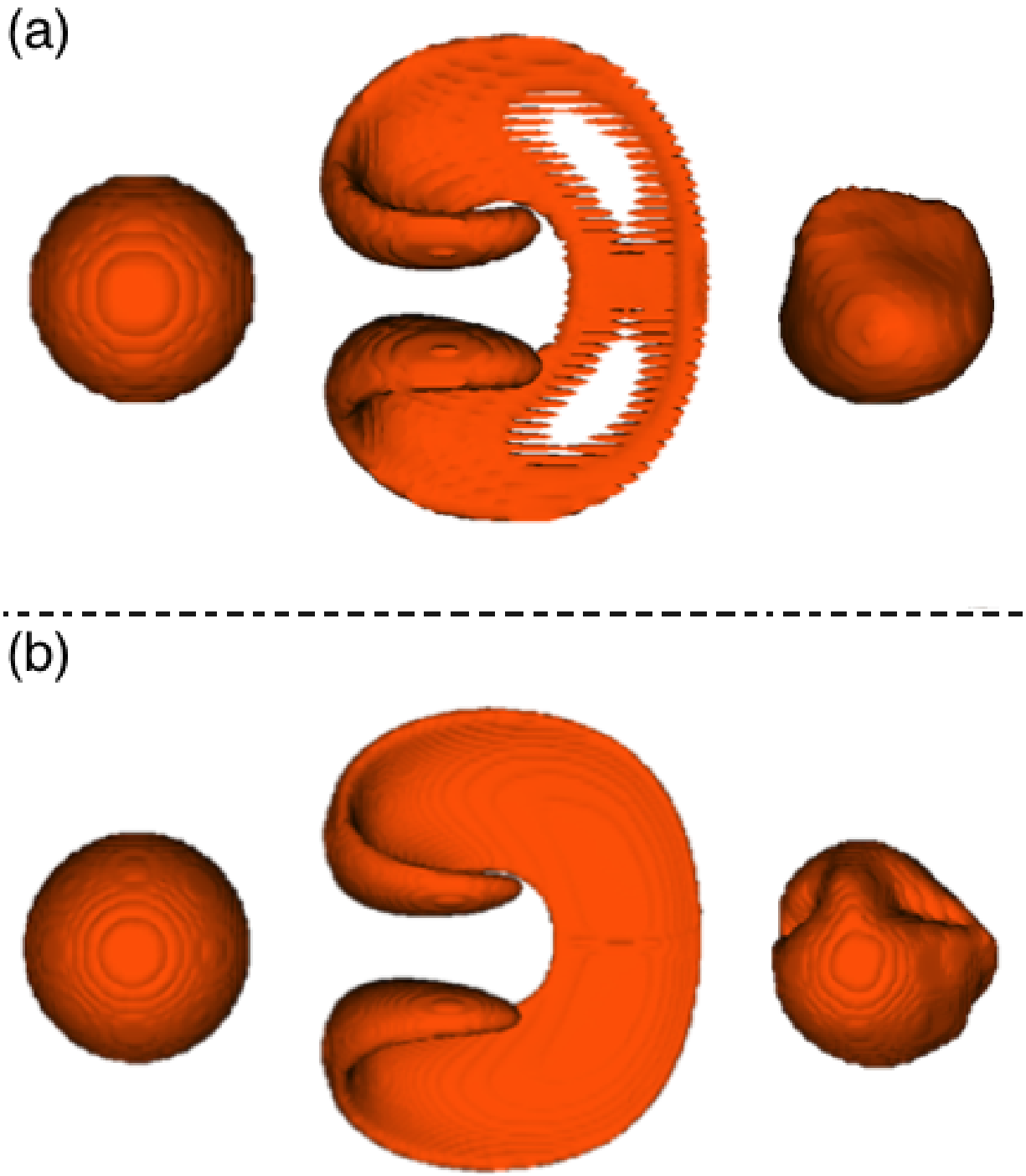

Fig. 3.29: Snapshots of the liquid sphere in a single shear vortex with CMLS, at initial position $t = 0$ (left), at maximum deformation $t = T/2$ (middle) and reversed back position $t = T$ (right), in (a) $[80 \times 80 \times 80]$ and (b) $[164 \times 164 \times 164]$ mesh sizes.

3.6 Summary

This section has investigated the interface capturing capabilities of VOF-CICSAM, LS and our novel CMLS, where all three were validated and compared. The VOF-CICSAM method presented good mass conservation properties, which is in agreement with the literature. However, interface information extraction, such as normals, interface location and curvature computations are lacking due to the VOF function discontinuity, particularly in the three-dimensional space. The LS method, provides better interface topology but mass loss is a major drawback during interface evolution.

The novel CMLS method, appears to be superior to both VOF and LS methods, with the lower mass loss and good interface topology properties. Even in coarse meshes of $R/\Delta \leq 8$, the relative mass errors were limited to 0.1%, whilst with mesh refinement the error dropped below 10^{-2} consistently, regardless of the test case. The CMLS indicated comparable properties to previous studies successfully, whilst in some cases showed better accuracy from other VOF-LS coupling methods.

Employing 5^{th} WENO for the LS advection/reinitialisation in the CMLS numerics, enabled a high order accuracy whilst any oscillatory transitions of discontinuous solutions were limited. Consequently, some of the mass loss present was also reduced. The use of GFM method provided sharp treatment of the interface along with robust expression of the surface tension forces. The curvature computations demonstrated acceptable convergence, with some limitations from the 5^{th} WENO, as a function of the stencil points. Moreover, as the CMLS equations are solved explicitly, some limitations for the time step Δt choice, still remain, with CPU run times increasing, that could be reduced by solving the NS equations implicitly.

Finally, the CMLS method extended in the three-dimensional space, similarly exhibited good results. Conclusively, this novel CMLS was chosen as the optimum method for more complex two-phase fluid flow cases, such as droplet break-up and liquid-gas jet break-up modelling, presented in next chapters.

Chapter 4

Liquid Drop Break-Up

4.1 Introduction

In the previous chapter, the most common interface capturing methods for multiphase fluid flow simulations were presented. An optimum choice was the in-house novel CMLS, which is employed for the remainder of this thesis. Single drop break-up processes provide a good foundation for liquid spray atomisation studies.

Faeth et al. [38] showed that the dense spray mixing rates can be partially controlled by secondary break-up, similar to drop vaporisation processes controlling the dilute spray mixing rates. Wu et al. [89], determined that drops formed in the primary break-up, are unstable near the secondary break-up regions. With their work as motivation, here the break-up process of a single liquid drop in a uniform gas flow is investigated.

Such phenomena are in terms of the dimensionless Weber and Reynolds numbers. Both Re and We numbers are expressed as a function of the Ohnesorge number, $Re = \sqrt{We}/Oh$. Doing so, the magnitudes of inertia, viscous and capillary effects are obtained conveniently, as Oh is independent of the external dynamic forces acting on a drop [53][76]. Employing these parameters, one can obtain a better understanding of the dynamics controlling the break-up processes and the formed droplet shape and size [49]. Here, the effective Weber parameter is in terms of the gas velocity whereas in liquid jet break-up is a function of air.

This section, studies the single drop break-up process under a range of We for a fixed Oh. Provided fixed fluid properties, Oh changes with the drop diameter. This approach enables simulations primarily driven by the increasing velocity flow [49], denoting the shape of the steady drop, the inner/outer flow field and the necessary body forces.

4.2 Break-up modes with various Weber number

Faeth et al. [57] developed a break-up mode map of drop deformation for $We - Oh$, Fig. 4.1. As the Weber number increases, five different modes are denoted, bag break-up, bag-stamen break-up, *multimode* break-up, sheet or shear thinning break-up and catastrophic break-up. Liquid jet break-up is mostly governed by various size droplets that undergo break-up and deformation.

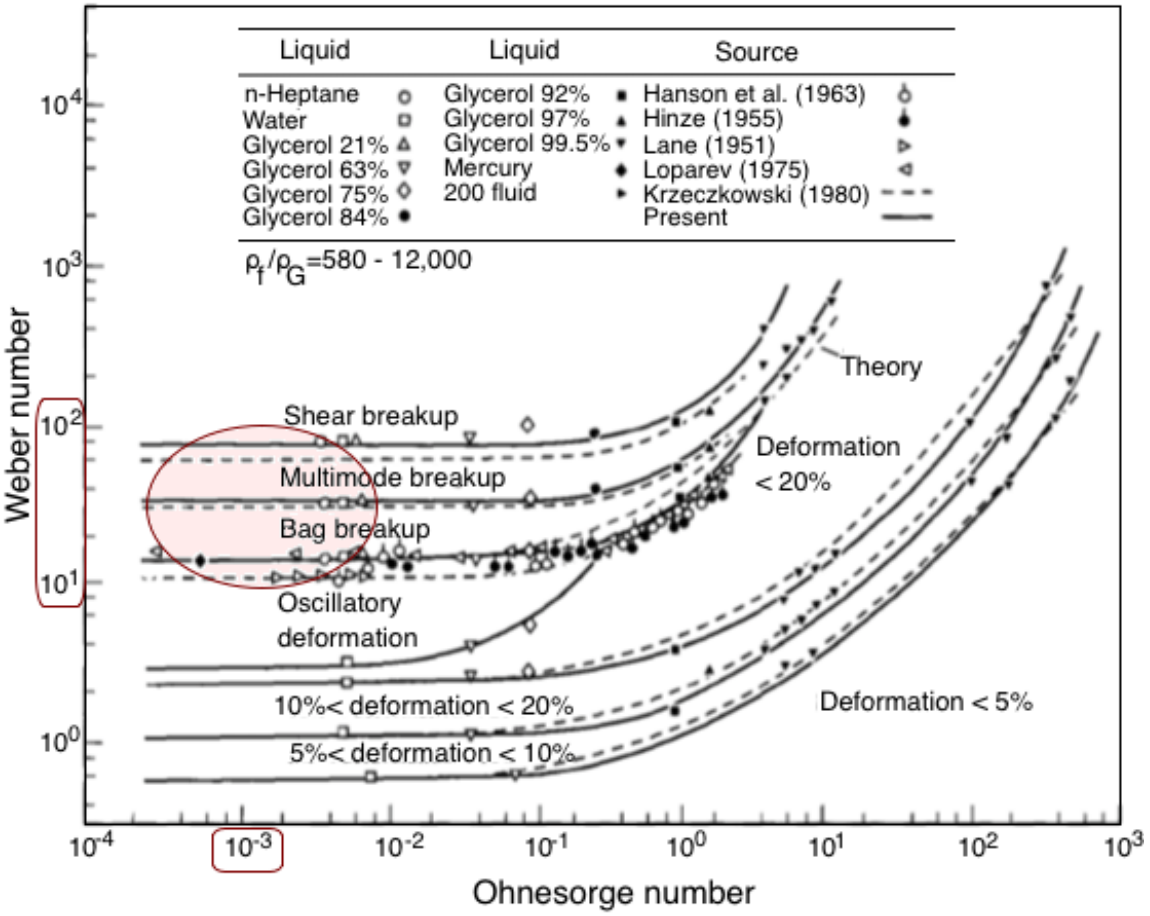

Fig. 4.1: Map denoting the break-up modes with drop deformation by Faeth et al. [57]. The red-marked areas denote the regions in present work.

Considering the red-marked areas in Fig. 4.1, our work develops at approximately $Oh \approx 10^{-3}$ with We ranging between $10^1 - 10^2$. Note, these values are linked to the computer power available for this work, whilst due to the viscosity presence extra limitations were imposed, (see Section 2.4.2.3). Consequently, the current results should present modes such as oscillatory deformation, bag/bag-stamen, multimode and shear break-up. Here, it should be noted that according to the break-up mode map, at low Oh values, (i.e. $Oh < 10^{-1}$), an 'independent' relationship exists between the break-up mode and the Ohnesorge number, denoting We as the major effective parameter.

In a single liquid drop break-up, the interface topology is less complex, whilst instability mechanisms typically integrated in liquid jet break-up, can also be found. Increasing We denotes a decrease in the stabilising surface tension forces, resulting to drops being more prone to break-up. In Theofanous et al. [118], a focused study on single liquid drop break-up and deformation was developed under the effects of different We numbers. In their experimental set up, the liquid drop breaks/deforms due to gas entering from the right inlet. Snapshots of each mode recorded are summarised in Fig. 4.2. A similar figure of various break-up modes was denoted in Pilch et al. [87], Fig. 4.3.

Both studies [87][118] discussed below were based on experimental data. However, in cases, the modes observed for specific We ranges, are not in full agreement with each other. In Theofanous et al. [118], the flow field was generated in a pulsed supersonic wind tunnel, consisting of a converging-diverging nozzle, for the flow channel connecting two tanks. In Pilch et al. [87], the experiments took place in a liquid-metal cooled fast breeder reactor and the break-up process was based on liquid drops being exposed to high-velocity flow of less density that the drops.

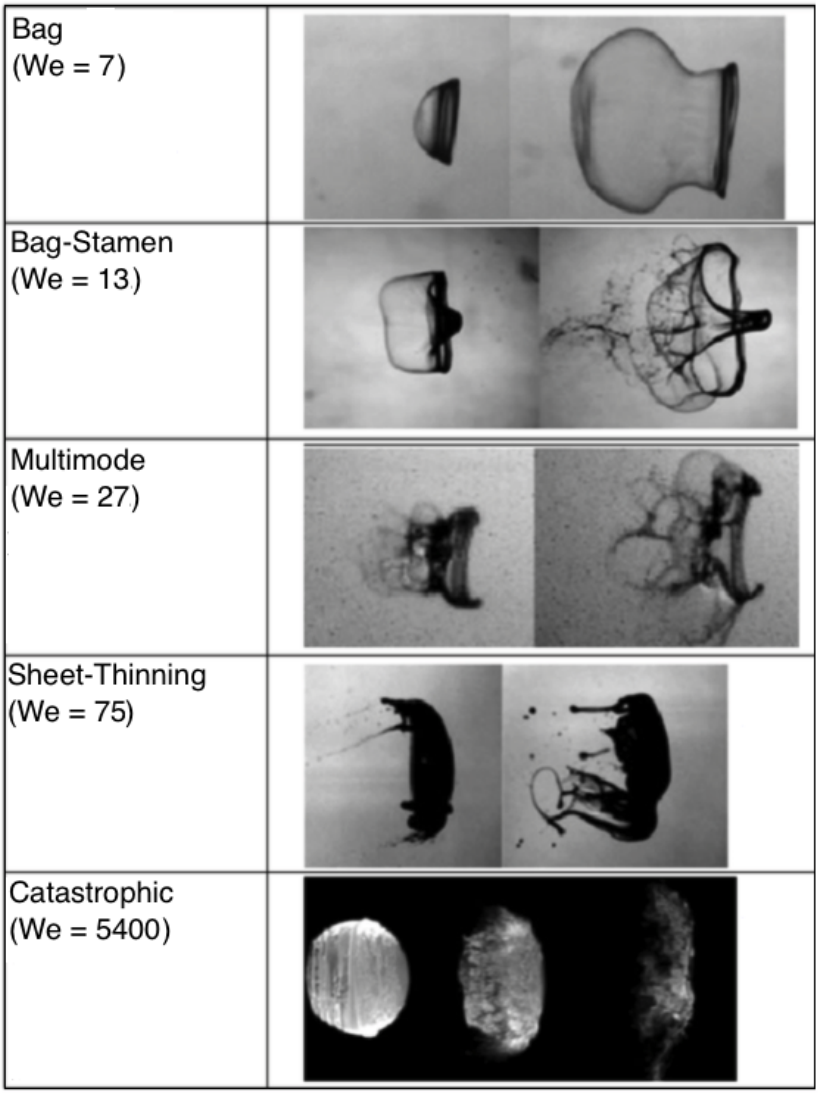

Fig. 4.2: Figure from Theofanous [118] illustrating various single drop break-up modes as a function of We for $Oh < 0.1$.

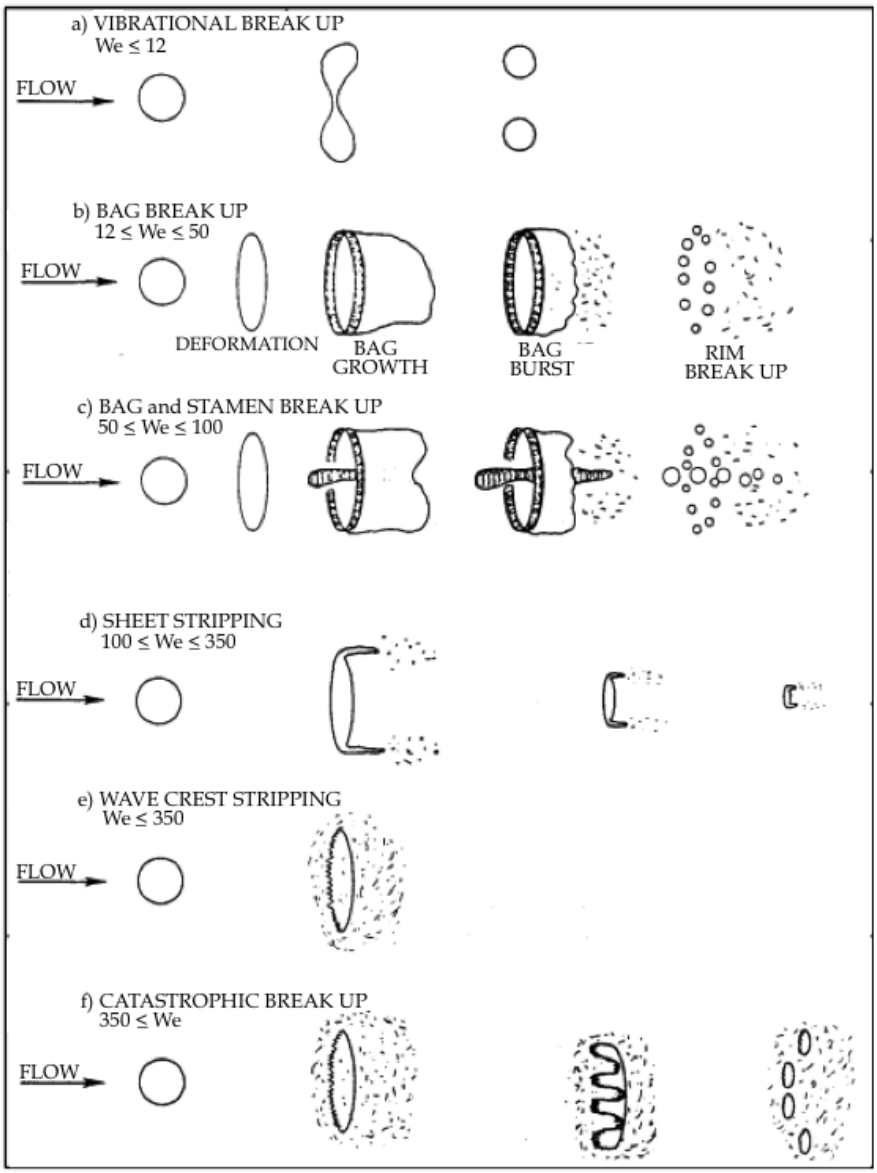

Fig. 4.3: Figure from Pilch et al. [87] illustrating various single drop break-up modes as a function of We for $Oh < 0.1$.

Considering Figures 4.2 and 4.3, at low We the destabilising aerodynamic force are balanced by the stabilising surface tension force. However, just under $We < 11$, results to more oscillatory drop deformation. For We increment over the critical number ~ 11, bag break-up is observed. Note, in Theofanous et al. [118] bag break-up is denoted for $We = 7$, whilst Pilch et al. [87] suggests bag break-up for $12 \leq We \leq 50$. In bag break-up, the drop is primarily deformed into a liquid disc and is then followed by a downstream blow at the disc centre. This finally results into a hollow bag that is attached to a toroidal ring, Fig. 4.2. The gas flow present creates further disturbances that lead to a bag burst into a large number of small scale droplets. Meanwhile, the toroidal ring undergoes a Plateau-Rayleigh instability that results in further break-up into large drops.

Moving a bit higher on the scale of $16 < We < 28$, bag-stamen break-up is usually observed, which is not explicitly demonstrated in Fig. 4.2. On the contrary, Pilch et al. [87] denotes bag-stamen break-up within $50 \leq We \leq 100$, Fig. 4.3. This break-up type is similar to bag break-up with only difference the formation of a stamen at the bag centre. Increasing We up to $30 < We < 80$, leads to *multimode* break-up that in return results in numerous bags formation. In this mode, the dual bag effect can be described as a multimode sub-regime. Previous studies, by Zhao et al. [48] and Theofanous et al. [118], suggest that the phenomena described above for low We (i.e. < 80), are primarily driven by the Rayleigh-Taylor instability mechanism, (see Section 3.4.3). In such cases, mainly RT controls the drop break-up morphology.

Going up the scale to $We > 80$, shear-stripping is the first mode observed by Theofanous et al. [118]. Here, the shear stress effects due to gas flow, lead to a liquid boundary layer formation, adjacent to the drop inner interface. With time, the adjacent boundary layer grwoth creates instabilities resulting into liquid mass being stripped off from the drop perimeter, Fig. 4.3. In the literature, a range of conclusions have being established with respect to drop deformation for $80 < We < 350$, that widely vary, particularly between computational and experimental work. The shear-stripping is generally considered to be a function of Re, however numerous studies are not in full agreement, [92][115].

Finally, at very large values of $We > 350$, catastrophic break-up is considered, concluded both in Theofanous et al. [118] and Pilch et al. [87], but also from Reinecke et al. [96]. In this mode, the 'windward' surface is primarily occupied by small wavelength waves whilst small droplets at the drop perimeter are slowly 'detached'. As time progresses, larger waves are formed that lead to drop flattening. These large wavelength waves fully penetrate the flat drop, resulting into large fragments formation, that break-up into droplets. During catastrophic break-up, large gas flow acceleration is acting on the drops. Reinecke et al. [96] concluded that catastrophic breakup is directly linked to the surface front waves growing in an unstable manner due to the rapid drop acceleration by the air stream. It was also noted, that these surface waves grow until they reach an amplitude size comparable to the drop dimensions, at this point, the drop is completely torn.

Theofanous et al. [117],[119], captured well a single liquid droplet under the effects of high airstream flow. The images demonstrated a partially smooth region at the front whilst small wavelengths waves were developed at the periphery, under the effects of the velocity gradient (typical phenomena of Kelvin-Helmholtz instability). Their experimental work showed that the liquid sheets develop under very large radial velocity. Contrary the shear-stripping mechanism does not justify such behaviour. They concluded that Kelvin-Helmholtz instability is the principal controlling mechanism of the break-up rate. Finally, their work suggests that for $We > 100$, shear forces effects are significant on the break-up along with the Rayleigh-Taylor instability, whilst for $We > 1000$, shear forces become dominant.

The Rayleigh-Taylor instabilities are typical in drop break-up processes. In such cases, the liquid drop front pressure is larger than the one at the back of the drop, forming a large pressure difference. Consequently, the low density gas flow present, considerably accelerates the high density liquid drop, forming RT instabilities. Note, in this section, the simulations are obtained at relatively low density ratios, which in cases denote slightly different conclusions with the theory.

Joseph et al. [27] studied experimentally the liquid drop break-up process at sudden exposure into a high-speed airstream. They noted that at high We, the break-up process is controlled by RT instabilities at very early times. Next it was stated that due to the shear gas flow from the high pressure stagnation point, the front drop corrugations are headed towards the drop equator. They finally suggested that the shear flow presence, could be liable to the Kelvin-Helmholz instability, since the stagnation point tangential velocity is zero there and minimal near it [27]. This in turn, results to negligible interactions with the RT instability.

4.3 Single Drop break-up in a Gas Flow

To begin our investigations we tested a liquid drop under the effects of $We = 10,\ 15,\ 22,\ 96$, with density ratio $\rho_L/\rho_G = 10$. The dynamic viscosities were taken as $\mu_G = 1.56\times10^{-3} Pa\cdot s$ and $\mu_L = 7.81 \times 10^{-3} Pa \cdot s$. The liquid drop diameter was $D = 0.2$. The equivalent free stream gas velocities were $U_G = 7.85m/s,\ 15.7m/s,\ 41.8m/s$. The domain size was chosen as $5D \times 2.5D$. This mesh spacing is strategically applied, based on the $We^G_{\Delta x}$ criteria, Eqn. 2.38, by Pitsch et al. [17]. A uniform domain of 1024×1024 is employed, with periodic boundary conditions. Doing so, the drops are well resolved whilst $We^G_{\Delta x} < 1$ is satisfied. The time step chosen is $\Delta t = 2.5 \times 10^{-5}$ with a courant $c = 0.2$. The relative set up parameters are detailed presented in Tab. 4.1. Note the surface tension σ and the Oh number values are obtained as a function of We.

U_G	We	Oh_L	σ	$We^G_{\Delta x}$
7.8	10	5×10^{-3}	1.23	0.09
	15	6.1×10^{-3}	0.82	0.15
15.7	22	7.4×10^{-3}	2.24	0.22
41.8	96	15.5×10^{-3}	3.64	0.48

Table 4.1: Drop break-up set up parameters for all We cases.

In the literature, a number of studies have denoted a time-dependence relationship for the analysis of drop deformation and break-up. In the previous works, of Chou et al. [19][129] and Faeth et al. [26], extensive investigations were carried out with respect to bag, multimode and shear break-up modes, respectively. In their studies, they were able to obtain time-breakup relationships for each mode. Recalling Pilch et al. [87] work, a characteristic break-up time derivation can be introduced by considering the forces acting on the droplet, thus pressure and inertial forces. One can relate these two as:

$$\frac{\rho_G}{2} U_G^2 A \sim \rho_L V \frac{U_G}{t} \tag{4.1}$$

where A is the drop cross-area and V is the drop volume. Here, A and V are proportional to D^2 and D^3 respectively [87]. Now, one can approximate U_G as:

$$U_G \approx 2D \frac{\rho_L}{\rho_G} \cdot t \tag{4.2}$$

where C_2 is a constant. Thus U_G has an inversely proportional relationship with time, yielding a characteristic (convective) time scale as:

$$t_C \approx \frac{2D}{U_G} \sqrt{\frac{\rho_L}{\rho_G}} \tag{4.3}$$

The above equation has been previously used in [19][26][129].

Pilch et al. [87] suggested that Eqn. (4.3) is a drop break-up dimensionless characteristic time due to RT or KH instabilities. Here, the general dimensionless time for this section is defined as $T = t/t_C$. In the two-dimensional framework, at first we consider the lowest Weber cases of $We = 10$ and $We = 15$, where the gas velocity is the same in both. Looking at Fig. 4.4, despite the small We variation, the break-up process is slightly different. From Theofanous et al. [118] and Figures 4.1 - 4.2, for $We = 10$, an oscillatory deformation is expected due to the stabilising surface tension force.

In our case, the We chosen is almost at the border between oscillatory and bag break-up, with our results clearly denoting oscillatory deformation, Fig. 4.4. The drop after reaching maximum oscillatory deformation, starts disintegrating into large ligaments and droplets. In the literature [118], for $11 < We < 16$ bag break-up has been recorded and for $16 < We < 28$ bag-stamen break-up. However, the latter one has not been fully presented in Fig. 4.2[118]. Here, at $We = 15$ the deformation starts similar to a bag-type mode, but with time it deforms with a more bag-stamen behaviour, with the main body presenting a 'light' bag-type mode with helix-type ligaments developing at the top and bottom of the drop.

Note, the selected Weber numbers here are close to the critical We_{cr}, with respect to the break-up mode recorded in the literature. Consequently, the expected modes according to the maps presented above could vary from the computational ones. Figure 4.5 shows 2D sample snapshots of the ligaments formed for $We = 15$, showing that the drops are well resolved and any flow scales involved are well captured.

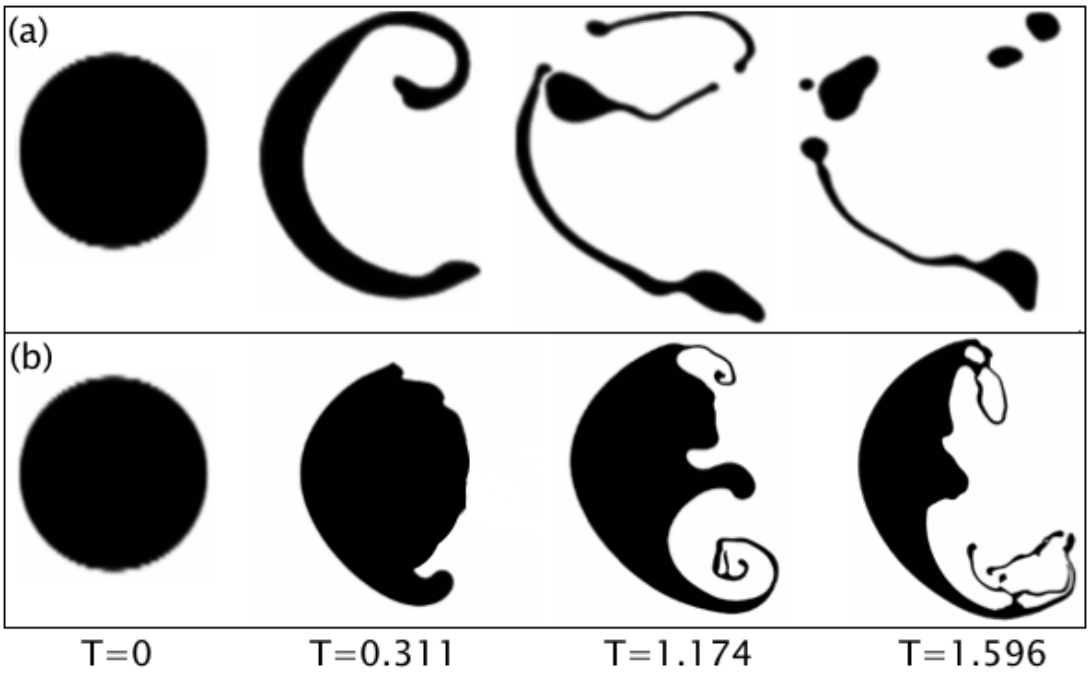

Fig. 4.4: Snapshots of drop deformation process, at the same computational times, for (a) $We = 10$ and (b) $We = 15$ in two dimensions.

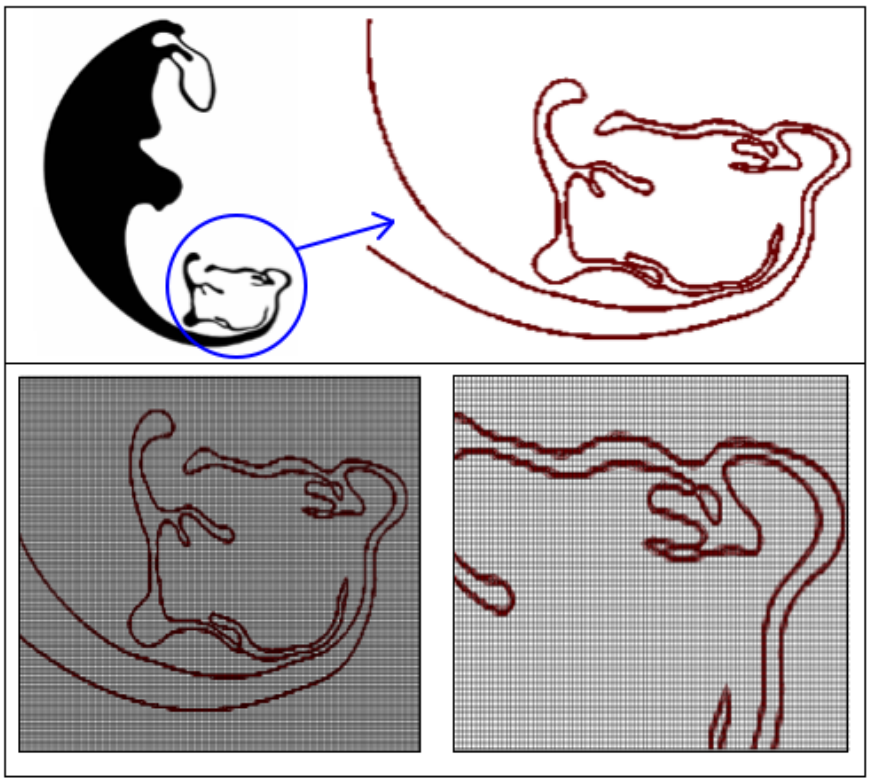

Fig. 4.5: Focused snapshots of drop deformation process for $We = 15$ at $T = 3.173$, demonstrating the captured resolution.

In the case of $We = 22$, Fig 4.6, similar behaviour is observed. The gas flow creates a bag deformation at the front of the drop, which slowly deforms at the top and bottom ends into very thin helix-type ligaments, finally resulting into multimode break-up. In theory for $16 < We < 28$ bag-stamen mode has been observed whilst for $30 < We < 80$ multimode [118]. However, previous data from Theofanous et al. [118] captured multimode break-up for $We = 27$.

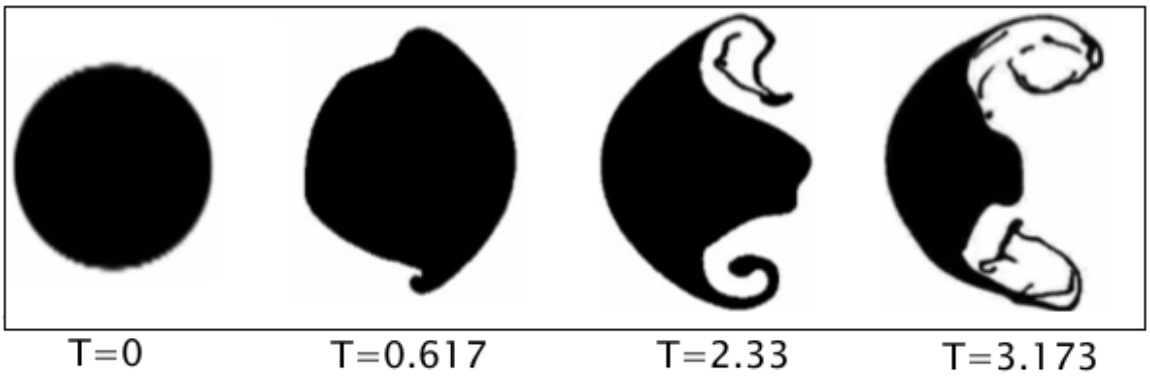

Fig. 4.6: Snapshots of drop deformation process for $We = 22$.

For $We = 96$, the drop stretches in both directions with small ligaments forming at the front of the deformed drop Fig. 4.7, denoting shear-stripping mode. As discussed, Pilch [87] presented shear stripping at $100 \leq We \leq 350$, whilst Theofanous [118] suggested shear-stripping occurs at $We > 80$. In this work, shear-stripping was captured at early computational times, for We falling higher than the Theofanous [118] range and lower than Pilch [87]. Figure 4.8 shows comparison snapshots with some of Theofanous [118] previous results.

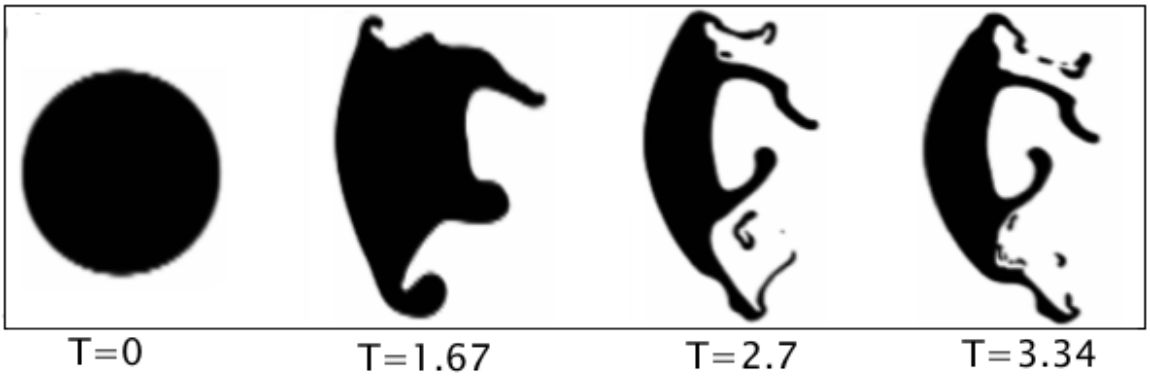

Fig. 4.7: Snapshots of drop deformation process for $We = 96$.

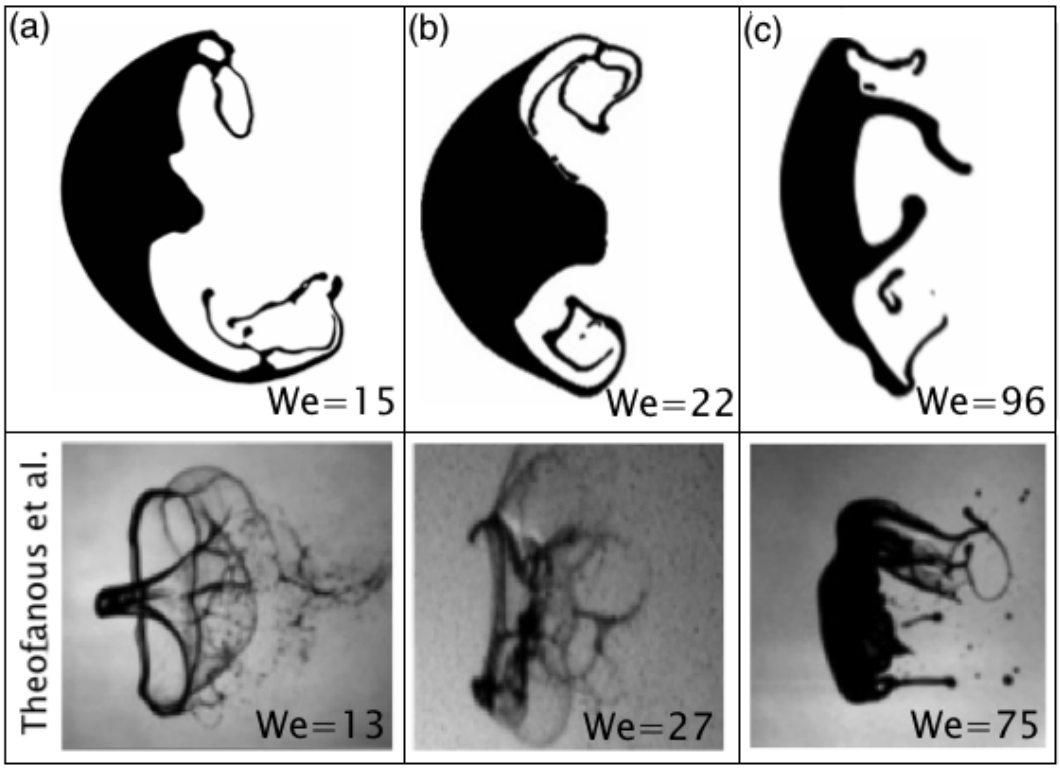

Fig. 4.8: Snapshots of each computational drop break-up in comparison with Theofanous et al. [118] results, for (a) [$We = 15,\ T = 1.596$] bag-stamen, (b) [$We = 22,\ T = 3.173$] multimode and (c) [$We = 96\ T = 3.34$] shear-stripping.

In the three-dimensional space, most cases show different break-up modes than the ones in two-dimensional framework. Figure 4.9 shows $We = 10$ and 15. In $We = 10$, bag break-up mode was recorded and for $We = 15$ bag-stamen. In Fig. 4.2, bag break-up was captured at $We = 7$, whilst in Fig. 4.3 at $We \geq 12$. Meanwhile, bag-stamen occurs at $16 < We < 28$ and $50 \leq We \leq 100$, from Figures 4.2 and 4.3, respectively. The present work, appears to be comparable with Theofanous et al. [118].

For $We = 22$, Fig. 4.10, multimode break-up was recorded, also captured in the two-dimensional space earlier. Finally at $We = 96$, the break-up mode is very similar to catastrophic behaviour, Fig. 4.10, rather than shear stripping as in the two-dimensional space. This is of particular interest, since literature [87][118] suggests much higher We numbers for such break-up to occur.

Here, we should mention that during the drop break-up investigations, a larger scale of We was tested, particularly within the range of 22 to 96. However, our findings showed large instabilities, with solutions failing to converge. In fact, as previously shown in Fig. 4.10, some noise in the solution is noted for $We = 96$, despite the density ratio being small. Due to the explicitly solved NS equations, requiring very small time steps and the need to resolve all scales (i.e. $Re \leq 2$ and $We < 1_{\Delta x}$), the CMLS was incapable of producing sufficient solutions in cases.

Although density ratios were kept low, due to the presence of viscosity, the 'physics' and in turn the 'stability' limitations in the present CMLS were not overcome (see Section 2.4.2.3). Therefore, the previously discussed numerical-difficulties in computational approaches of such processes was in fact encountered. Consequently, the results presented in the following sections regard the original parameter selection (i.e. $We = 10, 15, 22, 96$). However, with respect to the literature, the presented We allowed us to investigate the present CMLS capabilities in comparison with other current methods, for two-phase flow simulations.

In droplet break-up processes, there is a range of characteristic parameters, usually distinguished between deformation followed by break-up. Generally speaking and regardless the Weber number, the drop will initially deform to a maximum cross-stream diameter due to the unbalanced pressure field acting from the gas flow field. From there, the deformed liquid cylinder accelerates and Rayleigh-Taylor instabilities should form, that lead to the different break-up modes. In most cases, the liquid cylinder will finally break-up into ligaments and droplets. In the following sections, we investigate some of the important parameters affecting the break-up process.

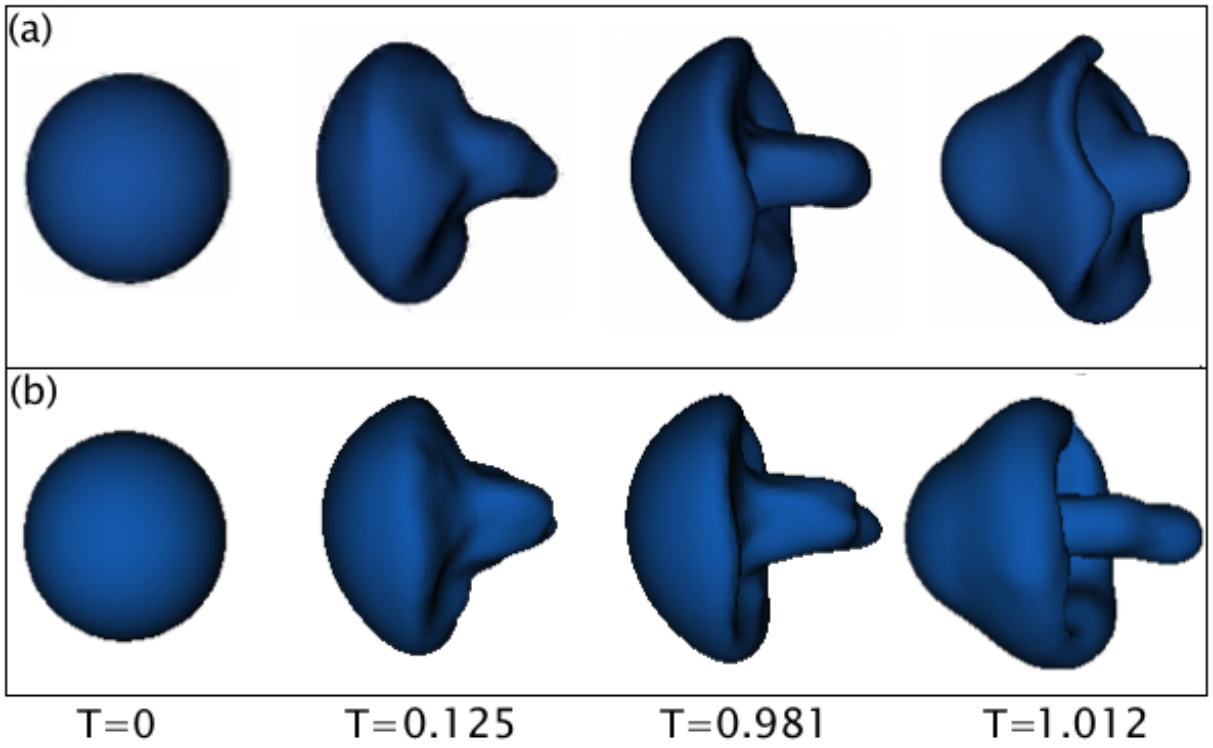

Fig. 4.9: Snapshots of drop deformation process, at the same computational times, for (a) $We = 10$ and (b) $We = 15$ in three dimensions.

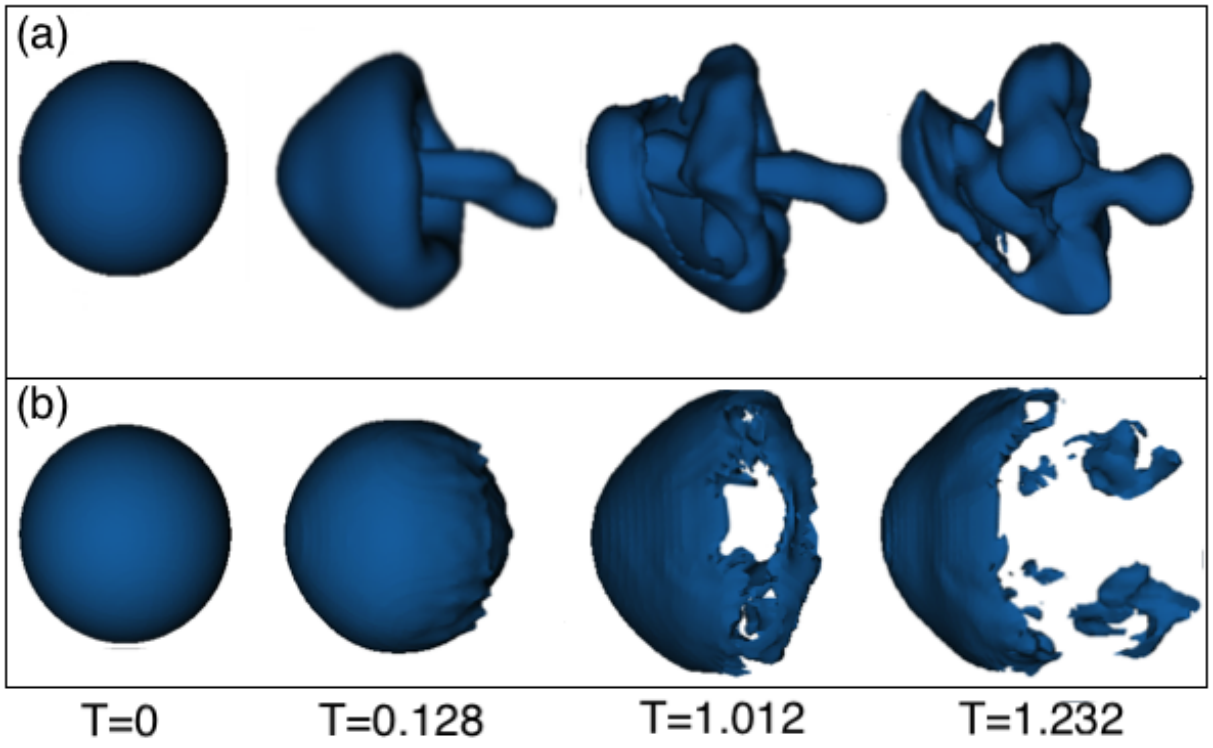

Fig. 4.10: Snapshots of drop deformation process, at the same computational times, for (a) $We = 22$ and (b) $We = 96$ in three dimensions.

4.3.1 Velocity and Pressure field effects

To further understand the drop break-up mechanism, the gas velocity and pressure field are analysed. The highest Weber, $We = 96$ was chosen at $T = 0.036$. Fig. 4.11 shows the predicted velocity and normalised pressure field, where the drop is still cylindrical and little velocity is present. Note, the pressure is normalised as $P^* = P/P_d$, where $P_d = 0.5\rho_G U_G^2$. As expected, at the back and front stagnation points, the gas velocity is decreased almost to zero, introducing high pressure in the gas phase. The lowest pressure points are located at the top and bottom drop periphery. The pressure field in Fig. 4.11 is consistent with the flow around a cylinder.

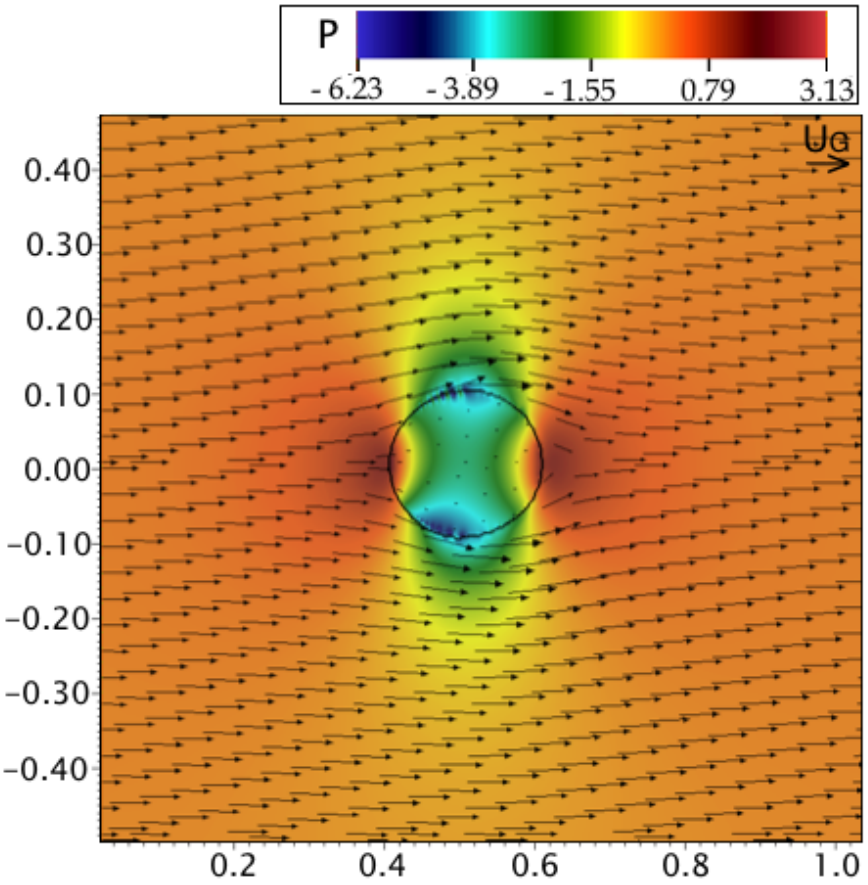

Fig. 4.11: Velocity and pressure field for $We = 96$ at $T = 0.036$.

As the drop is still cylindrical, the interfacial liquid pressure is denoted by the sum of the local gas pressure and the pressure jump due to surface tension, which for $T = 0.036$ is quasi-constant. Consequently, the gas pressure directly denotes the liquid phase pressure distribution. In Fig. 4.12, similarly the velocity and pressure fields are demonstrated for $We = 96$ at $T = 6.3$, where the drop has really deformed into a shear-stripping mechanism. Opposingly to $T = 0.036$, here the lowest pressure in the gas phase is located at the front of the drop, with the surrounding gas phase being occupied by the highest pressure.

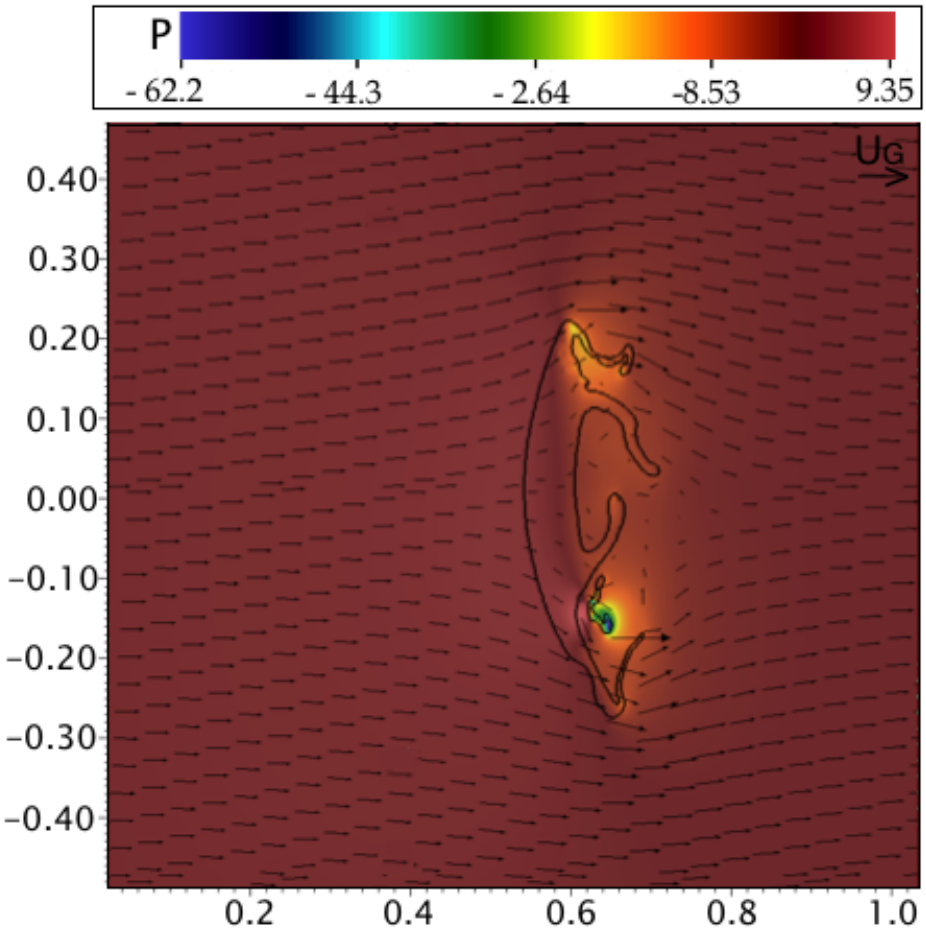

Fig. 4.12: Velocity and pressure field for $We = 96$ at $T = 6.3$.

At $T = 0.036$ the liquid velocity vector field follows the same direction with the pressure gradient at the front of the drop. Opposingly, at $T = 6.3$, Fig. 4.12, in some small areas at the drop front, the gas flow velocity field is almost in opposite direction than the flow surrounding the drop, thus the pressure gradient. Now, in a shear-stripping mechanism, it has been noted that due to the shear gas flow effects, an adjacent liquid boundary layer should form at the interface, which here is not the case.

4.3.2 Parent drop diameter and break-up initiation time

The break-up initiation time is directly related to the parent drop diameter. In any drop break-up case, the drop starts with a spherical shape of original diameter D_0. With time, the liquid drop starts evolving into a liquid disc that keeps stretching. At some point, a maximum cross-stream dimension is reached, D_{max}, before break-up occurs. The T_{IN} denotes the elapsed time of the drop deformation prior to any break-up. It is obtained manually, from the relative drop snapshots at maximum deformation before break-up process occurs. Figure 4.13 shows the initiation time definition as a function of D_{max}/D_0, for T just before and after $T_{IN} \sim D_{max}/D_0$. Amongst others, Faeth et al. [57] and Zhao et al. [48] investigated this correlation as a function of We.

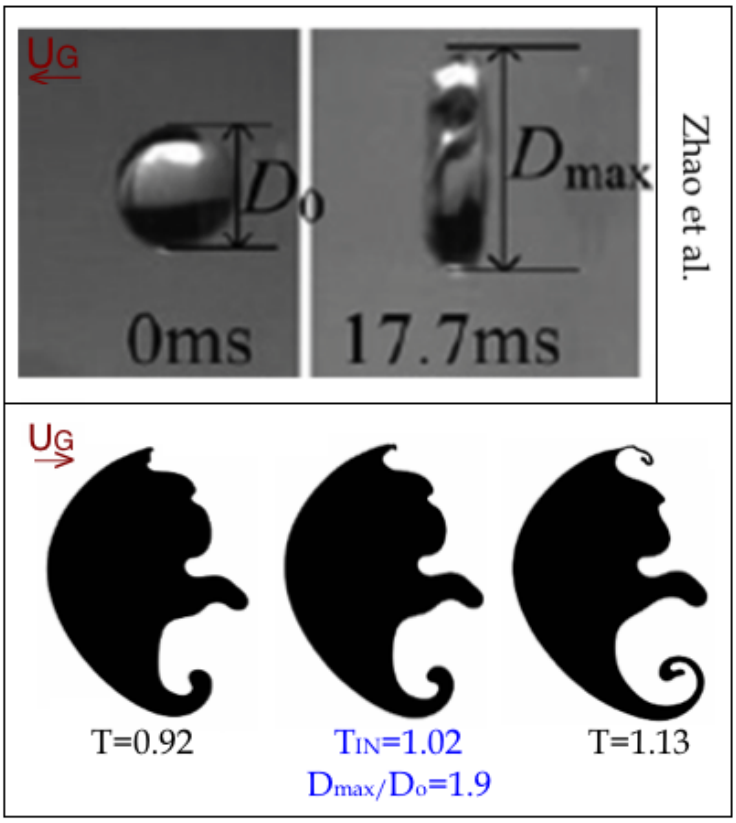

Fig. 4.13: Initiation time definition as a function of the maximum cross-stream D_{max}/D_0, Zhao et al. [48] sample image (top) and present work (bottom), for $We = 15$.

Figure 4.14 shows the normalised cross stream dimension, D_{max}/D_0, as a function of We, in comparison with the data extracted from Faeth et al. [57] and Xiao et al. [130]. Note, Xiao et al. [130] similarly compared their results with the previous works by Zhao et al. [48] and Dai et al. [26], where analogours trends with Fig. 4.14 were found. Theory suggests that increasing We should follow a small increase in D_{max}/D_0, [26][48][57], also observed in Figure 4.14. During drop deformation, a decrease in the aerodynamic force occurs acting on the drop, leading to either a finite break-up or deformation. Figure 4.15, shows the T_{IN} obtained at D_{max}/D_0 as a function of We is plotted. To compliment our study, we also employ the equivalent values from Xiao et al. [130], along with the fit presented in Pilch et al. [87] and Hsiang et al. [57].

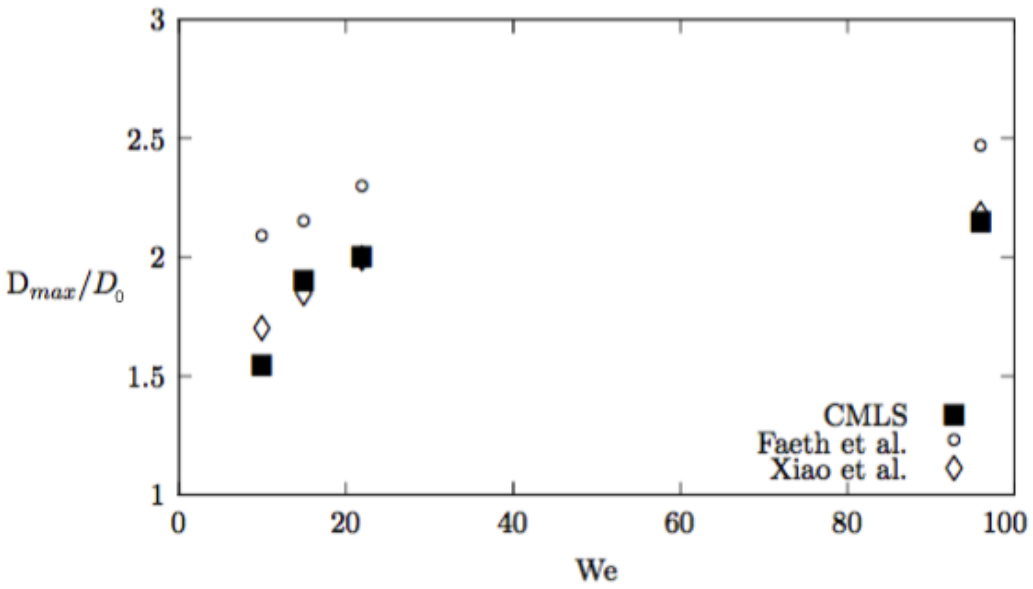

Fig. 4.14: Maximum cross stream dimension D_{max} obtained from T_{IN} as a function of We, in comparison with Faeth et al. [58] and Xiao et al. [130].

The results show high similarities to Xiao et al. [130] work and they fall close to the fit by Pilch et al. [87], with $We = 22$, falling slightly 'off' the fit trend. The results denote that as We increases, the computational deformation period reduces, as proposed by Pilch et al. [87] fit from experimental data. Note, as the drop is accelerated to the freestream velocity, the aerodynamic force exerted on the drop is decreasing. Therefore, the drop either breaks up in a finite time or only undergoes deformation. However, Pilch et al. [87] work for $We \approx We_{cr}$ suggests a possible infinite T_{IN}. More data on that topic has not been available in the literature yet.

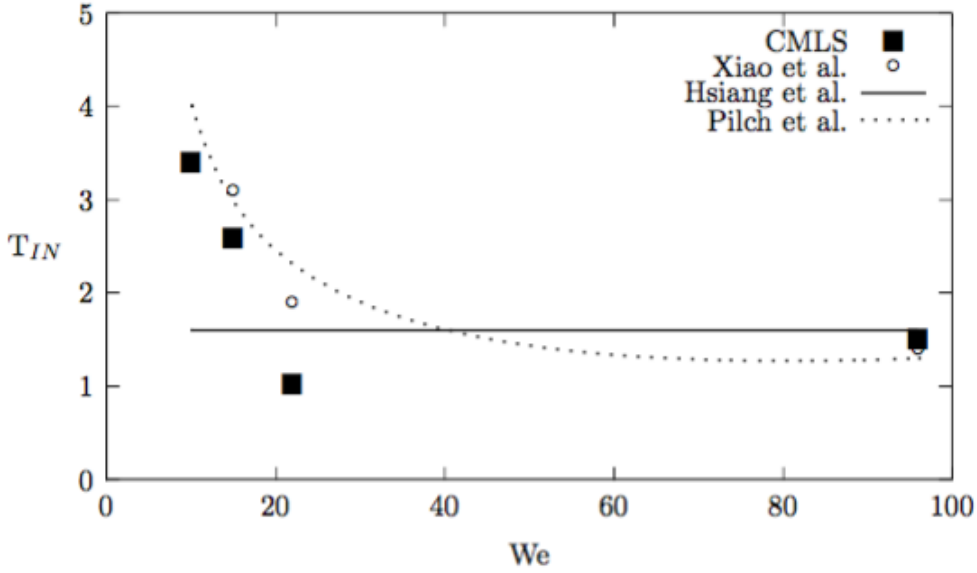

Fig. 4.15: Initiation time T_{IN} obtained at D_{max}/D_0 as a function of We, including Xiao et al. [130] with Hsiang et al. [57] and Pilch et al. [87] experimental data.

Following this, we examine the complete break-up time, T_B, for each We drop. To do so, we recorded the computational times of complete break-up from each case snapshots and translate it with respect to T. Pilch et al. [87] proposed a $T_B - We$ correlation, for $Oh < 0.1$, as:

$$\begin{aligned} T_B &= 6(We-12)^{-0.25} && 12 < We < 18, \\ T_B &= 2.45(We-12)^{0.25} && 18 < We < 45, \\ T_B &= 14.1(We-12)^{-0.25} && 45 < We < 351, \\ T_B &= 0.766(We-12)^{0.25} && 351 < We < 2670 \\ T_B &= 5.5 && 2670 < We <\sim 10^5 \end{aligned} \tag{4.4}$$

To compliment our findings, we employed the data from Xiao et al. [130] along with the experimental data from Hassler et al. [52]. Note, due to lack of data, we only present T_B in the range of $10 < We < 25$. The results are demonstrated in Fig. 4.16, along with the fitted lines for $12 < We < 18$ and $18 < We < 45$ by Pilch et al. [87].

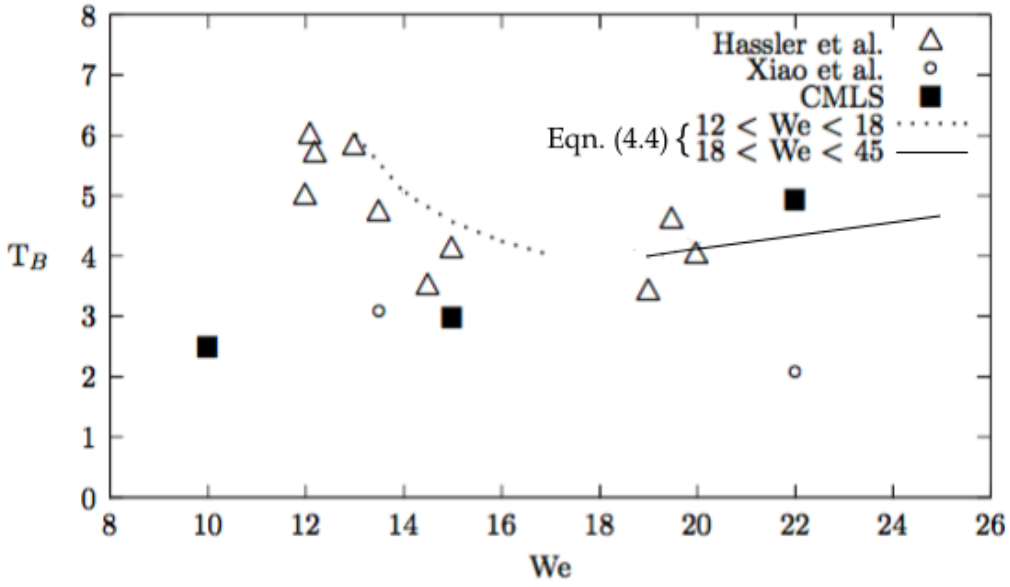

Fig. 4.16: Liquid drop complete break-up time T_B with We, in comparison with Xiao et al. [130] and Hassler et al. [52] experimental data along with correlations from Eqn. 4.4.

It is apparent, that the data falls closer to Xiao et al. [130], with Hassler et al. [52] data being slightly higher. Reasons for that, could be different density ratio choice or lower gas velocities, delaying a full break-up. With respect to Pilch et al. [87] correlation, the present $We = 15$ data falls slightly off the relative $T_B - We$ trend, however $We = 22$ is in good agreement. A parent drop denotes the total liquid (drop mass) to break further with time, whose velocity is recorded whilst the drop is still whole. Once break-up process begins, the parent drop velocity is defined at the edge of the leading drop (i.e. furthest point of the drop front) [26].

During break-up, the parent drop acceleration is very large, due to the on growing cross-stream dimension D/D_0 and the increasing drag coefficient C_D of the deformed drop. Typically, this high acceleration decreases post break-up, due to the instant large pressure difference. Deformed/break-up drops are usually much larger in comparison with the parent drop velocity [26][57]. With respect to the previous discussions, it can be stated that the drop behaviour during deformation/break-up is directly related to the initial properties of the 'injected' parent drop. The drag coefficient of a deformed drop during acceleration is simply computed with:

$$C_D = \frac{F_D}{\frac{1}{2}\rho_G U_G^2 \frac{\pi}{4} D^2} \tag{4.5}$$

Where F_D is the drag force acting on the drop, (Newton's motion second law), usually applying on a sphere or cylinder type cases. For a nearly spherical drop, $D/D_o \rightarrow 1$. In the literature, extended investigations have been recorded with respect to C_D and relative conclusions vary in cases [26][52][53][57][130].

Here, the velocity decay rate is based on the assumption that drag forces acting on the drop are comparable to those of a solid sphere. Thus, one can use the Stokes law, where C_D is a function of Reynolds and is typically considered in laminar flows, as:

$$C_D = \frac{24}{Re} \tag{4.6}$$

Considering the Weber range employed here, Eqn. (4.6) is sufficient for our analysis and Fig. 4.17 shows C_D as a function of Re. In Fig. 4.17, the points denote the actual C_D values along with the 'fit' line from Stokes law. The results are in agreement with the theory as $C_D = f(Re)$ should exponentially decay, suggesting that the droplets follow Stoke's Law and the liquid/gas interaction is correct.

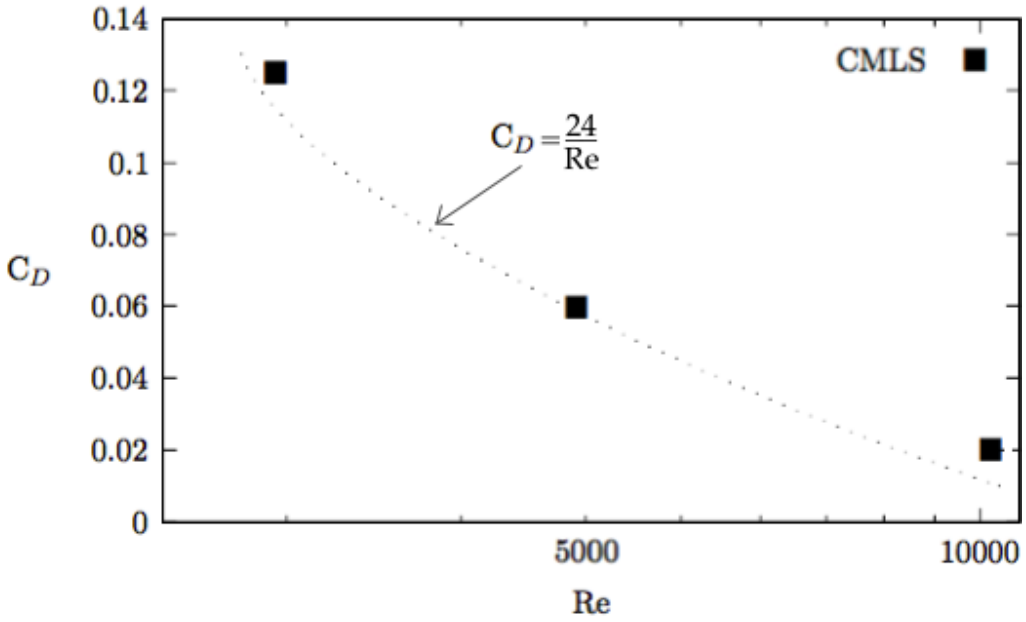

Fig. 4.17: Drop drag coefficient C_D as a function of Re computed with Eqn. (4.6).

4.3.3 Ohnesorge number effects on a single drop breakup

With respect to the break-up mode map by Faeth et al. [57], (Section 4.2), the liquid viscosity can significantly affect the drop deformation process inhibiting any break-up or deformation. Consequently, the liquid viscosity affects the critical Weber number We_{cr}, by distinguishing between deformation and break-up modes. Pilch et al. [87] and Gelfand et al. [45] provided empirical correlations for the critical Weber (We_{cr}) with Oh, from experimental data. Note, the correlations between the two works are quite different.

Later, Cohen et al. [21] presented a semi-empirical correlation, based on the secondary break-up energy transfer. Their focus was based on extracting information for the external flow conditions effects on We_{cr}, where the latter essentially denotes the minimum energy/force required for liquid drop primary break-up [21]. Their work suggested that as the drop viscosity increases, so does the Weber, due to the additional energy amount required to overcome the internal viscous depletion. The latter is true during during drop deformation and liquid phase mixing.

In such processes, the required break-up energy for a viscous drop of D_o, must be equal to the break-up energy at zero viscosity limits [21]. Based on this, they obtained a We_{cr}-Oh empirical correlation. The present thesis employs the empirical correlation, as originally proposed in Faeth et al. [57] and later in Brodkey et al. [14], denoted with:

$$We_{cr} = 12(1 + 1.077Oh) \tag{4.7}$$

Figure 4.18 shows the computational Weber with Oh_L, for a fitted line denoting We_{cr} as a function of Oh.

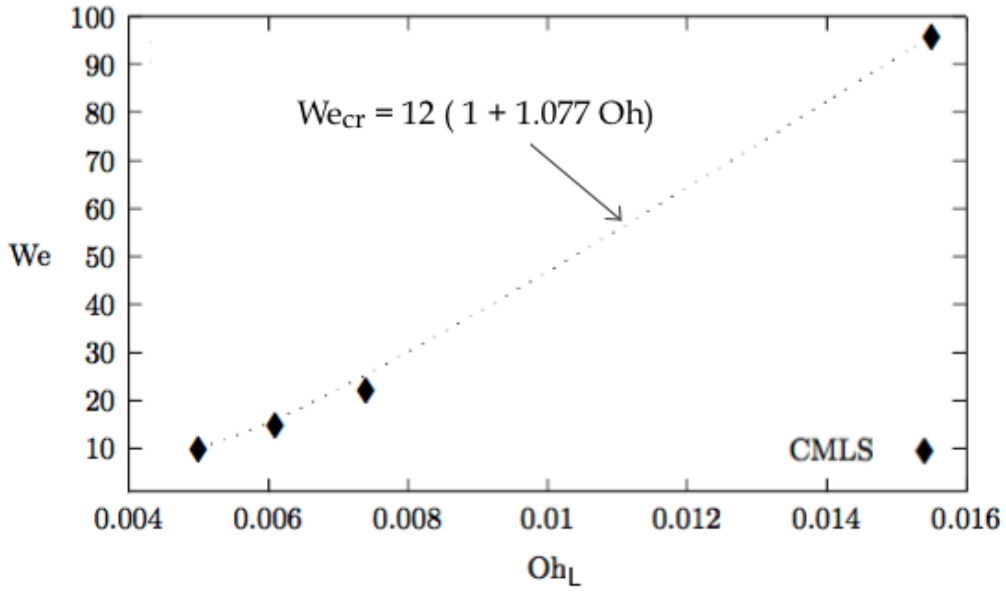

Fig. 4.18: Plot of computational Weber with Oh_L number, fitted with We_{cr} line from Eqn. (4.7).

Brodkey et al. [14] suggested that (4.7) is restricted to ($Oh < 5, We < 60$), whilst Faeth et al. [57] noted its application for ($Oh < 5, We < 200$). These restrictions for $Oh < 4$ rise from the fact that not enough data is available in those ranges. Xiao et al. [130] employed a similar correlation, based on their simulation results, as $We_{cr} = 12.3(1 + 1.1Oh)$.

In Pilch et al. [87], a further empirical correlation was proposed for the break-up initiation time T_{IN} with Oh, based on experimental data, reading:

$$T_{IN} = 1.9(We - 12)^{-0.25}(1 + 2.2Oh^{1.6}) \tag{4.8}$$

Meanwhile, Faeth et al. [58] proposed a different correlation for T_{IN}, also from their experimental measurements, reading:

$$T_{IN} = \frac{1.6}{1 - Oh/7}, \qquad [\, We < 10^3,\ Oh < 3.5\,] \tag{4.9}$$

Finally, Gelfand et al. [45], specifically recorded the bag break-up charactertistic time, for We_{cr} and suggested that Eqn. (4.8) holds for We_{cr}. In this work, the We numbers chosen are extremely close to the We_{cr}, apart from $We = 96$, so we employ Gelfand et al. [45] correlation as:

$$T_{IN} = \frac{1.6}{1 - Oh/7}, \qquad [\, We \approx We_{cr}\,] \tag{4.10}$$

Figure 4.19 shows T_{IN} in comparison with results from Pilch et al. [87] and Xiao et al. [130], for the fit line of Gelfand et al. [45]. Note, here T_{IN} is normalised with T. The present results are in good agreement with [45][87][130], where only T_{IN} for $Oh \approx 0.016$ falls 'off' the fit line. This is due to the $We = 96$ choice, not considered within the We_{cr} values.

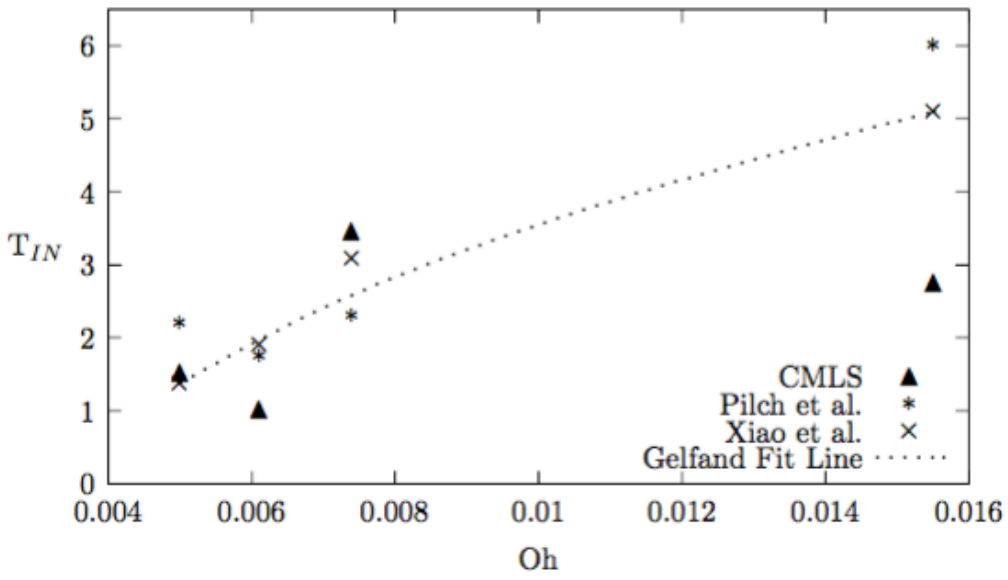

Fig. 4.19: Break-up initiation time T_{IN} with Oh, in comparison with previous works, [87], [130], [45].

4.3.4 Surface density evolution with various Weber numbers

To better understand liquid drop or jet break-up processes, the generation and destruction of Surface Density (area) is commonly employed. A family of methods exist to characterise spray regions evenly, the $\Sigma - Y$ model by Vallet et al. [4], currently known as the Eulerian-Lagrangian Spray Atomization (ELSA) model [80]. The $\Sigma - Y$ model computes both the liquid phase dispersion and the characteristic size of any fragments produced.

In the ELSA approach, a more general framework is used, solving the mean liquid surface density evolution, instead of individual 'atomization' phenomena [80][120]. The $\Sigma - Y$ approach is essentially a two-phase Eulerian model for turbulent flows, establishing a transport equation for the liquid-gas interface average area (the surface density). A second transport equation is used for the liquid mass fraction Y, to track its transport and model the liquid mix turbulence. Here, Σ is defined as the 'mean interfacial area per unit of volume' [4]. An increase in Weber is relative to a decrease in surface tension, resulting in drops being more prone to break-up and Σ increasing.

A transport equation is employed for the surface tension density $\bar{\Sigma}$ generation rate. The surface area transport equation, by Vallet et al. [4] reads:

$$\frac{\partial \bar{\Sigma}}{\partial t} + \frac{\partial u_j \bar{\Sigma}}{\partial x_j} = \frac{\partial}{\partial x_j}\left(D_\Sigma \frac{\partial \bar{\Sigma}}{\partial x_j}\right) + (A + \alpha)\bar{\Sigma} - V_s \bar{\Sigma}^2 \tag{4.11}$$

where D is a diffusion coefficient due to turbulent eddy viscosity. The A and α are inverse time scales denoting the surface area production rate and V_s is the characteristic velocity scale denoting the surface area destruction rate through collision and coalescence. In particular, A accounts for the surface density due to interface stretching by the mean velocity gradients, [4][120]. The α terms denotes the inverse time scale of processes where interface generation mechanism is due to turbulence or equivalently, due to droplet collision/break-up. Finally, V_s occurs from a V_s solution provided an equilibrium Σ_{eq} is set by the equilibrium radius of a droplet, where this surface density equilibrium can be expressed [120], as:

$$\bar{\Sigma}_{eq} = \frac{\tau_{prod}}{\tau_{dest}} \tag{4.12}$$

where τ_{prod} and τ_{dest} are the characteristic time rates for surface density production and destruction, respectively.

In the literature, numerous formulations have been proposed. However, in all approaches, the general aim is to obtain an equilibrium droplet diameter along with an atomisation process characteristic time scale [4][120]. Based on this, here we employ the transport equation as proposed in Trask et al. [120], reading:

$$\frac{\partial \bar{\Sigma}}{\partial t} + \frac{\partial u_j \bar{\Sigma}}{\partial x_j} = \frac{\partial}{\partial x_j}(D_\Sigma) + \frac{\Sigma}{\tau}\left(1 - \frac{\Sigma}{\Sigma_{eq}}\right) \tag{4.13}$$

where the last term on the RHS denotes the Σ evolution for a characteristic time τ.

Note, expressions (4.11) and (4.13) are the same, with a slight variation in the terms, according to the case in which the model is employed. Here, Σ_{eq} implies the surface density value at the end of a generation/destruction process, as the system reaches equilibrium. With respect to τ term, not enough data is provided in the literature suggesting the nature of τ as a growth or relaxation characteristic time scale. In cases, such as Trask et al. [120], τ is employed as a characteristic growth rate time. In this section, we treat τ as a relaxation/destruction time scale.

Figure 4.20 presents the normalised computational surface density evolution as a function of T. In all cases, we can see an initial transient growth, followed by a short peak and then a relatively constant Σ behaviour as the system reaches equilibrium. The transient region is the elapsed time during the drop deformation, prior to any actual break-up, denoted by T_{IN} on Fig. 4.20. For ($We = 10,\ 15\ , 96$) the T_{IN} appears relatively early, whilst for $We = 22$ later, almost half way through the surface density evolution. It should be noted, that for all We cases with the exception of $We = 22$, the system reaches equilibrium around the same time.

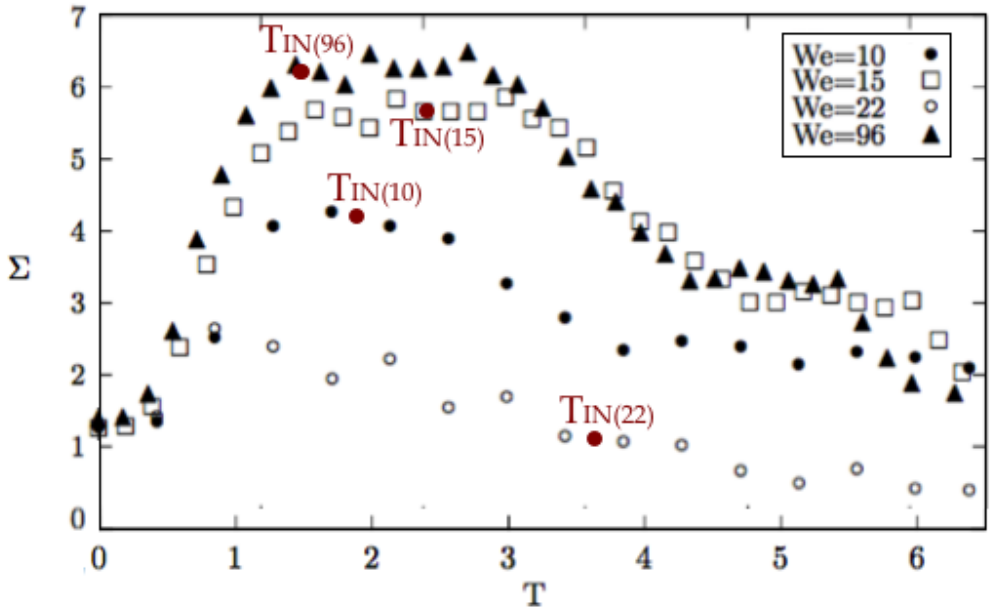

Fig. 4.20: Surface density evolution with T, for different We along with the T_{IN} positions denoted by dark red marks.

Figure 4.21 shows the surface area at the time of complete drop break-up, (i.e. Σ_{eq}). The Σ_{eq} is taken since the break-up process reaches a maximum before it goes to 'infinity', suggesting no more break-up occurs and the system reaches an 'equilibrium'. The single points in Fig. 4.21 occur from the Σ_{eq} at the equivalent We range from Figures 4.4, 4.6 and 4.7. For $We = 10,\ 15,\ 96$ the complete break-up surface area slightly increases as We increases, whilst $We = 22$ appears lower from all.

In principle, as We increases, the surface tension stabilising effects reduce, leading to less stable drop break-up processes. Considering now the results shown in both Figures 4.20 and 4.21, it appears that for larger We the system takes longer to reach equilibrium, whilst Σ slightly increases. Here, higher We denotes more break-up, Fig. 4.20. As the system reaches equilibrium (i.e. $\Sigma \to 0$), surface tension effects prevent any further break-up.

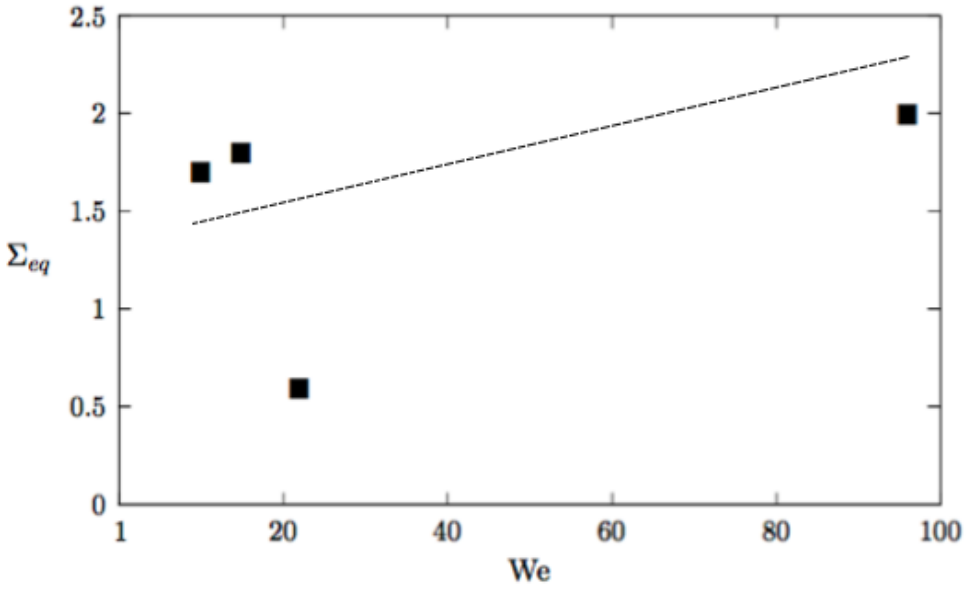

Fig. 4.21: Surface density at complete break-up Σ_{eq} as a function of We with a fitted line.

Assuming Σ is homogeneous in space, then any spatial variation in Eqn. (4.13) is negligible and for $\partial\Sigma/\partial x = 0$, one gets:

$$\frac{d\Sigma}{dt} = \frac{\Sigma}{\tau}\left(1 - \frac{\Sigma}{\Sigma_{eq}}\right) \tag{4.14}$$

following that as $t \to \infty$, then $d\Sigma/dt \to 0$, denoting $\Sigma \to 0$ or $\Sigma \to \Sigma_{eq}$. Now, Σ_{eq} and τ are assumed constant and independent of Σ. Setting $a = 1/\tau$ and $b = \alpha/\Sigma_{eq}$, yields:

$$\frac{d\Sigma}{dt} = a\Sigma - b\Sigma^2 \tag{4.15}$$

which after integration and simple manipulations, denotes:

$$t = -\frac{log\left(\left|\frac{\Sigma}{b\Sigma - a}\right|\right)}{a} + C \tag{4.16}$$

where C is a constant obtained from Eqn. (4.16), as $t = 0 \to \Sigma = 1$, since everything is normalised to initial conditions. Thus, one obtains a surface density expression as a function of time, reading:

$$\Sigma = \frac{\Sigma_{eq} exp(t/\tau)}{(\Sigma_{eq} - 1) + exp(t/\tau)} \tag{4.17}$$

Figure 4.22, shows the fit from (4.17) based on the previous results from Fig. 4.20. The constants values of Σ_{eq} and τ, are obtained from Fig. 4.21.

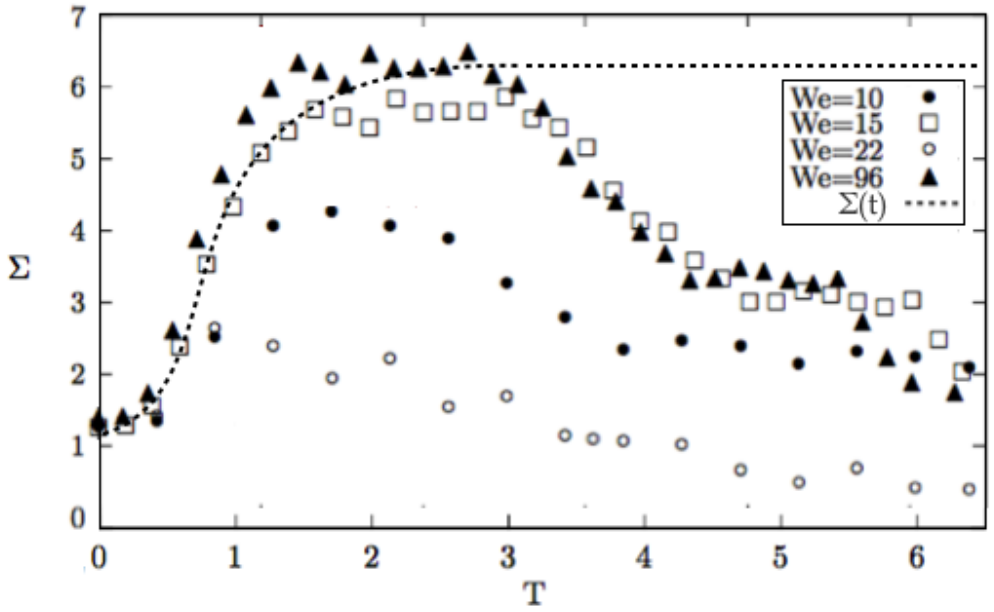

Fig. 4.22: Comparison of computational Σ evolution in time T with the fitted Σ from (4.17).

The behaviour of $\Sigma(t)$ shows a good fit until Σ_{max} is reached, suggesting that the characteristic time in Eqn. (4.13), strictly denotes the surface density growth. However, as the flow is non-homogeneous and as $t \to \infty$, then $\tau \sim dU/dy$. Meanwhile, the local shear gradient decrease with time, explaining the misfit behaviour after Σ_{max} (i.e. τ changes for $T > 3$). Conclusively, it could be proposed that (4.17) holds for $t < T_{IN}$ but not for $t > T_B$, where the flow is non-homogeneous.

4.4 Summary

This chapter studied the break-up process in a single drop at various Weber numbers. The two-dimensional break-up modes recorded were oscillatory deformation ($We = 10$), bag-stamen ($We = 15$), multimode ($We = 22$) and shear-stripping ($We = 96$). However, in three dimensions, for $We = 10$ and $We = 15$, bag- and bag-stamen modes were captured instead. For $We = 22$ multimode was noted again, whilst $We = 96$ showed a more catastrophic break-up behaviour, usually noted in much higher Weber numbers. Experimental data suggests that for $16 < We < 28$ bag-stamen break-up occurs whilst for $30 < We < 80$ multimode. The present results, appeared to be in good agreement with the literature, particularly in comparison with Theofanous et. al [118]. However, previous studies on break-up modes for various $We - Oh$, both by Theofanous et. al [118] and Pilch et al. [87], were not in agreement with each other. This was liable primarily to the experimental set up employed in each study. The present results showed that for $Oh < 10^{-1}$, an almost 'independent' relationship exists with We, not typically discussed in the literature. Therefore, the originally proposed break-up mode map in Faeth et al. [57] should be revised in cases.

Here, a key time-scale parameter was the initiation time T_{IN}, denoting the maximum drop deformation prior to break-up along with the complete break-up time, T_B. In T_{IN}, the main effective parameter is the drop maximum cross-stream dimension reached before break-up. Results showed that T_{IN} increases with Oh, which is expected by definition. Opposingly, T_B was found to increase with We, which was also noted in previous studies. Such behaviour was of particular interest, since theory suggests at higher We, surface tension effects are negligible. Therefore, one should expect that T_B should in fact decrease as We becomes larger. The maximum cross-stream dimension D_{max}/D_o slightly increases with We. The drop drag coefficient C_D was obtained as function of Reynolds, with C_D exponentially decaying as Re increases, following Stoke's law. The surface density Σ evolution with time was examined for all We cases. Here, Σ showed an initial transient growth, followed by a short peak before reaching equilibrium. In the case of $We = 22$ however a more unstable behaviour was observed with Σ being much lower than all.

The equivalent T_{IN} times were noted and for $We = 10,\ 15,\ 96$, T_{IN} appeared at much earlier computational times than for $We = 22$. Meanwhile, the equilibrium Σ_{eq} showed a small increase with We, where $We = 22$ was much less from all. However, Σ was larger at higher We with all systems reaching the same Σ_{eq} at different times, with the exception of $We = 22$ being lower. Such behaviour could be liable to the employed set up of fixed density ratios and increasing velocities with We, whilst the surface tension was computed directly from We. Due to the lack of quantitative literature data and strictly based in this work, a quasi-independent relationship is proposed between Σ and We. To summarise, the results were overall in good agreement with previous works, although the present We choices were close to critical Weber numbers, that are still under investigation. The drop break-up processes were well resolved using the novel CMLS method and important results were obtained, directly linked to liquid jet break-up processes following up.

Chapter 5

Planar Liquid Jet break-up

5.1 Introduction

Liquid jet break-up processes found in industrial applications, are highly complex to model due to the range of flow scales involved, making the computationally expensive. Detailed visualisations are required to study any instability mechanisms present, as fundamental questions regarding the physical scales integrated are still obscure [132].

This section, thoroughly investigates the destabilisation of a liquid jet in a quasi-planar set up, by a co-flowing gas injection. The quasi-planar choice is contradictory to industrial applications that use coaxial round jets. However, such set up provides better foundations for detailed investigations with respect to accurate measurements and visualisation of droplet formation processes. Quasi-planar set ups also provide clear capturing of any instabilities involved, such as the Rayleigh-Taylor and Kelvin-Helmholtz.

In this chapter, the configurations are based on the previous works by Tomar et al. [43] and Zaleski et al. [132]. The main effective parameters here are the Weber and Reynolds numbers, based on the liquid-to-gas Momentum/Dynamic pressure ratio M, with $M < 1$ denoting a Diesel-type injector and $M > 1$ typical Air-Blast atomisers. The results capture a range of flow scales such as large ligaments and droplets along with typical instability mechanisms. Both the Rayleigh-Taylor and Kelvin-Helmholtz instabilities were visualised along with hole formations within the waves, prior to any ligament generation, also noted in Zaleski et al. [132] previous studies.

5.2 Liquid Jet break-up Morphologies

In a typical liquid jet break-up onset growth process, the driving mechanisms are strictly linked to the liquid/gas interaction, creating small disturbances across the liquid interface. Parameters such as aerodynamic and viscous forces, liquid inertia and surface tension affect the break-up growth and morphology [90]. Although driving mechanisms have been extensively investigated, limitations are still present in understanding and measuring flow properties, particularly in the dense spray region. During industrial processes the actual break-up atomisation regime is of particular interest. However, to better predict these spray regions, the primary break-up conditions must first be studied. Properties such as nozzle outlet, liquid amount present, gas and liquid velocities, can significantly affect the break-up process behaviour, that in turn affect the Re and We parameters.

In Faeth et al. [89] studies, the fundamental spray features in a non-evaporation pressure-atomised jet were recorded, Fig. 5.1. Two main liquid phase regions were noted; (i) the liquid core defined by a continuously extended liquid phase at the nozzle outlet, and (ii) the dispersed flow extending beyond the liquid core surface that is sub-divided into two regimes. The multiphase mixing layer forms near the nozzle outlet and the dilute spray region develops far away from it. The latter is initiated by the ligaments and large blobs present, which in time breaks into smaller blobs and various scale droplets [58][90]. The primary jet break-up is strictly controlled by the liquid core, which is irregularly occupied with ligaments and large drops that during the secondary region entry are very unstable. The dense and dilute spray regions are significantly related to the primary liquid core properties, such as vorticities, disturbances and turbulence levels, fluids velocities and various scale structures present [58][89].

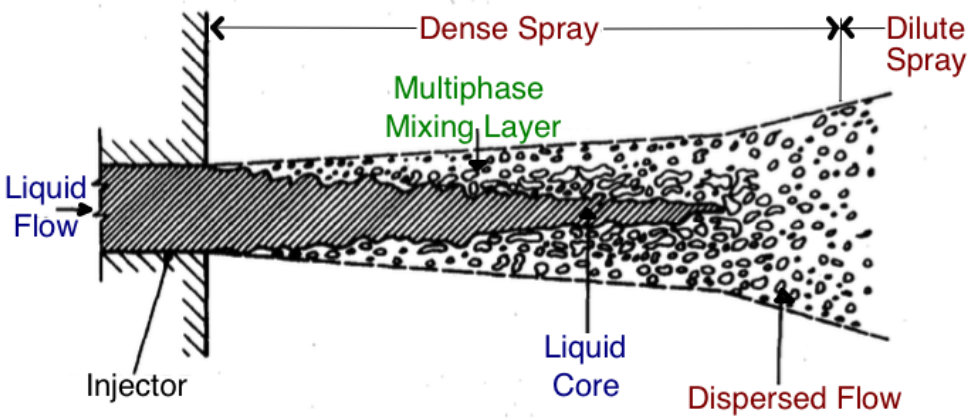

Fig. 5.1: Near-injector region morphology of a pressure-atomised spray by Faeth et al. [89].

Note, body forces are usually neglected in the primary regions, whilst the most influentials are that of capillary, inertial and viscous forces, [90]. At smaller scales, capillary forces tend to dominate, whilst at larger ones, the inertial effects take over [58], Fig. 5.1.

5.2.1 Driving Mechanisms in Liquid Jet break-up

Reitz et al. [67] studies in a round liquid jet configuration, presented the corresponding break-up regimes based on the jet break-up length with the jet velocity, Fig. 5.2. The $A-B$ area corresponds to the Rayleigh regime were capillary effects are the driving forces. The formed droplets diameter is much larger than the jet diameter, with the liquid jet break-up process taking place many jet diameters along the plane [67][90]. The $B-C$ area is defined by Weber's theory, where the capillary forces are over powered by the aerodynamic forces, leading to break-up length reduction and droplet formation of jet diameter size.

The $C-D$ area is characterised by liquid core droplets being stripped off, along with small turbulence behaviour present [67]. Here aerodynamic forces are still overruling, resulting to ligament formation along the liquid core surface, which in turn break into smaller than jet diameter droplets. Finally, $D \rightarrow$ area denotes the full atomisation region where the jet is under full turbulence, producing liquid phase perturbation that are intensified due to the aerodynamic forces [90]. Here drop formation originates at the nozzle outlet of much smaller size than the jet diameter. At the injection area, cavitation are produced that in cases promote turbulence or jet laminarisation, by reducing the passage wall friction (i.e. turbulent boundary layer removal) [67][90].

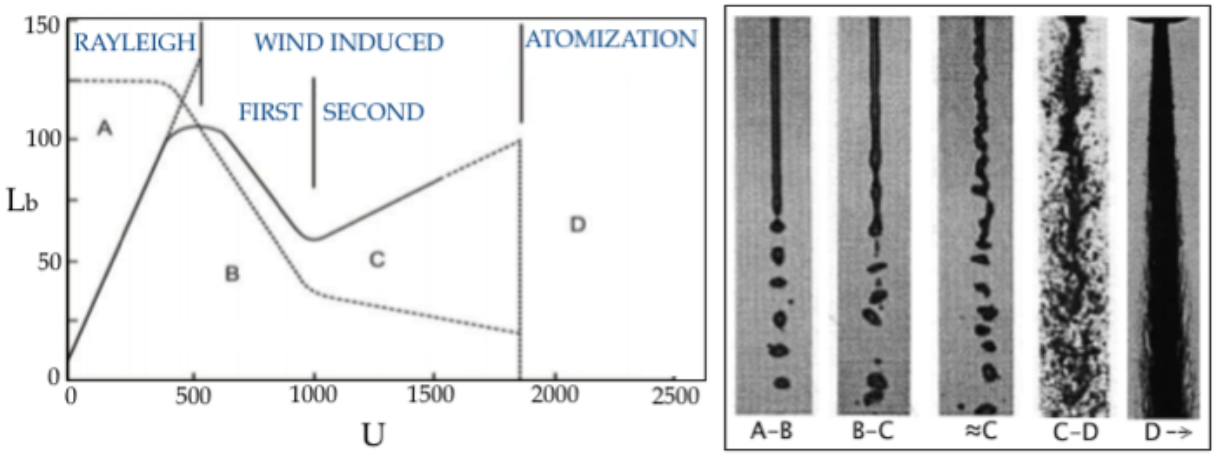

Fig. 5.2: break-up length with jet velocity plot (left) along with corresponding jet snapshots of each regime (right), for (i) Rayleigh regime $Re_L = 790$, $We_G = 0.06$, (ii) first-wind regime $Re_L = 5500$, $We_G = 2.7$, (iii) second-wind regime $Re_L = 16500$, $We_G = 24$, (iv) Rayleigh regime $Re_L = 28000$, $We_G = 70$, by Reitz et al. [67].

Based on this discussion and in a typical coaxial liquid jets framework, the effective parameters are We, Re and Oh numbers. In the literature [39][67][90], a set of criteria were proposed for the cylindrical liquid jet break-up regimes evaluation, summarised in Tab. 5.1.

break-up Regime	**Criteria**
Rayleigh	$We_L < 8$
	$We_L > 8$, $We_G < 0.4$
First-Wind Induced	$0.4 < We_G < 13$
Second-Wind Induced	$13 < We_G < 40.3$
Atomisation	$40.3 < We_G$

Table 5.1: Summarised criteria for cylindrical liquid jet break-up regimes evaluation [67][90].

Meanwhile, in Farago et al. [39] work on air-assisted atomisation, five break-up regimes were noted, Axisymmetric Rayleigh, Non-Axisymmetric Rayleigh, Membrane, Fibre and Super pulsating. To better understand the Weber and Reynolds effects, they presented a regimes map as a function of We_G and Re_L, Fig. 5.3. Meanwhile, Lasheras et al. [65], by employing an atomiser of different geometrical set up (i.e. liquid diameter and liquid/gas diameter ratio), concluded on a different break-up regime map. The main difference in comparison with Farago et al. [39] was in the break-up boundaries identified, Fig. 5.3. They also presented relative snapshots of each mode observed, Fig. 5.4, at various Re_L and We_G numbers. In their work, they noted the high influence of the M ratio, on top of the We and Re effects.

Despite the boundaries difference in the $We_G - Re_L$ maps between Lasheras et al. [65] and Farago et al. [39], the actual regimes classifications, Fig. 5.3, were in agreement for both studies, with respect to the morphology. In the sections to follow, we investigate the theories presented above through a series of simulations. The $M - We_G$ effects are extensively investigated along with any integrated instability mechanisms involved. Both qualitative and quantitative analysis are developed for different set up parameters, of the quasi-planar jets employed. With respect to Tab. 5.1 this work develops within the First- and Second-wind induced regimes.

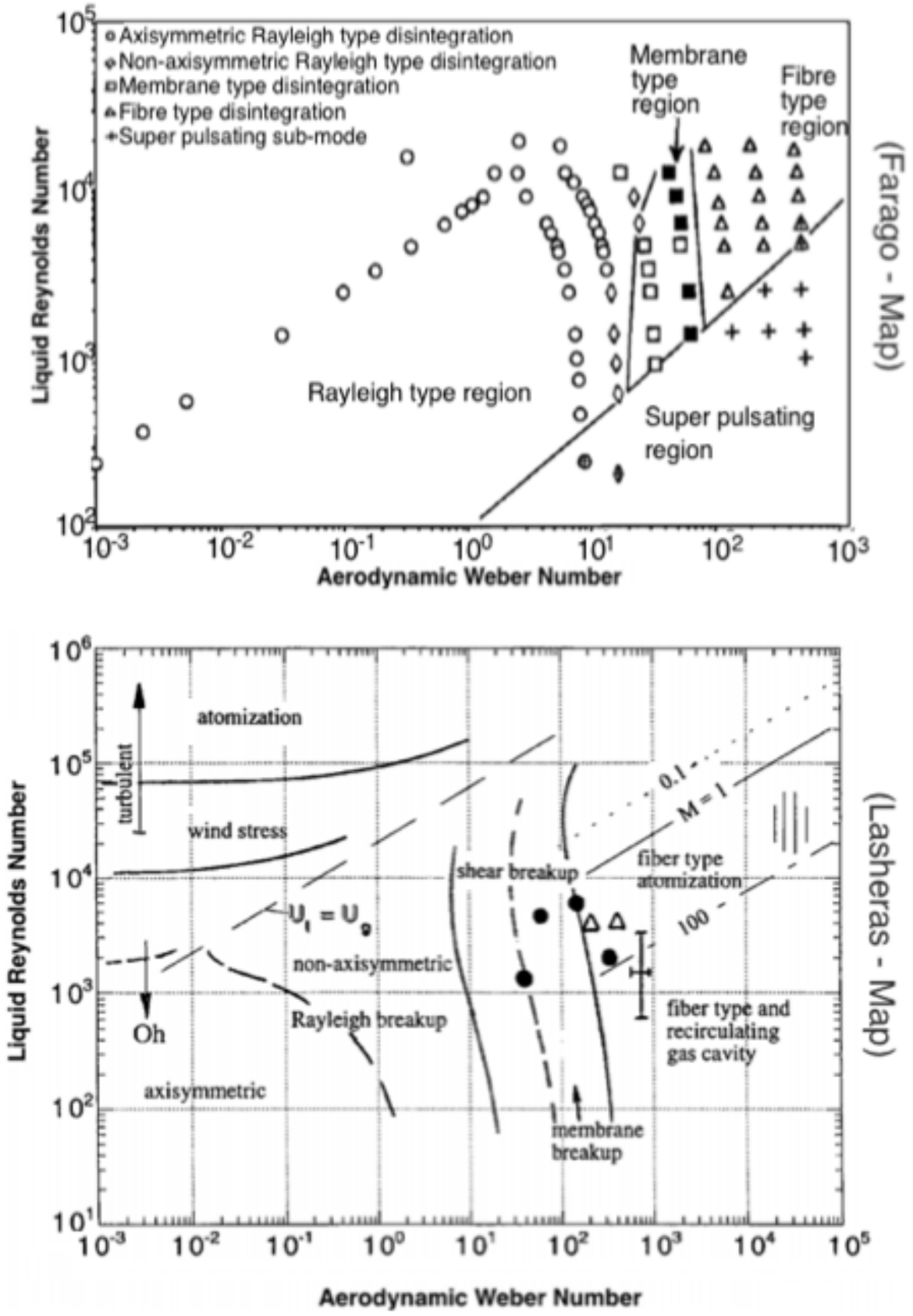

Fig. 5.3: Atomisation regimes map classification for $We_G - Re_L$, by Farago et al. [39] (top) and Lasheras et al. [65] (bottom).

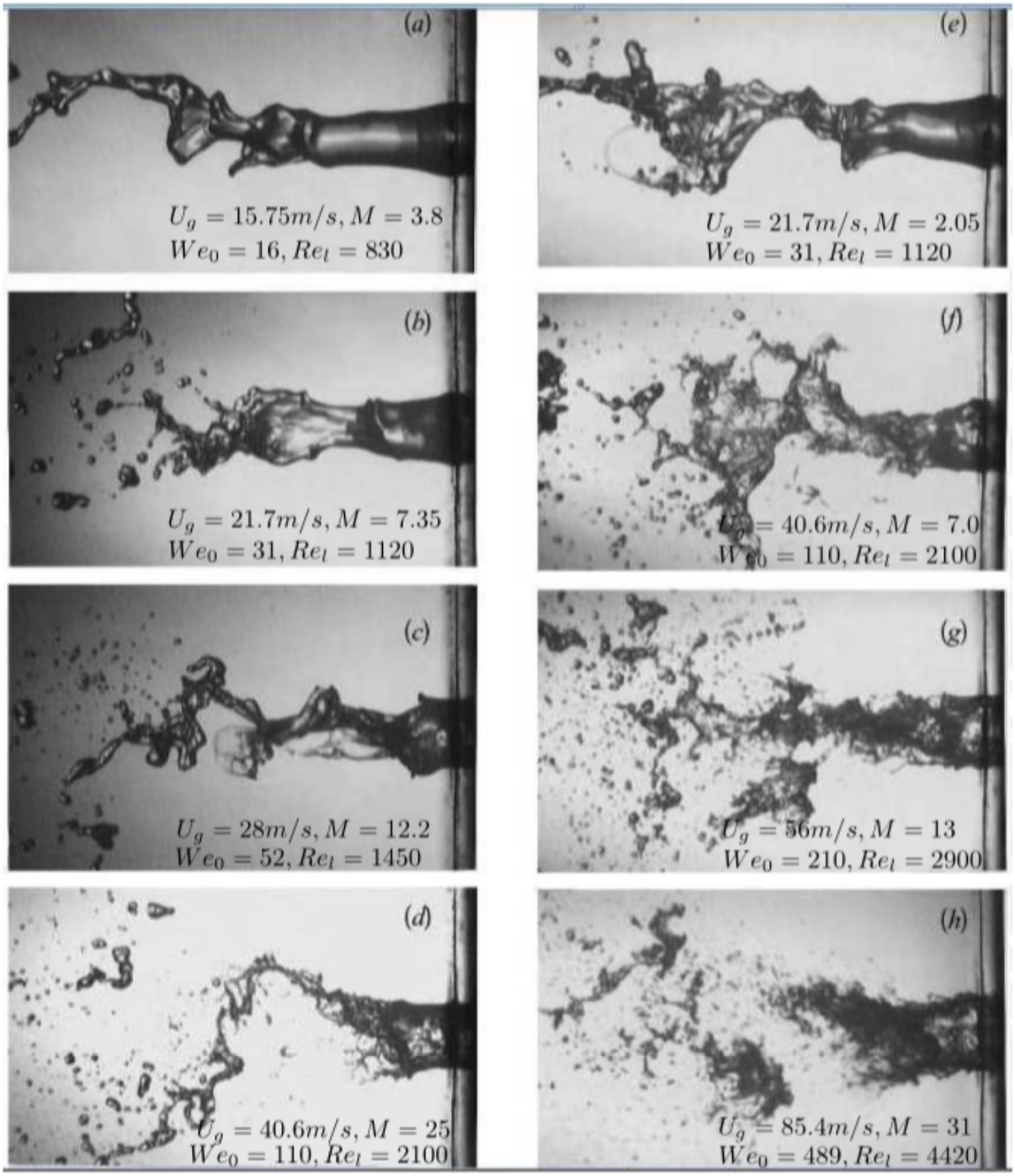

Fig. 5.4: Sample snapshots of break-up morphology in air-assisted atomisation, by Lasheras et al. [65].

5.3 Quasi-Planar Jet in Coaxial Gas Flow

5.3.1 Domain Set Up

The computational set up configuration is of a liquid jet in a canonical spray injection, introduced both in Tomar et al. [43] and Zaleski et al. [132]. Here, liquid is placed at the bottom of the domain along with a plate separating any premixing of liquid and gas. Figure 5.5 is the original three-dimensional set up with same properties applying for the two-dimensional simulations. The boundary conditions applied are airflow velocity both at the top and bottom of the domain, whilst the outlet is treated with convective flow. The simulations were run at different mesh sizes in two dimensional space of 512×256 and 1024×512, whilst in three dimensions a $512 \times 256 \times 64$ mesh was employed. The thickness of both the liquid h_L and the gas h_G were fixed at $h_L = h_G = 0.2$.

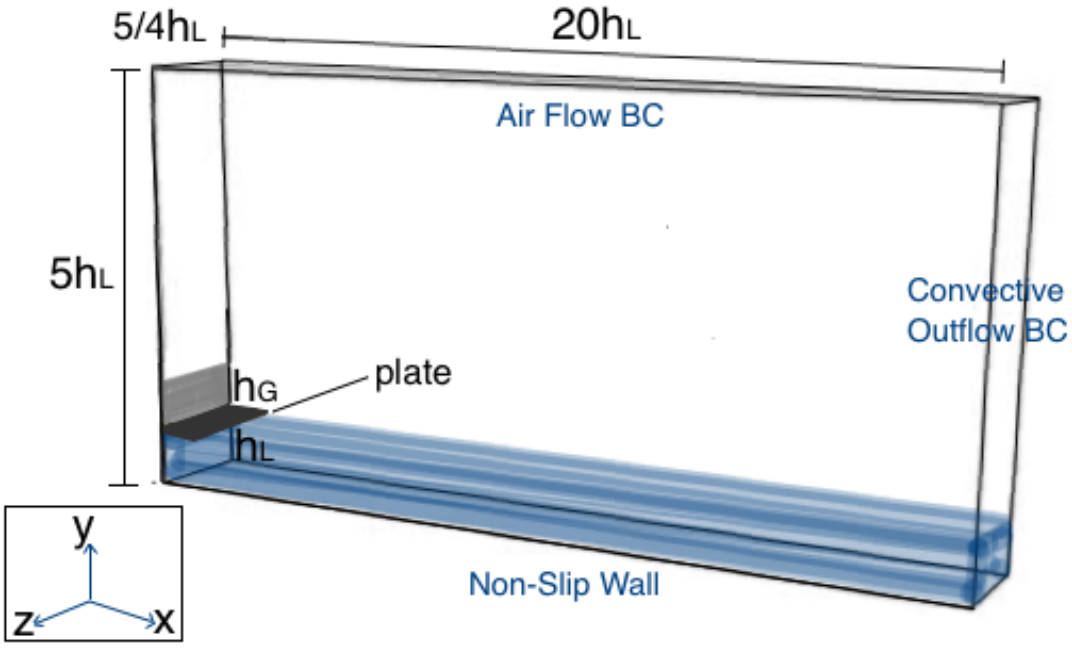

Fig. 5.5: Initial set up configuration of the spatially evolved planar jet along with the domain boundary conditions applied in three dimensional space.

For the velocity inlet conditions, two different profiles were employed for investigation. In the first approach a piecewise constant profile of $U_L - U_G$ was applied, denoting no incoming boundary layer, (i.e. $\delta_G = 0$). Here, δ_G is simply based on the gas Reynolds as $\delta_G = 6.05 Re_G^{-1/2} h_G$ [43] and for easier comparisons later, we shall name this Jet-1. The second velocity profile was based on the previous studies by Zaleski et al. [132], reading:

$$u|_{x=0} = \begin{cases} U_{o,G} erf((y - H - e)\delta_G) erf((2H - y)\delta_G), & if \quad y < H \\ U_{o,L} erf((H - y)\delta_G) & if \quad H < y < 2H \\ 0 & if \quad y > 2H \end{cases} \tag{5.1}$$

where $U_{o,G}$ and $U_{o,L}$ are the maximum gas and liquid inlet velocities, respectively. The erf error function mimics the δ_G and δ_L boundary layer thickness in gas and liquid (i.e. $\delta_G \neq 0$).

The remainder boundary velocity was set to zero [132] and we shall name this Jet-2. The inlet velocity conditions applied and in turn the boundary layer, have shown to considerably affect the break-up process. Meanwhile studies [43][132][131] suggest that δ_G is more relevant and thus the present study is developed based on $\delta_G = \delta_L$.

5.3.2 Physical Parameters

Throughout the investigations, the main effective parameters considered are the dynamic pressure ratio M, the gas Weber We_G and Reynolds Re_G numbers. Here We_G and Re_G are based on the inlet gas boundary layer thickness δ_G, as $We_{G,\delta} = \rho_G U_G^2 \delta_G / \sigma$ and $Re_{G,\delta} = \rho_G U_G \delta_G / \mu_G$. Generally speaking, the two-phase layer mixing is strictly controlled by the vorticity thickness of the gas. Provided δ_G is of the order of the separating plate thickness, the flow behind the separator plate strongly defines the most unstable frequency [131]. Thus $We_{G,\delta}$ and $Re_{G,\delta}$ are critical for the interface instability behaviour. In this work, $\delta_G/e = 9$. The general We and Re can be similarly expressed based on h_L with $We_{G,h} = We_{G,\delta} h_L/\delta$ and $Re_{G,h} = Re_{G,\delta} h_L/\delta$.

The smallest grid size simulated is $h_L/1024 = 1.95\mu m$. The time step was chosen as $\Delta t = 2.5 \times 10^{-4}$ for a courant number of $c = 0.05$. The density ratio was kept constant for all simulations at $\rho_L/\rho_G = 20$ along with $U_{air} = 1m/s$. For the most part of this work, the Reynolds numbers were fixed as $Re_L = 50$ and $Re_G = 1000$, enabling visualisations strictly based on the $M - We_G$ choices. Next, the gas Reynolds was increased to $Re_G = 4000$ and compared with the lower Re_G, to investigate the effects in changing the boundary layer thickness. The gas velocity is strictly fixed at $U_G = 2$m/s. Doing so we can visualise the jet behaviours under smaller and higher Re and We effects at different M ratios. The remainder physical parameters were computed based on the M and We_G choices in each case. The relative set up parameters for all cases are summarised in Tab. 5.2. To ensure good resolution properties of the computations, we employed Pitsch et al. [17] criteria from Eqn. (2.38) suggesting $We^G_{\Delta x} < 1$. Note, $We_G = 40$ appears to fall within Menard et al. [112] proposed criteria, of $We^G_{\Delta x} \leq 10$. The results are presented for a dimensionless time $T = t/t^*$, where $t^* = h_L/U_{air}$.

M	We_G	$We^G_{\Delta x}$	
4	10	0.39	$U_G = 2m/s$, $U_{air} = 1m/s$ $Re_L = 50$, $Re_G = 1000$
	20	0.78	
	40	*1.56*	
8	10	0.39	
	20	0.78	
	40	*1.56*	
16	10	0.39	
	20	0.78	
	40	*1.56*	
0.002	1	$3e \times 10^{-2}$	$U_G = 5m/s$, $U_L = 1m/s$ $Re_L = 5000$, $Re_G = 1000$

Table 5.2: Summarised Weber and Reynolds based set up parameters for all M cases.

5.3.3 Liquid-Assisted break-up

This work mainly focuses in air-blast assisted jet break-up, however strictly in this section a case of 'diesel' type injectors is examined. Liquid-assisted jets provide good sampling foundations with respect to free-surface motion and singularity formation resulting to drop break-up. They can also give information on surface tension and viscosity effects, both very effective parameters in jet break-up processes [36]. Consequently, $M << 1$ jet types are more predominant in the relative literature [10][36]. In theory $M \approx 1$ denotes 'quasi-laminar' jets and no break-up should occur. Consequently, here we study liquid-assisted break-up for $M << 1 = 0.002$ and compare it with $M = 1$, with $\delta_G \neq 0$.

Figure 5.6 shows snapshots in the two-dimensional space. For $M = 1$, the gas and liquid Reynolds are taken from Tab. 5.2. For $M << 1$, a 'diesel' type injector is used where liquid is the driving force. Thus, $We_G << We_L$ with $We_G = 1$ and $We_L = 500$, whilst for the Reynolds parameters we used $Re_L = 5000$ and $Re_G = 1000$. In $M = 1$, the jet appears 'quasi-laminar' as expected, with no break-up present. Liquid-assisted jets are strongly linked to the Kelvin-Helmholtz instability modelling, that enable the primary break-up prediction of the diesel liquid core [10]. In $M << 1$ the interface is fully characterised by wave accumulation under the KH instability. These waves develop into interfacial 'finger-like' ligaments along with minor holes trapped within.

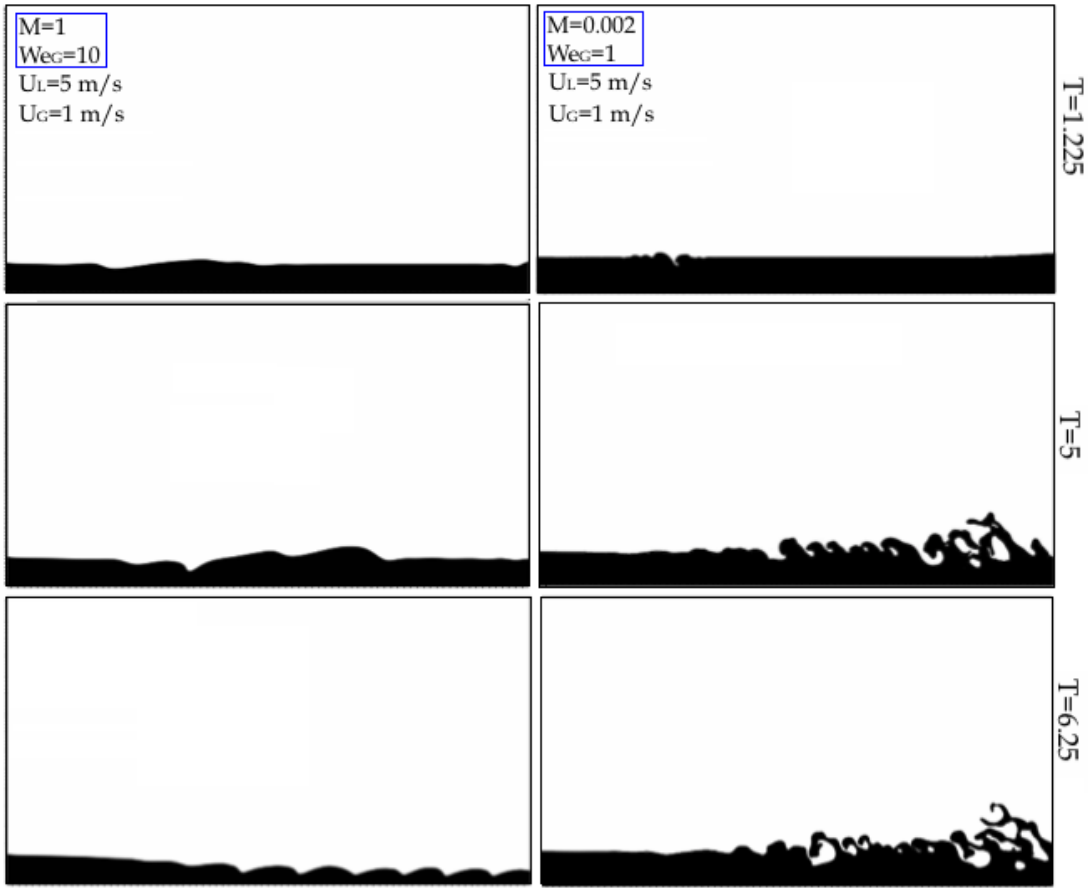

Fig. 5.6: Snapshots of liquid jets for $M = 1$ (left) and $M << 1$ (right) for 512×256 mesh size, with $\delta_G \neq 0$, in two-dimensions.

Figure 5.7, shows the hole formation process due to waves accumulation, with time. As the wavelength (λ) decreases and the waves accumulate closer together (i.e. $\delta\lambda$ reduces), hole formation occurs within the waves. Theory [10][56] suggests that at high Re, which is also the case here, potential droplet size during secondary break-up should scale with δ_L.

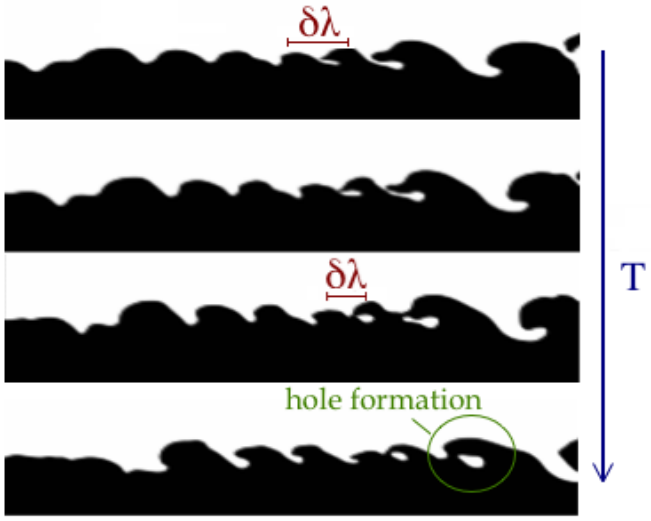

Fig. 5.7: Hole formation as wavelength $\delta\lambda$ decreases with time.

Figure 5.23 shows the surface density evolution with time T, for both M ratios, where the $\Sigma(t)$ expression from Eqn. (4.17) is fitted. The Σ evolution for $M = 1$ clearly shows no significant interface 'activity', characterised by a minimal peak throughout its linear behaviour. On the contrary $M << 1$, initially shows a constant (transient) growth, followed by a small peak. Within short time the peak grows even further, denoting the previously captured wave formation and KH instabilities at the liquid interface. Here, $\Sigma(t)$ fits the trend but not the actual data, possibly suggesting that in this case $1/\tau \sim \partial U_L/\partial y \approx \Delta U/\delta$.

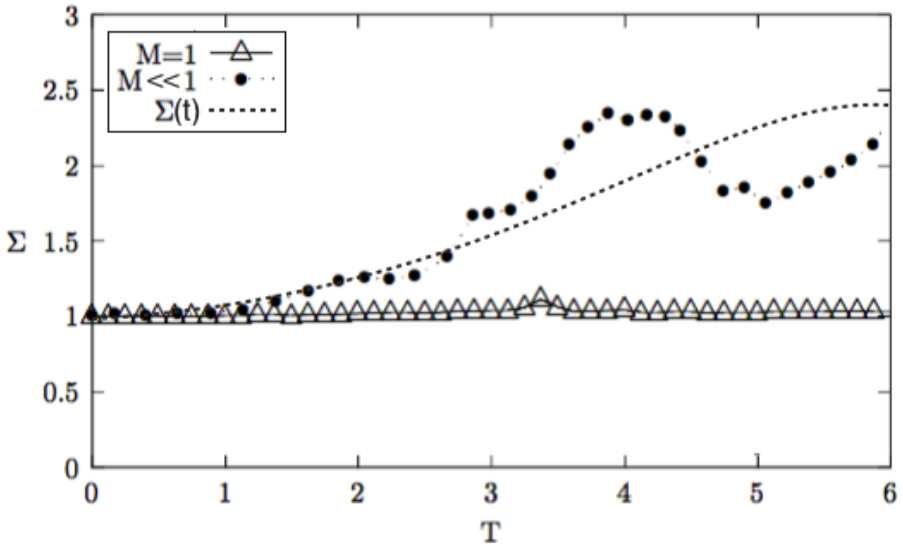

Fig. 5.8: Surface density evolution with time for $M = 1$ and $M << 1$, fitted with $\Sigma(t)$ from Eqn. (4.17).

5.3.4 Air Blast Assisted - Coarse Mesh

In this section, we examine the break-up process of air-blast assisted jets, for $\delta_G = 0$. The results are shown for all M ratios, Tab. 5.2, at $We_G = 10$ and 40. Figure 5.9 shows snapshots for $We_G = 10$ and $We_G = 40$ for all dynamic ratios at $T = 6.25$. Generally at $M = 4$ and 8, for $We_G = 10$, 'quasi-laminar' behaviour is captured with some small interface disturbances, whilst $M = 16$ shows a weak break-up with small ligament formation near the inlet. Meanwhile, at $We_G = 40$ strong break-up is observed in all M cases. Here, for $M = 4$, large ligament formation is developed across the interface, with some minor droplets present. Away from the jet inlet, the area is occupied by large-sized ligaments forming near the domain boundaries, creating high instabilities and filaments formation. However, the high viscosity ratio present limits any further break-up. Finally, for $M = 8,\ 16$ a more similar behaviour is captured between them.

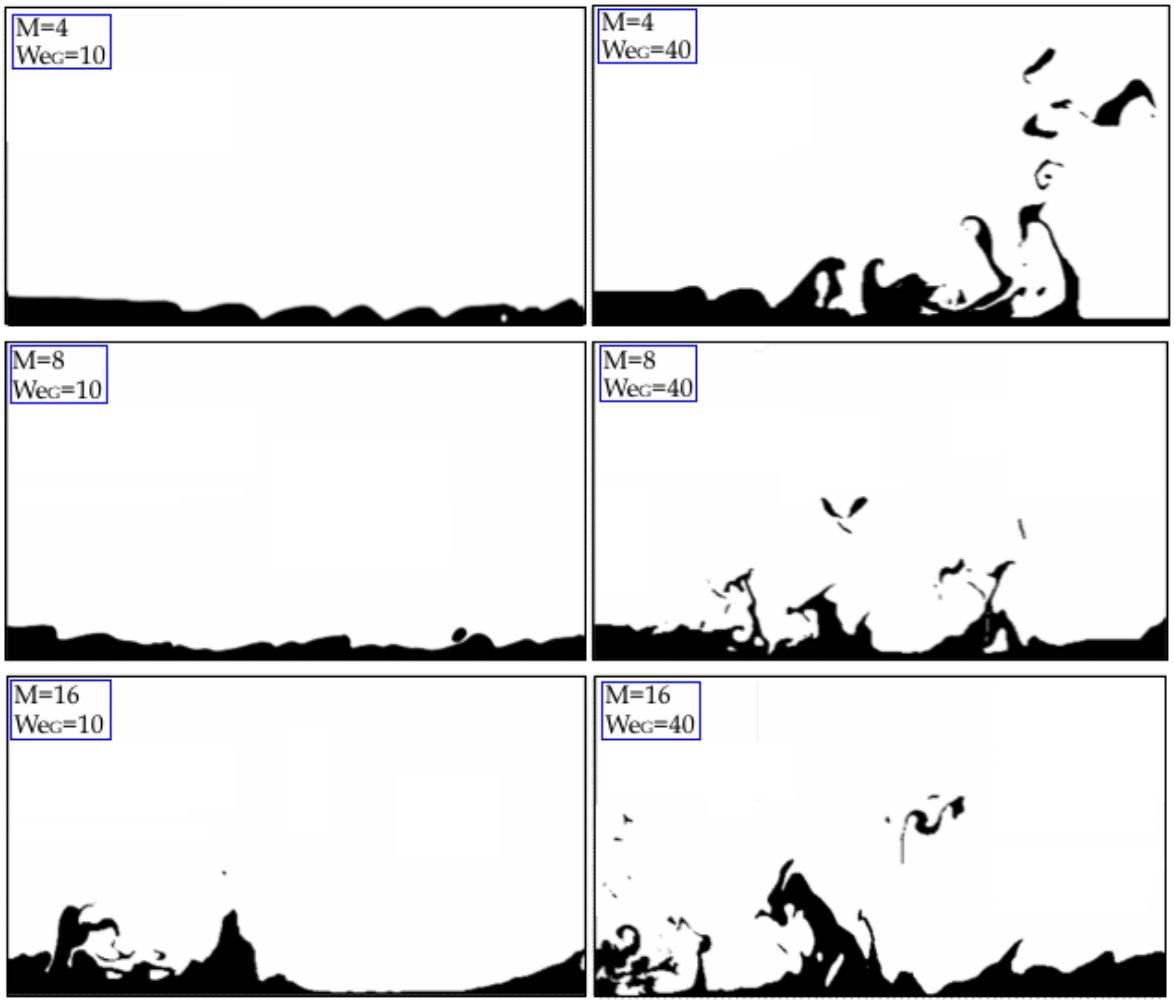

Fig. 5.9: Snapshots of liquid jet for $We_G = 10,\ 40$ at different dynamic ratios of $M = 4,\ 8,\ 16$, for 512×256 mesh size, at $T = 6.25$, with Jet-1 [43] set up.

Both jets present strong surface disturbances, with ligaments being stripped off from the liquid core along with small droplets and hole formation. In $M = 8$ the higher break-up is developed in the middle part of the liquid core, whereas for $M = 16$ strong break-up is captured at the jet inlet. In comparison with $M = 4$, the break-up is mostly occupied by structures forming near the liquid core length, occupied both by drops and smaller filaments. It could be said that $M = 8,\ 16$ is more unstable than $M = 4$, also seen in other studies [39][65][90]. Overall, as M increases, the jet behaviour goes from a multiphase mixing layer towards a more dispersed flow. However for the computational time used, strong atomisation was not recorded.

At this point, it could be proposed that within the range of $8 < M < 16$ and $10 < We_G < 40$ a critical M and We_G exists, respectively, within which break-up behaviour will be developed. Thus lower $We_G - M$ denote more stable systems of no break-up and possibly some disturbances. However if one individually increases M or We_G, break-up behaviour will be captured. To further validate this assumption, we present a series of snapshots strictly at $We_G = 20$ for all M ratios, Fig. 5.10. It is clear that all jets demonstrate very similar break-up behaviours.

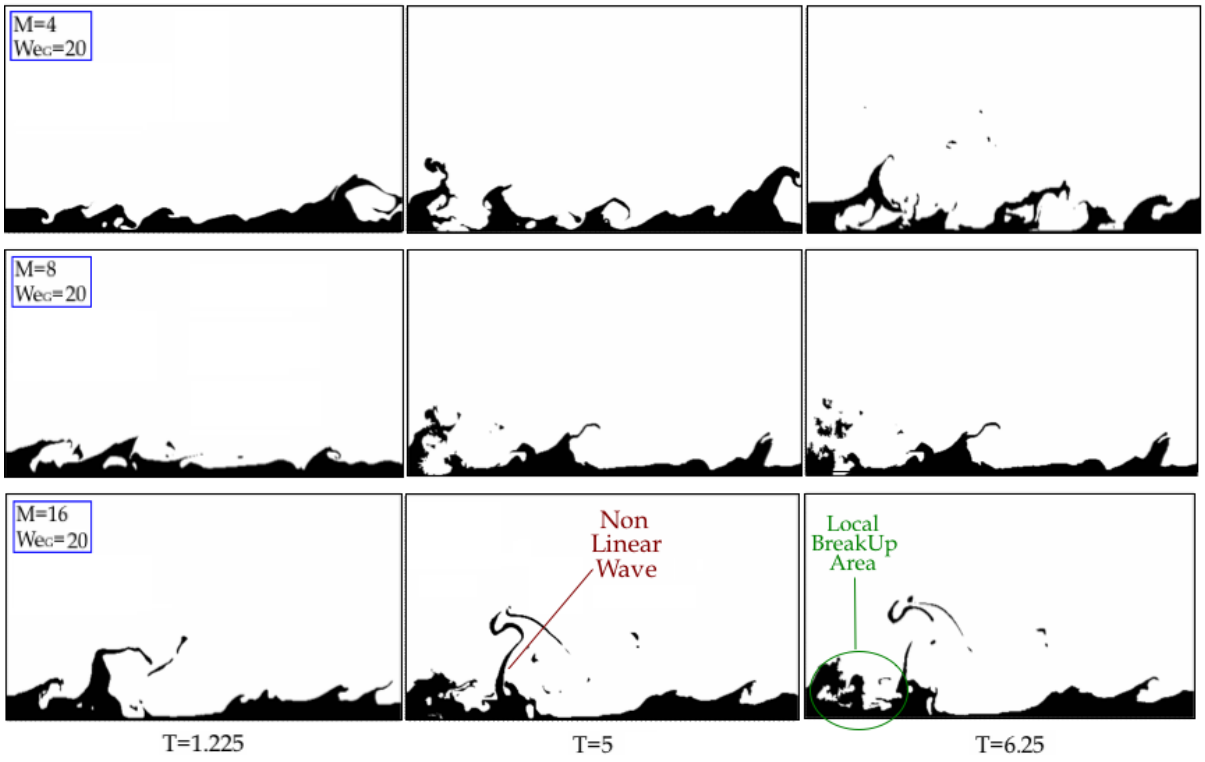

Fig. 5.10: Snapshots of liquid jet for $We_G = 20$ at different dynamic ratios of $M = 4,\ 8,\ 16$ for 512×256 mesh size, with Jet-1 [43] set up.

At lowest M, strong interface disturbances are noted with some ligament formation and small droplets away from the liquid core. In $M = 8$, the jet shows droplet formation from early times with particularly strong break-up at the jet inlet. For $M = 16$, ligaments are developed early and break into smaller ligaments and droplets with time. Comparing Figures 5.9 and 5.10, strong break-up behaviour is captured for $We_G = 20$, whilst for $We_G = 40$ the break-up process increases with M.

In Fig. 5.10, a key behaviour is noted at $M = 16$, where a non-linear wave is formed that grows into a thin ligament with time, despite the small $\Delta U_{L,G}$ difference. This non-linear wave appears almost as an 'obstacle' to the gas flow direction, with a large 'liquid-empty' area forming at the front of the wave, Fig. 5.10. With time this wave grows higher than the gas jet height, resulting into a larger almost-empty liquid area formation at the front and a smaller break-up area at the back. Consequently an almost 'negative' drag at the back of the wave is developed, resulting into a violent local break-up near the jet inlet. Finally, the non linear wave stretches to its maximum and detaches from the liquid core into ligament and drops.

Note, this 'liquid-empty' behaviour was captured in all M cases for $We_G = 20$ at some scale, and was also observed for $M = 16$ at $We_G = 10,\ 40$. Figure 5.11 shows a break-up correlation map of M with We_G, for strictly $Re_L = 50$; with the points representing all the $M - We_G$ combinations employed. Here, the 'quasi-laminar' regime regards low $M - We_G$ combinations, where no break-up occurs, U_L controlled regime. At higher M but small We_G, the stable regime is considered, where some break-up is present, with small interface disturbances and liquid core attached ligaments. Next follows the break-up regime, denoting the break-up process occupied by various flow scales yet remains 'stable', U_G controlled regime. Finally for high We_G the system becomes unstable and almost a 'quasi-independent' relationship was noted with M.

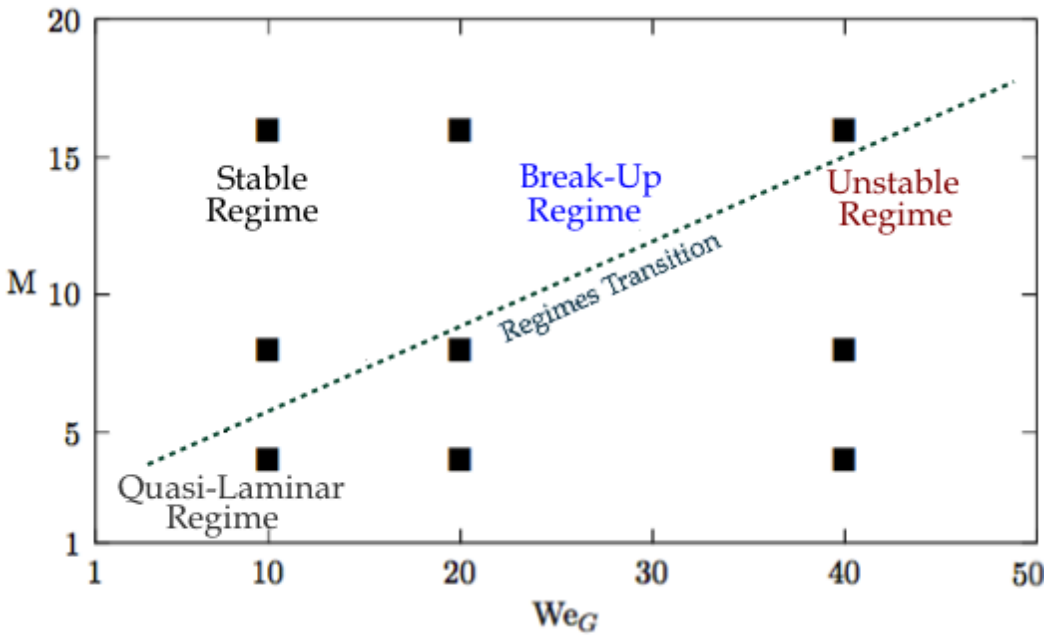

Fig. 5.11: Break-up map of Dynamic Pressure ratio as a function of the gas Weber, denoting the corresponding system break-up regimes (two-dimensional).

Note, the break-up correlation map shown in Figure 5.11 is strictly based on the present results. However, similar relationships were noted in previous studies [132][131].

5.3.5 Boundary Layer Effects in Air-Assisted Jets

Based on the $M - We_G$ map in Fig. 5.11, this section develops for $M = 16$ at $We_G = 20$, focusing on the effects of the boundary layer in the jet break-up behaviour (i.e. $\delta_G = 0$ and $\delta_G \neq 0$). The study is developed in a refined mesh of 1024×512. Figures 5.12 and 5.13 show snapshots for $Re_G = 1000$ and 4000, respectively. As the mesh is refined and $Re_{L,G}$ changes, the boundary layer effects can be further examined, that significantly affect the formation of any instabilities and driving mechanisms present. In both δ_G cases, the liquid break-up process is characterised by a range of interface disturbances, including holes, large ligaments and small droplets present.

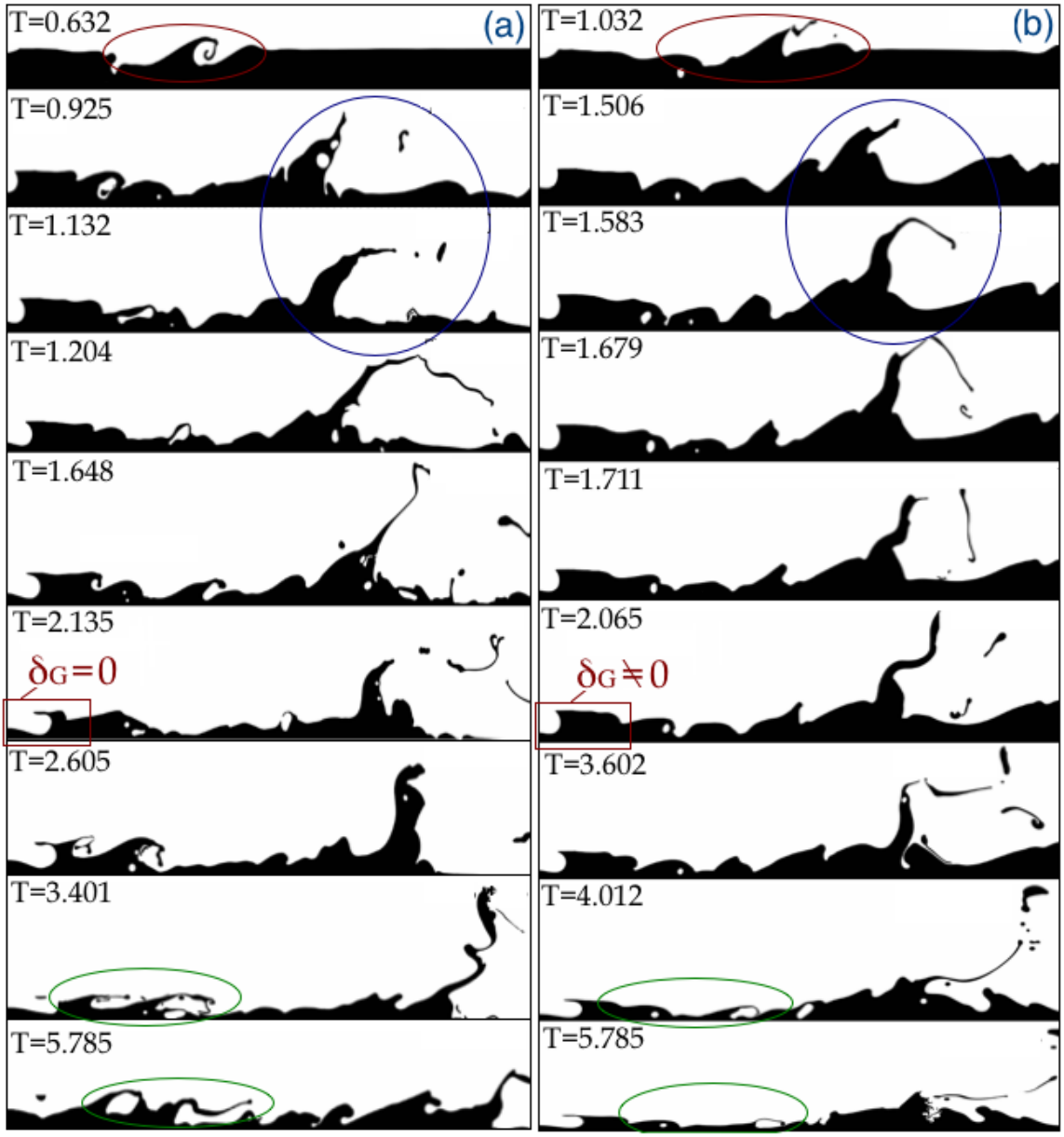

Fig. 5.12: Snapshots of liquid jet break-up for [$M = 16$, $We_G = 20$, $Re_G = 1000$], in a 1024×512 mesh size for (a) $\delta_G = 0$ and (b) $\delta_G \neq 0$.

For $\delta_G = 0$ we notice a strong presence of the unstable wave 'phenomena' as previously noted for the coarser cases. Similarly here, it grows much higher than the gas height into a large ligament before it breaks into smaller ligaments and droplets. Meanwhile, at the front an almost empty liquid area is formed. For $\delta_G \neq 0$, it could be said that the break-up process is slightly more 'stable'. The unstable wave phenomena is also noted, where it grows higher than the gas height but not as much. It also appears to form and break into ligaments faster and less violently. Furthermore, the back area of the unstable wave shows much higher break-up for $\delta_G = 0$ than $\delta_G \neq 0$.

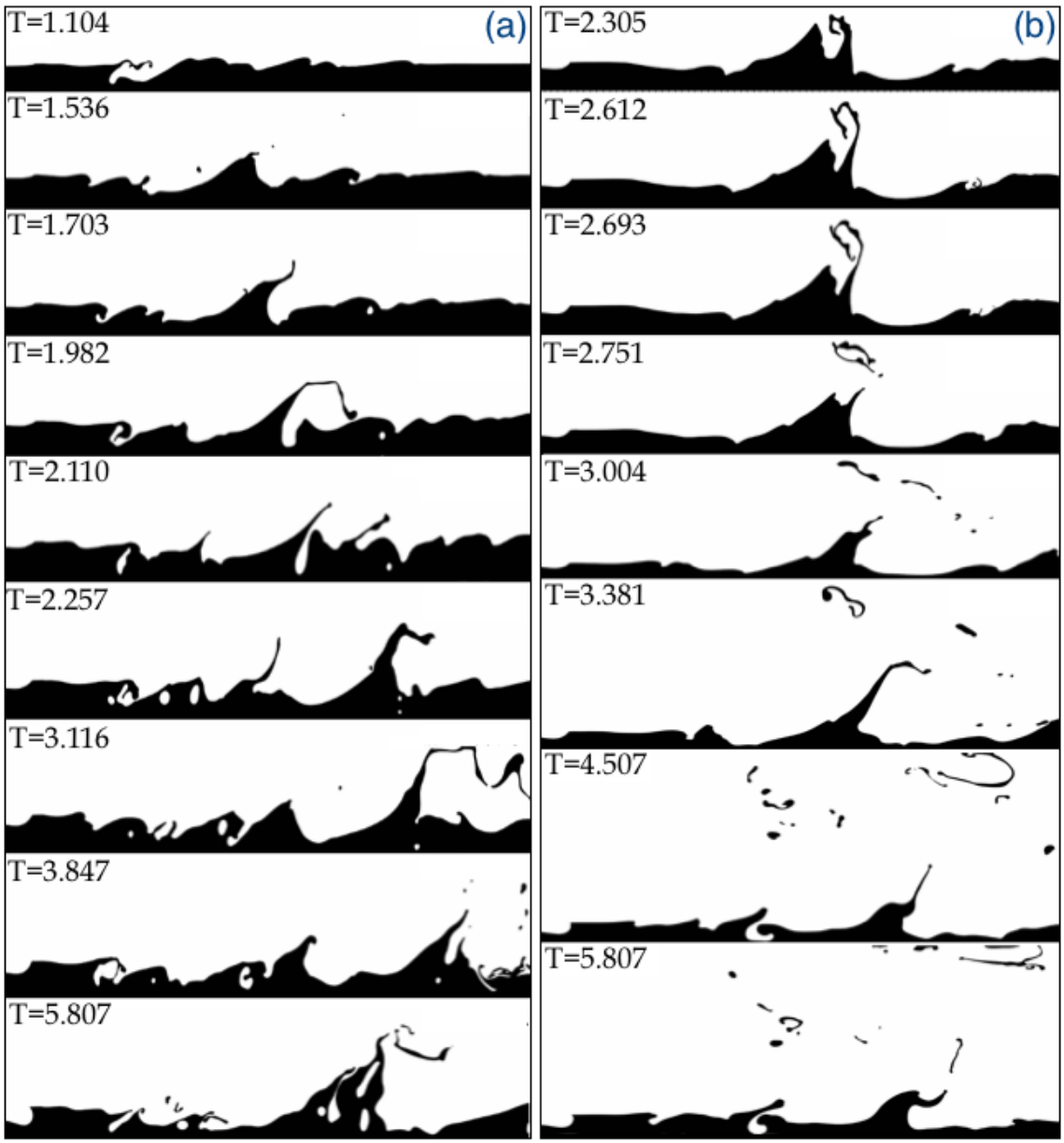

Fig. 5.13: Snapshots of liquid jet break-up for $[M = 16,\ We_G = 20,\ Re_G = 4000]$, in a 1024×512 mesh size for (a) $\delta_G = 0$ and (b) $\delta_G \neq 0$.

At higher gas Reynolds numbers, various sized structures are still present, such as holes, ligaments and drop formation, along with the 'unstable' wave phenomena. For $\delta_G = 0$, numerous wave formations are observed with holes captured within. Here, the unstable wave similarly grows higher than the gas height but forms and breaks much faster. The related 'liquid-empty' area noted earlier, is not observed here. Looking at Jet-2 [132] (i.e. $\delta_G \neq 0$), the liquid core throughout can be defined as 'quasi-laminar' with no presence of holes or surface disturbances. Note, at $Re_G = 4000$, for $\delta_G \neq 0$, less snapshots are shown with respect to the unstable wave phenomena. This is strictly due to the faster growth and break-up of the wave, than for $\delta_G = 0$, which here it grows much higher than the gas height and breaks into multiple ligaments. Within short time the broken ligament moves away from the liquid core and further breaks into various sized droplets and smaller ligaments.

It could be noted, that for higher Reynolds the total break-up process appears less vigorous as a function of a fixed We_G throughout, hinting that possibly a 'quasi-dependent' relationship exists. In addition, for $\delta_G = 0$ the total jet behaviour is highly more unstable, with larger interface instabilities presents than in $\delta_G \neq 0$. Meanwhile as Re_G increases δ_G decreases, resulting into more break-up throughout the jet. Figure 5.14 shows the velocity profile of the 'unstable' wave for $Re_G = 1000$, in both δ_G cases.

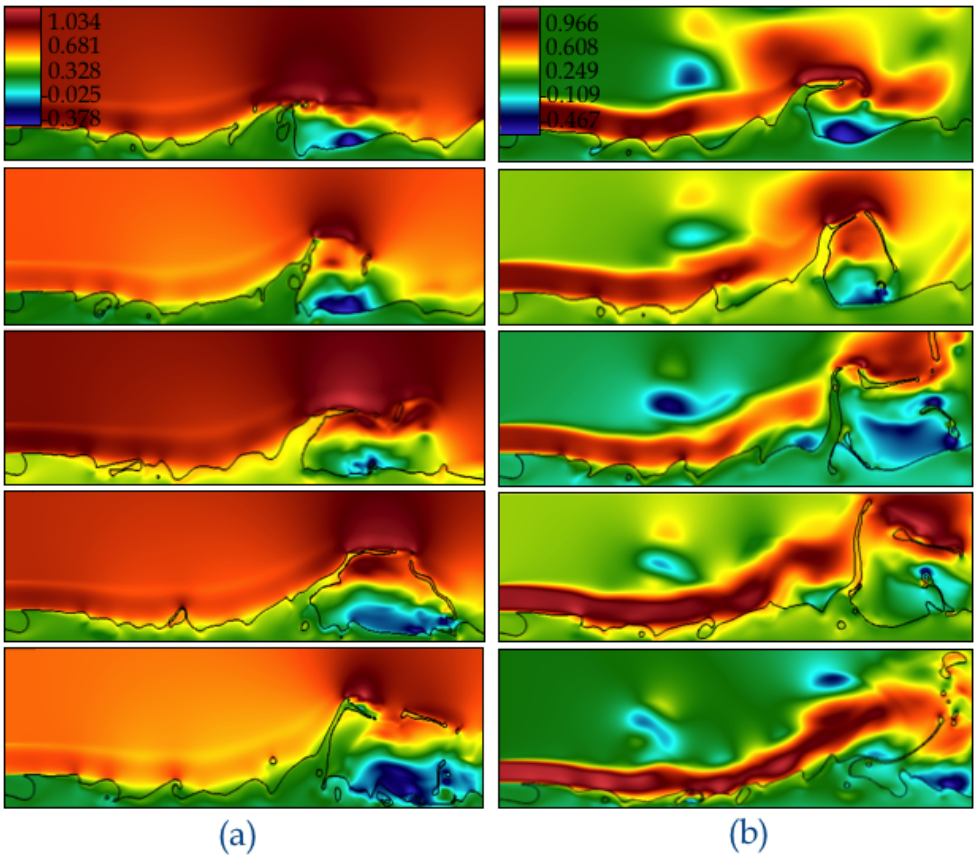

Fig. 5.14: Velocity profile for $[M = 16,\ We_G = 20,\ Re_G = 1000]$, in a 1024×512 mesh size for (a) $\delta_G = 0$ and (b) $\delta_G \neq 0$.

The velocity profiles between the two is rather vast, as expected. In $\delta_G = 0$, the highest velocity component (i.e. gas) is almost equally distributed throughout the non-liquid areas of the domain, whilst $\delta_G \neq 0$, is distributed just above the gas/liquid interface. Here, the velocity at the wave front is positive and under the large liquid-attached ligament is negative for both δ_G cases. Consequently, that almost liquid-empty area forma at the front and the growth of the wave is much higher than the gas height. Adding to that, the gas/liquid velocities employed here, are considerably smaller than in typical industrial jets. However the break-up process recorded in both, is rather excessive, possibly denoting the significance of both the Reynolds and the Weber numbers.

Figures 5.15 and 5.16 show snapshots in the three-dimensional space for $\delta_G = 0$ and $\delta_G \neq 0$, at $[M = 16,\ We_G = 20,\ Re_G = 1000]$. Note, the snapshots are taken at the same T time for comparison purposes. Both δ_G cases show quite similar behaviours at same T, opposingly to the two-dimensional ones (i.e. Figures 5.12-5.13). At early computational flow times, the KH instability is recorded in both, with the 'unstable' wave phenomena developing in a larger scale for $\delta_G = 0$. From there, the RT instability takes over, resulting into large ligaments and droplets of much larger size then the jet inlet, near the front of the 'unstable' waves. Note, in $\delta_G = 0$, more interface perturbations and relative various sized fragments are formed, of larger size.

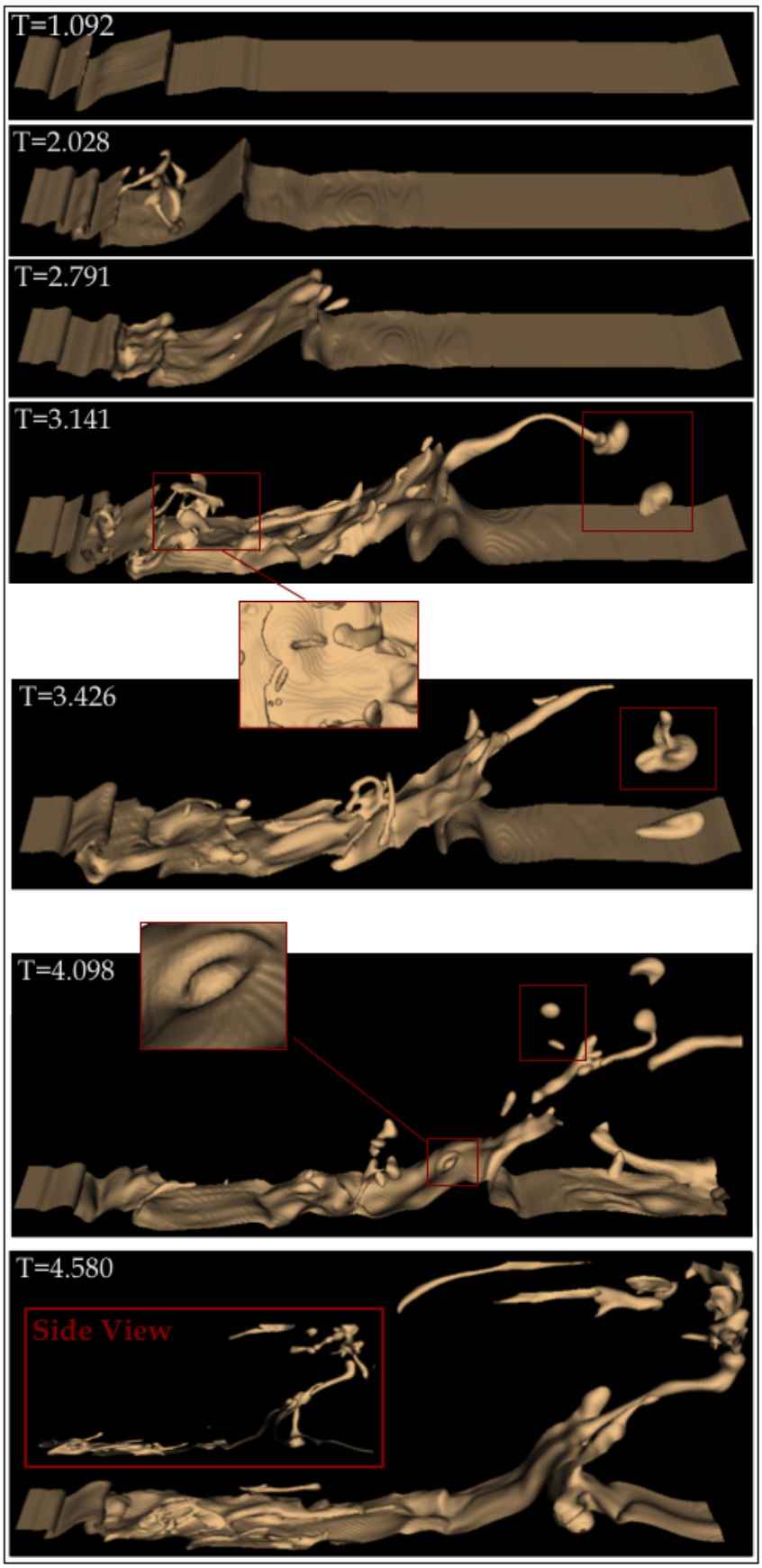

Fig. 5.15: Snapshots of liquid jet break-up in a $512 \times 256 \times 64$ mesh size with $\delta_G = 0$, for $[M = 16,\ We_G = 20,\ Re_G = 1000]$.

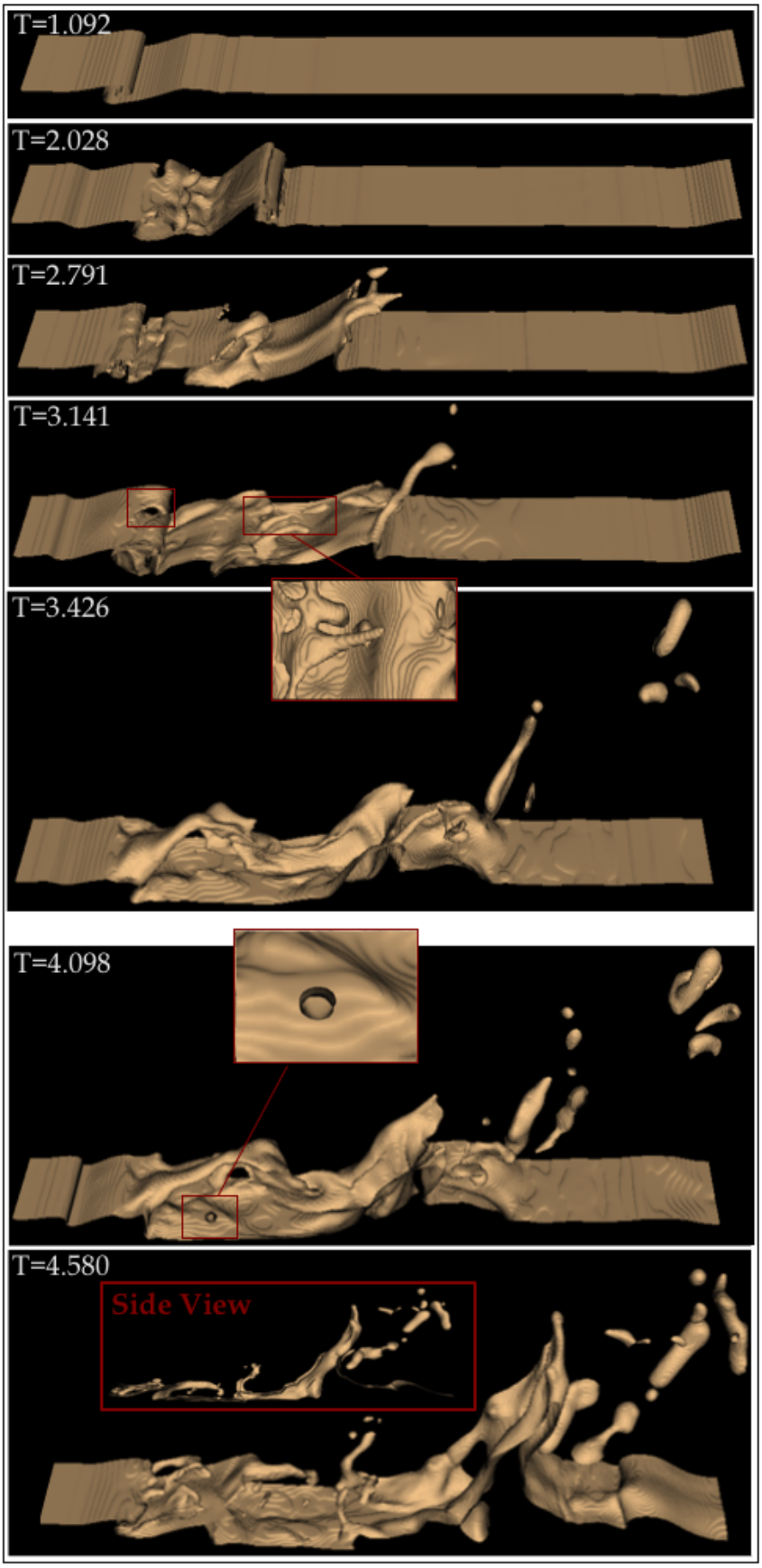

Fig. 5.16: Snapshots of liquid jet break-up in a $512 \times 256 \times 64$ mesh size with $\delta_G \neq 0$, for $[M = 16,\ We_G = 20,\ Re_G = 1000]$.

Figure 5.17 shows the velocity profile snapshots for $M = 4$ at $We_G = 40$, in the two- and three- dimensional space. It appears, that the coarse mesh velocity profile is in fact very similar to the three three-dimensional one, as expected. In both cases, primarily a small Kelvin-Helmholtz instability wave is noted across the interface. However, in the two-dimensional case, the wave shows higher roll up formation. Here, the coaxial gas velocity acts at the top of any interface perturbations present and reaches its maximum value during the KH wave formation and under the RT instability.

Based on the various phenomena observed a more quantitative analysis follows. Note, since the two- and three- dimensional results demonstrate very similar behaviours, the following sections are developed with respect to the two-dimensional framework.

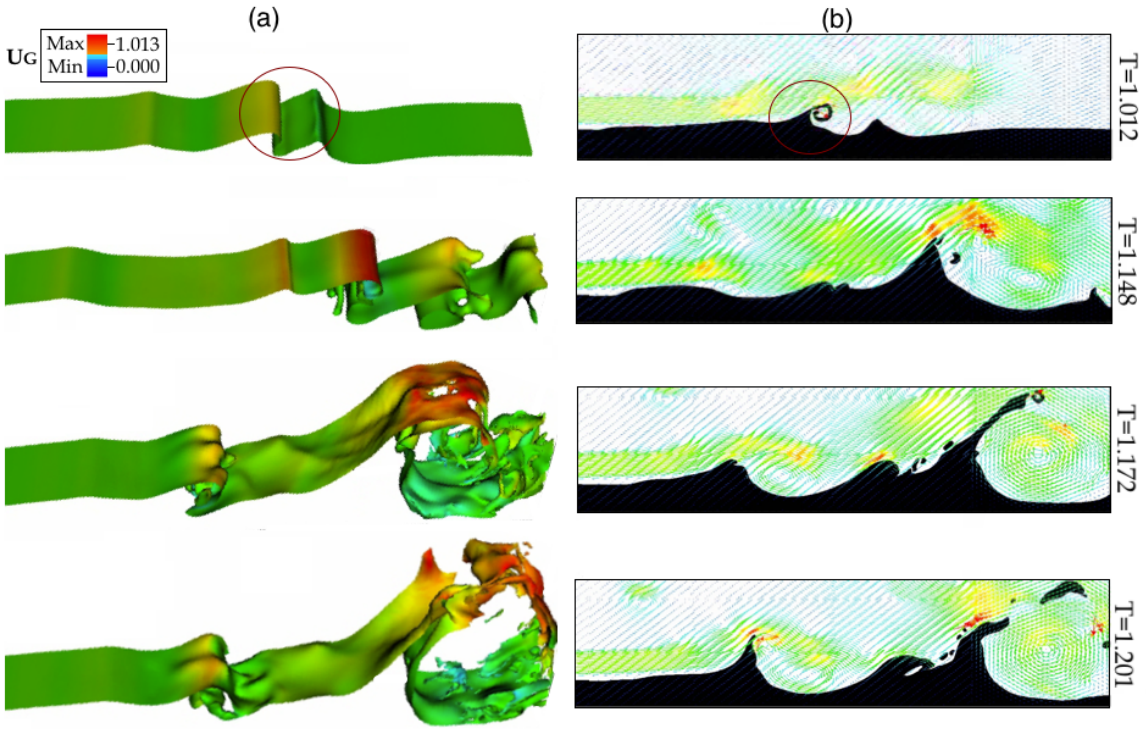

Fig. 5.17: Velocity field for $[M = 4,\ We_G = 40,\ Re_G = 1000]$, for $\delta_G \neq 0$, in (a) three- and (b) two- dimensional space.

5.3.6 Driving Mechanisms in Jet break-up

The previous results showed a range of interface perturbations with various size fragments present. This sections focuses strictly on the jet break-up driving mechanisms, such as the Kelvin-Helmholtz and Rayleigh-Taylor instabilities. Experimental work [73][124] suggests that jet break-up initially occurs from the shear instability, when the boundary layer interacts with the liquid at the nozzle exit, resulting into longitudinal wave formation along the liquid/gas interface [28][124].

This process is analogous to the Kelvin-Helmholtz instability, whose most unstable longitudinal wavelength λ_{KH} is directly linked and 'controlled' by δ_G. The secondary driving break-up mechanism occurs from the acceleration of the longitudinal waves by the gas stream, resulting into wave crests that give rise to the Rayleigh-Taylor instability [1][28]. The RT instability essentially controls the growth of any present ligaments and its break-up into droplets. Fig. 5.18 shows the principle growth mechanism of KH and RT instabilities. It should be noted that λ_{KH} is always larger than λ_{RT}.

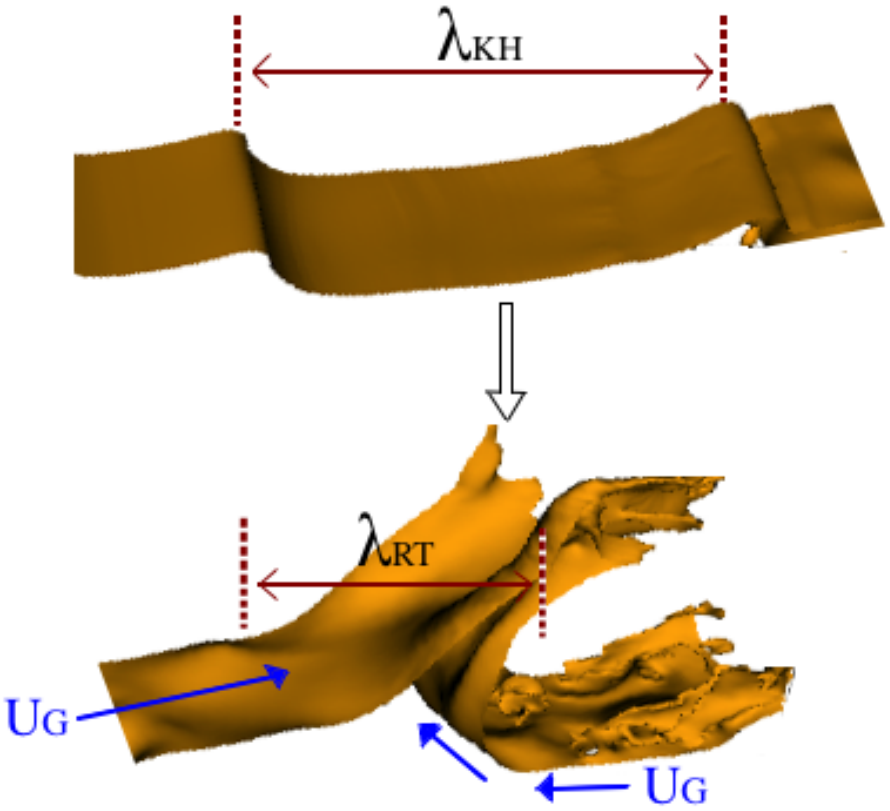

Fig. 5.18: Principle schematic of Kelvin-Helmholtz and Rayleigh-Taylor instabilities in liquid jet primary break-up mechanisms in three-dimensional space.

In cases of large Weber numbers, Villermaux et al. [124] suggested that the most unstable wavelength can be estimated with:

$$\lambda_{KH} \approx C_{KH}\sqrt{\left(\frac{\rho_L}{\rho_G}\right)}\delta_G \tag{5.2}$$

where $C_{KH} = 2$, in coaxial air-blast atomizers, [124]. Meanwhile, the largest Rayleigh-Taylor instability wavelength can be computed [28] as:

$$\lambda_{RT} = 2\pi\sqrt{\frac{3\sigma}{\rho_L \alpha_L}} \tag{5.3}$$

with α_L denoting the liquid acceleration, which from the literature [31][73], can be estimated using:

$$\alpha = \frac{1}{2}\frac{C_D \rho_G (U_G - U_c)^2}{\rho_L h_L} \tag{5.4}$$

where h_L is the liquid inlet height and C_D is a constant denoted as $C_D = 2$ in Marmottant et al. [73]. The U_c parameter accounts for the interface convection velocity, originally proposed by Dimotakis et al. [31] as:

$$U_c = \frac{\sqrt{\rho_G}U_G + \sqrt{\rho_L}U_L}{\sqrt{\rho_G} + \sqrt{\rho_L}} \tag{5.5}$$

Previous results showed the KH instability is the driving mechanisms of the 'unstable' wave phenomena, which by the end of the simulations takes the form of the RT instability. As KH is δ_G dependent, it could be suggested that the 'unstable' wave is 'quasi-dependent' on δ_G and thus Re_G. Small Reynolds suggest that the jet break-up process is viscous dominated, resulting in large fragments and droplet formation. At slightly larger Re, jet oscillations are expected as a function of the jet axis, leading to some jet disintegration under the aerodynamic forces.

In Figures 5.12 and 5.13, as Re increases, the KH-RT instabilities behaviour varies, with the 'unstable' wave phenomena showing relatively distinct behaviours at different Re. Figure 5.19 shows the computational growth rate ω_{RT} as a function of T, for varying δ_G and Re_G. The ω_{RT} values, were manually obtained from the jet snapshots and are shown in the two-dimensional space. Each ω_{RT} 'data-point' is approximately estimated with $\sim (\lambda_2 - \lambda_1/t_2 - t_1)$. In Fig. 5.19, the time axes are employed to show at which instant the 'unstable' wave occurs, during the simulations. Here, λ_0 and λ_{RT} points, denote the wavelengths at first occurrence and at maximum deformation, respectively, prior to any break-up into ligaments/droplets.

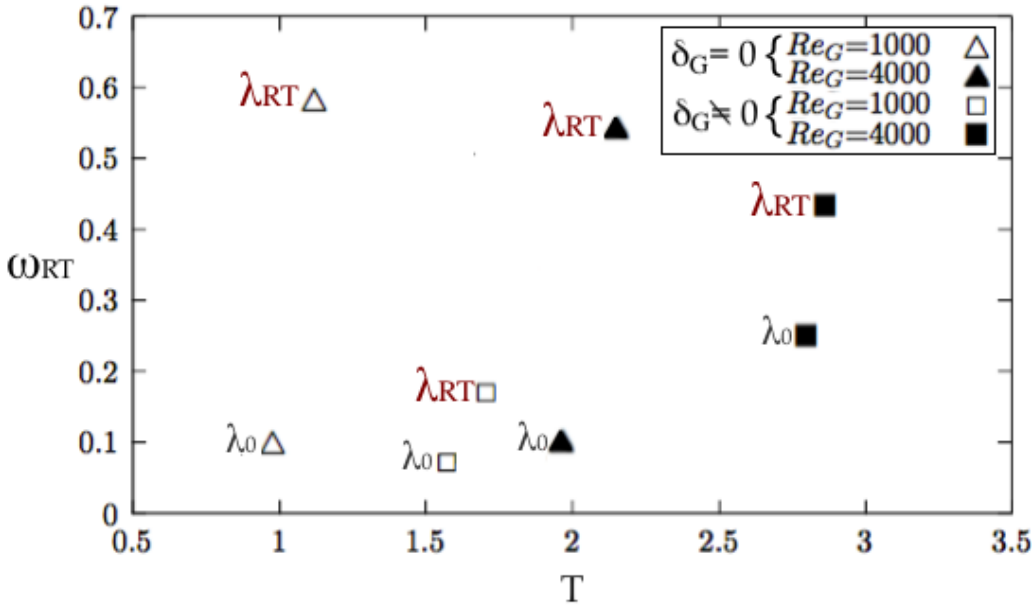

Fig. 5.19: Computational Rayleigh-Taylor wavelength growth rate as a function of T and δ_G, in the two-dimensional framework. Here λ_0 denotes the initial wavelength when it first occurs and λ_{RT} is the largest computational wavelength reached before it breaks into smaller scaled fragments.

Comparing ω_{RT} for different δ_G, the 'unstable' wave grows for a longer period of time in $\delta_G = 0$, regardless of Re_G. The λ_{RT} is also much larger in $\delta_G = 0$ than in $\delta_G \neq 0$. This suggests that the boundary layer presence both significantly delays the formation of the 'unstable' wave phenomena and reduces its growth rate. Here, we also employed Eqn. (5.3) to compute the equivalent theoretical largest wavelength in each case. The theoretical values for $Re_G = 1000$ and $Re_G = 4000$, denoted $\lambda_{RT} = 0.004$ and $\lambda_{RT} = 0.05$, respectively. In both cases, the theoretical λ_{RT}, are significantly smaller than the computational ones. This is somewhat expected, as Eqn. (5.18) is strictly proposed for coaxial round jets, whilst here a quasi-planar set up is used.

Previous experimental work in Raynal et al. [95] and Marmottant et al. [74], suggested the wavelength frequency f, can be derived from Dimotakis velocity expression, Eqn. (5.5). They showed that f is comparable to the velocity where the liquid/gas dynamic pressures are balanced, thus $f \sim U_c\lambda$. However, for high M ratios of ≥ 4, the the frequency scaling becomes of $f \sim \sqrt{\rho_G/\rho_L}U_G\lambda$, [23][74][95]. Figure 5.20 shows the frequency $f \sim \sqrt{\rho_G/\rho_L}U_G\lambda$ as a function of the separating plate to the gas boundary layer thickness ratio, e/δ_G. The results are shown for $M = 16$ at $We_G = 20$, for both $\delta_G = 0$ and $\delta_G \neq 0$. Here λ accounts for the wavelength at the first instant of the unstable wave formation (i.e. λ_0).

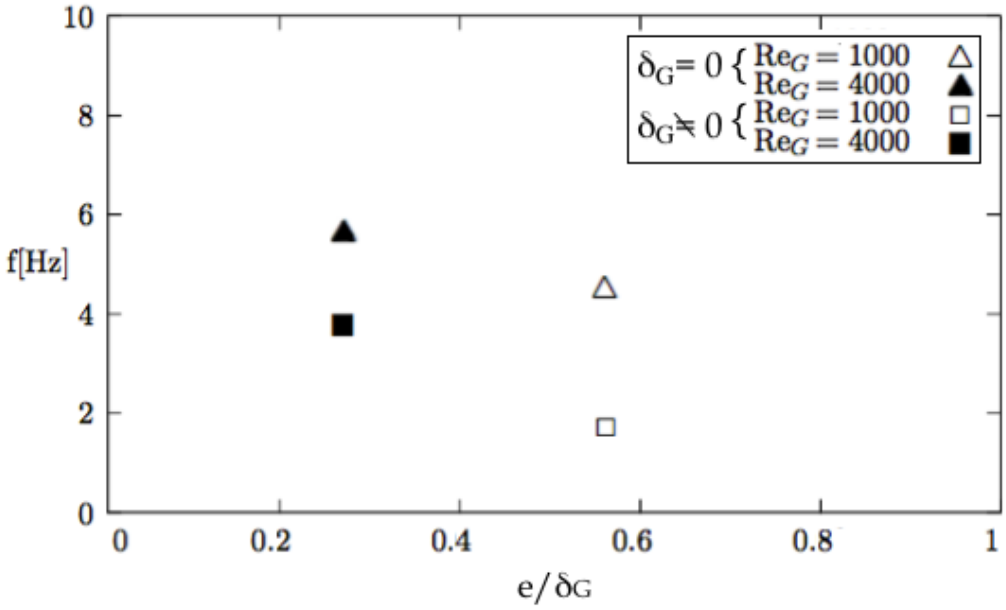

Fig. 5.20: Computational frequency as a function of e/δ_G ratio for $M = 16$ at $We_G = 20$, for $\delta_G = 0$ and $\delta_G \neq 0$.

Figure 5.20 shows that for $\delta_G = 0$ the unstable wave frequency increases, validating the earlier results where $\delta_G \neq 0$ limits the wave presence and growth. It is also noted that the frequency decreases as e/δ_G ratio increases. This behaviour was previously denoted in Zaleski et al. [23]. It is proposed that an e/δ_G ratio larger than the threshold value ~ 1, significantly influences the frequency. Provided δ_G is of the order of e thickness, the most unstable f is strongly characterised by the flow [94].

As previously introduced, the gas/liquid velocity difference across the interface results in the KH wave formation which propagates downstream. Zaleski et al. [132] suggested that as the interfacial KH wave develops more, the curvature radius decreases, resulting to liquid sheet formation. It is considered, that liquid sheets form post the KH wave and prior to the RT instability, with transverse instabilities developing at the liquid sheet edge. Thus it could be characterised as an in-between 'wave' from KH to RT, Fig. 5.22; that defines the RT instability growth behaviour and in turn the jet break-up process.

In such cases and provided the liquid viscosity effects are small (i.e. almost negligible), the Ohnesorge number is employed [126], whose characteristic length is the liquid sheet thickness ℓ_s. With time this liquid sheet stretches under the gas stream effect and ℓ_s decreases. A capillary time scale of the liquid sheet growth can be defined as:

$$\tau_{ca} = \sqrt{\frac{\rho_L \ell_s^3}{\sigma}} \tag{5.6}$$

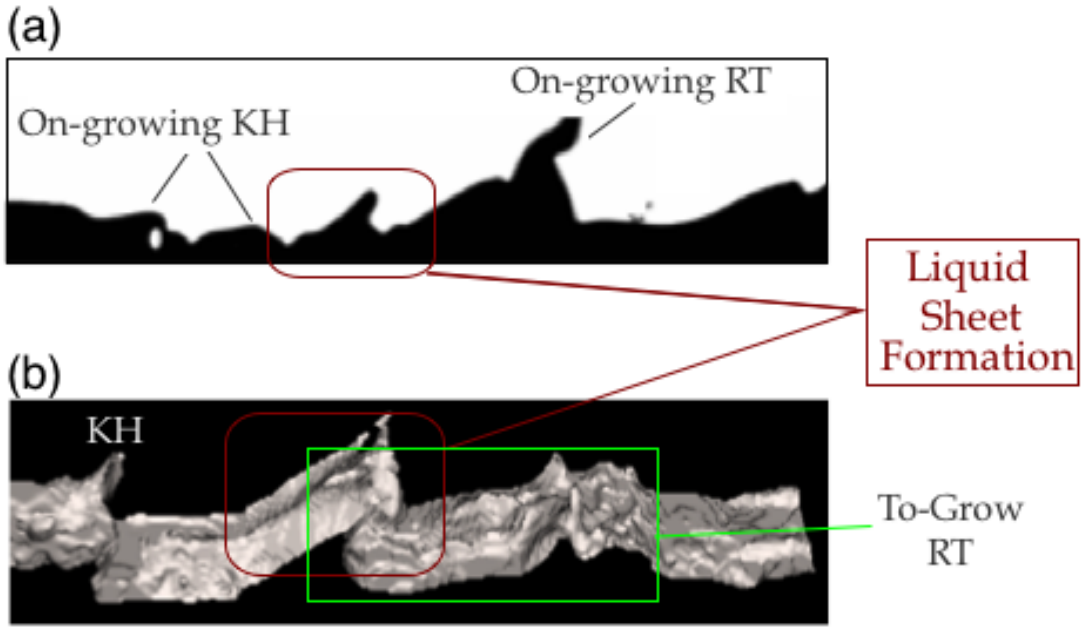

Fig. 5.21: Liquid sheet formation in (a) two-dimensional and (b) three-dimensional space, post KH and prior to RT driven instabilities.

Here, Eqn. (5.6) could be defined as a growth measurement of these liquid sheets, however, is usually employed in capillary driven jet break-up processes. Literature suggests [36][126], that these liquid sheet instabilities are less noted at higher We, whose wavelength is independent of the density and velocity of the liquid [36]. Figure 5.22 shows the τ_{ca} behaviour as a function of We_G and Oh, for all M ratios with $\delta_G = 0$, where ℓ_s was manually estimated from the jet snapshots.

Here τ_{ca} shows to exponentially decay with increasing We_G, validating that such instabilities are reduced at larger We. However, τ_{ca} linearly increases with Oh, independently of M. Although the Oh values are relatively small, they are finite. This hints that the liquid motion is affected by the viscosity, opposing to the literature suggesting that these liquid sheets form at almost negligible viscosity [36][126]. Thus it can be proposed that an $Oh - We_G$ correlation exists for the liquid sheets formation, with Oh being inversely proportional to We_G.

Such analysis is typical of high surface tension driven break-up cases, such as oils burners and ink-jet printing. However, based on the latter discussion, it could be of some significance even in typical industrial injectors (i.e. GT and IC engines).

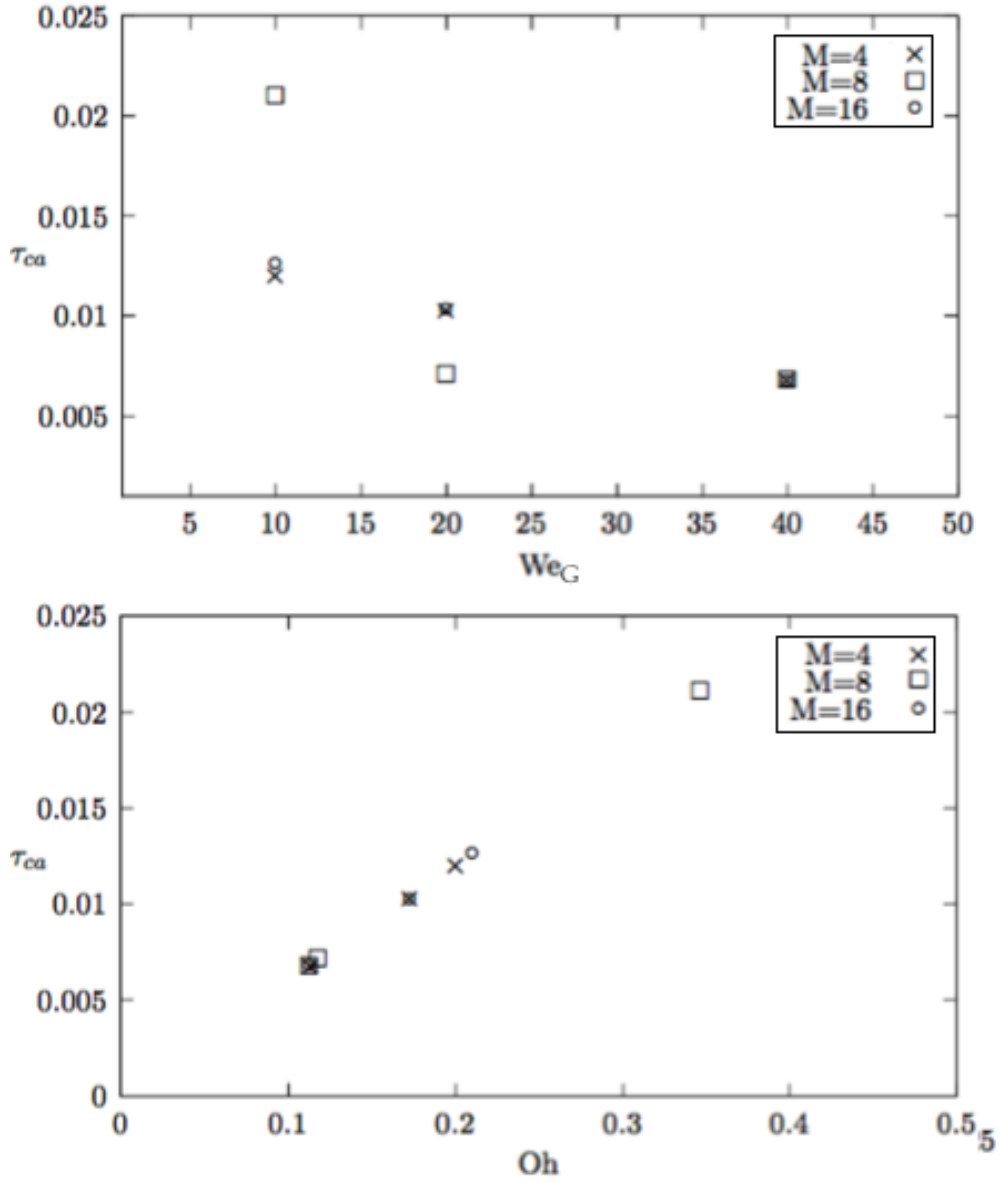

Fig. 5.22: Plots showing the capillary time scale τ_{ca} with We_G (top) and Oh (bottom), at different M ratios, for $\delta_G = 0$.

5.3.7 Surface Density Evolution

In this section we study the surface density evolution at a range of $M - We_G$ as a function of time T. Figure 5.23 shows the Σ evolution in all coarse jets at $Re_G = 1000$ for $\delta_G = 0$. Note, in this section the Σ evolution is examined strictly as a function of time, opposingly to most studies that show the spatial surface density variations. Doing so, Σ remains just a quantity measurement enabling observations of the total jet behaviours as a function of other parameters, such as We, Re and δ_G.

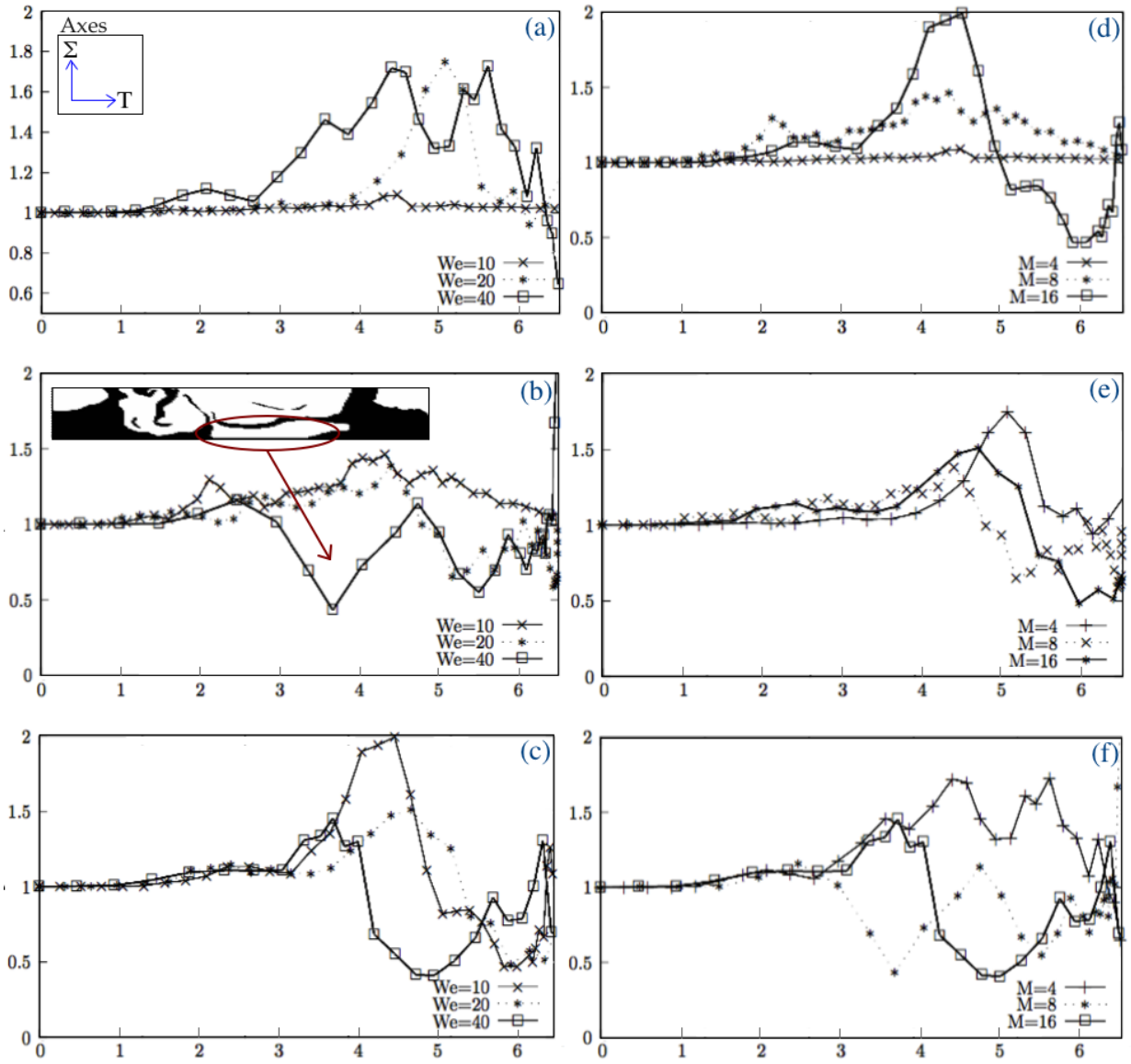

Fig. 5.23: Surface density evolution for different $M - We_G$ combinations with time T, at (a) $M = 4$, (b) $M = 8$, (c) $M = 16$, (d) $We_G = 10$, (e) $We_G = 20$ and (f) $We_G = 40$.

For $M = 4$, Σ increases with We_G, showing a more constant behaviour at lower We_G and large peaks at higher We_G. Stronger break-up is shown for $M = 8$ with Σ evolving in a less stable manner, independent of We_G. At $We_G = 40$, a higher peak is recorded at the end of the simulation, suggesting further break-up is following. Meanwhile, for $M = 16$ all jets show a rather unstable Σ evolution of similar manner, defined by an early peak followed by a large decrease. With respect to the fixed We_G cases and varying M, as We_G increases, the surface density peaks become more often and at earlier times, denoting the amount of instabilities and fragments present is increased. Lower $M - We_G$ combinations show a more settle growth, such as $M = 4$, $We_G = 10$ that reach equilibrium early. In Fig. 5.23, most cases show a 'negative' Σ behaviour (i.e. $\Sigma < \Sigma_{max} = 1$), possibly liable to the recurring 'liquid-empty' areas. A sample snapshot of a 'liquid-empty' case is shown for validation purposes, at $M = 8, We_G = 40$.

Figure 5.24 shows the surface density evolution for $\delta_G = 0$ and $\delta_G \neq 0$, with increasing Re_G, along with the fit of $\Sigma(t)$ from Eqn. (4.17). Here, the dots represent the initiation time of the 'unstable' wave growth. The dark red dots denote the absence of δ_G, where b_1 and b_2 imply that the phenomena was captured twice during the break-up process. The green dots denote the initiation time for $\delta_G \neq 0$. Note, the a-dots are for $Re_G = 1000$ and b-dots are for $Re_G = 4000$. For $Re_G = 1000$ both set ups show that the unstable wave grows later in time throughout the break-up, in comparison with $Re_G = 4000$. For $\delta_G = 0$ the break-up begins at earlier times than it does for $\delta_G \neq 0$, regardless of the δ_G thickness. All four cases show a short initial transient growth followed by increasing peaks, as the break-up process develops. The $\delta_G = 0$ case, does demonstrate a slightly more stable growth for both Reynolds parameters. It should be noted, that for $\delta_G \neq 0$ at $Re_G = 4000$, the surface density eventually grows the most from all four cases, hinting that for quasi-planar set ups, δ_G does in fact affect the break-up process.

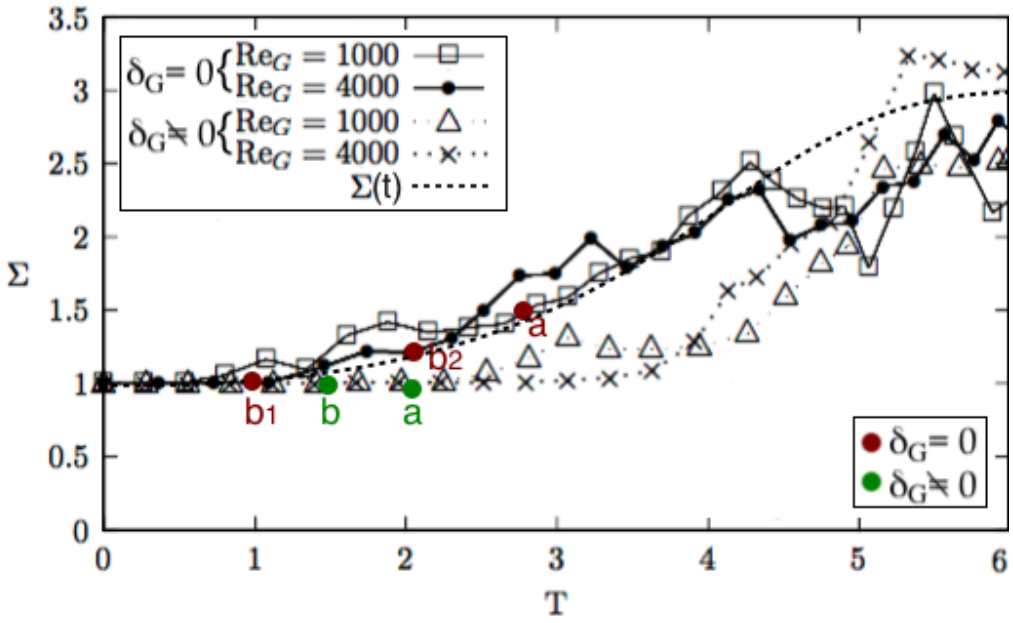

Fig. 5.24: Surface density evolution in a 1024×512 mesh, with $M = 16$ at [$Re_G = 1000,\ 4000$]; for $\delta_G = 0$ and $\delta_G \neq 0$. The dots represent the 'unstable' wave initial growth/occurance time. The fit line $\Sigma(t)$ comes from Eqn. (4.17).

Figure 5.25, shows a non typical correlation, between the break-up initiation time for each jet along with the maximum surface density Σ_{max} at the end of the break-up process. It could be suggested that the presence of δ_G, somewhat delays the break-up process, however it gives rise in Σ_{max}.

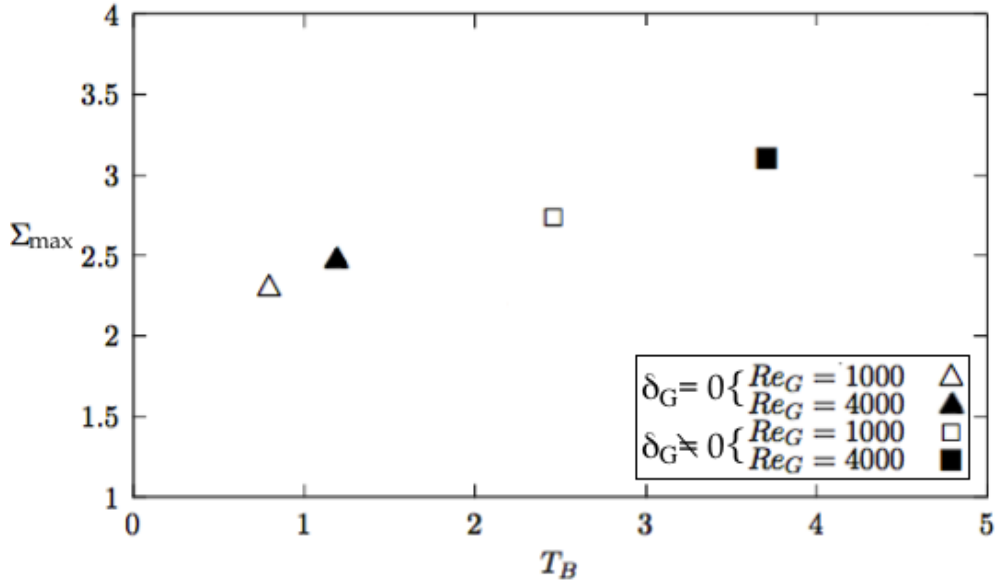

Fig. 5.25: Surface density equilibrium (Σ_{max}) as a function of the jet break-up initiation time T_B, in a 1024×512 mesh, at [$M = 16,\ Re_G = 1000, 4000$].

The $\Sigma(t)$ from Eqn. (4.17) shows a good fit with the present data, denoting a transient growth followed by an increase as it reaches a maximum plateau. In comparison with the liquid droplet break-up, Section 4.3.4, here Σ is considerably more consistent and $\Sigma(t)$ fits the data well. However, with time an equilibrium behaviour should be observed in the present jets, assumed as the short plateau region at the highest Σ of each (i.e. $\Sigma_{eq} = \Sigma_{max}$, Fig. 5.25). Also, the data in Fig. 5.24, was for a fixed We of varying Re, whereas in the droplets it was the opposite. It could be concluded that $\Sigma(t)$ from Eqn. (4.17) fits better jet-like processes rather than single droplet break-up cases, with τ strictly denoting a characteristic growth time scale.

5.4 Summary

The present section investigated the liquid jet break-up process in the primary region, for a quasi-planar jet, both in the two- and three-dimensional space. To ensure all scales are resolved, the $We^G_{\Delta x}$ criteria was used. Two velocity profiles were applied, of a piecewise linear profile (i.e. $\delta_G = 0$) and one that mimics the liquid/gas boundary layer thickness (i.e. $\delta_G \neq 0$). The study was developed as a function of the Dynamic Pressure ratio and the gas Weber numbers. It was concluded that any jet break-up occurs strictly for $M \neq 1$, whilst for $8 < M < 16$ and $10 < We_G < 40$ a critical M and We_G exist, respectively, where break occurs. The latter was concluded strictly on the present results, however previous studies have noted similar behaviours.

Two driving mechanisms were captured and analysed, the Kelvin-Helmholtz and the Rayleigh-Taylor instabilities. Here,the effective parameters proved to be the boundary layer and the gas Weber number. During the break-up process, a key phenomena was recorded, the 'unstable' wave resulting from the KH instability which then grows higher than the gas inlet height. In many cases, a 'liquid-empty' areas was captured that formed at the front of the 'unstable' wave. The presence of the gas boundary layer (i.e. $\delta_G \neq 0$), showed to both reduce and delay the formation of the 'unstable' wave.

Another interface perturbation captured was the liquid sheet, that forms post the KH and prior to the RT instabilities. The capillary time scale τ_{ca}, denoting the growth of these sheets, showed to exponentially decay as We_G increased, suggesting that the liquid sheets are overpowered at higher Weber numbers. However, τ_{ca} linearly increased with Oh, denoting that liquid sheet formation is in fact influenced by the viscosity, although the latter is considered almost negligible in such cases. In all cases τ_{ca} showed to be independent of the M ratio.

The surface density evolution was examined for both $\delta_G = 0$ and $\delta_G \neq 0$. For $\delta_G = 0$, the surface density was slightly higher than for $\delta_G \neq 0$. Here, Σ was able to capture the equivalent 'liquid-empty' areas due to the 'unstable' wave phenomena, by reaching values < 1. The jet Σ was considerably more consistent with time, in comparison to the droplet break-up case. This is of particular interest, as the liquid/gas velocities here, were in fact much smaller than the ones in the droplets. Consequently, from the present investigations, it could be proposed that Σ is 'quasi-dependent' on $U_L - U_G$, but 'quasi-independent' of Re, hence of δ_G and We.

Chapter 6

Conclusions and Future Work

6.1 Major Remarks

In GT and IC engines, liquid droplet and jet break-up processes of spray atomizers can significantly affect the performance of such systems and in return the environmental pollution. The focus of this work is to study and understand such processes with the aid of CFD tools. A novel two-phase flow applicable method, the CMLS method, was developed and extensively validated both in single liquid droplet break-up and in the primary break-up of liquid jets. The relative working procedures were acquired as follow:

- **DNS Modelling**
  Due to the complexities in representing multiphase fluid flows, a modelling method of both accurate and good mass conservation properties is required. Here, two previous available methods were considered, the Volume of Fluid and the Level Set method. Based on the capabilities and drawbacks, an in-house novel conservative Level Set (CMLS) method was developed. This CMLS overcame some of the limitations previously found in VOF and LS, by denoting sharp and accurate solutions of minimal mass loss.

  The novelty in the present interface modelling approach was based on the LS-VOF coupling, that was strictly processed only when necessary according to the current mass properties. The interface reconstruction was developed with particular attention, since the LS was directly linked to the area computation. The CMLS solutions were mass accurate, even in very coarse meshes, (i.e. droplets of $R/\Delta \leq 4$), with mass errors limited to 0.1% and for $R/\Delta > 8$ errors were dropped down to 10^{-2}, consistently.

  High order accuracy and sharp interfaces were obtained using 5^{th} WENO and the GFM method, respectively. Doing so, numerical oscillations in the presence of discontinuous solutions were overcome. Due to the stencil points using 5^{th} WENO, the convergence rate of the curvature computations was limited. To capture both the viscous and capillary effects along with the smallest scales size present (i.e. $We < 1$ and $Re \leq 2$ in a local cell), some limitations are imposed in choosing the appropriate time steps and mesh size. However, all integrated flow scales considered in this work, were well resolved both in the two- and three-dimensional space.

The CMLS method obtained sharp interfaces due to the presence of LS. In the LES context, the mesh size essentially defines the resolved scales size, whilst in DNS, restrictions on the Reynolds number occur for a fixed mesh size. Thus, perovided the interfaces are well defined to account for the $Re \leq 2$ restrictions, the CMLS method could be extended in the LES framework. However, the We limitations would still be an issue and the smallest size captured would be limited to $20\mu m$.

- **Droplet Break-Up:**
  Liquid droplet break-up processes were investigated under the Weber number effects, both in the two- and three-dimensional space. A range of break-up modes were recorded, that in cases were in disagreement with the available literature. It was concluded that the droplet liquid viscosity significantly affects the critical Weber number (We_{cr}), which in turn distinguishes between the different deformation and break-up modes.

  As in previous studies, the present break-up modes at We_{cr}, remained inconclusive. In cases, the break-up modes captured were not of the same We range typically suggested in the literature. In particular, at $We = 22$, results were inconsistent both in the qualitative and quantitative context. Also, the three-dimensional results of $We = 96$, showed a break-up behaviour that is typically registered at much higher We.

  Based on the present results an independent relationship was noted between the We and Oh numbers, for $Oh < 10^{-1}$ that was also confirmed in previous studies. However final conclusions on the the drop deformation/break-up modes as a function of $We - Oh$ are still under investigation. It was also concluded that the liquid/gas interactions in the droplets are a function of Re, by following Stoke's Law. Note, this is valid by definition strictly for low Reynolds numbers, such as in this work.

  The droplets break-up initiation time was strictly related to the drop maximum cross-stream dimension, prior to any break-up. It also showed to increase with Oh, which is expected by definition. On the contrary, the times of complete break-up showed to increase with We. Such behaviour opposes the theory that at higher We surface tension becomes negligible and break-up should occur faster. Current studies work on high We numbers by focusing more on catastrophic break-up cases.

- **Jet Break-Up:**
  Planar liquid jet break-up processes were studied based on the dynamic pressure ratio M and the gas We numbers, both in the two- and three-dimensional space. All various sized scales involved were resolved by employing mesh sizes that satisfy the $We_{\Delta x}$ criteria. The focus was mainly on Air-Blast assisted jets (i.e. $M > 1$), not typically found in the literature.

  It was concluded that any break-up/atomisation occurs for $M << 1$ and $M > 1$, with $M \approx 1$ showing light 'atomizing' behaviours. From all $M - We_G$ combinations employed, it was concluded that break up occurs for a critical M and We_G, in the ranges of $8 < M < 16$ and $10 < We_G < 40$, respectively.

Based on that, a relative $M - We_G$ break-up correlation map was proposed and was in good agreement with some previous studies, where relative relationships were examined. The gas boundary layer effects where examined. In any case, a range of fragments and instabilities were captured. A key phenomena observed was the 'unstable' wave, resulting from the KH instability, which under the RT instability grew higher than the gas inlet, with time. The gas boundary layer presence (i.e. $\delta_G \neq 0$), showed to both reduce and delay the 'unstable' wave phenomena, but not remove it completely.

Increasing the gas Reynolds number showed no significant effects on the growth rate (ω_{RT}) of the 'unstable' wave, suggesting a 'quasi-independent' relationship exists between the Re considered here and ω_{RT}. Finally, the 'unstable' wave frequency appeared to decrease as the δ_G/e ratio increased. Liquid sheet formation was also captured, post the KH instability and prior to the RT growth. A capillary time scale τ_{ca}, characterising the growth of these sheets, decayed exponentially with increasing gas Weber, as it was overpowered at higher We values.

However, τ_{ca} linearly increased with the Ohneshorge number, suggesting that the liquid viscosity is an influential parameter in the liquid sheet formation, opposingly to the theory (i.e. almost negligible viscosity). This was of particular interest, as such approach is commonly found in high surface tension driven break-up processes, (i.e. oil burners). However, it could be applicable, to some extend, in industrial injectors.

- **Surface Density:**
  The surface density evolution was investigated, both in the droplet and jet break up processes. The $\Sigma - Y$ model was employed, from which a $\Sigma(t)$ expression was extracted and fitted in both two-phase flow processes. Assuming homogeneous flow, the actual $\Sigma(t)$ behaviour was characterised by an initial constant behaviour, followed by a transient growth before it reached a peak/plateau.

  In the droplet break-up cases, the total Σ behaviour was relatively inconsistent amongst the various We choices. Meanwhile, $\Sigma(t)$ fitted the data until Σ_{max} was reached, but showed to be invalid for times after complete break-up, where the flow was non-homogeneous. It was there suggested, that the characteristic time scale (τ) is strictly denotes the Σ growth and after Σ_{max}, τ scales with dU/dy. The present results showed that Σ is 'quasi-independent' on We.

  In the jet break-up cases, Σ was slightly higher in $\delta_G = 0$ than in $\delta_G \neq 0$. However, for all jet-cases simulated, Σ showed similar behaviours as a function of time, opposingly to the droplets case. Such behaviour raised some questions with respect to the liquid/gas velocities applied in both processes. As the jet velocities were much smaller than the droplet ones, it was proposed that Σ could be 'quasi-dependent' on $U_L - U_G$. Similarly to the droplets case, in this work Σ is 'quasi-independent' of both Re and We.

6.2 Future Work

- The CMLS curvature computations using the implicit function with the LS, overcomes some of the convergence rate limitations and large spurious velocities present. However, due to the stencil points integrated in the 5^{th} WENO method and in cases where interfaces are near the domain boundaries, generates poor results. A different approach could be to alternate between curvature computational approaches, available in the literature [130][134], according to current needs.

- In the present LS, integrated in the CMLS method, the use of a numerically smeared sign function during reinitialisation provides accurate distance profile reconstruction, however creates CFL limitations. The hyperbolic tangent function in [75][84] should be examined.

- The present droplet deformation/break-up investigations, were within critical Weber numbers, whilst most studies in the literature operate within comparable We values, amongst each other. A good approach would be to employ 'new' We, both away from critical ones and under gas velocities typically found in industrial jet applications. Another suggestion would be the study of more than one droplets within the same domain, of different initial size with each other, also typical of jets.

- The liquid jet break-up processes were developed in a quasi-planar framework, opposingly to typical industrial cylindrical jets. However, studies have shown that such set ups provide fundamental answers to any remaining questions, thus more relative investigations should be developed. Also, any available quantitative analysis models, must be further validated and accordingly extended in quasi-planar applications. Further investigations should be carried out with respect to the driving mechanisms in jet morphologies, such as the RT and KH instabilities. Existent relationships partially fail to account for other possible effective parameters involved.

- In view of the current $\Sigma - Y$ models available in the literature, more work is required. Particularly in the droplet break-up processes that are directly linked and affect the potential jet break-up behaviour, new closures in the source terms must be examined for non-homogeneous break-up processes.

Bibliography

[1] A. Cartellier A. Delon, J.P. Matas. Flapping instability of a liquid jet. In *8th International Conference on Multiphase Flow*, 2013.

[2] K.Y. Lervag A. Ervik and S.T. Munkejord. A robust method for calculating interface curvature and normal vectors using an extracted local level set. *J. Phys. Fluids*, 2014.

[3] S. Osher A. Harten, B. Engquist and S. Chakravarthy. Uniformly high-order accurate essentially non-oscillatory schemes iii. *J. Comp. Phys.*, 71:231–303, 1987.

[4] A. Burluka A. Vallet and R. Borghi. Development of an eulerian model for the atomization of a liquid jet. *Atom. and Sprays*, 11:619–642, 2001.

[5] D. Adalsteinsson and J.A. Sethian. A fast level set method for propagating interfaces. *J. Comp. Phys.*, 118:269–277, 1995.

[6] D. Adalsteinsson and J.A. Sethian. The fast construction of extension velocities in level set methods. *J. Comp. Phys.*, 148:222, 1999.

[7] M.J. Andrews and P. O'Rourke. The multiphase particle-in-cell (mp-pic) method for dense particle flow. *Int. J. Mult. Flow*, 22:379–402, 1996.

[8] T. Menard B. Duret, J. Reveillon and F.X. Demoulin. Improving primary atomization modeeling through dns of two-phase flows. *Int. J. Mult. Flow*, 55:130–137, 2013.

[9] G.K. Batchelor. *An Introduction to Fluid Dynamics.* Cambridge University Press, 2000.

[10] J.C. Beale and R.D. Reitz. Modelling spray atomisation with the kelvin-helmholtz/ rayleigh-taylor hybdrid model. *Atom. and Sprays*, 1999.

[11] P.B. Bochev. Analysis of least-squares finite element methods for the navier-stokes equations. *SIAM J. Numer. Anal.*, 34:1817 – 1844, 2006.

[12] J.P. Boris and D.L. Book. Flux-corrected transport iii: Minimal error fct methods. *J. Comp. Phys.*, 20:397–431, 1976.

[13] C.E. Brennen. *Fundamentals of Multiphase Flows.* Cambridge University Press, 2005.

[14] R.S. Brodkey. The phenomena of fluid motions. Addison Wesley, Reading, MA, 1969.

[15] X. Margot S. Patouna A. Cessou C. Hespel, J.B. Blaisot and B. Leordier. Influence of nozzle geomtry on spray shapre, particle size, spray velocity and ait entrainment of high pressure diesel spray. Conference on Thermo- and Fluid Dynamic Processes in Diesel Engines, 2010.

[16] S. Chen and G. Doolen. Lattice boltzmann model for fluid dynamics. *Annu. Rev. Fluid Mech. 3*, 30:329364, 1998.

[17] V. Le Chenadec and H. Pitsch. A monotonicity preserving conservative sharp interface flow solver for high density ratio two-phase flows. *J. Comp. Phys.*, 249:185–203, 2013.

[18] V.L. Chenadec. *A stable and conservative framework for detailed numerical simulation of primary atomization.* PhD thesis, Stanford University, 2012.

[19] W.H. Chou and G.M. Faeth. Temporal properties of secondary drop breakup in the bag breakup regime. *Int. J. Mult. Flow*, 24:889–912, 1998.

[20] R.W. Claus. Direct numerical simulations of temporal evolving mixing layer subject to forcing. *NASA Technical Memorandum*, 1986.

[21] R.D. Cohen. Effect of viscosity on drop breakup. *Int. J. Mult. Flow*, 20:211–216, 1994.

[22] A.A. Amsden C.W. Hirt and J.L. Cook. An arbitrary lagrangian-eulerian computing method for all flow speeds. *J. Comp. Phys.*, 14:227–253, 1974.

[23] S. Marty S. Popinet J. Hoepffner A. Cartellier D. Fuster, J.P. Matas and S. Zaleski. Instability regimes in the primary breakup region of planar coflowing sheets. *Cambridge University Press*, 736:150–176, 2013.

[24] A. Nadim R. Scardovelli D. Gueyffier, J. Li and S. Zaleski. Volume-of-fluid interface tracking with smoothed surface stress methods for three- dimensional flows. *J. Comp. Phys.*, 152:423456, 1999.

[25] R. Liu D. Lycett-Brown, K.H. Luo and P. Lv. Binary droplet collision simulations by a multiphase cascaded lattice boltzmann method. *Phys. Fluids*, 26:023–303, 2014.

[26] Z. Dai and G.M. Faeth. Temporal properties of secondary drop breakup in the multimode breakup regime. *Int. J. Mult. Flow*, 27:217–236, 2001.

[27] J. Belanger D.D. Joseph and G.S. Beavers. Break up of a liquid drop suddenly exposed to a high-speed airstream. University of Minnesota.

[28] M.T. Deng. *LES combined with statistical model of spray formation closely to airblast atomizer.* PhD thesis, Leon University, 2011.

[29] O. Desjardins and H. Pitsch. A spectrally refined interface approach for simulating multiphase flows. *J. Comp. Phys.*, 228:1658–1677, 2009.

[30] N. Dimela and S. Navarro-Martinez. Surface density evolution in liquid breakup. volume 1. ICLASS 2015, 13th Triennial International Conference on Liquid Atomization and Spray Systems, August 2015.

[31] P.E. Dimotakis. Two-dimensional shear layer entrainment. *J. American Institute of Aeronautics and Astronautics*, 24:1791–1796, 1986.

[32] M.R. Davidson D.J.E. Harvie and M. Rudman. An analysis of parasitic current generation in volume of fluid simulations. *J. Australian Math. Society*, 46:133–149, 2005.

[33] R. Samtaney D.R. Reynolds and C.S. Woodward. A fully implicit numerical method for single-fluid resistive magnetohydrodynamics. *J. Comp. Phys.*, 219:144–162, 2006.

[34] R.H.J. Willden E. Ferrer, D. Moxey and S.J. Sherwin. Stability of projection methods for incompressible flows using high order pressure-velocity pairs of same degree: Continuous and discontinuous galerkin formulations. Global Science Preprint.

[35] G. Brenner E. Monaco and K.H. Lup. Numerical simulation of the collision of two microdroplets with a pseudopotential multiple-relaxation-time lattice boltzmann model. *Microfluidics and Nanofluidics*, 16:329–346, 2014.

[36] J. Eggers and E. Villermaux. Physics of liquid jets. *Reports on Progress in Physics*, 71, 2008.

[37] H. Mrema F. Ferguson and M. Dhanasar. The performance evaluation of an improved finite volume method for solving the navier-stokes equation. In *53rd AIAA Aerospace Sciences Meeting*, 2015.

[38] G.M. Faeth. Structure and atomisation properties of dense turbulent sprays. In *23rd Symposium on Combustion*, pages 1345–1352, 1990.

[39] Z. Farago and N. Chigier. Morphological classification of disintegration of round liquid jets in a coaxial air stream. *Atom. and Spray*, 2:137–153, 1992.

[40] J.H. Ferziger and M. Peric. *Computational Methods for Fluid Dynamics*. Springer, 3rd edition, 2013.

[41] T. Frank. Advances in computational fluid dynamics (cfd) of 3-dimensional gas-liquid multiphase flows. Germany, April 2005.

[42] G.H. Yeoh G. Keshavarzi and T. Barber. Comparison of the vof and clsvof methods in interface capturing of a rising bubble. *J. Computational Multiphase Flows*, 5:43–55, 2012.

[43] S. Zaleski G. Tomar, D. Fuster and S. Popinet. Multiscale simulations of primary atomization. *Computers & Fluids*, 39:1864–1874, 2010.

[44] A. Esmaeeli D. Juric N. Al-Rawahi W. Tauber J. Han S. Nas G. Tryggvason, B. Bunner and Y.J. Jan. A front tracking method for the computations of multiphase flow. *J.Comp.Phys*, 169:708–759, 2001.

[45] B.E. Gelfand. Droplet breakup phenomena in flows with velocity lag. *Energ. Combust.*, 22:201–265, 1996.

[46] R. Goldman. Curvature formulas for implicit curves and surfaces. *Computer Aided Geometric Design*, 22:632–658, 2005.

[47] V.R. Gopala and B.G.M. van Wachem. Volume of fluid methods for immiscible-fluid and free-surface flows. *J. Chem. Eng.*, 141:204–221, 2007.

[48] W.F. Li H. Zhao, H.F. Liu and J.L. Xu. Morphological classification of low viscosity drop bag breakup in a continuous air jet stream. *Phys. Fluids*, 22, 2010.

[49] J. Han and G. Tryggvason. Secondary breakup of axisymmetric liquid drops. ii. impulsive acceleration. *Phys. Fluids*, 13, 2001.

[50] J. Han and G. Tryggvason. Secondary breakup of liquid drops in axisymmetric geometry. i. constant acceleration. *Phys. Fluids*, 11:3650–3667, 2001.

[51] F. H. Harlow and J. E. Welch. Numerical calculation of time-dependent viscous incompressible flow of fluid with free surface. *Phys. Fluids*, 8:2182–2189, 1965.

[52] G. Hassler. Breakup of large water drops under the influence of aerodynamic forces in a steady stream at subsonic velocities. In *3rd Int. Conf. on Rain Erosion and Related Phenomena*, 1970.

[53] B.T. Helebrook. Numerical studies of droplet deformation and break up. In *Americas 14th Annual Conference of Liquid Atomization and Spray Systems*. ILASS, 2001.

[54] M. Herrmann. A balanced force refined level set grid method for two-phase flows on unstructured flow solver grids. *J. Comp. Phys.*, 227:2674–2706, 2008.

[55] C.W. Hirt and B.D. Nichols. Volume of fluid (vof) method for the dynamics of free boundaries. *J. Comp. Phys.*, 39:201–225, 1981.

[56] J.W. Hoyt and J.J. Taylor. Waves on water jets. *J. Fluid Mech.*, 83:119–127, 1997, b.

[57] L. P. Hsiang and G. M. Faeth. Near-limit drop deformation and secondary break up. *Int. J. Mult. Flow*, 18(5):635–652, 1992.

[58] L.P. Hsiang and G.M. Faeth. Drop deformation and breakup due to shock wave and steady disturbances. *Int. Journal. Multiphase Flow*, 21:545–560, 1995.

[59] Y.J. Ren I. Elishakoff and M. Shinozuka. Improved finite element method for stochastic problems. *Chaos, Solitons & Fractals*, 5:833–846, 1995.

[60] X.Y. Hu J. Luo and N.A. Adams. A conservative sharp interface method for incompressible multiphase flows. *J. Comp. Phys.*, 284:547–565, 2015.

[61] G.S. Jiang and D. Peng. Weighted eno schemes for hamilton-jacobi equations. *J. Sci. Comp.*, 21:2126–2143, 2000.

[62] D.B. Kothe J.U. Brackbill and C. Zemach. A continuum method for modelling surface tension. *J. Comp. Phys.*, 100:335–354, 1992.

[63] Y. Yang K. Luo, C. Shao and F. Jianren. A mass conserving level set method for detailed numerical simulation of liquid atomization. *J. Comp. Phys.*, 298:495–519, 2015.

[64] H.P. Langtangen. Solving nonlinear ode and pde problems. Center for Biomedical Computing, Simula Research Laboratory and Department of Informatics, University of Oslo, 2016.

[65] J.C. Lasheras and E.J. Hopfinger. Liquid jet instability and atomization in a coaxial gas stream. *Annu. Rev. Fluid Mech.*, 23:275–308, 2000.

[66] B.P. Leonard. Simple high-accuracy resolution program for convective modeling of discontinuities. *Int. J. Num. Methods Fluids*, 8:1291–1318, 1988.

[67] S.P. Lin and R.D. Reitz. Drop and spray formation from a liquid jet. *Annual Review Fluid Mech.*, 30:85–105, 1998.

[68] B. Srinivasan M. Georg and A. Jameson. An improved gas-kinetic bgk finite-volume method for three-dimensional transonic flow. *J. Comp. Phys.*, 220:856–878, 2007.

[69] L. Wu M. Huang and B. Chen. A piecewise linear interface-capturing volume-of-fluid method based on unstructured grids. *Num. Heat Transfer, Part B:Fundamentals*, 61:412–437, 2012.

[70] M. Behbahaninejad G. Ahmadi M. Mahdavimanesh, A.R. Noghrehabadi and M. Dehghanian. Lagrangian particle tracking: Model development. *J. Life Science*, 10:34–41, 2013.

[71] P. Smereka M. Sussman and S. Osher. A level set aproach for computing solutions to incompressible two-phase flows. *J. Comp. Phys.*, 114:146–159, 1994.

[72] E. Maitre. Review of numerical methods for free interfaces. 2006.

[73] P. Marmottant. *Atomisation dun liquide par un courant gazeux.* PhD thesis, Institut National Polytechnique de Grenoble., 2001.

[74] P. Marmottant and E. Villermaux. On spray formation. *J. Fluid Mech.*, 498:73–111, 2004.

[75] J. McCaslin and O. Desjardins. A localised reinitialisation equation for the conservative level set method. *J. Comp. Phys.*, 2014.

[76] G.H. McKinley and M. Renardy. Wolfgang von ohnesorge. Massachusetts Institute of Technology, 2011.

[77] O. Desjarding M.G. Pai, I. Bermejo-Moreno and H. Pitsch. Role of weber number in primary break up of trubulent liquid jets in crossflow. *Center of Turb. Research*, 2009.

[78] J.J. Monaghan. Smoothed particle hydrodynamics. *Institute of Physics*, 68:1703–1759, 2005.

[79] A.K.B. Hong A.Y.N. Yassin N. Rusli, E.H. Kasiman and N. Amin. Numerical computation of a two-dimensional navier-stokes equation using an improved finite difference method. *Matematika*, 27:1–9, 2011.

[80] S. Navarro-Martinez. Large eddy simulation of spray atomization with a probability density function method. *Int. J. Mult. Flow*, 2014.

[81] W.F. Noh and P.R. Woodward. Slic (simple line interface calculation). *Springer*, 59:330340, 1976.

[82] R. Nourgaliev and T. Theofanous. High-fidelity interface tracking in compressible flows: Unlimited anchored adaptive level set. *J. Comp. Phys.*, 224:836–866, 2007.

[83] M. Owkes O. Desjardin, J. McCaslin and P. Brady. Direct numerical and large-eddy simulation of primary atomisation in complex geometries. *Atom. and Sprays*, 11:1001–1048, 2013.

[84] V. Moureau O. Desjardins and H. Pitsch. An accurate conservative level set/ghost fluid method for simulating turbulent combustion. *J. Comp. Phys.*, 227:8395–8416, 2008.

[85] N.A. Patankar and D.D. Joseph. Lagrangian numerical simulation of particulate flows. *Int. J. Mult. Flow*, 27:1685–1706, 2001,b.

[86] C. S. Peskin. The immersed boundary method. *Acta Numerica*, 11:479–517, 2002.

[87] M. Pilch and C.A. Erdman. Use of break up time date and velocity history data to predict the maximum size of stable fragments for acceleration-induced break up of a liquid drop. *Int. J. Mult. Flow*, 13:741–757, 1987.

[88] J.E. Pilliod and E. G.Puckett. Second-order accurate volume-of-fluid algorithms for tracking material interfaces. *J. Comp. Phys.*, 2:465–502, 2004.

[89] L.K. Tseng P.K. Wu and G.M. Faeth. Primary breakup in gas/liquid mixing layers for turbulent liquid. *Atom. and Spray*, 2:295–317, 1992.

[90] T. Pringuey. *Large Eddy Simulation of Primary Liquid-Sheet Break Up.* PhD thesis, University of Cambridge, 2012.

[91] B. Merriman R. Fedkiw, T. Aslam and S. Osher. A non-oscillatory eulerian approach to interfaces in multimaterial flows (the ghost fluid method). *J. Comp. Phys.*, 152:457–492, 1999.

[92] A.A. Ranger and J.A. Nicholls. Aerodynamic shattering of liquid drops. *J. American Institute of Aeronautics and Astronautics*, 1969.

[93] R. Rannacher. Finite element methods for the incompressible navier-stokes equations. Institute of Applied Mathematics, 1999.

[94] B.F. Rayana. *Contribution a l'etude des instabilites interfaciales liquide-gaz en atomisation assistee et taille de gouttes.* PhD thesis, Institut National Polytechnique de Grenoble., 2007.

[95] L. Raynal. *Instabilite et entranement a linterface dune couche de melange liquide-gaz.* PhD thesis, Universite Joseph Fourier, Grenoble, 1997.

[96] W. Reinecke and G.D. Waldman. A study of drop breakup behind strong shocks with applications to flight. *AVCO Government Products Report*, 1970.

[97] M. Rudman. Volume tracking methods for interfacial flow calculations. *Int. J. Numer. Meth. Fluids*, 24:671–691, 1997.

[98] D.B. Johnson S. Chen and P.E. Raad. The surface marker method. 1:223–234, 1991.

[99] S.K. Mattha C. Zoppou S. Geiger, S. Roberts and A. Burri. Combining finite element and finite volume methods for efficient multiphase flow simulations in highly heterogeneous and structurally complex geologic media. *Geofluids*, 4:284–299, 2004.

[100] C. Vuik S. Van der Pijl, S.P. Segal and P. Wesseling. A mass-conserving level-set method for modelling of multi-phase flows. *Int. J. Num. Methods Fluids*, 47:339–361, 2005.

[101] A. Salih and S. Ghosh. Some numerical studies of interface advection properties of level set method. *Sadhana*, 34(2), 2009.

[102] R. Scardovelli and G. Tryggvason. *Direct Numerical Simulations of Gas-Liquid Multiphase Flows.* Cambridge, 2011.

[103] R. Scardovelli and S. Zaleski. Direct numerical simulation of free-surface and interfacial flow. *Annu. Rev. Fluid Mech.*, 31:567–603, 1999.

[104] I.A. Segal. Finite element methods for the incompressible navier-stokes equations. Research School for Fluid Mechanics.

[105] J.A. Sethian. Theory, algorithms, and applications of level set methods for propagating interfaces. *Acta Numerica*, 1995.

[106] C.W. Shu and S. Osher. Efficient implementation of essentially non-oscillatory shock-capturing schemes. *J. Comp. Phys.*, 77:439–471, 1988.

[107] I. Skuratovsky and A. Levy. Finite volume approach for solving multiphase flows in vertical pneumatic dryers. *Int. J. Num. Methods for Heat & Fluid Flow*, 14(8), 2004.

[108] D.M. Snider. An incompressible three-dimensional multiphase particle-in-cell model for dense particulate flows. *J. Comp. Phys.*, 170:523–549, 2001.

[109] G. Son. Efficient implementation of a coupled level-set and volume-of-fluid method for three-dimensional incompressible two-phase flows. *Numerical Heat Transfer Part B*, 43:549–565, 2003.

[110] M. Sussman and E. G. Puckett. A coupled level set and volume-of-fluid method for computing 3d and axisymmetric incompressible two-phase flows. *J. Comp. Phys.*, 162:301–337, 2000.

[111] J. Aubin T. Abadie and D. Legendre. On the combined effects of surface tension force calculation and interface advection on spurious currents within volume of fluid and level set frameworks. *J. Comp. Phys.*, 297:611–636, 2016.

[112] S. Tanguy T. Menard and A. Berlemont. Coupling level set/vof/ghost fluid methods: Validation and application to 3d simulation of the primary break-up of a liquid jet. *Int. J. Mult. Flow*, 33:510–524, 2007.

[113] N. Takemitsu. Finite difference method to solve incompressible fluid flow. *J. Comp. Phys.*, 61:499–518, 1985.

[114] K. Takizawa and T. Tezduyar. Space-time interface-tracking with topology change (st-tc). *Comp. Mechanics*, 54:955–971, 2014.

[115] G. I. Taylor. *The shape and acceleration of a drop in a high-speed air stream.* Cambridge University Press, 1949.

[116] T. E. Tezduyar. Interface-tracking and interface-capturing techniques for computation of moving boundaries and interfaces. *Comp. Mechanics*, pages 5–10, 2004.

[117] G.J. Li T.G. Theofanous and T.N. Dinh. Aerobreakup in rarefied supersonic gas flows. *J. Fluid Eng.*, 126:516527, 2004.

[118] T.N. Dinh T.G. Theofanous, G.J. Li and C.H. Chang. Aerobreakup in disturbed subsonic and supersonic flow fields. *J. Fluid Mech.*, 593:131–170, 2007.

[119] T.G. Theofanous. Aerobreakup of newtonian and vicoelastic liquids. *Annu. Rev. Fluid Mech.*, 43:661690, 2011.

[120] N.A. Trask. *Implementation of an Eulerian Atomization Model to characterize primary spray formation.* PhD thesis, University of Masschusetts, 2010.

[121] O. Ubbink. *Numerical prediction of two fluid systems with sharp interfaces.* PhD thesis, Imperial College of Science, Technology & Medicine, 1997.

[122] A. Ovsyannikov V. Sabelnikov and M. Gorokhovski. Modified level set equation and its numerical assessment. *J. Comp. Phys.*, 278:1–30, 2014.

[123] H. K. Versteeg and W. Malalasekera. *An Introduction to Computational Fluid Dynamics: The Finite Volume Method.* Pearson Education Limited, 1995.

[124] E. Villermaux. Mixing and spray formation in coaxial jets. *J. Propulsion and Power*, 14:807–817, 1998.

[125] M. Marekb W. Aniszewskia, A. Bogusawskib and A. Tyliszczakb. A new approach to sub-grid surface tension for les of two-phase flow. *J. Comp. Phys.*, 2014.

[126] J.H. Snoeijer M. Versluis M.P. Brenner W. van Hoeve, S. Gekle and D. Lohse. Break up of diminutive rayleigh jets. *Phys. Fluids*, 2010.

[127] T. Waclawczyk and T. Koronowicz. Comparison of cicsam and hric high-resolution schemes for interface capturing. *J. Theor. and Applied Mech.*, 46(2):325–345, 2008.

[128] Y. Wang. *Solving incompressible Navier-Stokes equations on heterogeneous parallel architectures.* PhD thesis, Universite Paris-Sud, 2015.

[129] L.P. Hsiang W.H. Chou and G.M. Faeth. Temporal properties of drop breakup in the shear breakup regime. *Int. J. Mult. Flow*, 27:217–236, 1997.

[130] F. Xiao. *Large Eddy Simulation of liquid jet primary breakup.* PhD thesis, Loughborough University, 2012.

[131] D. Fuster S. Zaleski G. Tryggvasson Y. Ling, T. Arrufat and R. Scardovelli. Turbulent multiphase flow characteristics in gas assisted atomisation. 13th Triennial International Conference on Liquid Atomization and Spray Systems, Tainan, Taiwan, 2015.

[132] G. Tryggvason Y. Ling, D. Fuster and S. Zaleski. Spray formation: a numerical closeup. *Cornell University E-Prints*, 2015.

[133] M. Yun. Numerical studies on hamilton-jacobi equation in non-orthogonal coordinates. *J. Appl. Math & Computing*, 21:603–622, 2006.

[134] M.R.G. Zoby. *Liquid Droplets and Gas Interactions in Two-Phase Flow.* PhD thesis, Imperial College of Science, Technology & Medicine, 2010.

Appendix A

Basic Equations

The basic principles of mass, momentum and energy conservation can be expressed, which can yield the fluid flow governing equations.

A.1 Mass Conservation

Consider a volume V, fixed in space, where any mass changes within the volume occurs if mass flows in/out through the boundary S, Fig. A.1. Mass conservation states that inflow should balance outflow volume and can be described by:

$$\frac{d}{dt}\int_V \rho \, dv = -\oint_S \rho \mathbf{u} \cdot \mathbf{n} \, ds \tag{A.1}$$

which is the mass conservation equation in integral form, for incompressible flows. The mass flow out of the volume, through surface element ds is $\rho u \cdot n ds$, where ρ is the density, u the velocity and n the outward normal. Hence, the mass conservation principle is:

$$\frac{\partial \rho}{\partial t} + \nabla \cdot (\rho \mathbf{u}) = 0 \tag{A.2}$$

Where the left-hand side is the rate of mass change in V and right-hand side the net flow through S. Then, by employing the *divergence theorem* for the fluxes through S and the derivative within the integral, one obtains:

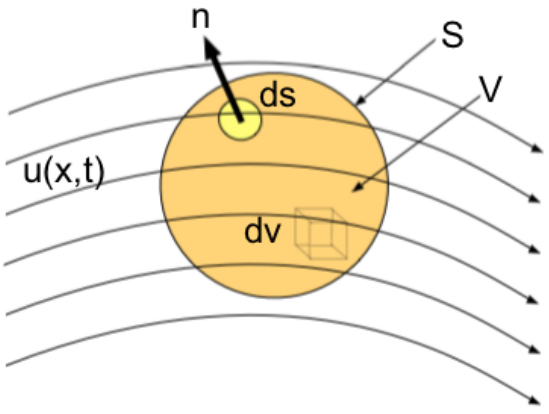

Fig. A.1: Fixed control volume V, showing surface S and flow passing through it.

A.2 Momentum Conservation

Employing the momentum conservation, one can obtain the motion equation. The momentum conservation states that in a fixed control volume V, the fluid momentum change rate is the difference in the flux momentum across S along with the net forces acting on V, as follow:

$$\frac{\partial}{\partial t}\int_V \rho \mathbf{u} dv = -\oint_S \rho \mathbf{u}(\mathbf{u}\cdot\mathbf{n})ds + \int_V \mathbf{f} dv + \oint_S \mathbf{n}\cdot\mathbf{T} ds \tag{A.3}$$

In (A.3) the first term in the right is the flux momentum through S [102]. The first term in the left-hand side is the total body force n V and the last term is the total surface force. Note, f is the force per unit V and is usually the gravitational force so that $f = \rho g$. Recalling the argument from (A.2) then (A.3) must hold for every point in the fluid flow [102]. Therefore:

$$\frac{\partial \rho}{\partial t} = -\nabla\cdot(\rho u u) + f + \nabla\cdot T \tag{A.4}$$

Then by combining the substantial derivative definition and continuity equation one obtains:

$$\rho\frac{Du}{Dt} = f + \nabla\cdot T \tag{A.5}$$

Also known as the *Cauchy's equation of motion*. Note, (A.5) is true for any continuous medium. Here, T is the stress, p is the pressure, I is the unit tensor and μ the viscosity. Note, S is the strain rate and is $S = \frac{1}{2}(\nabla u + \nabla u^T)$ [102]. Finally, λ is viscosity's second coefficient. Combining T expression with (A.5), one gets:

$$\rho\frac{Du}{Dt} = \mathbf{f} - \nabla p + \nabla(\lambda\nabla\cdot\mathbf{u}) + \nabla\cdot(2\mu S) \tag{A.6}$$

Also known as the NS equation for Fluid Flow.

A.3 Interface Motion

Considering the interface location of a curve in 2D, reading $x(\alpha) = (x(\alpha), y(\alpha))$, separating two fluids Fig. A.2, then $d\mathbf{x}/du$ returns a vector tangent to the curve with $ds^2 = dx^2 + dy^2$. As a result, $\mathbf{t} = d\mathbf{x}/ds$ is the unit tangent and $|d\mathbf{x}/ds| = 1$. Finally, the unit normal $\mathbf{n}$ is perpendicular to the curve, so that $\mathbf{t} \cdot \mathbf{n} = 0$. Note, the normal orientation is arbitrary [102].

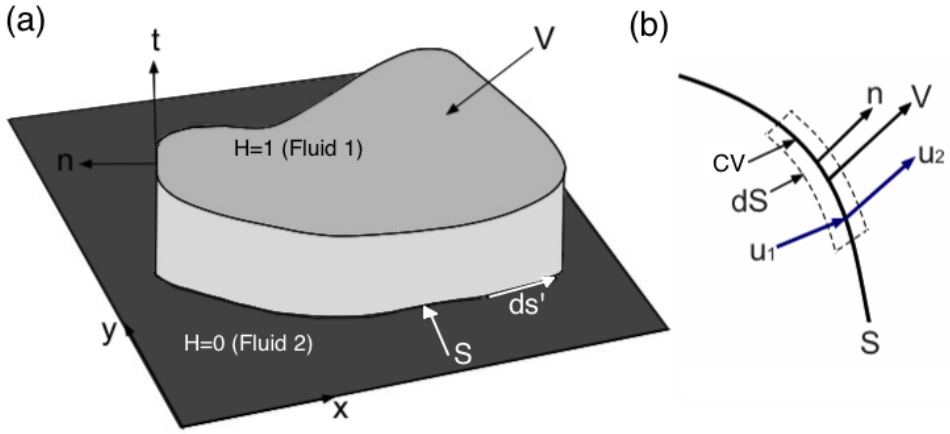

Fig. A.2: Demonstration of (a) the Heaviside step function separating two fluids and (b) a portion of the interface S in a control volume (CV) with its boundary (δS).

A.4 Convective and Diffusive Term

- **Convective Term:** Regarding for instance the x-momentum, the Convective Term is of:

$$CONV = \frac{\partial \rho u^2}{\partial x} + \frac{\partial \rho uv}{\partial y} + \frac{\partial \rho uw}{\partial z} \tag{A.7}$$

  Which regards the normal plus the cross terms. With respect to Fig. **??**, in the x-direction one gets:

$$\frac{\partial \rho uu}{\partial x} \approx \frac{\rho_r u_r u_r - \rho_l u_l u_l}{\Delta x_P} = \frac{\rho_r u_r}{\Delta x_P}\left(\frac{u_P + u_R}{2}\right) - \frac{\rho_l u_l}{\Delta x_P}\left(\frac{u_P + u_L}{2}\right) \tag{A.8}$$

- **Diffusive Term:** The Diffusive term on x-momentum is:

$$DIFF = \frac{\partial}{\partial x}\left(\Gamma \frac{\partial \phi}{\partial x}\right) \tag{A.9}$$

Appendix B

Finite Volume Methods (FV)

Consider the generic conservation equation for ϕ, where all fluid properties and the velocity field are known. In FV the integral form of the conservation equation is initially employed as:

$$\int_S \rho\phi\mathbf{u}\cdot\mathbf{n}dS = \int_S \Gamma grad\phi\cdot\mathbf{n}dS + \int_\Omega q_\phi d\Omega \tag{B.1}$$

Note, the solution domain for FV is subdivided to a finite number of small CVs. For this analysis one can consider the Staggered grid demonstrated in Chapter 3. FV methods hence approximate the values at the CV face centre.

B.1 Upwind Difference Scheme (UDS)

Considering the ϕ_e approximation, at the node 'e', it can be compared to employing *backward* or *forward difference* approximation, see Chapter 3, for the 1st derivative, with respect to the flow direction. So, in UDS, ϕ_e approximation is:

$$\begin{cases}\phi_P & if \quad (\mathbf{u}\cdot\mathbf{v})_e > 0\\ \phi_E & if \quad (\mathbf{u}\cdot\mathbf{v})_e < 0\end{cases} \tag{B.2}$$

This approximation satisfies strictly the boundedness criteria unconditionally, thus none oscillatory solution [40]. However, it is numerically diffusive. Now, considering Taylor series expansion with respect to P, one gets:

$$\phi_e = \phi_P + (x_e - x_P)\left(\frac{\partial\Phi}{\partial x}\right)_P + \frac{(x_e - x_P)^2}{2}\left(\frac{\partial^2\Phi}{\partial x^2}\right)_P + H \tag{B.3}$$

with H representing higher-order terms. Note, UDS approximation detains the first terms on the RHS, only, hence UDS is a first order scheme and its truncation error term is diffusive, featuring a diffusive flux [40].

Appendix C

Staggered Arrangement

There are two main grid arrangements employed by discretisation methods, the Colocated and the Staggered arrangement. In the Colocated, all the variables are stored in the cell nodes. This results to pressure oscillations in the order of Δx, which requires the use of a smoothing function. The Staggered arrangement, initially introduced by Harlow and Welch (1965) [102], begins by choosing a CV around the pressure points, Fig. C.1.

In incompressible flows, the pressure is employed to enforce the velocity field divergence to zero. If net inflow is increased in the CV, the pressure must be increased and vice versa in case of net outflow. Here, the CV centre stores the scalars, thus pressure, density and viscosity. Meanwhile, the velocity components required for the diffusive terms, are stored at the middle of the CV faces. The x-velocity is displaced on the right by half a grid cell and similarly the y-velocity by half a grid cell upwards. The mass fluxes computation in the continuity equation can be done directly.

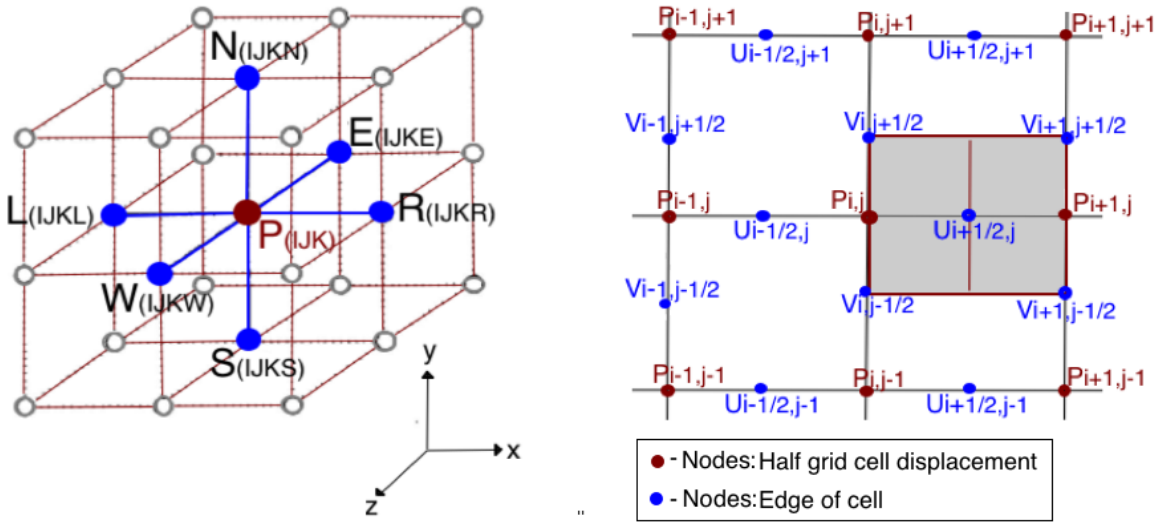

Fig. C.1: Staggered grid arrangement in three-dimensions (left), along with the grid locations of the stored scalars and velocities, in two-dimensions (right).

Appendix D

Boundary Conditions

The Boundary Conditions (BC) implemented are of crucial importance as they can significantly effect each case under investigation. In this in-house code, the main boundary conditions employed are Inflow, Outflow (or Convective), Air Flow, Slip Wall/Symmetry Line, Non-Slip and Periodic and applied in a Staggered grid.

Inflow
For both single- and multi- phase flow, the literature has shown that the inlet conditions can majorly affect the predicted flow development. In incompressible flows, the velocity inlet and the pressure inlet/outlet, are the most crucial to permit the flow to enter and exit the domain appropriately. This results from the disturbance of a fixed mean velocity field at the inlet. In a Staggered grid, the normal velocities and the pressure BC are rather simple. In staggered grids the boundaries coincide with the normal velocities location. The tangential velocity however needs to be treated with extra care as its located half a grid space from the walls. To overcome this, ghost points are employed and given a wall velocity, the tangential velocity is described by linear interpolation [102].

Outflow
The outflow boundary can significantly affect the computational solution in cases where the outflow varies a lot. It is usually desirable to use a long domain so that the outflow BC shall not affect the flow region under investigation. In this work, the outflow BC is mostly treated with Convective outflow, using

$$\frac{\partial \mathbf{u}^*}{\partial t} + U_{CON}\frac{\partial \mathbf{u}^*}{\partial n} = 0 \tag{D.1}$$

where U_{CON} is an advection velocity and n denotes the normal direction to the outer boundary.

Wall

At the Wall the BC can be classified between slip or non-slip wall. Generally speaking, staggered grids enable easy treatment of the pressure and normal velocity conditions, however the tangential velocity must be treated more carefully. So considering point $v_{i,j+1/2}$, then the left node velocity ($v_{i-1,j+1/2}$) must be obtained. However, the latter node is not included in the boundary, hence ghost points method must be employed. In cases of incompressible viscous fluids, it is important for the fluid to stick to the wall, thus one needs the fluid velocity to match the wall velocity. To obtain Slip Wall boundary, the ghost point velocity must equal the domain velocity. As a result, and by employing CDS approximation, the tangential velocity will then be zero and the boundary will read $v_{i-1,j+1/2} = v_{i,j+1/2}$. For Non-slip the ghost point velocity (as described for inflow BC). In this case must equal the wall velocity ($\mathbf{u} = U_{WALL}$) which now reads $v_{i-1,j+1/2} = 2v_{B,j+1/2} - v_{i,j+1/2}$. Here, $v_{B,j+1/2}$ is the tangential wall velocity obtained by linear interpolation applied at the ghost points.

Periodic

In many cases, periodic boundary conditions are employed for simplicity. Considering for example the x-direction then the periodic BC will simply read $\mathbf{u}(x, y, z) = \mathbf{u}(x + L, y, z)$, where L is the period length and the formula can easily be applied for y and z directions accordingly.

Appendix E

Runge Kutta 3rd Order Scheme

The RG method in principle solves the form of $\psi_t = \mathcal{L}(\psi, t)$, where $\mathcal{L}(\psi, t)$ is a spatial discretisation operator; denoting $\mathcal{L}(\psi, t) = \vec{u} \cdot \nabla\psi$. One should note, the operator is not usually linear nor has to be. To advance the solution for ψ at time step t_{n+1}, the process is achieved in three steps as:

$$\begin{aligned} \psi^1 &= \psi^n + \Delta t\ \mathcal{L}(\psi^n, t^n) \\ \psi^2 &= \tfrac{3}{4}\psi^n + \tfrac{1}{4}\psi^1 + \tfrac{1}{4}\Delta t\ \mathcal{L}(\psi^1, t^n) \\ \psi^{n+1} &= \tfrac{1}{3}\psi^n + \tfrac{2}{3}\psi^1 + \tfrac{2}{3}\Delta t\ \mathcal{L}(\psi^2, t^n) \end{aligned} \tag{E.1}$$

where ψ^n is at t^n and Δt is the time step.

Appendix F

Hamilton-Jacobi Equations in Level Set Context

In principle, Hamilton-Jacobi systems refer to non-linear hyperbolic partial differential equations. In principle context, the simplest non-linear PDE is the nonlinear transport equation reading:

$$u_t + uu_x = 0 \tag{F.1}$$

Here the wave velocity $c = u$ depends on the disturbance size and is independent of the x position. Smaller waves are overruled by larger faster waves. For depression waves $u < 0$ (left direction motion) and for elevation waves $u > 0$ (right direction motion) [133]. One can denote a characteristic curve to (F.1); as the solution of an ODE defined as:

$$\frac{dx}{dt} = u(t, x) \tag{F.2}$$

whose characteristic curve is u solution dependent which is characteristic variable based; resulting in a circular 'system'. Now, similarly in the Level Set context, solution of the reinitialisation equation results in discontinuous derivatives integrated in a continuous solution [133]. The two-dimensional HJ equation, Eqn. (2.65) discretisation yields:

$$\psi_{i,j}^{n+1} = \psi_{i,j}^{n} - \Delta t S(\psi_{i,j}^{0}) G(\psi)_{i,j} \tag{F.3}$$

with

$$G(\psi)_{i,j} = \begin{cases} \sqrt{max(\alpha_+^2, b_-^2) + max(c_+^2, d_-^2)} - 1 & if \quad \psi_{i,j}^0 > 0 \\ \sqrt{max(\alpha_-^2, b_+^2) + max(c_-^2, d_+^2)} - 1 & if \quad \psi_{i,j}^0 < 0 \end{cases} \tag{F.4}$$

Where the nearby grid point gradients read:

$$\begin{aligned} \alpha &= D_x^- \psi_{i,j} = \tfrac{\psi_{i,j} - \psi_{i-1,j}}{\Delta x}, \qquad b = D_x^+ \psi_{i,j} = \tfrac{\psi_{i+1,j} - \psi_{i,j}}{\Delta x} \\ c &= D_y^- \psi_{i,j} = \tfrac{\psi_{i,j} - \psi_{i,j-1}}{\Delta y}, \qquad d = D_y^+ \psi_{i,j} = \tfrac{\psi_{i,j+1} - \psi_{i,j}}{\Delta y} \end{aligned} \tag{F.5}$$

Appendix G

Implicit Function Theorem

In an implicit planar curves formulation, the curvature is of second order; denoting that the first and second derivatives appear [46]. Curvature is only gradient $\vec{\nabla F}$ and hessian $\mathbf{H}(F)$ dependent, in implicit planar curves $F(x, y) = 0$; the relative notation in two-dimensions reads:

$$\begin{aligned} \vec{\nabla F} &= \left(\tfrac{\partial F}{\partial x} \ \tfrac{\partial F}{\partial y}\right) = (F_x \ F_y), \\ \mathbf{H}(F) &= \begin{pmatrix} \frac{\partial^2 F}{\partial x^2} & \frac{\partial^2 F}{\partial x \partial y} \\ \frac{\partial^2 F}{\partial x \partial y} & \frac{\partial^2 F}{\partial y^2} \end{pmatrix} = \left(\begin{smallmatrix} F_{xx} & F_{xy} \\ F_{yx} & F_{yy} \end{smallmatrix}\right) = \nabla(\vec{\nabla F}) \end{aligned} \tag{G.1}$$

Here, $F(x, y)$ gradient is perpendicular to the level curves, $F(x, y) = c$, whilst the $\vec{\nabla F}$ gradient is parallel to the $F(x, y) = 0$ normal [46]. Thus $\vec{\nabla F} = (F_x, F_y)$ and the unit normal is:

$$\mathbf{n} = \frac{\nabla F}{|\nabla F|} = \frac{(F_x, F_y)}{\sqrt{F_x^2 + F_y^2}} \tag{G.2}$$

Meanwhile the tangent reads $\mathbf{t}(F) = \kappa \times \nabla F = (-F_y, F_x)$ and the unit tangent yields:

$$\mathbf{t}(F) = \frac{tan(F)}{|\tan(F)|} = \frac{(-F_y, F_x)}{\sqrt{F_x^2 + F_y^2}} \tag{G.3}$$

Thus the implicit planar curvature [46] reads:

$$\kappa = -\frac{T(F) * \mathbf{H}(F) * T(F)^T}{|\vec{\nabla F}|} = -\frac{(-F_y, F_x) * \left(\begin{smallmatrix} F_{xx} & F_{xy} \\ F_{yx} & F_{yy} \end{smallmatrix}\right) * \left(\begin{smallmatrix} -F_y \\ F_x \end{smallmatrix}\right)}{(F_x^2 + F_y^2)^{3/2}} \tag{G.4}$$